# *Tuning the Magnetocaloric Properties of Nanomagnetic Materials for Magnetic Refrigerant Applications*

*Thesis submitted to*

***University of Calicut, Kerala***

*in partial fulfillment of the requirements*
*for the award of the degree of*

***DOCTOR OF PHILOSOPHY IN PHYSICS***

*Under the Faculty of Science*

*by*

***Smitha Bhaskaran***

*Under the guidance*

*of*

***Dr Veena Gopalan E***

*Assistant Professor*


*Post Graduate and Research Department of Physics*

*Vimala College (Autonomous), Thrissur-680009*

2025

# VIMALA COLLEGE

*(Autonomous)*

**THRISSUR - 680 009, KERALA, INDIA**

**Ph : +91 0487 - 2332080, 2328232**

**Visit us : www.vimalacollege.edu.in** **E-mail: mail@vimalacollege.edu.in**

*(Affiliated to the University of Calicut & Nationally Re-accredited with A+Grade-4th Cycle)*


*Date : 27-03-2025*

## CERTIFICATE

This is to certify that the thesis entitled **"Tuning the Magnetocaloric Properties of Nanomagnetic Materials for Magnetic Refrigerant Applications"** submitted to University of Calicut in partial fulfillment of the requirements for the award of the degree of **Doctor of Philosophy in Physics** under the Faculty of Science, is a record of the authentic work carried out by Ms Smitha Bhaskaran, at Vimala College (Autonomous), Thrissur, under my guidance. The work presented in this thesis has not been submitted for any other degree or diploma of this or any other University and has undergone plagiarism check using iThenticate software at C.H.M.K. Library, University of Calicut, and the similarity index found within the permissible limit.

**Dr Veena Gopalan E**

# Declaration

I hereby declare that the work presented in the thesis entitled ***"Tuning the Magnetocaloric Properties of Nanomagnetic Materials for Magnetic Refrigerant Applications"*** is based on the original work done by me under the guidance of Dr Veena Gopalan E, Assistant Professor, Post Graduate and Research Department of Physics, Vimala College (Autonomous), Thrissur and has not been included in any other thesis submitted previously for the award of any degree. The contents of the thesis are undergone plagiarism check using iThenticate software at C.H.M.K. Library, University of Calicut, and the similarity index found within the permissible limit. I also declare that the thesis is free from AI generated content.

**SMITHA BHASKARAN**

**Dr VEENA GOPALAN E**

Thrissur

# *ACKNOWLEDGEMENT*

I wish to formally acknowledge all those whose support, guidance, and encouragement have been instrumental in the successful completion of this doctoral thesis. Their contributions have been deeply appreciated and have significantly shaped the course of this research.

I am deeply indebted to my Guide Dr. Veena Gopalan E, Assistant Professor, Post Graduate and Research Department of Physics, Vimala College (Autonomous), Thrissur whose unwavering support, inspiration, and invaluable guidance have been instrumental in shaping this research. Her inspiring mentorship and boundless patience have helped me navigate the complexities of this journey, making even the most challenging situations manageable and strengthening my commitment to this research. Her dedication, hard work, affection and keen ability to recognise and develop my potential have greatly influenced my academic journey and contributed to my achievements. I would like to extend my heartfelt gratitude and love for her presence in both my academic and personal life, and I cherish the profound impact she made on this work.

I would like to express my sincere thanks to Dr Sr Beena Jose, Principal, Vimala College (Autonomous), Thrissur, for allowing me to pursue my research work at Vimala College (Autonomous). I extend my heartfelt gratitude to the Vice Principal and former HOD of the Department of Physics, Dr Malini K A, for her inspirational talks and comforting words, which provided immense support in my research journey. With pleasure, I sincerely acknowledge Dr Mini Krishna K, HOD, Department of Physics and all the facult members, Dr Aneesh George, Dr Dhanya Johnson, Dr Jovia Jose, Dr Regina Jose, Mrs Laveena Varghese, Mr Santhosh P Jose in Physics Department. I am also grateful to the members of my doctoral committee, Dr. Antony Joseph ( Department of Physics, Calicut University) Prof..Mohamed Shahin Thayyil ( Department of Physics, Calicut University) and Dr. Hussain K, (Department of Botany, SNGS College, Pattambi) for their constructive comments and helpful suggestions which have greatly enriched this work. My sincere thanks to the Lab assistants of Physics Department, Kochechi and

Mareena chechi. I also thankfully acknowledge the support and guidance of Prof. M R Anantharaman (Rtd), Magnetics lab, Department of Physics CUSAT. I would like to extend my sincere gratitude to Dr Senoy Thomas, Assistant Professor and Ms Navya, Research scholar at Magnetics Lab CUSAT for their support during my research. I would like to express my sincere thanks to Dr Imaddin A. Al-Omari, Professor, Sultan Qaboos University for magnetic and magnetocaloric measurements. I also bestow my sincere gratitude to Mr. R Elumali, Technician Grade II, Central Instrumentation Facility, Pondicherry University for the magnetic measurements. I extend my sincere thanks to Mr. Narayanan P V, Junior Technician, SAIF, Indian Institute of Technology, Madras. My sincere thanks to Dr. Narayanan T N, Associate Professor, TIFR, Hyderabad and Mr. Anu, Technician, Inter-University Instrumentation Centre, Mahatma Gandhi University, Kottayam for HRTEM measurements. I would like to extend my heartfelt gratitude to Dr Shibu M Eappen, Scientific Officer, STIC CUSAT, for XRD, SEM and EDAX analysis. My sincere thanks are also due to Dr. Sujay Chakravarty, Scientist F, UGC-DAE-CSR center Kalpakkam node for the magneto resistance measurements. I would like to extend my heartfelt gratitude to Amala Cancer Research Center for in vitro Cytotoxicity measurements.

I should thank my co-researchers Ms Sharon, Ms Vinitha, Ms Rasmi, Ms Haripriya, Ms Rachana and Ms Aswathy for their good company and support during the long hours of experiments. Special words of thanks to the master's students under my mentorship Ms. Honey Ross, Ms Jismi, Ms Sangeetha, Ms. Athira, and Ms Aibel John. Sincere thanks to Mr. Shanu, Research Scholar, St. Thomas College, Thrissur for his support in my research work.

I also extend my sincere thanks to my colleagues at Government Vocational Higher Secondary School, Kalpakancher. for their great support . My sincere thanks to my colleagues at Government Samithy Higher Secondary School, Meladoor for their assistance in my official work, their love and great support in fulfilling my dream. My sincere thanks to Anju, my colleague and HSST for supporting me in my tough times during this research. I also extend my thanks to my friends for their love and motivation to complete my research work.

I will be grateful to my family members for enduring countless hardships to support me in pursuing my doctoral research. I have no words to express my sincere thanks to my father (Bhaskaran), and my mother (Bhaimy), to whom my research is not just my goal but their dream as well. Their unconditional love, prayers, encouragement, sacrifices, and unwavering faith in me have been my greatest source of strength. I am especially grateful to my brother (Baiju)and my sisters-in-law for their encouragement and support, which played a significant role in helping me to complete this thesis. My sincere thanks to Gourinand, nephew, for providing me with technical assistance in my research work.

Last, but not least, I would like to express my deepest gratitude and love to my beloved husband, Shanmughan A R (Ettan), whose unwavering support, patience, and encouragement have been my greatest strength throughout this research journey. I am truly grateful to have him by my side, inspiring me every step of the way. I extend my heartfelt gratitude and love to my daughter Lakshmi (Lachu) and my son Sabarinadh (Unni) whose constant support and sacrifices have played a crucial role in the completion of this research. Their patience, love, and encouragement have been my greatest sources of emotional strength and their technical assistance during this challenging journey. I dedicate this thesis to my Ettan, Lachu and Unni.

Above all I express my profound gratitude to God Almighty for His abundant blessings, granting me the strength, curiosity, and perseverance to complete this endeavour. Without His blessings and guidance, this journey would not have been possible.

**Smitha Bhaskaran**

# *ABSTRACT*

Magnetic refrigeration based on the magnetocaloric effect is becoming an emerging technology to replace conventional gas compression refrigeration as it is environmentally friendly, compact and highly efficient. Materials with magnetocaloric properties close to room temperature will be preferred for residential and commercial use as magnetic refrigerants. This research explores synthesis, characterisation and magnetocaloric properties of perovskite manganites, ferrites and nanocomposites. The structural, compositional, magnetic and magnetocaloric properties of the lanthanum sodium manganite ($La_{0.5}Na_{0.5}MnO_3$) and cobalt substituted lanthanum sodium manganite ($La_{0.5}Na_{0.5}Co_xMn_{1-x}O_3$) in the perovskite system, cobalt substituted copper ferrite ($Cu_xCo_{1-x}Fe_2O_4$) and zinc substituted copper ferrite ($Cu_xZn_{1-x}Fe_2O_4$) in the ferrite system and cobalt polystyrene nanocomposites samples are investigated by employing X-ray diffraction (XRD), Transmission Electron Microscopy (TEM), Fourier-transform Infrared spectroscopy (FTIR), Energy-Dispersive X-ray spectroscopy (EDAX), and Vibrating Sample Magnetometry (VSM). The magnetocaloric properties of the samples are analysed around the transition temperature which is determined by Zero Field Cooled and Field Cooled (ZFC-FC) measurements. The magnetic entropy change is estimated from the magnetisation isotherms taken around the transition temperature and hence identified a potential magnetic refrigerant material near room temperature and lower temperatures.

Keywords

1. Transition temperature
2. Magnetocaloric effect
3. Magnetic entropy change
4. Adiabatic temperature change
5. Magnetic cooling
6. Magnetic refrigerator

# *ABSTRACT (Malayalam)*

പരമ്പരാഗത ഗ്യാസ് കംപ്രഷൻ റഫ്രിജറേഷനു പകരം ഉപയോഗി ക്കാവുന്ന ഒരു പുതിയ സാങ്കേതികവിദ്യയായി മാഗ്നെറ്റോകലോറിക് ഇഫക്റ്റിനെ അടിസ്ഥാനമാക്കിയുള്ള മാഗ്നെറ്റിക് റഫ്രിജറേഷൻ മാറിക്കൊണ്ടിരിക്കുന്നു, കാരണം അത് പരിസ്ഥിതി സൗഹൃദവും, ഒതുക്കമുള്ളതും, ഉയർന്ന കാര്യക്ഷമതയുള്ളതുമാണ്. അന്തരീക്ഷ താപനിലയോട് അടുത്ത് മാഗ്നെറ്റോകലോറിക് ഗുണങ്ങളുള്ള വസ്തുക്കൾ മാഗ്നെറ്റിക് റഫ്രിജറന്റായി റെസിഡൻഷ്യൽ, വാണിജ്യ ആവശ്യങ്ങൾക്ക് മുൻഗണന നൽകും. പെറോവ്സ്കൈറ്റ് മാംഗനൈറ്റുകൾ, ഫെറൈറ്റുകൾ, നാനോകോംപോസിറ്റുകൾ എന്നിവയുടെ സിന്തസിസ്, വിശകലനം, മാഗ്നെറ്റോകലോറിക് ഗുണങ്ങൾ എന്നിവ ഈ ഗവേഷണം പര്യവേക്ഷണം ചെയ്യുന്നു. പെറോവ്സ്കൈറ്റ് സിസ്റ്റത്തിലെ ലാന്തനം സോഡിയം മാംഗനൈറ്റിന്റെയും ($La_{0.5}Na_{0.5}MnO_3$) കോബാൾട്ട് പകരമുള്ള ലാന്തനം സോഡിയം മാംഗനൈറ്റിന്റെയും ($La_{0.5}Na_{0.5}Co_xMn_{1-x}O_3$) ഘടനാപരവും കാന്തികവും മാഗ്നെറ്റോകലോറിക് ഗുണങ്ങളും, ഫെറൈറ്റ് സിസ്റ്റത്തിലെ കോബാൾട്ട് പകരമുള്ള കോപ്പർ ഫെറൈറ്റും ($Cu_xCo_{1-x}Fe_2O_4$), സിങ്ക് പകരമുള്ള കോപ്പർ ഫെറൈറ്റും ($Cu_xZn_{1-x}Fe_2O_4$), കോബാൾട്ട് പോളിസ്റ്റൈറൈൻ നാനോകോംപോസിറ്റുകളുടെ സാമ്പിളുകളും എക്സ്-റേ ഡിഫ്രാക്ഷൻ (XRD), ട്രാൻസ്മിഷൻ ഇലക്ട്രോൺ മൈക്രോസ്കോപ്പി (TEM), ഫ്യൂറിയർ-ട്രാൻസ്ഫോം ഇൻഫ്രാറെഡ് സ്പെക്ട്രോസ്കോപ്പി (FTIR), എനർജി-ഡിസ്പേഴ്സീവ് എക്സ്-റേ സ്പെക്ട്രോസ്കോപ്പി (EDAX), വൈബ്രേറ്റിംഗ് സാമ്പിൾ മാഗ്നെറ്റോമെട്രി (VSM) എന്നിവ ഉപയോഗിച്ച് പരിശോധിക്കുന്നു. സീറോ ഫീൽഡ് കൂൾഡ് ആൻഡ് ഫീൽഡ് കൂൾഡ് (ZFC-FC) അളവുകൾ വഴി നിർണ്ണയിക്കപ്പെടുന്ന സംക്രമണ താപനിലയ്ക്ക് ചുറ്റും സാമ്പിളുകളുടെ മാഗ്നെറ്റോകലോറിക് ഗുണങ്ങൾ വിശകലനം ചെയ്യുന്നു. സംക്രമണ താപനിലയ്ക്ക് ചുറ്റും എടുത്ത മാഗ്നെറ്റൈസേഷൻ ഐസോതെർമുകളിൽ നിന്നാണ് കാന്തിക എൻട്രോപ്പി മാറ്റം കണക്കാക്കുന്നത്, അതിനാൽ അന്തരീക്ഷ താപനിലയ്ക്കും താഴ്ന്ന താപനിലയ്ക്കും സമീപം ഒരു സാധ്യതയുള്ള കാന്തിക റഫ്രിജറന്റ് മെറ്റീരിയൽ തിരിച്ചറിഞ്ഞു.

**Keywords**

1. സംക്രമണ താപനില
2. മാഗ്നെറ്റോകലോറിക് പ്രഭാവം
3. മാഗ്നെറ്റിക് എൻട്രോപ്പി മാറ്റം
4. അഡിയബാറ്റിക് താപനില മാറ്റം
5. മാഗ്നെറ്റിക് കൂളിംഗ്
6. മാഗ്നെറ്റിക് റഫ്രിജറേറ്റർ

*Dedicated to my dearest Ettan, Lachu and Unni.....*

# *PREFACE*

The demand for environmentally friendly and energy-efficient cooling technologies is more critical than ever in the modern world, where rising atmospheric temperatures pose an imminent threat. Climate change is accelerated by the extensive use of conventional cooling systems, which promotes an endless cycle of increasing demands for cooling and environmental pollution. In this situation, magnetic refrigeration emerges as a promising alternative, offering an eco-friendly and highly efficient cooling mechanism based on the magnetocaloric effect. This thesis titled *"Tuning the Magnetocaloric Properties of Nanomagnetic Materials for Magnetic Refrigerant Applications"* presents a detailed investigation of the structural, magnetic and magnetocaloric properties of nanomagnetic materials among three different systems, perovskite oxides, ferrites and nanocomposites and hence the identification of a near room temperature magnetic refrigerant material. This thesis is divided into nine chapters.

**Chapter 1** provides a general introduction to the different types of magnetism and magnetic materials. The basic concept of magnetic refrigeration as well as the theory of magnetocaloric effect (MCE) and the characteristic MCE values of are extensively presented in this chapter. The summary of the literature survey of the research work conducted in the context of MCE materials and magnetic refrigerant applications is also briefed. The structure and properties of the important MCE materials of the present work perovskites, ferrites and nanocomposites, are presented. The objectives of our research work are also elucidated in this chapter.

**Chapter 2** describes the various experimental techniques employed for the structural, magnetic and magnetocaloric characterisation of the synthesised materials. It also presents the synthesis techniques employed to prepare the nanomagnetic materials in this study. It also details the working principle of each characterisation tool used in this research work

**Chapter 3** presents the investigation on the effect of structural and magnetic properties of cobalt substitution in lanthanum sodium manganite perovskite materials. It provides a comparative study of the structural properties of the as prepared and sintered

$La_{0.5}Na_{0.5}Mn_{1-x}Co_xO_3$ perovskite nanomaterials. Furthermore, the room temperature magnetic properties of the as prepared and sintered samples are analysed by the M-H magnetisation measurements and compared*

**Chapter 4** examines the tuning of magnetocaloric properties of $La_{0.5}Na_{0.5}Mn_{1-x}Co_xO_3$ perovskites with varying the cobalt concentration. Temperature-dependent magnetisation measurements (ZFC-FC) were recorded as an initial procedure of magnetocaloric characterisation of the synthesised samples. It explores the magnetocaloric properties of the samples by estimating the magnetic entropy change from the magnetisation isotherms recorded around the transition temperature. It also describes the critical behaviour analysis of lanthanum perovskites from the Arrott's plots.

**Chapter 5** provides the synthesis, structural and magnetic characterisation of cobalt substituted copper ferrite, $Cu_{1-x}Co_xFe_2O_4$, nanomaterials. The structural analysis was confirmed with XRD, TEM and FTIR characterisation. It also details morphological and compositional characterisation using SEM and EDAX measurements. The magnetic properties of the synthesised samples at room temperature and low temperature were outlined in this chapter.

**Chapter 6** presents the synthesis, structural and magnetic characterisation if zinc substituted copper ferrite, $Cu_{1-x}Zn_xFe_2O_4$, nanoparticles. The structural analysis of the samples was examined from XRD, TEM and FTIR measurements. This chapter also provides the morphological and compositional characterisation of the samples. It also explores the magnetic characterisation of the samples at room temperature and low temperature. The comparison of structural and magnetic properties of the $Cu_{1-x}Co_xFe_2O_4$ and $Cu_{1-x}Zn_xFe_2O_4$ samples is incorporated in this chapter.

**Chapter 7** outlines the tuning of magnetocaloric properties of cobalt/zinc substituted copper ferrite ($Cu_{1-x}Co_xFe_2O_4$, $Cu_{1-x}Zn_xFe_2O_4$) samples near room temperature. It details the ZFC-FC measurements and magnetisation isotherms of these samples recorded in the lower temperature region. The estimation and comparison of MCE properties of $Cu_{1-x}Co_xFe_2O_4$ and $Cu_{1-x}Zn_xFe_2O_4$ are also depicted.

**Chapter 8** describes the synthesis, structural, magnetic, and magnetocaloric properties of cobalt polystyrene nanocomposites. This chapter provides the structural analysis of the sample by XRD, its magnetic characterisation by M-H curves at room temperature and lower temperature, and ZFC-FC measurements at a lower temperature. It also explores the magnetocaloric properties of the synthesised cobalt polystyrene nanocomposites near room temperature.

**Chapter 9** the final chapter of this thesis provides the general conclusion and the scope for future research work. This chapter summarises the results of the research work carried out on the synthesised perovskites $La_{0.5}Na_{0.5}Mn_{1-x}Co_xO_3$, ferrites $Cu_{1-x}Co_xF_2O_4$ and $Cu_{1-x}Zn_xFe_2O_4$ and cobalt polystyrene nanocomposite. The future prospects of the work are also outlined.

## PUBLICATIONS


[1] S. Bhaskaran, H.R.J. Manjaly, E.V. Gopalan, On the structural and dielectric properties of sol-gel synthesized copper doped lanthanum sodium manganite (LNCMO) nanoparticles, AIP Conf Proc 2082 (2019). https://doi.org/10.1063/1.5093851.

[2] S. Bhaskaran, I.A. Al-Omari, V.E. Gopalan, Effect of magnetic and nonmagnetic cation substitution on structural and magnetic properties of copper ferrite nanoparticles, AIP Conf Proc 2783 (2023) 0–4. https://doi.org/10.1063/5.0158619.

[3] S. Bhaskaran, I.A. Al-Omari, E.V. Gopalan, On the enhanced coercive field and anisotropy observed in cobalt substituted copper ferrite nanoparticles prepared by a modified sol-gel method, J Alloys Compd 884 (2021) 161095.. https://doi.org/10.1016/j.jallcom.2021.161095

[4] S. Bhaskaran, J. Francis, P.W. Ann Maria, K.A. Malini, E. Veena Gopalan, A comparative study of structural properties of oleic acid coated metal nanoparticles (Co, Ni, Fe) by co-precipitation method, Mater Today Proc (2023). https://doi.org/10.1016/j.matpr.2023.11.125.

[5] S. Bhaskaran, Laveena Varghese, V S Sharon, K A Malini, E Veena Gopalan, Probing the Near Room Temperature Magnetocaloric Properties and Critical Behaviour in Sol-gel Synthesized Lanthanum Sodium Manganite Nanoparticles, J Alloys Compd, (2025),184097. https://doi.org/10.1016/j.jallcom.2025.184097


## PRESENTATIONS

1. Presented a Poster on "On the Structural and Dielectric properties of sol-gel synthesized Copper doped Lanthanum Sodium Manganite(LNCMO) nanoparticles" in International Conference on Optoelectronic And Nano Materials For Advanced Technology(ICONMAT) held at CUSAT on 3rd January to 5th January 2019.
2. Presented a Poster on "Effect of Magnetic and Nonmagnetic Cation Substitution on Structural and Magnetic Properties of Copper Ferrite Nanoparticles" in International Conference NANOicon 2022 – CUSAT Golden Jubilee International Conference, organized by Inter University Centre for Nanomaterials and Devices (IUCND), Cochin University of Science and Technology, Kerala, India during January 11-15, 2022.
3. Presented a Poster on "Investigation on the structural and magnetic properties of Zinc substituted Copper ferrite nanoparticles by a modified sol-gel technique " in the International Conference on Functional Materials for Advanced Technologies 1 organized by the Department of Physics, Central University of Kerala during 2-4 January 2023.
4. Presented a paper entitled "A Comparative Study Of Structural Properties Of Oleic Acid Coated Metal Nanoparticles(Co, Ni, Fe) By Co-precipitation Method" in the International Conference on Science and Technology of Advanced Materials (STAM.23) during April 18- 20, 2023.

# CONTENTS

# List of Tables

## List of Figures

***Page No.***

# Chapter 1

# Introduction

## Objectives

We are entering the era where materials and devices will be engineered at the atomic level to create unprecedented functionality." – Richard Feynman. Magnetic refrigeration is a promising cooling technology, that has been focused on research for domestic and commercial applications. The theory of magnetism, magnetic nanoparticles, the magnetocaloric effect (MCE), MCE materials, the literature survey and the research objectives are described.

## 1.1 Introduction

Material science and engineering are advancing rapidly, driven by the development of innovative devices and the adaptation of existing technologies through the use of novel materials. Since the development of new materials have a direct impact on technological advancements, this area is extremely intriguing. Magnetism is a fundamental phenomenon related to magnetic fields, which arise from the orbital and spin motion of electrons. In material science, magnetic materials have always been crucial to society and research, playing a key role in the advancement of nanoscale technologies. "Our civilization runs on electricity and magnetism, from the smallest microchip to the largest power plant." – Nikola Tesla.

## 1.2 Magnetism

The magnetic behaviour of materials is related to the different types of motions of the electrons in their atoms. Atoms contain many electrons, each moving in its orbit and spinning about its axis. The magnetic moment associated with each kind of motion is a vector quantity, which is parallel to the axis of spin and normal to the plane of the orbit, respectively. The important magnetic parameters are magnetic induction B and magnetic field H, where B is expressed in $Wb/m^2$, usually termed as Tesla, and H is in A/m.

The magnetic induction gives the response of a material to the magnetic field (H) can be expressed as $= \mu_0(H + M)$ , where M is the magnetisation of the material (magnetic moment per unit volume) expressed in A/m and $\mu_0$ is the magnetic permeability of free space in H/m. Other magnetic parameters describing the magnetic behaviour are permeability and susceptibility. Permeability ($\mu$) can be defined as the measure of how a material allows magnetic flux to pass through it. It is given by the ratio of B to H ($\mu$=B/H). Susceptibility ($\chi$) defines the measure of how a material is magnetised in response to the applied magnetic field and is given by the ratio of M and H ($\chi$=M/H). Susceptibility is a dimensionless quantity, while permeability has the unit

of A/m. The relationship between them can be given by $\frac{\mu}{\mu_0} = 1 + \chi$ [1]

### *1.2.1 Different types of magnetism*

The magnetic materials are classified based on the magnetic behavior of materials in response to the applied magnetic fields. The different types are diamagnetism, paramagnetism, ferromagnetism, antiferromagnetism, and ferri magnetism [1,2].

**Diamagnetism**

All materials exhibit diamagnetism, which tends to oppose the applied magnetic field and, therefore, to be repelled by a magnetic field. Diamagnetic materials have atoms with no net magnetic moment, as there are no unpaired electrons. The number and orientations of the electrons are such that the vector sum of the magnetic moment is zero in the absence of a magnetic field. When a magnetic field is applied, a net dipole moment opposite to the magnetic field is induced in the atoms or molecules. When the applied magnetic field is stronger, the induced moment will also be stronger and result in a negative magnetic susceptibility. Another characteristic property of a diamagnetic material is that the susceptibility is temperature independent. Examples of diamagnetic materials are Gold, copper, silver, mercury, diamond, tin etc.

**Paramagnetism**

The atoms or ions in the material have non-zero magnetic moments due to a few number of unpaired electrons and are classified as paramagnetic materials. Paramagnetism describes a feeble magnetism that exhibits positive magnetic susceptibility. The application of a magnetic field can reduce the spin disorder, as a result, it can acquire a small magnetisation in the direction of the applied magnetic field.

For paramagnetic materials, the magnetisation can be expressed as[2]

$$M = C\left(\frac{H}{T}\right) \tag{1.1}$$

where H is the strength of the magnetic field and T is the temperature C is the Curie constant given by $\mathrm{C} = \frac{\mu^2 N}{3Ak_B}$, $\mu$ is the effective magnetic moment, N is the Avogadro Number, A is the atomic weight, $k_B$ is the Boltzmann constant. The susceptibility of a paramagnetic material is defined as

$$\chi = \frac{C}{T} \tag{1.2}$$

The susceptibility of a paramagnetic material is small and positive and is inversely proportional to temperature. Aluminium, Chromium, Manganese, etc., are some examples of paramagnetic materials.

**Ferromagnetism**

Ferromagnetic materials exhibit magnetic properties even in the absence of an applied magnetic field. In contrast to paramagnetic materials, in ferromagnets, the magnetic moments are strongly coupled to each other. Strong interactions can be observed in the atomic magnetic moments of magnetic materials such as iron, nickel, cobalt, etc. The positive exchange interactions favour a parallel arrangement of magnetic moments in neighbouring atoms. Due to magnetic interactions, susceptibility becomes large at a specified temperature known as the Curie temperature $T_c$, rather than at 0K as in a paramagnet. This competes with the thermal agitation and yields a net magnetic moment in the absence of a magnetic field. This magnetisation is called spontaneous magnetisation, which occurs in the absence of a magnetic field, mainly caused by the spin contributions of electrons. When a magnetic field is applied, spontaneous magnetisation occurs below this temperature as the interactions overcome thermal agitation. Atomic moments align either parallel or antiparallel in the presence of a magnetic field as a result of the interactions, which are caused by electronic

exchange forces. At 0K, when all of the individual moments are parallel, the spontaneous magnetisation reaches its maximum value of $M_0$. The susceptibility of a ferromagnetic material is large and positive, which is defined by the Curie Weiss Law [1,2]

$$\chi = \frac{C}{T-\theta} \tag{1.3}$$

Above its Curie temperature $T_c$, a ferromagnet becomes paramagnetic, and its susceptibility then follows the Curie Weiss law, with a value of θ approximately equal to $T_c$.

The hysteresis behaviour is another remarkable characteristic of ferromagnetism, which defines the property of these materials to retain their original magnetisation after removing the applied magnetic field. The remaining magnetisation present in the material on decreasing the field to zero after achieving the saturation magnetisation is called remanent magnetisation ($M_r$). Coercivity ($H_c$) is defined as the reverse field required to reduce the magnetisation to zero. The ferromagnetic materials are classified based on the hysteresis behaviour: hard magnets and soft magnets. Hard magnetic materials are permanent magnets, which are difficult to magnetise and demagnetise and have a large coercive field. The soft magnets are easily magnetised and demagnetised and are characterised by high saturation magnetisation, low coercive field.

**Ferrimagnetism**

Ferrimagnets maintain their magnetisation in the absence of a field, just like ferromagnets do. However, nearby pairs of electron spins tend to point in opposite directions. According to the two sublattice model, which explains magnetism in ferromagnetic materials, neighbouring magnetic moments are aligned antiparallel yet spontaneously magnetise because their magnetic moments are not equal. In an ideal geometrical configuration, the sublattice of electrons pointing in one direction has a greater magnetic moment than the sublattice pointing in the opposite direction, thus producing a total magnetic moment equal to the difference between their magnitudes.

[1,2]. Ferrimagnetic transition metal oxides belong to ferrites, which find large technological applications[3,4].

**Antiferromagnetism**

In antiferromagnetism, the individual magnetic moments in a domain are antiparallel. An antiferromagnet at 0K consists of interpenetrating and identical sublattices of magnetic ions, each spontaneously magnetised to saturation in zero applied field but in opposite directions. An antiferromagnet has no net spontaneous magnetic moment, and it can acquire a moment only when a magnetic field is applied. The tendency to align the moments in an antiparallel direction is strong enough to act even in the absence of an applied magnetic field below a critical temperature $T_N$, called Neel's temperature. This antiparallel alignment results in a small positive susceptibility because an applied field tends to align the spins. Antiferromagnetic substances have a positive susceptibility at all temperatures, however, it increases with a decrease in temperature and attains a maximum at the critical temperature $T_N$. Like the Curie temperature in ferromagnetic materials, the Neel temperature ($T_N$) is for antiferromagnetic materials. Above the Neel temperature, antiparallel alignment is disturbed and returns to a paramagnetic state. Nickel oxide, chromium and hematite are some examples of antiferromagnets [5,6]. The different types of magnetism are shown in Fig. 1.1.

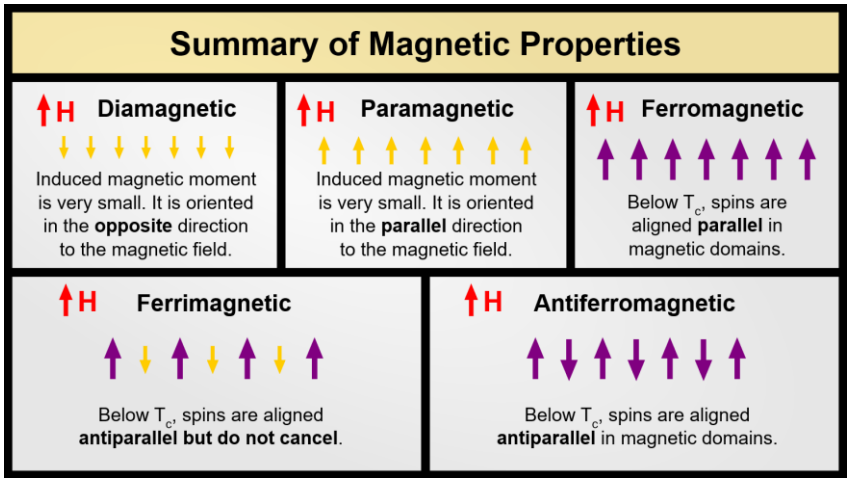


**Figure 1.1**. Different types of magnetism

## 1.3. Nanomagnetism

Nanomaterials have extremely small sizes of the order of nanometers at least in one dimension. Engineered nanomaterials are resources fabricated at the molecular (nanometre) level to take advantage of their small size and novel properties which are generally not seen in their conventional, bulk counterparts. The main reasons for the different properties of the materials at the nanoscale are increased relative surface area to volume ratio and quantum size effects. The shape or morphology of nanomaterials plays an important role in classifying them based on their number of dimensions. Zero dimensional nanoparticles are those materials whose all three dimensions are confined in the nano range (eg. quantum dots, nanoshells). One-dimensional nanomaterials are those whose two dimensions confined in the nano range (eg.nanotubes, nanowires). Two-dimensional materials have one dimension at the nanoscale (eg.nanosheets, nanofilms). Scientists and engineers from several disciplines including physics, chemistry, biology, and material science use nanoscience principles for advanced applications in energy, medicine, computing, and elsewhere.

Magnetic materials at the nanoscale exhibit enhanced magnetic properties than those of bulk. Magnetic nanoparticles are employed in permanent magnets and hard disc recording media, which are all composed of assemblies of nanoscale magnetic grains. Ultrafine magnetic particles with nanometric diameters are shown to have unique features. Superparamagnetism, single domain nature, and occasionally odd phenomena like spin glass and frustration are the defining characteristics of magnetic nanoparticles. Another interesting feature is the change of coercivity in ultrafine particles. The peculiar behaviour of nanoparticles is primarily explained by two main factors: surface effects and finite-size effects. The surface area to volume ratio of the particle increases as the size of the particle decreases. This ratio becomes significantly large for nanoparticles, causing a large portion of the atoms to reside on the surface compared to those in the core of the particle. The special features of these particles are described below[1,2,7].

### *1.3.1 Single Domain Particles*

In a magnetic material, the region where the magnetic moments are aligned uniformly is referred to as magnetic domains. There may be a minimum domain size in a material below which the advantages of reduced magnetostatic energy are exceeded by the energy cost of magnetic domain formation. This suggests that a single particle with a size similar to the smallest domain size would not fragment into distinct domains. Qualitatively, single domain particles are formed when a particle is smaller than around 100 nm, since a domain wall just cannot fit inside it. A single domain particle possesses high magnetostatic energy but no domain wall energy, whereas a multidomain particle has higher domain wall energy but lower magnetostatic energy. When the direction of the externally applied field is reversed, the magnetisation must rotate from the hard direction to the new easy direction, since the particle is unable to respond by domain wall motion [8].

The M-H curve for a single domain particle can be calculated using Stoner-Wohlfarth Model [1]. Here, the concept of coherent domain rotation is examined. If the magnetisation of the particle lies at an angle φ to the direction of a single domain magnetic field H, which is applied at an angle $\theta$ to the easy axis of uniaxial anisotropy, the energy density of the system is described as

$$E = KSin^2(\theta - \varphi) - \mu_0 H M_s Cos\varphi \tag{1.4}$$

where $K$ is the anisotropic constant and $M_s$ is the spontaneous magnetisation. The direction of magnetisation at any given value of the applied magnetic field is determined by minimising the magnetic energy. The first term of this equation represents the magnetic anisotropy energy and the second term represents the energy of coupling with the applied field. The spins in an isolated particle are held in a particular direction by the magnetic anisotropy energy, which originates from the spin-orbital interactions of the electrons. The anisotropic energy per particle is defined as

$$E_\alpha = KVSin^2\theta \tag{1.5}$$

where $V$ is the volume. The maximum energy barrier, $KV$, separates the two energetically equivalent easy magnetisation directions. As the particle size decreases the anisotropic energy decreases and reaches a point where $E_\alpha$ is small. This results in the loss of magnetism in the absence of an applied magnetic field due to the free rotation of the particle's magnetisation. This spin flipping occurs at a temperature called the blocking temperature, $T_B$, which depends on the particle size and other factors like anisotropic constant, applied magnetic field etc. For temperatures $T > T_B$, the isolated (non-interacting) single-domain particle becomes superparamagnetic and, in this state, the magnetic moment of the particle behaves as that of a single atom.

### *1.3.2. Coercivity in fine particles*

The schematic diagram of the variation of coercivity with particle diameter is shown in Fig. 1.2. As the particle size is increased, the coercivity is found to increase to a maximum and then tends toward zero. In multidomain particles, the magnetisation changes by domain wall motion. The size dependence of coercivity is given by the equation [2]

$$H = a + \frac{b}{D} \tag{1.6}$$

where $a$ and $b$ are constant and $D$ is the particle diameter.

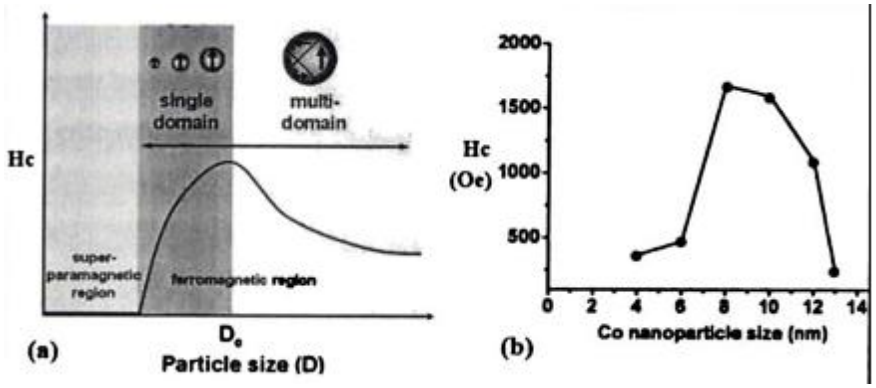


**Figure 1.2.** Variation of coercivity with particle size

The coercivity is zero when the diameter is less than a value which is known as the critical diameter $D_s$ for the magnetic system. At this diameter, the thermal effects are now strong enough to demagnetise a previously saturated assembly of particles spontaneously. Such particles are called superparamagnetic and the phenomenon is known as superparamagnetism.

### 1.3.3. *Superparamagnetism*

As the size of the single domain particles becomes small, they can spontaneously reverse the magnetisation from one easy direction to the other even in the absence of an applied field. This is because the value of $KV$ (where $K$ is the magnetic anisotropy constant and $V$ the volume of the particle) decreased to a point where the thermal energy fluctuations could overcome the anisotropy forces. The assemblies of small particles show behaviour similar to paramagnetic materials, but with much larger magnetic moments as the thermal energy overcomes the anisotropy energy. This large magnetic moment is the moment of the single domain particle and is equal to $m=M_sV$, which can be quite large and is of the order of thousands of Bohr Magnetons. An applied field would tend to align this giant moment, but $k_BT$ would resist the alignment just as it does in a paramagnet. Hence, this phenomenon is called superparamagnetism[2,8,9].

The superparamagnetic systems show two distinct features: (i) magnetisation curves measured at different temperatures superimpose when $M$ is plotted as a function of $H/T$, since both remanence and coercivity are zero, there is no hysteresis. The anisotropy energy KV represents an energy barrier to the total spin reorientation; hence, the probability for jumping the thin barrier is proportional to the Boltzmann factor $e^{-KV/k_BT}$ . At high temperatures $KV < k_BT$, the moments on the particles can fluctuate rapidly. The relaxation time τ of a particle is given by

$$\tau = \tau_0 \exp{-\left(\frac{KV}{k_BT}\right)} \tag{1.7}$$

where $\tau_0$ is typically $10^{-9}$ s. These fluctuations slow down (τ increases) as the sample is cooled and the system appears static when τ becomes much larger than the measuring time of the particular laboratory experimental technique.

For superparamagnetic behaviour choosing τ = 100 s and $\tau_0$ = 10.9 s, we can obtain the critical volume as

$$V_{sp} = \frac{25k_BT}{K} \tag{1.8}$$

A particle with a volume less than this acts superparamagnetically on the 100s experimental time scale. The equation can be rearranged to yield the superparamagnetic transition temperature $T_B$.

$$T_B = \frac{KV}{25k_B} \tag{1.9}$$

$T_B$ is called the blocking temperature. Below $T_B$, the free movement of the magnetic moment is blocked by the anisotropy. The system appears superparamagnetic above $T_B$.

Magnetic nanoparticles are at the forefront of the cutting-edge research due to their wide technological applications. Magnetic nanoparticles are shaping the future of electronics, health, and environmental sustainability through ongoing advancements in surface modification, functionalisation, and nanomaterial synthesis. Magnetic nanoparticles are employed as an active component in biomedical products, catalysts, recording tape, ferrofluids, flexible disc recording medium and magnetic refrigeration[4,10–17].

## 1.4. Magnetic Refrigeration

Refrigeration is a vital technology for food preservation, medical storage, and climate control. Vapor compression-based conventional refrigeration systems have been accepted in the industry for decades. But their dependence on artificial refrigerants like hydrofluorocarbons (HFCs) and chlorofluorocarbons (CFC's)

endangers the environment resulting in ozone depletion and global warming[18]. Magnetic refrigeration has emerged as a promising technology for environmentally friendly, compact, and energy efficient cooling systems [15,19]. Magnetic refrigeration has promising technological applications including domestic refrigeration, industrial cooling, air conditioning, etc. A well-known method for magnetic cooling is the field-induced magnetic entropy change which is based on the magnetocaloric effect (MCE). Developing inexpensive, readily producible, tuneable $T_c$, chemically stable magnetocaloric materials are the challenge in this field of research. The primary requirement for this type of cooling method is the existence of a spin system whose magnetisation strongly depends on temperature and magnetic field.

## 1.5 Magnetocaloric Effect (MCE)

Magnetocaloric effect (MCE) is the fundamental principle behind magnetic refrigeration, a promising cooling technology. The magnetocaloric effect was originally discovered by Warburg in the element iron in 1881. MCE is an intrinsic thermodynamic property of a magnetic material arising from the entropy change due to the coupling of the magnetic spin system with the magnetic field. When a magnetic field is applied adiabatically in a ferromagnetic material, the total entropy of the system remains constant during the magnetisation process. When a magnetic field is applied to a ferromagnetic material the magnetic spins are oriented in the direction of the applied field resulting in a reduction of magnetic entropy ($\Delta S_m$) which in turn increases the lattice and electronic entropy to compensate for the total entropy of the system constant[20]. This causes an increase in the temperature of the system, which depends on the strength of the applied magnetic field. This adiabatic temperature change $(\Delta T_{ad})$ and the isothermal magnetic entropy change ($\Delta S_m$) are called the characteristic MCE values.

### 1.5.1 Theory of MCE

MCE of a magnetic material is characterised either by a reversible change in temperature *($\Delta T_{ad}$)* in the material when the magnetic field changes adiabatically or the reversible change of magnetic entropy *($\Delta S_m$)* when the applied magnetic field changes isothermally[19]. When the magnetic field applied to a magnetic material is changed by *$\Delta H$,* two different processes can occur. The first is the isothermal process that occurs when the magnetic field is changed, the substance remains in thermal equilibrium with its surroundings. Since the material exchanges heat with its surroundings to offset the change in the magnetic field, the temperature of the substance stays constant in this situation. The entropy of the material is then changed by

$$\Delta S_m(T)_{\Delta H} = (S(T)_{Hf} - S(T)_{Hi})_T \tag{1.10}$$

Entropy measures the order in the magneto-thermodynamic system, low entropy corresponds to a higher order and vice versa. The total entropy *S (T, H)* of a magnetic material is the sum of contributions of lattice entropy *($S_{lat}$)* caused by the vibrations of the crystal lattice, magnetic entropy *($S_m$)* arising from the magnetisation of the material and electronic entropy *($S_e$)* due to the free electrons of the material[21]. The adiabatic demagnetisation on a magnetic material increases magnetic entropy and reduces lattice entropy, resulting in a cooling effect known as magnetic cooling. The total entropy of the system at constant pressure can be expressed by equation (1.11)

$$S(T,H) \quad = \quad S_{lat}(T) + S_m(T,H) + S_{el}(T) \tag{1.11}$$

The second process is adiabatic, which occurs when the magnetic field is modified but the material is isolated from the surroundings and, therefore, the total entropy of a solid remains constant. The temperature of a magnetic material is then changed by

$$\Delta T_{ad}(T)_{\Delta H} = (T(S)_{Hf} - T(S)_{Hi})_S \tag{1.12}$$

where $\Delta T_{ad}$ is called adiabatic temperature change. The adiabatic temperature change indirectly characterises both the temperature difference between the cold and the hot ends of the refrigerator and the cooling capacity. A schematic diagram of the magnetic refrigeration cycle is shown in Fig. 1.3. The application of a magnetic field increases the temperature of the refrigerant above the hot reservoir and expels heat to the reservoir. When the material is demagnetised adiabatically, it is cooled down to a temperature lower than the cold reservoir, and heat is transferred from the load to the refrigerant[22].

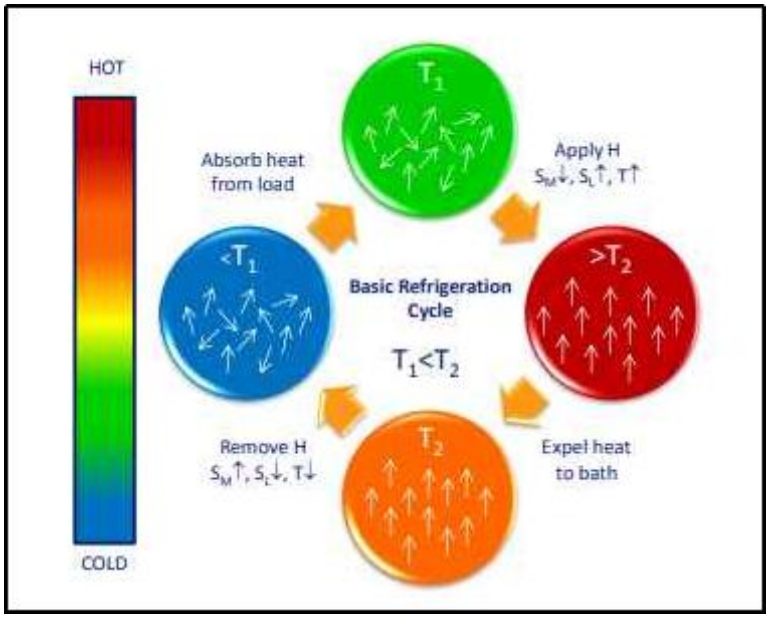


**Figure 1.3.** A schematic diagram of a simple magnetic refrigeration cycle.

### 1.5.2 *Thermodynamics of MCE*

The source of the magnetocaloric effect can be described based on thermodynamics, which relates the magnetic variables (magnetisation and magnetic field) to entropy and temperature.

The magnetic properties of the materials are related to Maxwell's thermodynamic relations as

$$\left(\frac{\partial S}{\partial H}\right)_T = \left(\frac{\partial M}{\partial T}\right)_H \tag{1.13}$$

The Maxwell's relation can be derived in terms of internal energy U, and Gibbs free energy G. The Gibbs free energy G for systems with constant pressure can be defined for a paramagnetic salt as

$$G = U - TS - MH \tag{1.14}$$

The differential form of first law of thermodynamics is

$$dU = dQ + dW \tag{1.15}$$

where dQ is the heat energy flowing into the system and dW is the work done on the system. For a paramagnetic salt, the work done is the magnetic work. For an infinitesimal reversible process

$$dQ = TdS \tag{1.16}$$

Using equations 1.14, 1.15, and 1.16, the total differential of Gibbs free energy can be defined as

$$dG = -SdT - MdH \tag{1.17}$$

For the Gibbs free energy, the equations of states are

$$\mathrm{S} = -\left(\frac{\partial \mathrm{G}}{\partial \mathrm{T}}\right)_{\mathrm{H}} \text{ and } \qquad \mathrm{M} = -\left(\frac{\partial \mathrm{G}}{\partial \mathrm{H}}\right)_{\mathrm{T}} \tag{1.18}$$

Differentiating partially *S* by *H* and *M* by *T* and equating the right-hand sides,

$\left(\frac{\partial S}{\partial H}\right) = \left(\frac{\partial M}{\partial T}\right)$ , Maxwell's relation can be obtained.

The magnetic entropy change can be calculated by integrating equation (1.13)

$$\Delta S_m\,(T,\Delta H) = \int_{H1}^{H2}\left(\frac{\partial M(T,H)}{\partial T}\right)_H\, dH \tag{1.19}$$

$$\Delta S_m = \frac{1}{\Delta T}\int_{H1}^{H2}(M_{i+1}(T_{i+1},H_{i+1}) - M_i(T_i,H_i))dH \tag{1.20}$$

where $M_i$ and $M_{i+1}$ are the experimental values of magnetisation at temperatures $T_i$ and $T_{i+1}$ respectively under an applied magnetic field of $H_i$. Since the magnetisation is material dependent and is a function of unknown temperature and magnetic field, the analytic integration by equation (1.19) is impossible. So numerical integration of equation (1.20) is performed on a finite number of magnetic isotherms and is obtained by

$$\Delta S_m\,(T,H) = \sum_i \frac{M_{i+1}(T_{i+1},H)-M_i(T_i,H)}{T_{i+1}-T_I}\Delta H \tag{1.21}$$

Alternately, the magnetocaloric property of a magnetic material can be calculated from adiabatic temperature change and isothermal magnetic entropy change by probing calorimetric measurements. The heat capacity C at a constant parameter x is defined as

$$C_x = \left(\frac{\partial Q}{\partial T}\right)_x \tag{1.22}$$

where $\partial Q$ is the amount of heat changing the system temperature on $dT$.
Using equation 1.16 specific heat capacity can be expressed as

$$C_x = T\left(\frac{\partial S}{\partial T}\right)_x \tag{1.23}$$

The isothermal magnetic entropy change at a field $H$ can be calculated as

$$S_m(T,\Delta H) = \int_{H1}^{H2}\left(\frac{C(T)}{T}\right)_H dH \tag{1.24}$$

Using the following thermodynamic relations

$$\left(\frac{\partial T}{\partial H}\right)_S = -\left(\frac{\partial S}{\partial H}\right)_T \left(\frac{\partial T}{\partial S}\right)_H \tag{1.25}$$

$$C(T,H) = T\left(\frac{\partial S}{\partial T}\right)_H \tag{1.26}$$

where *C (T, H)* is the heat capacity at a constant magnetic field.

The temperature change due to the change of magnetic field under an adiabatic – isobaric process *dP=0* (this process is usually realised in magnetocaloric experiments) can be expressed using equation 1.25 as

$$dT = \frac{T}{C(T,H)}\left(\frac{\partial M}{\partial T}\right)_H dH \tag{1.27}$$

By integrating equation 1.27, the finite temperature change $\Delta T = T_2 - T_1$ (where $T_2$ and $T_1$ are the final and initial temperatures respectively) under adiabatic magnetisation can be calculated.

$$\Delta T_{ad}(T,\Delta H) = -\int_{H1}^{H2}\left(\frac{T}{C(T,H)}\right)_H \left(\frac{\partial M(T,H)}{\partial T}\right)_H dH \tag{1.28}$$

Second-order phase (SOPT) transition material shows lower dependence of specific heat on the magnetic field compared to the first order material (FOPT) [23].So for a second order material, considering the field independence equation (1.28) can be further written as

$$\Delta T_{ad} = \frac{T}{C(T,H)}\Delta S_m \tag{1.29}$$

Equation 1.29 describes the indirect measurement of adiabatic temperature by calorimetric measurement[20].

Fig 1.4 depicts the isothermal entropy change or adiabatic temperature change for a given field variation determined by comparing two iso-field entropy curves.

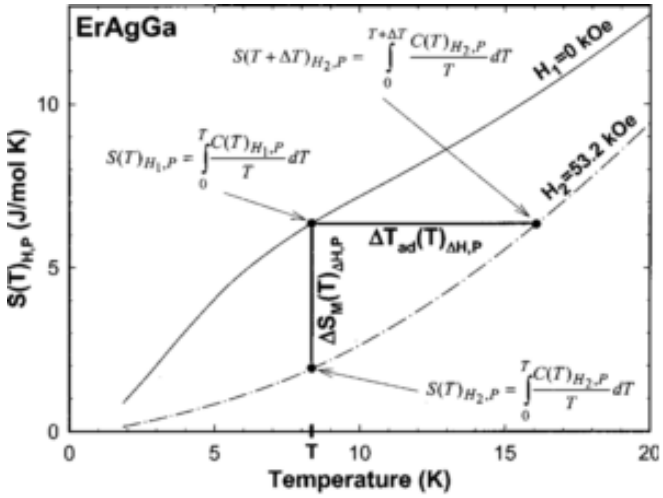


**Figure.1.4** Illustration of the isothermal entropy change and adiabatic temperature change from two isofield entropy curves. The figure is taken from the reference [21]

### *1.5.3 MCE Measurements*

There are two techniques for the measurement of the MCE characteristics values ($\Delta T_{ad}$ , $\Delta S_m$ ) (1) direct technique and (2) indirect technique. In the direct technique, MCE is measured as adiabatic temperature change ($\Delta T_{ad}$) and in the indirect technique, it is measured as isothermal magnetic entropy change ($\Delta S_m$) or as adiabatic temperature $\Delta T_{ad}$ from specific heat measurements.

**Direct Technique**

In the direct technique, the temperature of the sample is measured using a thermocouple arrangement with and without a magnetic field. The adiabatic temperature change can be measured as

$$\Delta T_{ad} = T_{i-} T_0 \tag{1.30}$$

The direct measurement of MCE can be carried out using contact and non-contact techniques[19]. In contact technique, the temperature sensor is kept in direct thermal contact with the sample while in non contact method, the temperature of the sample is measured without the sensor being in contact with the sample. During the direct MCE measurement, a rapid change of magnetic field is required. The

measurements can be carried out on immobile samples when a change in magnetic field is produced either by moving the sample in and out of a uniform magnetic field volume, or by charging or discharging the magnet. Direct MCE measurements can be possible in large magnetic fields using immobilized samples and pulse magnets whereas, an electromagnet can produce only small fields. The accuracy of the direct experimental techniques depends on the errors in the thermometry, errors in the field setting, the quality of the compensation scheme to eliminate the effect of the changing magnetic field on the temperature sensor reading[19]. The quality of thermal insulation of the sample is a critical source of error when the MCE is large and thus disorders the adiabatic condition. The experimental arrangement for the direct measurement of adiabatic temperature change is shown in Fig.1.5

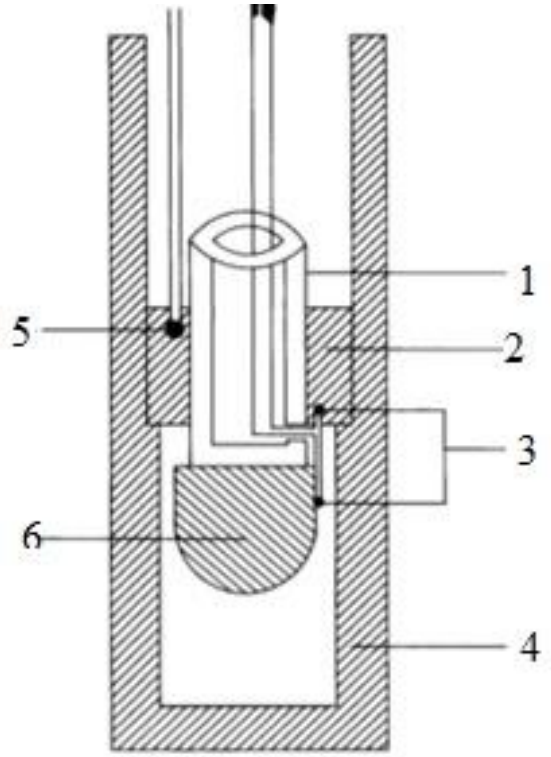


**Figure.1.5**. Experimental setup for MCE measurements employing a differential thermocouple2a: (1) insulating Plexiglas tube, (2) copper ring, (3) differential thermocouple measuring AT, (4) copper screen, (5) thermocouple measuring the average temperature T, (6) sample[24]

The direct method to quantify MCE is practically difficult because special care is required to maintain the adiabatic condition and the contact of the sample container.

**Indirect Technique**

The indirect technique of magnetocaloric measurements can be obtained by probing magnetic field-dependent magnetisation measurements at different temperatures (magnetic isotherms) and from heat capacity-dependent magnetisation measurements.

*(i ) Isothermal entropy change (M-H isotherms)*

The indirect technique of MCE measurement can calculate magnetic entropy change by probing isothermal magnetisation curves (M-H isotherms) at different temperatures. Since the stabilization of temperature is the longest step in the process of collecting magnetisation data, the entire measurements were obtained isothermally by varying the magnetic field. Magnetic field dependent magnetisation is measured at different temperatures and magnetic isotherm (M-H) curves are recorded with these data. The magnetic entropy change $\Delta S_m$ can be estimated from two magnetisation isotherms measured at two temperatures $T_1$ and $T_2$ for an average temperature $T_{av} = ½ (T_1+T_2)$ in a magnetic field changing isothermally by $\Delta H = H_2 – H_1$[20]. An alternate method to calculate the magnetic entropy change is to determine the product of the area between the magnetic (M-H) isotherms and the reciprocal of the temperature difference as given by the equation (1.20). The accuracy of $\Delta S_m$ from magnetisation measurements is typically reported to be in the range of 3-10% because numerical integration is involved and the actual differentials (*dM, dT* and *dH*) are substituted, respectively, by the experimentally measured $\Delta M$, $\Delta T$ and $\Delta H$.

*(ii) Calorimetric method (Specific heat measurements)*

The indirect technique of MCE measurement can calculate both the adiabatic temperature change ($\Delta T_{ad}$) accompanied by isothermal magnetic entropy change ($\Delta S_m$), probing the heat capacity measurements. The adiabatic temperature change ($\Delta T_{ad}$) can be calculated from the experimentally measured heat capacity as a

function of temperature at two constant magnetic fields $H_F$ and $H_I$. This method is considered to be free from errors compared to the direct technique to determine $(\Delta T_{ad})$ because the measurement is performed under a constant magnetic field at a lower sweep rate of temperature[20]. The heat capacity of the samples is measured as a function of temperature at constant pressure, and the magnetic entropy change can be calculated by employing the formula

$$\Delta S_m = \int_0^T \frac{C(T,H)}{T} dT + S_0 \quad \text{where } S_0 \text{ is the zero field entropy.} \qquad (1.31)$$

The adiabatic temperature change $(\Delta T_{ad})$ can be calculated from the heat capacity measurements as per equation (1.28).

## 1.6 Active Magnetic Refrigeration (AMR)

J. Barclay introduced the new concept of Active Magnetic Refrigerator in 1982. Active Magnetic Regenerator refrigerator is an advanced magnetic cooling system based on the magnetocaloric effect, which manifests itself as a temperature change of a magnetocaloric material (MCM) on the adiabatic demagnetisation of the magnetic field on the material. Since many known MCMs can attain an adiabatic temperature change by a few degrees under a one Tesla magnetic field, a regenerative cycle must be used to provide temperature spans that are equivalent to those of cooling systems based on vapour compression. Magnetic refrigeration is an advanced cooling technology based on the magnetocaloric effect. This technique can be used to attain extremely low temperatures, as well as the ranges used in common refrigerators. A magnetic material in a solid phase is used as a working material in the magnetic refrigerator which undergoes heating or cooling while magnetising or demagnetising. As a result, the vapour-compression cycles of evaporation-condensation and compression expansion can be replaced by the magnetisation-demagnetisation cycles of solid refrigerant materials. According to theoretical calculations and the results of earlier investigations, it is demonstrated that the magnetic heat cycles are much more efficient than the vapour-compression cycles. The high power efficiency, compatibility, low wearability, safety and environment friendly are some of the advantages of a magnetic heat machine. The disadvantages of magnetic cooling

devices include the higher cost of magnetic refrigerators including the expensive sources of magnetic field and possibly magnetocaloric material of the working body. Another is that the presence of a magnetic field source may limit the number of possible applications of magnetic refrigerators[25].

A magnetic refrigerator is generally composed of a magnetocaloric material (MCM) in the form of a porous structure called the Active Magnetic Regenerator (AMR). The fundamental components of magnetic refrigerators are a structure to generate the magnetic field, two external heat exchanges, and the fluid that transfers heat from the magnetocaloric material in the AMR through two external heat exchangers from the cooling space and to the surroundings[26]. A schematic diagram of an AMR refrigerator is shown in Fig.1.6.

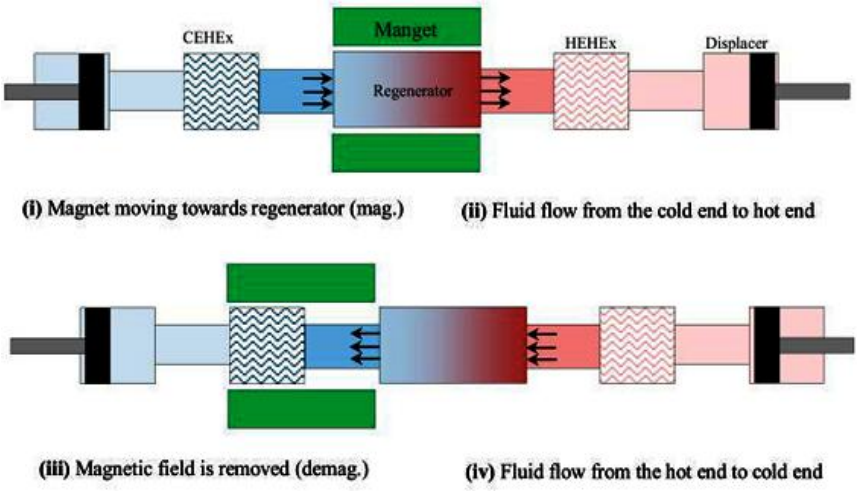


**Figure 1.6.** Schematic diagram of Active Magnetic Refrigerator **(AMR)**

The four processes of an AMR refrigeration cycles are:

(a) Adiabatic magnetisation: the regenerator is exposed to the magnetic field and experiences a temperature rise under adiabatic conditions;

(b) Iso-magnetic heat transfer (cold blow): heat transfer fluid flows from the cold side of heat exchanger to the hot side under a constant magnetic field;

(c) Adiabatic demagnetisation: the regenerator is moved off the magnetic field resulting in a temperature drop and

(d) Iso-magnetic heat transfer (hot blow): heat transfer fluid flows in a reverse direction i.e. from the hot side to the cold side under a constant magnetic field.

Based on the movement of the magnetic field, two kinds of configurations are possible, reciprocating and rotating. In reciprocating mode, the regenerator moves in and out of the magnetic field in a reciprocating manner. The reciprocating motion can be provided either by moving the magnetic source or by moving the magnetic material. In rotary mode, the regenerator rotates about a fixed axis and moves in and out of the field in a circular path. Compared to reciprocating systems, the rotary arrangement may be much more compact and operate at comparatively higher frequencies[27].

The investigation on the magnetic refrigerator has been progressed since the magnetocaloric effect was first observed in 1881 by Warburg. The first refrigerator based on magnetic cooling was demonstrated in 1933. The first prototype magnetic refrigerator based on the magnetocaloric effect was built by Brown in 1976 at NASA[28]. The statistical data reported by A. Kitanovski *et.al* in the review paper on magnetic refrigerators clarifies that the number of prototype refrigerators increases every year, leading to the fact that the research has been progressing on the magnetocaloric energy conversion near room temperature [29]. Thereafter, many prototype reciprocating and rotating refrigerators were designed and built in worldwide labs. Green *et al.* 1990, Zimm *et al.* 1998 [30], Blumenfeld *et al.* 2002 [31], Clot *et al.* 2003, Richard *et al*. 2004, Kawanami *et al.* 2005[32], Lu *et al.* 2005, Huang et al. 2006 [33], Zheng *et al.* 2009, Arnold *et al.* 2011[34], Shassere *et al.* 2012, and Cheng *et al* 2013 are some of the works on reciprocating prototype magnetic refrigerators. Nakamura *et.al* developed a room-temperature magnetic refrigerator with air as the heat transfer medium in 2008[35]. Recently developed magnetic refrigerators have been reported by Kitanovski *et al*. 2015[29], Greco *et al.* 2019, V. Lupponglung *et al.* 2019, Kamran et al 2016 [36], B. Huang *et al.* 2019 [33]. Several researchers reviewed the development of rotary and reciprocating magnetic refrigerators[26,27,37,38]

The magnetic refrigeration technology has advanced significantly towards practical applications as of February 2025, though it is still not widely available commercially. The following business enterprises have created prototype systems and are pursuing commercialisation: Cooltech Applications introduced the Magnetic Refrigeration System (MRS), the first commercial magnetic cooling system, with cooling capabilities ranging from 200W to 700W in 2016. Medical refrigerators, display cabinets, beverage dispensers, retail plugins and wine cellars are just a few of the commercial refrigeration applications for which the MRS product line was optimised. At industry gatherings like Chillventa 2024, MAGNOTHERM has demonstrated its innovative products, demonstrating its leadership in magnetic refrigeration technology. The business concentrates on creating magnetic cooling solutions that are economically feasible, discarding conventional materials like gadolinium in favour of more affordable substitutes. Another company working on the advancement of magnetic refrigeration technology is Camfridge.

## 1.7 Literature Survey

### *1.7.1 Different types of MCE*

**Conventional MCE Behaviour-Caret-like MCE**

The isothermal entropy change $\Delta S_{m,}$ and the adiabatic temperature change $\Delta T_{ad}$ are shown to be proportional to the derivative of the magnetisation with respect to temperature at a constant magnetic field (Equations 1.19 and 1.28). At a constant magnetic field, adiabatic temperature change, $\Delta T_{ad,}$ is also proportional to the absolute temperature and inversely proportional to the heat capacity. So, it is expected that any material should have the largest $\Delta S_m$ and $\Delta T_{ad}$ in the vicinity of a spontaneous magnetic-ordering temperature, where its magnetisation changes rapidly with temperature. Therefore, conventional ferromagnets typically display a “caret-like” curve as shown in Fig.1.7 which is exhibited by a pure single crystalline Gd. Conventional behaviour can be characterised by the temperature of the MCE peak, its full width at half maximum, and the values of $\Delta S_m$ and $\Delta T_{ad}$.

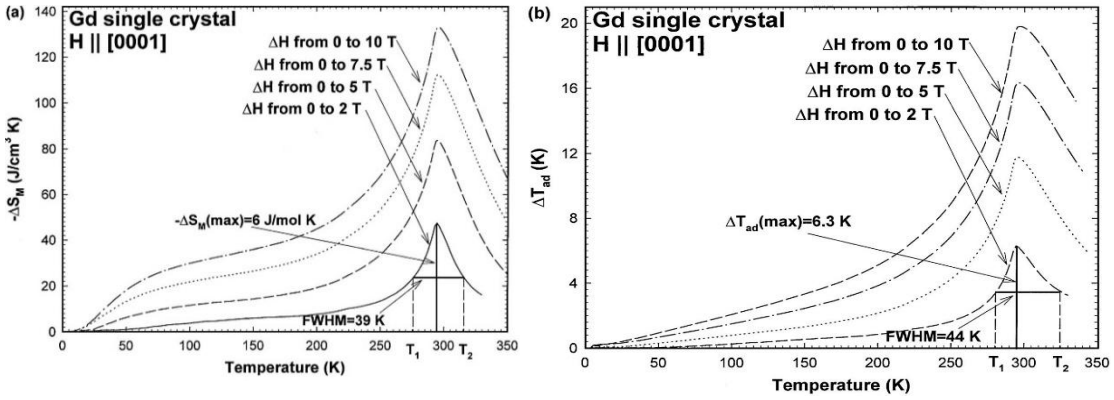


(a) (b)

**Figure 1.7.** A conventional caret-like behavior (*a*) $\Delta S_m (T)_{\Delta H}$ and (*b*) $\Delta T_{ad} (T)_{\Delta H}$ in single crystal-Gd [39]

## Anomalous Magnetocaloric effects

### (i) Skew caret MCE -Table like MCE

The anomalous behaviour of the magnetocaloric effect is closely related to the anomalous changes in the magnetic structure of solids that result in an unusual behaviour of $\partial M/\partial T$ and C (T, H), which carries over to both $\Delta S_m$ and $\Delta T_{ad}$. When a material experiences two or more consecutive magnetic orderings close to one another, it can result in one of the most often reported MCE anomalies. Subsequently, rather than a typical caret-like form, a "skewed caret" that sometimes approaches a flat and nearly consistent shape can be seen, which is also known as “table-like” MCE. Fig. 1.8 illustrates the magnetocaloric action in $(Gd_{0.6}Er_{0.4})AlNi$ (35). While the $\Delta T_{ad}(T)_{\Delta H}$ (Figure 1.8 (b)) is nearly constant between 16 and 36 K, the $\Delta S_m (T)_{\Delta H}$ (Fig.1.8 (a)) exhibits a skewed caret. As noted for $(Dy_{0.5}Er_{0.5})$ $Al_2$ and also depicted in Figure 1.8, an abnormal MCE behaviour is seen in materials with low lying crystalline electric field levels and materials with various magnetic orderings.

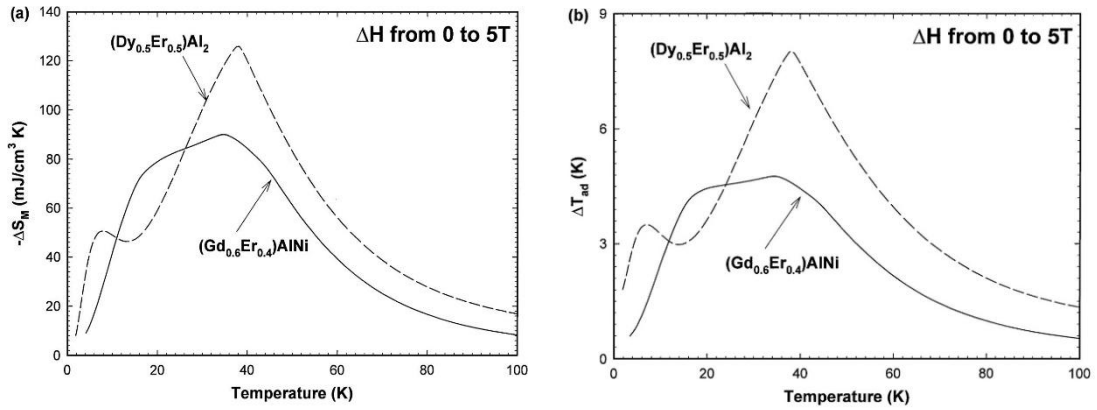


**Figure. 1.8.** The skewed caret (table-like) and multiple peak behavior (*a*) $\Delta S_m (T)_{\Delta H}$ and (*b*) $\Delta T_{ad}(T)_{\Delta H}$ [39]

### (ii) Giant or Skyscraper MCE

Some magnetocaloric materials undergo first order magnetic transition from ferromagnetic to paramagnetic transition with the rise in temperature. In a first-order magnetic phase transition, the *dM/dT* is large compared to the second order transition; hence, such a group of materials exhibits a large magnetocaloric effect. An increase in the magnetic field does not change the magnetocaloric effect significantly while, continuing to increase the $\delta_{FWHM}$ considerably, which shifts the upper-temperature limit of MCE towards the higher temperature and therefore continues to increase the cooling capacity. The lower temperature MCE limit is determined by the temperature at which the transition takes place at the lowest magnetic field, it is independent of the *dH*. This type of anomalous behaviour is called the Giant or skyscraper magnetocaloric effect. The "skyscraper-like" magnetocaloric effect (MCE) describes a sharp and tall peak in the entropy change plot. Materials going through a first-order magnetic phase transition, such as a ferromagnetic-to-ferrimagnetic transition, usually exhibit this characteristic behaviour. The examples of the materials exhibiting sky scraper MCE are $Gd_5(Si_xGe_{1-x})$ alloys and Fe-Rh alloys[40,41].

The three types of MCE behaviour are shown in Fig.1.9. In the figure, $(Dy_{0.5}Er_{0.5})Al_2$ exhibits a caret-like conventional MCE behaviour, which is due to second order paramagnetic to ferromagnetic transition at 40K. $Gd_5(Si_{0.33}Ge_{3.67})$ exhibits a tall sharp peak due to a first order ferromagnetic to ferromagnetic phase transition belonging to skyscraper MCE. The flat-like (table-like) MCE exhibited by $(Gd_{0.54}Er_{0.46})AlNi$ is due to multiple transitions in this material.

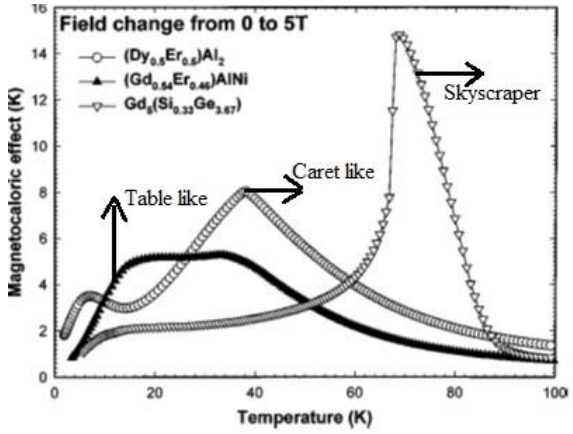


**Figure 1.9**. Three types of MCE.

The engineer creating the thermodynamic cycle for MRs is concerned with the shape of the MCE peak. For instance, a material with a table-like MCE would be selected for an MR employing an Ericsson cycle, where the entropy change must be constant over the intended temperature range. The optimal MCE behaviour for an AMR cycle is a linear temperature rise with rising temperature; this is hard to achieve with either the caret- or skyscraper-like MCE. To get around this, several magnetic materials with various $T_c$ 's can be used and layered in an AMR regenerator bed[42].

The magnetocaloric effect depends mainly on the nature of phase transition, it can be classified based on phase transition as First Order magnetic Phase Transition (FOMT) and Second Order Magnetic Phase Transition (SOMT). FOMT takes place when there is an abrupt change in magnetisation usually associated with a structural change, such as lattice distortion and volume change. This change in magnetisation

results in a significant magnetic entropy change and adiabatic temperature change, which are the characteristic properties of Giant MCE (GMCE).

### *1.7.2 Magnetocaloric Materials (MCM)*

The performance of active magnetic refrigeration (AMR) is strongly influenced by the type of magnetocaloric material (MCM) used. The criteria for choosing magnetic materials suitable for magnetic refrigeration applications were described by Pecharsky and Gschneidner [27,43] . Curie temperature is an important characteristic of MCM that governs its application in magnetic refrigeration. The magnetic domain of ferromagnetic material changes to paramagnetic above Curie temperature and the material exhibits maximum values for the magnetisation gradient ($\partial M/\partial T$) around this temperature. A magnetic material with Curie temperature around room temperature is preferred for near-room temperature applications. Gadolinium (Gd), for instance, is a great candidate for magnetic refrigeration in this temperature range due to its Curie temperature of 293.6 K. Additionally, the material should exhibit a significant change in magnetic entropy and adiabatic temperature. As the magnetic refrigeration cycle is reversible, there must be less thermal and magnetic hysteresis in the ferromagnetic material employed in the regenerator. Magnetic refrigerants with a small lattice entropy (high Debye temperature) are preferred for room-temperature magnetic refrigerators. The availability of magnetic material and the cost involved during its preparation are important factors that should be considered while selecting it.

The potential magnetocaloric materials are characterized by large isothermal magnetic entropy change, $|\Delta S_m|$ and large adiabatic temperature change $\Delta T_{ad,}$ over a wide temperature range[21,44]. Significant relative cooling power (RCP) and high magnetic entropy change values at low external magnetic fields are characteristics of potential magnetocaloric material for room-temperature magnetic refrigerant applications[45,46]. These properties are typically found to be enhanced close to the magnetic transition temperature ($T_c$) where the ordering results in a rapid reduction in

magnetisation, which can manifest as a large magnetic entropy change, but it need not be the same[47]. The nature of the magnetic transition also plays an important role in deciding the working temperature of magnetic refrigerant materials.

According to the magnetic transition, magnetocaloric materials are usually classified into two groups, first order magnetic transition (FOMT) and second order magnetic transition (SOMT) materials. The first order magnetic transition depicts a discontinuous change in magnetisation at the transition temperature along with some latent heat. As a first order transition should theoretically occur at a constant temperature, $\left(\frac{\partial M}{\partial T}\right)_H$ may be infinitely large giving rise to a giant magnetocaloric effect (GMCE). Pecharsky and Gschneidner reported that Gd-Si-Ge and Mn-Sb-As alloys exhibit a giant MCE with a magnetic order-disorder transition[19,48]. Even though a giant and sharp $\Delta S_m$ and $\Delta T_{ad}$ can be observed in the FOMT materials, the magnetic and thermal hysteresis, as well as slow kinetics, exist in the first order transition. This inevitably leads to low energy efficiency during the cooling cycles as a result of irreversibility which limits the performance of a magnetic refrigerator [43]. It is noteworthy that the second order transition is typically spread over a large temperature range, which is preferable for active magnetic refrigerants, whereas the first order transition can focus the magnetocaloric effect over a small temperature range[49]. A second order magnetic transition (SOMT) shows a reversible magnetic transition from the low temperature ferromagnetic to high temperature paramagnetic state with a continuous change in magnetisation at the transition temperature. The magnetic materials with a second order transition exhibit a moderate MCE value over a wide temperature range without any latent heat around the transition temperature, which is desirable for magnetic refrigerant applications. Some of the SOMT materials exhibiting magnetocaloric properties are superparamagnetic ferrites, Ni-Mn-based Heusler alloys, Lanthanum manganites and Fe-based alloys [50,51]. Later, M.Phan reported a $\Delta S_m$ of 10.5 J/kg/K around 300 K in SOMT material La-Ca-Sr-Mn-O manganites [52]. Magnetic materials generally used for magnetic refrigeration are rare

earth materials, Heusler alloys, Perovskites, and Ferrites. The discovery of the Giant MCE (GMCE) in $Gd_5(Si_2Ge_2)$ in 1997 marked a significant advancement in the study of such materials[40].

### 1.7.3 *Pure Metals*

W. F. Giaugue and D.P. Macdougall first reported the magnetocaloric effect experimentally in $Gd\sim(SO_4)_3.8H_20$ material at liquid helium temperature in 1933[53]. Tishin *et. al*. studied experimentally the MCE properties of pure lanthanide metals (Gd, Tb, Er, Dy, Tm, Ho and reported their RCP values[54]. Gadolinium (Gd) is regarded to be one of the best magnetic refrigerant materials for air conditioning and refrigeration as it has the largest near-room temperature magnetocaloric effect. Gd has an impressive relative cooling power RCP (S) of 2-14 J/cm$^3$ and RCP (T) of 240 K and 2000 K for an applied field of 2to10 T. When Terbium is cooled at 230 K, a first order phase change from a helical antiferromagnetic to a ferromagnetic state takes place at 221 K. The direct measurement of MCE at a low magnetic field shows that the MCE in Tb is slightly negative around 221 K and positive around 231 K. A maximum performance of MCE, RCP (T) of 820 K$^2$ is reported at 180 K for a $\Delta H$ of 7T for Ho. The direct measurement of MCE in Ho shows that a relatively small and constant value of MCE is observed in a high magnetic field, $\Delta H=6T$. Pure Er possesses one of the most complex magnetic structures among heavy lanthanides. On cooling to around 86 K, it orders, antiferromagnetically, and at about 19 K it undergoes a first-order phase transition from antiferromagnetic to ferromagnetic. Direct measurements of the MCE in Er under magnetic fields up to 7.5 T showed a consistent value of 4K extending between 25 and 100 K. Zimm et. al reported a maximum MCE of 2.5 K at 8.5 K for $\Delta H=7T$ for Neodymium. The MCE structure of Nd consists of a double peak, a combination of two caret-shaped peaks located at magnetic ordering temperature[55].

In the review paper of Gshneidner on magnetocaloric materials, it is shown that Gd is the best magnetocaloric material among the seven pure lanthanide materials that were studied experimentally by Tishin, Zimm, and others[41]. One of the most extensively researched magnetic refrigerant materials is gadolinium. However, its

applications near room temperature are commercially limited because the cost of Gd is quite expensive at ~$4000/kg. The only rare earth that orders magnetically close to room temperature is gadolinium, often considered a simple Heisenberg ferromagnet, or a typical classical ferromagnet. In Gd, the MCE has a typical caret-like shape suggesting that it would not be ferromagnetic in low-magnetic fields below 292 K, forming behaviour peaks at the Curie temperature.

### *1.7.4 Gadolinium based compounds*

To increase the MCE in Gd, several alloys including Gd and other rare earth elements have been created. Research has been done on Gd-RE alloys with RE=lanthanide (Tb, Dy, Er, Hoor Y). However, the alloying simply lowers $T_c$, which is undesirable since we deviate from room temperature, and the MCE value does not significantly rise in comparison to pure Gd. A review on magnetocaloric materials suggests that MCE has been studied in the following intra-lanthanide compounds. $Gd_{0.85}Y_{0.15}$ and $Gd_{0.85}Tb_{0.15}$; $Gd_{0.75}Y_{0.25}$ and $Gd_{0.48}Y_{0.52}$ ; $Gd_{0.52}Y_{0.48}$ ; $Gd_{1-x}Tb_x$, where $x$ =0.2, 0.4, and 0.7 ; $Gd_{1-x}Dy_x$, where $x$=0.12, 0.28, 0.44, and 0.70 ; $Gd_{1-x}Dy_x$, where $x$=0.1, 0.2, and 0.3 ; $Gd_{0.73}Dy_{0.27}$ ; $Gd_{1-x}Ho_x$, where $x$=0.2, 0.4, 0.6, and 0.8 ; $Gd_{0.80}Ho_{0.20}$ ; $Gd_{0.9}Er_{0.1}$ and $Gd_{0.69}Er_{0.31}$ ; $Gd_{0.84}Er_{0.16}$ ; and $Gd_{1-x}Er_x$, where $x$=0.2, 0.4, 0.6, and 0.8 [41]. The magnetic-ordering temperature of Gd is lowered by adding another lanthanide metal, which also often lowers the MCE. Shao *et al*. reported one of the most intriguing findings that, in comparison to bulk alloys of the same stoichiometry (direct MCE measurements), $Gd_{0.85}Y_{0.15}$ nano powders (average particle size 20 nm) exhibit an MCE increase of around 10 to 15% between 250 and 300 K[56].

**Gd-Si-Ge compounds**

After a break, in 1997, Pecharsky and Gschneidner in Ames laboratory reported giant MCE in Gd-Si-Ge compounds which is twice as large as in Gd[40]. Even though a maximum entropy change $\Delta S_m$ of 18.5 J/kg/K and adiabatic temperature change $\Delta T_{ad}$ of 15 K have been reported at 5 T, the Curie temperature of this alloy is 276 K, which is lower than that of Gd, 294 K, making this difficult to be used as a room temperature

magnetic refrigerant material. Researchers have also investigated doping at Gd sites or$(Si_{1-x}Ge_x)_4$ and used hydrostatic pressure treatments to obtain good MCE characteristics with $T_C$ at ambient temperature[57].

### *1.7.5 Metallic Alloys*

**La($Fe_{1-x}Si_x$) alloys.**

La($Fe_{1-x}Si_x$)alloys are some of the most promising materials for room-temperature magnetic refrigeration applications. An analysis of La($Fe_{11.4}Si_{1.6}$) by Hu *et al.* revealed a greater $\Delta S_m$ and a sharper magnetisation transition than La($Fe_{10.4}Si_{2.6}$). They determined a $\Delta S_m$ of 19.4 J/kg/K in a 5T.10 2T magnetic field. GMCE have been reported in La($Fe_xSi_{1-x})_{13}H_{1.0}$ with $\Delta S_m$ of 28 J/kg/K and $\Delta T_{ad}$ of 8.1 K at a lower field of 2T at 184 K [58]

**3d -Metal based Alloys**

In Fe, Co, and Ni, the magnetocaloric effect, $\Delta T_{ad}$, has been measured at the corresponding Curie points of 1042 K (769°C), 1386 K (1113°C), and 633 K (360°C)[41].

Normal caret-like magnetocaloric peaks are seen in all of them. Weiss & Piccard measured the magnetocaloric effect in Ni in four different magnetic fields of up to 1.50 T, in Co in ten different magnetic fields of up to 2.32 T, and in Fe in three magnetic fields of up to 0.8 T by Potter [59] and at 3.0 T by Hirschler & Rocker. It is reported in the review of MCE that several 3*d*-based intermetallic compounds, Mn($As_{1-x}P_x$), $Ni_2(Mn_{1-x}V_x)Sn$, $Ni_2(Mn_{1-x}Nb_x)Sn$, $Mn_{3-y-x}Cr_yAlC1C_x$, $(Hf_{0.83}Ta_{0.17})Fe_2C_x$, FeRh, and $Cr_3Te_4$ have been investigated for their magnetocaloric properties[41]. Xuexi Zhang *et.al.* reported GMCE in Ni-Mn-In alloys near room temperature [60]. Reports suggest that MCE has been reported in bulk metallic glass materials such as $Ho_{20}Er_{20}Co_{20}Al_{20}RE_{20}$, $Fe_{45}Cr_{15}Mo_{14}C_{15}B_6Y_2Ni_3$ [61,62]. Further investigations on MCE in the room temperature range were carried out in Ni-Mn-Ga alloys, La-Fe-Co-S alloys, and Mn-Fe-P-As alloys, [18,63].H Wada *et.al* reported GMCE in Mn-As-Sb compounds with a $\Delta S_m$ of 30 J/kg/K at 318 K at 5T [48]. Mn-As shows a giant MCE

among the transition-metal-based compounds. The substitution of Sb for As can tune the Curie temperature from 230 K to 315 K without a considerable change in $\Delta S_m$. Xiaodong Si *et. al.* reported a decrease in maximum magnetic entropy change from 3.08 to 2.67 J/kg/K with Si doping in $Mn_{1-x}CoGeSi_x$ [64].

### *1.7.6 Perovskite Oxides*

Perovskite-type oxides exhibit a significantly smaller magnetic hysteresis, higher chemical stability and electrical resistivity, favouring a low value of eddy current heating compared with rare earth metals and their alloys. These materials are considered to be more suitable candidates for magnetic refrigeration at high temperatures, especially near room temperature [18,65,66]. Zhang Y, *et.al* reported MCE in $PrNiMnO_6$ double perovskites at a lower temperature and Jerbi *et.al* reported MCE properties in $Pr_{0.5}A_{0.05}Sr_{0.45}MnO_3$ composites [1,38,39]. Wang H *et.al* reported MCE properties in $Nd_{1-x}Sr_xMnO_3$ [67]

The perovskite lattice ($ABO_3$) is generally considered to be made up of larger A cations that are XII-fold coordinated by oxygen and smaller B cations within oxygen octahedra. The ions occupying the A and B lattice sites are detailed in Fig. 1.10. Generally, perovskite materials crystallize in three different structures, cubic, orthorhombic and rhombohedral symmetry as shown in Fig.1.11 and Fig.1.12.

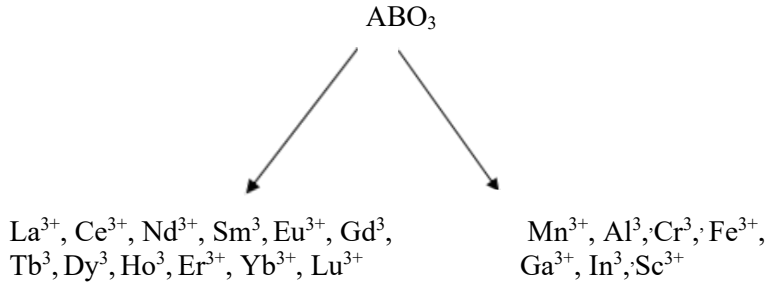


**Figure.1.10.** The ions occupying the A and B lattice sites in a Perovskite

The family of perovskite structures is named after the mineral $CaTiO_3$ which exhibits an orthorhombic structure with space group *Pnma.* The most symmetric structure observed for the $A^{3+}B^{3+}O_3$ perovskites is rhombohedral $R\bar{3}c$ (e.g. $LaAlO_3$) which involves a rotation of the $BO_6$ octahedra with respect to the cubic structure. The

structure of an ideal cubic perovskite is displayed in Fig. 1.11, where the A cations are shown at the corners of the cube, and the B cation in the centre with oxygen ions in the face-centred positions[68].

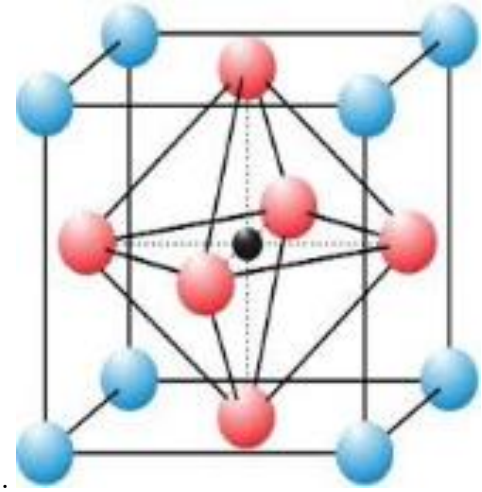

**Figure. 1.11.** Structure of an ideal cubic perovskite

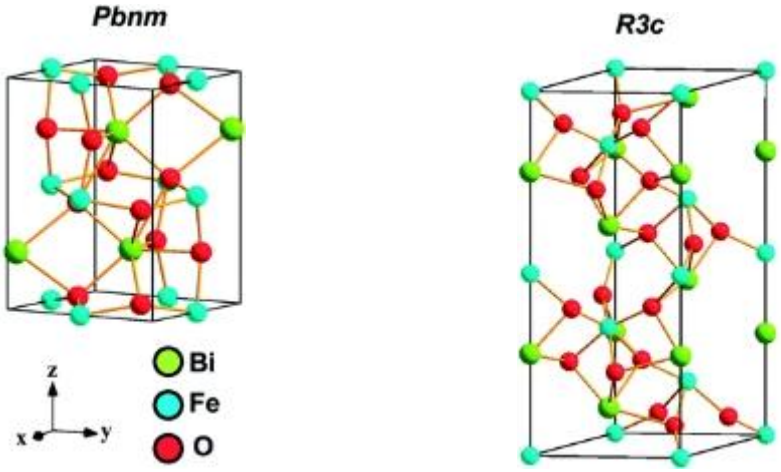


(a) (b)

**Figure.1.12.** (a) Orthorhombic structure (b) Rhombohedral structure

## Manganites

Perovskite-type manganese oxide materials generally known as perovskite manganites have a general formula of $R_{1-x}M_xMnO_3$, where R stands for trivalent rare-

earth elements such as La, Pr, Nd, Sm, Eu, Gd, Ho, Tb, etc., and M stands for divalent alkaline earth ions such as $Sr^{2+}$, $Ca^{2+}$, $Ba^{2+}$, and $Pb^{2+}$ or for alkaline ions, $Na^{1+}$, $K^{1+}$, $Ag^{1+}$, etc. The deformation of the $MnO_6$ octahedron resulting from the Jahn–Teller effect is one of the potential causes of the lattice distortion observed in perovskite. In the perovskite structure, the connective arrangement of the $MnO_6$ octahedra resulting in an orthorhombic or rhombohedral lattice, causes further lattice deformation [18].

Manganites with an $ABO_3$ structure exhibiting large MCEs are expected to be good candidates for magnetic refrigeration at various temperatures because of magnetic properties like large saturation magnetisation and tunable Curie temperature. Cost-effectiveness, shorter production times, relative ease of production, resilience to corrosive environments, chemical stability, good structure, environmental friendliness, SOMT behaviour, superior MCE properties, and easily adjustable $T_C$ within the room-temperature range are just a few benefits of perovskite manganites.

Exchange interactions can impact the magnetic characteristics of perovskite manganites by attracting the presence of $Mn^{3+}$ and $Mn^{4+}$ ions. Because of this, researchers are looking into it as a potential substitute material for magnetic refrigeration technology. The double exchange/superexchange mechanism between mixed valence states of Mn ions and the strong spin lattice coupling underlie the magnetism in a manganite. The doping or substitution of ions in the lattice can affect the $Mn^{3+}$–$O^{2-}$-$Mn^{4+}$ double exchange inside the perovskite manganite, thereby causing changes in the Curie temperature $T_C$, the maximum magnetic entropy change $|\Delta S_m|$ and the relative cooling efficiency (RCP). There are review papers in the MCE properties of manganites indicating that a lot of work has been done in manganites, specifically in lanthanum manganites [18,69].

### *1.7.7 Lanthanum Manganites*

Lanthanum manganite is an inorganic substance with the molecular formula $LaMnO_3$. Lanthanum manganite is composed of oxygen octahedra with a central Mn atom that forms the perovskite structure. A substantial Jahn–Teller distortion of the

oxygen octahedra in $LaMnO_3$ distorts the cubic perovskite structure into an orthorhombic structure. Neutron scattering shows $LaMnO_3$ often has lanthanum vacancies, hence this material is usually referred to as $LaMnO_{3+\delta}$. In this perovskite, these vacancies produce a structure with a rhombohedral unit cell. The $LaMnO_{3+\delta}$ semiconductor exhibits a ferromagnetic order at temperatures less than 140 K. Lanthanum manganite is an electrical insulator and an A-type antiferromagnet. It is the parent compound of a number of significant alloys, often referred to as rare-earth magnates or colossal magnetoresistance oxides. These families include lanthanum strontium manganite, lanthanum calcium manganite and others. Among the manganite perovskite materials, lanthanum manganite with the $ABO_3$ structure and its compounds exhibit a large MCE near room temperature, which is comparable to gadolinium [52,70–72]. MCE properties are reported in lanthanum manganites near and above room temperature[73–75].

In lanthanum manganite, both the La and the Mn are in the +3-oxidation state. When some of the La atoms are substituted with divalent atoms such as Sr or Ca produces a similar amount of tetravalent $Mn^{4+}$ ions. Such doping or substitution can produce various electronic effects, which form the basis of a rich and complex electron correlation phenomena that yield diverse electronic phase diagrams in these alloys. Some properties of lanthanum manganites are that the perovskite lanthanum strontium manganite (LSMO) has a high electrochemical activity for the $O_2$ reduction reaction, high thermal stability and high electrical conductivity etc.

Oxygen atoms form an octahedron around the manganese atoms in lanthanum manganites. The oxygen atoms are ionized to $O^{2-}$, lanthanum to $La^{3+}$, and the manganese atoms are either ionized to $Mn^{3+}$ or to $Mn^{4+}$ depending on the doping level. As a result, the 3 or 4 electrons present in the 3d shell of the manganese atoms play an important role in determining the electrical and magnetic behaviour. The interactions between the different manganese atoms determine the overall magnetic and electrical behaviour. This results in the 3d shell of the manganese atoms being filled with either 4 or 3 electrons. The electrical and magnetic behaviour is largely determined by the

electrons in the 3d shell of the manganese atoms. The overall magnetic and electrical behaviour depends on the interactions between the different manganese atoms. The four counteracting processes, double exchange interaction, superexchange interaction, Jahn-Teller effect and charge ordering play a role in the behaviour of the 3d electrons.

*(a) Double exchange interaction:*

The double exchange mechanism explains the ferromagnetism in mixed valence transition metal oxides, especially manganites. The electronic interaction between transition metal ions and foreign dopants in a transition metal oxide makes the double exchange interaction possible. Here double exchange interaction is a electron transfer mechanism which involves two neighbouring manganese atoms and their connecting oxygen. (Fig. 1.13)

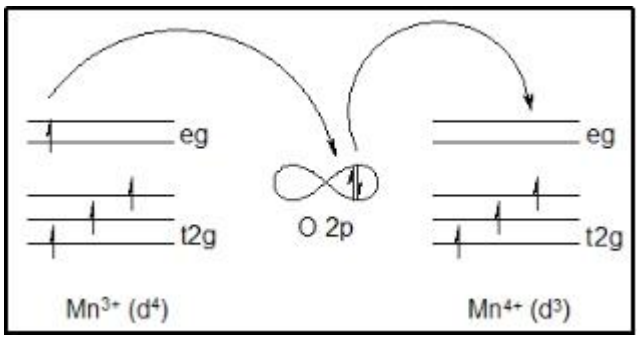


**Figure. 1.13.** Double exchange interaction

One of the $e_g$ states of one of the manganese atoms is occupied, while the other $e_g$ shell is unoccupied. One electron tunnel from the oxygen atom to the manganese atom without $e_g$ electrons. The $e_g$ electron from the other manganese atom then tunnels to the free 2p orbitals of the oxygen atom. As a result, one electron from one manganese atom is transferred to the next. This is how double exchange interaction induces electrical conductivity. Only states with parallel spin are possible, since electrons retain their spin while tunnelling. This is because the double exchange interaction only occurs between manganese atoms whose $t_{2g}$ electrons have their spins aligned. The double exchange interaction reduces the energy of the electrons by

increasing their freedom. Ferromagnetism is therefore induced by electrons of neighbouring manganese atoms aligning their spins in an energetically favourable manner.

*(b) Super exchange interaction:*

Super exchange results from the electrons having come from the same donor atom and being coupled with the receiving ions' spins. In this interaction, the magnetic moments interact directly through space or a nonmagnetic anion and are strongly localised on the magnetic centres. If the two next-to-nearest neighbour positive ions are connected at 90° to the bridging non-magnetic anion, then the interaction can be ferromagnetic. For example, consider the structure $Mn^{3+}$ - $O^{2-}$ - $Mn^{3+,}$ the two Mn ions can interact with each other by virtual hopping of electrons through an $O^{2-}$ being "in the way". (Fig. 1.14).

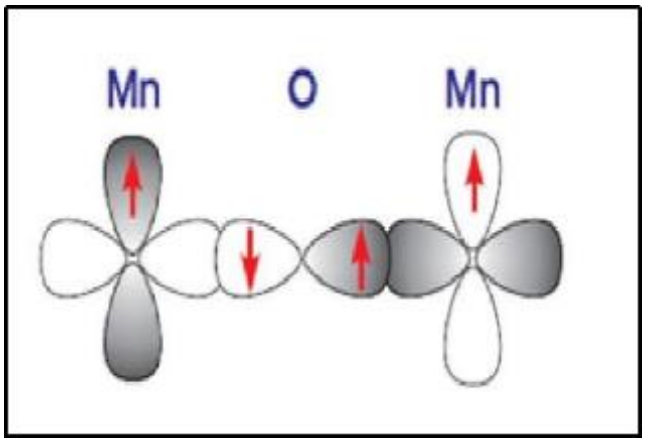


**Figure 1.14** Super exchange interaction

*( c) Jahn-Teller effect*:

The Jahn-Teller effect is a geometric distortion of a non-linear molecular system that reduces its symmetry and energy. Typically this distortion is observed among octahedral complexes where the two axial bonds can be shorter or longer than

those of the equatorial bonds. According to the Jahn-Teller theorem, any molecule or complex ion in an electronically degenerate state will be unstable relative to a configuration of lower symmetry in which the degeneracy is absent. When several manganese atoms have a half-filled $e_g$ shell, the Jahn Teller distortions are only favorable and hence Jahn Teller effect is doping dependent.

*(d) Charge ordering:*

Charge ordering is caused by Coulomb repulsion between $e_g$ electrons at different manganese atoms. This configuration is so stable that electrons retain their positions preventing electrical conduction. This stability can be due to Coulomb repulsion or electron-phonon coupling.

### *1.7.8 Substituted Lanthanum Manganites*

Recently, the investigations have focused on the doping/ substitution of cations in the A site and B site of lanthanum manganite which tunes the magnetic and magnetocaloric properties of these perovskites. $LaMnO_3$ compounds behave like antiferromagnetic insulators at lower temperatures and paramagnetic insulators at higher temperatures. When a divalent cation (Ca, Sr, Ba or Pb) is substituted for trivalent La in the range ($0.2 < x < 0.4$), the material becomes a metallic ferromagnet below the Curie temperature [76]. This is due to the presence of mixed valence states of Mn, $Mn^{3+,}$ and $Mn^{4+}$, which gives rise to a competition between the antiferromagnetic superexchange and ferromagnetic double exchange interaction; the magnetic properties can be varied with the partial substitution of $La^{3+}$ by divalent cations.

Most of the research work on the MCE properties of lanthanum manganites has been carried out on the divalent cation substitution at the A site. It is interesting that the important research works in calcium doped lanthanum manganite were carried out by Zhong, Morelli, and Guo all are in 1996. Guo *et. al*. reported large MCE in polycrystalline $La_{1-x}Ca_xMnO_3$ with $0.2 \leq x \leq 0.33$ [77,78]. It was observed that $\Delta S_m$ reaches a maximum value of -5.5 J/kg/K at 230 K, -4.7 J/kg/K at 224 K and -4.3 J/kg/K

at 260 K for x=0.2,0.25 and 0.33 compositions respectively for $\Delta H$= 1.5T which is greater than that of Gd in the same magnetic field [77]. Zhang *et. al* reported $\Delta S_m$ 0.6 J/kg/K for 1T over a wide MCE and 2.6 J/kg/K at 260 K for a 3T magnetic field [79]. There are several reports on the investigation of MCE of La-Ca-Mn-O perovskites as they exhibit entropy distribution over a wide temperature range [63,72,80–82].

**$La_{1-x}Sr_xMnO_3$**

To tune magnetocaloric properties in the room temperature range, several efforts were made to explore the MCE's of Sr substituted lanthanum manganite [45,73,83–87]. The transition temperature of substituted lanthanum manganite can be increased by the doping of Sr in the La site in a small percentage. There are many reports on the La-Ca-Sr-Mn-O perovskites to tune the transition temperature to near room temperature. Szewczyk *et. al*. first reported the MCE of $La_{0.845}Sr_{0.155}MnO_3$ polycrystalline manganite with $\Delta S_m$ and $\Delta T_{ad}$ -6.06 J/kg/K and 3.3 K respectively at 234 K for a magnetic field of 7T [88]. Later the same authors measured the MCEs of $La_{1-x}Sr_xMnO_3$ (x=0.120, 0.135, 0.155, 0.185, and 0.200) systematically [89]. The MCE increased with the Sr-doped content, except for the x=0.120 composition. The highest value of $\Delta T_{ad}$ obtained was 4.15 K for a 7T magnetic field for x =0.2 composition. Reshmi *et. al.* reported a magnetic entropy change of 3 J/kg/K and RCP of 132 J/kg at 290 K for a 5T magnetic field in $La_{0.67}Sr_{0.33}MnO_3$ [45]. M. Koubaa *et. al* reported a maximum entropy change of 0.84 J/kg/K at 220 K in an applied field of 2T. It is shown that Na substitution for Sr decreases $\Delta S_m$ and transition temperature to 0.47 J/kg/K and 185 K respectively for x=0.1 composition [90].

**$La_{1-x}Ba_xMnO_3$**

Several researchers explored their work in the MCE properties of Ba-substituted lanthanum manganite to tune the transition temperature and enhance the RCP values[71,91–93]. Zhang H et.al reported room temperature MCE properties in $La_{1-x}Ba_xMnO_3$ compounds [94].

**$La_{1-x}A_xMnO_3$ (A – Na, K, Ag)**

The monovalent substitution (Na, K, Ag) in the A site of Lanthanum manganites introduces the mixed valence state of $Mn^{3+}/Mn^{4+}$ pairs, which contributes to ferromagnetism in manganites. Substitution of $Na^+$ and $K^+$ in the A site of lanthanum manganite can tune the MCE peak temperature. The transition temperature can be tuned for $La_{1-x}Na_xMnO_3$ in the range 195 – 334 K and for $La_{1-x}K_xMnO_3$ compounds in the range 230-334 K [95]. There are a few reports on the magnetic and magnetocaloric properties of sodium-substituted lanthanum manganites[96–99]. In 1996 Morelli *et. al.* first reported the MCE properties of $La_{0.67}Na_{0.33}MnO_3$ perovskite film with a maximum entropy change of 2.06 J/kg/K at 252 K for a 5T magnetic field [75]. Zhong *et.al* reported a magnetic entropy change of 1.96 J/kg/K for a field of 1T at 334 K in $La_{0.8}Na_{0.2}MnO_3$ [95] Soma Das *et. al.* reported $\Delta S_m$ of 1.48 J/kg/K at 312 K in $La_{0.85}Na_{0.15}MnO_3$ [100]. The higher substitution of Na in the La site contributes to the magnetic interaction by the double exchange interaction and the induced vacancies in the La or O sites, which play an important role in the magnetic ordering. There are only a few reports on the higher sodium substituted lanthanum manganites. Sethulakshmi *et al.* reported a maximum magnetic entropy change of 1.5 J/kg/K near room temperature in a magnetic field of 5T [101].

It is noteworthy that investigations have been carried out by substituting Na in La-Ca-Mn-O compounds to enhance the MCE [102]. Nesrine Mechi *et.al.* reported a maximum magnetic entropy change of 3.06 J/kg/K at 275 K for a 5T magnetic field in $La_{0.6}Ca_{0.2}Na_{0.2}MnO_3$[103]. S. Choura Maatar *et.al.* reported that the Curie temperature increases from 240K to 330K with the increase in Na content in $La_{0.8}Ca_{0.2-x}Na_xMnO_3$ while a decrease of $\Delta S_m$ from 4.56 J/kg/K to 2.3 J/kg/K has been observed[104]. F.Ayadi *et al.* reported a maximum entropy change $\Delta S_m$ of 1.93 J/kg/K in a magnetic field of 2T at 350K in $La_{0.7}Sr_{0.2}Na_{0.1}MnO_3$[105]. A Jerbi *et.al* studied the MCE of $Pr_{0.5}A_{0.05}Sr_{0.45}MnO_3$ (A=Na and K) and observed $\Delta S_m$ of 1.60 J/kg/K and 1.66 J/kg/K around $T_c$ for Na and K substitution respectively[65]. Researchers have investigated

the magnetocaloric properties of potassium-doped lanthanum manganites. Soma Das reported the magnetocaloric properties of $La_{1-x}K_xMnO_3$ with a magnetic entropy change of 3.00 J/kg/K at 310 K [70,106]. The substitution of Ag in the A site of lanthanum manganite also plays a crucial role in the enhancement of magnetic entropy change and relative cooling power. I.Walha *et. al* reported an increase of $\Delta S_m$ from 6.59 to 8.24 J/kg/K and RCP with 10 % Ag doping in $La_{0.6}Ca_{0.4}MnO_3$ at 267 K [107].

Among the perovskite cobaltites, $LaCoO_3$ is an amazing candidate due to its fascinating properties such as high electronic and ionic conductivity, catalytic activity, spin-state transition and colossal magnetoresistance[108]. Among the transition metals, Co is preferred because two spin-state transitions are expected for the cobalt ion, from a low-spin to a high-spin configuration, via an intermediate spin state. Then, the partial substitution of Co by a B cation may considerably modify its electronic structure and hence improve its important applications. The literature survey reveals that some researchers previously reported the electric, magnetic, catalytic, magnetocaloric, and magnetoresistive properties of $La_{1-x}A_xCoO_3$(A=Sr, Ca, Te, Ba..) perovskite materials [109–111] . V A. Ryzhov reported the existence of FM clusters in Ca-doped Lanthanum Cobaltite[108]. There are many reports on the magneto-resistive, structural, electrical, and catalytic properties of Sr-doped Lanthanum cobaltites[6,13,112]. The magnetic and MCE properties of A site-doped $La_{1-x}B_xMnO_3$ compounds have been extensively studied by many researchers. Magnetocaloric effect had been reported in Te substituted Lanthanum $La_{0.7}Te_{0.3}Mn_{0.7}Co_{0.3}O_3$[113]. Electrical conductivity and magnetic properties of Lanthanum barium cobaltite have also been studied [5].

### *1.7.9 Ferrites*

Ferrites are the compounds of two metallic oxides consisting of iron oxide and any of the bivalent elements (Ni, Mn, Mg, Zn, Cu, Fe, etc.). Ferrites exhibit the permanent type of magnetism referred to as ferrimagnetism. Ferrites are classified based on their crystal structure into four types: spinel, garnet, ortho, and hexagonal,

and according to their magnetic properties as soft ferrites and hard ferrites. Spinel ferrites are the simplest among these groups and are detailed below.

**Spinel Ferrites**

The spinel ferrites are metal oxides with the general formula $AB_2O_4$, where O stands for oxygen, B for Al, Cr, or Fe, and A for Mg, Fe, Zn, Mn, Ni, etc. The spinel ferrites have a face-centered cubic crystal structure with $A^{2+}\ B_2^{3+}\ O_4^{2-}$formulation ($A^{2+}$ = $Fe^{2+}$, $Zn^{2+}$, $Co^{2+}$, $Mn^{2+}$, $Ni^{2+}$, $Mg^{2+}$, etc.) A and B can be divalent, trivalent, or quadrivalent cations, and anions are oxides. The unit cell of spinel contains 16 trivalent ions, 32 oxygen ions, and 8 divalent metal ions[114,115] is shown in Fig. 1.15.

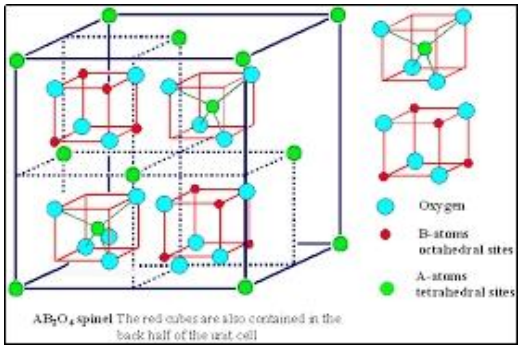


**Figure.1.15.** Unit cell of the spinel structure

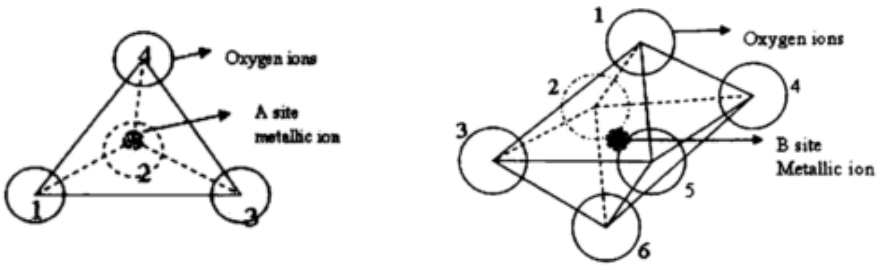


(a) (b)

**Figure. 1.16. (a)**Tetrahedral coordination **(b)**Octahedral coordination

Figure 1.16 (a) shows the tetrahedrally coordinated A sites, while Figure 1.16 (b) shows the octahedrally coordinated B sites. The oxygen anions are arranged in a face-centered cubic pattern, creating two types of interstitial space between the anions.

In a unit cell, there are eight formula units of $MFe_2O_4$. In a unit cell of 32 oxygen anions, there are 32 octahedral sites and 64 tetrahedral sites. In a spinel ferrite structure, the octahedral sites are larger than the tetrahedral sites, and 8 of the 64 tetrahedral sites and 16 of the 32 octahedral sites are occupied by cations. The magnetic moments of the cations at the tetrahedral sites are oriented in the same direction but antiparallel to that of the octahedral sites.

Spinel ferrites are categorized as normal spinel, inverse spinel, and mixed spinel based on the distribution of cations in the tetrahedral and octahedral sites [2,114]. In normal spinel, trivalent cations are occupied in the octahedral B site and divalent cations are lodged in the tetrahedral A sites. Bulk $ZnFe_2O_4$ is a typical example of normal spinel, with $Fe^{3+}$ cations incorporated at octahedral positions and $Zn^{2+}$ cations occupying tetrahedral sites[116]. In the inverse spinel, divalent cations occupy the octahedral B sites half of the trivalent cations occupy the tetrahedral A site and the remaining half reside in the octahedral B site. A typical example of an inverse spinel is $CoFe_2O_4$, $Co^{2+}$ cations occupy the octahedral B site, and as a trivalent cation, $Fe^{3+}$ occupies the tetrahedral A and octahedral B sites equally[117]. The intriguing and relevant electrical and magnetic characteristics of the spinel are controlled by the distribution of iron and divalent metal ions among the tetrahedral and octahedral sites of the spinel lattice. Based on the site ratio and stoichiometry, the cations in a random spinel structure are distributed equally over two sites, as shown in $(M_{\delta}^{2+}Me_{1-\delta}^{2+})_A[M_{1-\delta}^{2+}Me_{1+\delta}^{3+}]_BO_4$, where δ is the inversion parameter[2]. The value of the inversion parameter depends on the preparation method and constituents of ferrites. If the inversion parameter, $\delta = 1$, the spinel is a complete normal spinel; if $\delta = 0$, the spinel is a complete inverse spinel; if δ falls between these two extremes, the spinel is called a mixed spinel, for instance, $\delta = 1/3$. $MgFe_2O_4$ is a typical example of mixed spinel.

**Magnetic properties of ferrites**

Ferrites exhibit ferrimagnetism. The superexchange interaction between metal electrons and oxygen ions serves to provide ferrites with their ferrimagnetic properties. Several factors that affect the magnetic characteristics of ferrites include the kind of

cations, heat treatment, preparation technique, site preference, cation energy, and Madelung energy. Neel uses Heisenberg's theory of forces to explain the magnetisation in ferrites. According to this theory, the exchange energy between two adjacent atoms having spin angular momentum is given by the following equation.

$$E_{ex} = -2J_{ex}\, S_i S_j \tag{1.32}$$

where $E_{ex}$ is the exchange energy, $S_i$ and $S_j$ are the total spins of adjacent atoms, and $J_{ex}$ is the exchange integral. The value of $J_{ex}$ determines the ferri-, ferro-, or antiferromagnetism. There are three kinds of magnetic interactions between magnetic ions in spinels. Magnetic interaction arises through intermediate $O_2^-$ ions through a super exchange process, and the magnetic ions are located in two crystallographically distinct lattice locations [48]. When these magnetic moments interact with the anions (super exchange) in a spinel, the moments of the A and B site ions align, forming a ferrimagnetic ordering with A-A and B-B parallel but A-B antiparallel. It has been shown experimentally that spinel ferrites have a negative interaction energy, which results in an antiparallel orientation. However, ferrites have a net magnetisation as a result of the unequal magnetisation magnitudes of the A and B sublattices. The A-B interaction is the strongest of the three interactions, while the A-A interaction is the weakest. Because of the predominance of the A-B interaction, the spins of the A- and B-site ions in ferrite will be oppositely magnetised in the A and B sublattices, resulting in a magnetic moment that is equal to the difference between their spins. Generally, the saturation magnetisation of the sublattice *B* ($M_B$) is greater than that of *A* ($M_A$), resulting in a net saturation magnetisation of $M_s = M_B - M_A$ .

**MCE in Ferrite Materials**

The literature research indicates that there are not many publications on the MCE characteristics of spinel ferrite. The higher $T_c$ value and low $-\Delta S_m$ values exhibited by the ferrites are the main reasons. Some researchers investigated the MCE properties in ferrites. Even though there are only a few reports on the investigations of magnetocaloric properties in ferrites. MCE was reported in superparamagnetic ferrites,

$Mn_{0.68}Zn_{0.25}Fe_{2.07}O_4$, and cobalt ferrite[117–121]. According to the literature review, current studies have been performed on the MCE characteristics of ferrites. M. A. Islam *et al* reported a maximum magnetic entropy change of 0.66 J/kg/K at 675 K, for $CoFe_2O_4$. 1.98 J/kg/K for $Co_{0.875}Cr_{0.125}Fe_2O_4$ at 740 K and 1.8 J/kg/K for $Co_{0.75}Cr_{0.25}Fe_2O_4$ at 735 K for an applied field of 5T[119]. A.Hamad *et.al*. reported inverse and conventional MCE effects in $Ni_{0.4}Cu_{0.2}Zn_{0.4}Fe_{2-x}Dy_xO_4$ [122]. Murli Kumar *et.al.* reported the effect of Gd doping on the MCE properties of barium hexaferrite [123].

### *1.7.10 Magnetic Nanocomposites*

Composites are composed of two materials in which one of the materials is called the reinforcing phase, which is in the form of fibres, sheets, or particles, and is embedded in the other material called the matrix phase. A nanocomposite is a matrix to which nanoparticles have been added to improve a particular property of the material. Nanocomposites are synthetic materials designed for enhanced performance in any number of unique applications. Magnetic nanocomposites in which magnetic particles, which are in the nano regime, are embedded in a nonmagnetic matrix. The metal reinforced polystyrene nanocomposites are promising candidates for a wide variety of engineering applications including catalysis, chemical sensing, biomedical applications, electronics, photonics and for the fabrication of electromagnetic and optical devices[8,124–126].

Among these materials, our research has been focused on the magnetocaloric properties of the perovskite manganites, ferrite materials and nano composites.

## 1.8. Motivation and Objectives

Global warming and ozone depletion contributed by greenhouse gases used in conventional gas compression refrigerator necessitated the development of a more energy efficient and environmentally friendly active technology. Magnetic refrigerators have become a viable substitute for traditional vapor-compression refrigerators because of their great efficiency, small size, and environmental friendliness. Many studies on the magnetocaloric effect (MCE) in different materials

have been carried out in recent years. Commercial magnetic refrigeration systems have been created by several researchers, and companies all over worldwide are investing in this technology. However, a major challenge in the development of magnetic refrigerators is the high cost of refrigerant materials. Therefore, the search for cost-effective magnetic refrigerant materials that operate near room temperature and can be synthesized through simple and efficient methods remains a key focus of research.

Although a lot of study has been done on low-temperature magnetocaloric effect (MCE) materials, current studies have concentrated on near-room-temperature MCE materials because of their potential for usage in both home and business settings. Since gadolinium has high MCE capabilities at temperatures near room temperature, its discovery represented a major turning point in this sector. However, gadolinium is not feasible for widespread commercial use because of its expensive cost. To address this challenge, we can think of nanomagnetic materials with excellent magnetic properties as promising MCE materials. Magnetocaloric effect in nanomagnetic materials can be tuned through size dependent interactions, tunable phase transitions and improved magnetic characteristics. Perovskite manganite nanomagnetic materials shows strong electron correlations and double exchange interactions enabling control over transition temperature for being used in magnetocaloric applications in different temperature regimes. Lanthanum manganites, which demonstrate promising MCE characteristics near ambient temperature can be a good choice. Ferrites are materials with good chemical stability, low cost and eco-friendly materials which makes them a good candidate in the search for sustainable cooling solutions. Metal nanocomposites offer high thermal conductivity and reduced hysteresis losses which is favourable for magnetic cooling applications. The literature reports indicate these three categories of nanomagnetic materials can be tuned for practical refrigerants for magnetic cooling over a wider temperature range because of their significant entropy change and readily tuneable Curie temperature. These materials are feasible for commercial use also since they are not only affordable but also simple to synthesise in large quantities.

The research aims to synthesise and characterise perovskite manganites, ferrites and metal nanocomposites to explore their potential for magnetocaloric applications. The specific objectives of the work are as follows.

- Synthesis of nanomagnetic materials by sol-gel autocombustion method
    - Perovskites
        - Lanthanum Sodium Manganite $La_{0.5}Na_{0.5}MnO_3$
        - Cobalt substituted Lanthanum Sodium Manganite ($La_{0.5}Na_{0.5}Co_xMn_{1-x}O_3$)
    - Ferrites
        - Cobalt substituted Copper Ferrite ($Cu_{1-x}Co_xFe_2O_4$)
        - Zinc substituted Copper Ferrite ($Cu_{1-x}Zn_xFe_2O_4$)
- Synthesis of Metal nanocomposites- Cobalt-polystyrene nanocomposites.
- Structural and compositional analysis of the samples.
- Magnetic characterisation of the samples.
- MCE characterisation of the samples.
- Identifying the potential of the nanomagnetic materials for magnetic refrigeration applications.

**REFERENCES**

[1] Sochin Chikazumi, C.D.Graham., Physics of Ferromagnetism, Clarendon Press, Oxford, 1997.

[2] B.D. Cullity, C.D. Graham, Introduction to Magnetic materials, John Wiley & Sons, Inc., Hoboken, N J., 2009

[3] J. Smit, H.P.J. Wijn, Advances in Electronics and Electron Physics 6 (1954) 69–136.

[4] V. V. Jadhav, S.D. Shirsat, U.B. Tumberphale, R.S. Mane, Spinel Ferrite Nanostructures for Energy Storage Devices (2020) 35–50.

[5] I. Szpunar, S. Wachowski, T. Miruszewski, K. Dzierzgowski, K. Górnicka, T. Klimczuk, M.H. Sørby, M. Balaguer, J.M. Serra, R. Strandbakke, M. Gazda, A. Mielewczyk-Gryń, Journal of the American Ceramic Society 103 (2020) 1809–1818.

[6] N. Alhokbany, S. Almotairi, J. Ahmed, S.I. Al-Saeedi, T. Ahamad, S.M. Alshehri, J King Saud Univ Sci 33 (2021) 101419.

[7] V.F. Puntes, K.M. Krishnan, A.P. Alivisatos, Science 291 (2014) 2115-2117.

[8] V. Gopalan, On the Synthesis and Multifunctional Properties of some Nanocrystalline Spinel Ferrites and Nanocomposites, DyuthiCusat, (2009).

[9] H.E. Stanley, V.K. Wong, Am J Phys 40 (1972) 927–928.

[10] Q.A. Pankhurst, N.K.T. Thanh, S.K. Jones, J. Dobson, J Phys D Appl Phys 42 (2009).

[11] S.Y. Srinivasan, K.M. Paknikar, D. Bodas, V. Gajbhiye, Nanomedicine 13 (2018) 1221–1238.

[12] S.M. Ansari, R.D. Bhor, K.R. Pai, D. Sen, S. Mazumder, K. Ghosh, Y.D. Kolekar, C. V. Ramana, Appl Surf Sci 414 (2017) 171–187.

[13] J. Deng, L. Zhang, H. Dai, H. He, C.T. Au, Ind Eng Chem Res 47 (2008) 8175–8183.

[14] A.O. Ayaş, S.K. Çetin, G. Akça, M. Akyol, A. Ekicibil, Mater Today Commun 35 (2023) 105988.

[15] V. Franco, J.S. Blázquez, J.J. Ipus, J.Y. Law, L.M. Moreno-Ramírez, A. Conde, Prog Mater Sci 93 (2018) 112–232.

[16] Q. Wang, Q. Wu, H. Cheng, X. Li, N. Yu, M. Pan, Y. Yu, J. Fang, X. Hu, H. Ge, H. Yang, J Eur Ceram Soc 43 (2023) 6665–6680.

[17] L. Li, M. Yan, J Alloys Compd 823 (2020) 153810.

[18] M.H. Phan, S.C. Yu, J Magn Magn Mater 308 (2007) 325–340.

[19] V.K. Pecharsky, K.A. Gschneidner, J Magn Magn Mater 200 (1999) 44–56.

[20] V.K. Pecharsky, K.A. Gschneidner, J Appl Phys 86 (1999) 565–575.

[21] V.K. Pecharsky, V.K. Pecharsky, K.A. Gschneidner, K.A. Gschneidner, A.O. Pecharsky, A.M. Tishin, Phys Rev B Condens Matter Mater Phys 64 (2001) 1444061–14440613.

[22] M.Shatruk, J.K.Clark, Comprehensive Inorganic Chemistry III, Third Edn. (2023), 236.

[23] V. Franco, J.S. Blázquez, A. Conde, Appl Phys Lett 89 (2006) 6–9.

[24] M.D. Kuz'min, A.M. Tishin, Cryogenics 32 (1992) 545–558.

[25] R. Gimaev, Y. Spichkin, B. Kovalev, K. Kamilov, V. Zverev, A. Tishin, International Journal of Refrigeration 100 (2019) 1–12.

[26] J. Tušek, S. Zupan, I. Prebil, A. Poredoš, Strojniski Vestnik, Journal of Mechanical Engineering 55 (2009) 293–302.

[27] M.S. Kamran, H.O. Ahmad, H.S. Wang, Renewable and Sustainable Energy Reviews 133 (2020) 110247.

[28] G. V Brown, G. V Brown, J Appl Phys 47(8) 3673-3680, 1976.

[29] A. Kitanovski, J. Tušek, U. Tomc, U. Plaznik, M. Ožbolt, A. Poredoš, Magnetocaloric Energy Conversion, 2015.

[30] C.Zimm, A. Jastrab, A. Sternberg, V. Pecharsky, K. Gschneidner, Jr.,M. Osborne, I. Anderson, Adv. Cryo. Eng., 43 (1998) 1759–1766.

[31] P.E. Blumenfeld, F.C.Prenger, A.Strnberg, C.Zimm,AIP Conf.Proc.,613 (2002) 1019–1026.

[32] T. Kawanami, K. Chiba, K. Sakurai, M. Ikegawa, International Journal of Refrigeration 29 (2006) 1294–1301.

[33] J. Huang, J. Liu, P. Jin, H. Yan, J. Qiu, L. Xu, J. Zhang, Rare Metals 25 (2006) 641–644.

[34] D.S. Arnold, A. Tura, A. Rowe, International Journal of Refrigeration 34 (2011) 178–191.

[35] K. Nakamura, T. Kawanami, S. Hirano, M. Ikegawa, K. Fumoto, 2008 2nd International Conference on Thermal Issues in Emerging Technologies, ThETA 2008 (2008) 381–390.

[36] M.S. Kamran, J. Sun, Y.B. Tang, Y.G. Chen, J.H. Wu, H.S. Wang, Appl Therm Eng 102 (2016) 1126–1140.

[37] B. Huang, J.W. Lai, D.C. Zeng, Z.G. Zheng, B. Harrison, A. Oort, N.H. van Dijk, E. Brück, International Journal of Refrigeration 104 (2019) 42–50.

[38] C.R.H. Bahl, T.F. Petersen, N. Pryds, A. Smith, Review of Scientific Instruments 79 (2008).

[39] A.M. Tishin, V.K. Pecharsky, K.A. Gschneidner, Phys Rev B 57 (1998) 3478–3490.

[40] V.K. Pecharsky, K.A. Gschneidner, Phys Rev Lett 78 (1997) 4494–4497.

[41] K.A. Gschneidner, V.K. Pecharsky, annurev matsci 30 (2000) 387–429.

[42] K.A. Gschneidner, V.K. Percharsky, J Appl Phys 85 (1999) 5365–5368.

[43] K.A. Gschneidner, V.K. Pecharsky, International Journal of Refrigeration 31 (2008) 945–961.

[44] F. Zhang, K. Westra, Q. Shen, I. Batashev, A. Kiecana, N. van Dijk, E. Brück, J Alloys Compd 906 (2022) 164337.

[45] C.P. Reshmi, S. Savitha Pillai, K.G. Suresh, M.R. Varma, Solid State Sci 19 (2013) 130–135.

[46] S.K. Estemirova, V.Y. Mitrofanov, S.A. Uporov, R.I. Gulyaeva, J Magn Magn Mater 502 (2020) 166593.

[47] A. Smith, C.R.H. Bahl, R. Bjork, K. Engelbrecht, K.K. Nielsen, N. Pryds, Adv Energy Mater 2 (2012) 1288–1318.

[48] H. Wada, Y. Tanabe, Appl Phys Lett 79 (2001) 3302–3304.

[49] I. Walha, M. Smari, T. Mnasri, E. Dhahri, J Magn Magn Mater 454 (2018) 190–195.

[50] F. Zhang, K. Westra, Q. Shen, I. Batashev, A. Kiecana, N. van Dijk, E. Brück, J Alloys Compd 906 (2022) 164337.

[51] N. Sethulakshmi, I.A. Al Omari, M.R. Anantharaman, Bulletin of Materials Science 38 (2015) 1545–1552.

[52] M. Phan, S. Yu, N.H. Hur, Appl. Phys. Lett. 86, 072504 (2005)3 (2005) 10–13.

[53] W.F. Giauque, D.P. MacDougall, Physical Review 43 (1933) 768.

[54] A.M. Tishin, Cryogenics 30 (1990) 127–136.

[55] C.B. Zimm, A.J. DeGregoria, 471 (2008) 471–480.

[56] Y.Z. Shao, J.K.L. Lai, C.H. Shek, J Magn Magn Mater 163 (1996) 103–108.

[57] E. Yüzüak, I. Dincer, Y. Elerman, Journal of Rare Earths 30 (2012) 217–221.

[58] S. Fujieda, A. Fujita, K. Fukamichi, Appl Phys Lett 81 (2002) 1276–1278.

[59] H.H. Potter, Proceedings of the Royal Society of London. Series A, Containing Papers of a Mathematical and Physical Character 146 (1934) 362–387.

[60] X. Zhang, M. Qian, R. Su, L. Geng, Mater Lett 163 (2016) 274–276.

[61] J. Huo, L. Huo, J. Li, H. Men, X. Wang, A. Inoue, C. Chang, J.Q. Wang, R.W. Li, J Appl Phys 117 (2015).

[62] Y. Lv, Q. Chen, Y. Huang, Journal of Rare Earths 37 (2019) 404–409.

[63] T.-L. Phan, P. Zhang, T.D. Thanh, S.C. Yu, J Appl Phys 115 (2014).

[64] X. Si, Y. Liu, Y. Shen, W. Yu, X. Ma, Z. Zhang, Y. Xu, T. Gao, J Mater Sci 53 (2018) 3661–3671.

[65] A. Jerbi, A. Krichene, N. Chniba-Boudjada, W. Boujelben, Physica B Condens Matter 477 (2015) 75–82.

[66] Y. Zhang, H. Li, Dan Guo, L. Hou, X. Li, Z. Ren, G. Wilde, Ceram Int 44 (2018) 20762–20767.

[67] H. Wang, F. Dong, H. Wang, B. Zhao, Y. Wang, W. Tan, J Appl Phys 136 (2024) 0–16.

[68] B.D. Cullity, S.R. Stock, Elements of Xray Diffraction, Prentice-Hall, New York (2001).

[69] J. Romero Gómez, R. Ferreiro Garcia, A. De Miguel Catoira, M. Romero Gómez, Renewable and Sustainable Energy Reviews 17 (2013) 74–82.

[70] S. Das, T.K. Dey, J Alloys Compd 440 (2007) 30–35.

[71] M. Iqbal, M.N. Khan, A.A. Khan, N. Zafar, J Alloys Compd 769 (2018) 766–776.

[72] K. Laajimi, M. Khlifi, E.K. Hlil, M.H. Gazzah, J. Dhahri, J Magn Magn Mater 491 (2019) 165625.

[73] C.A. Taboada-Moreno, A.M. Bolarín-Miró, F. Pedro-García, C.A. Cortés-Escobedo, F. Sánchez-De Jesús, J Magn Magn Mater 570 (2023) 170542.

[74] V.E. Salazar-Muñoz, A. Lobo Guerrero, S.A. Palomares-Sánchez, J Magn Magn Mater 562 (2022) 169787.

[75] D.T. Morelli, A.M. Mance, J. V. Mantese, A.L. Micheli, J Appl Phys 79 (1996) 373–375.

[76] A. Gómez, E. Chavarriaga, I. Supelano, C.A. Parra, O. Morán, Physics Letters, Section A: General, Atomic and Solid State Physics 382 (2018) 911–919.

[77] Z.B. Guo, Y.W. Du, J.S. Zhu, H. Huang, W.P. Ding, D. Feng, Phys Rev Lett 78 (1997) 1142–1145.

[78] Z.B. Guo, J.R. Zhang, H. Huang, W.P. Ding, Y.W. Du, 904 (1997) 25–27.

[79] X.X. Zhang, J. Tejada, Y. Xin, G.F. Sun, K.W. Wong, X. Bohigas, Appl Phys Lett 69 (1996) 3596–3598.

[80] F. Azim, J. Mohapatra, J.P. Liu, S.R. Mishra, MRS Adv 9 (2024) 790–796.

[81] V.E. Salazar-Muñoz, S.A. Palomares-Sánchez, I. Betancourt, A.A. Torres-Castillo, J.G. Cabal Velarde, A. Lobo Guerrero, J Magn Magn Mater 538 (2021) 168296.

[82] J. Xu, Z. Zou, Physica B Condens Matter 557 (2019) 52–55.

[83] S.K. Estemirova, V.Y. Mitrofanov, S.A. Uporov, G.A. Kozhina, Solid State Sci 124 (2022) 106806.

[84] M.A.A. Bally, M.A. Islam, M.Z. Ahasan, F.A. Khan, J Magn Magn Mater 557 (2022) 169462.

[85] C.A. Taboada-Moreno, F. Sánchez-De Jesús, F. Pedro-García, C.A. Cortés-Escobedo, J.A. Betancourt-Cantera, M. Ramírez-Cardona, A.M. Bolarín-Miró, J Magn Magn Mater 496 (2020) 165887.

[86] K. McBride, J. Cook, S. Gray, S. Felton, L. Stella, D. Poulidi, CrystEngComm 18 (2016) 407–416.

[87] O. Kaman, P. Veverka, Z. Jirák, M. Maryško, K. Knížek, M. Veverka, P. Kašpar, M. Burian, V. Šepelák, E. Pollert, Journal of Nanoparticle Research 13 (2011) 1237–1252.

[88] A. Szewczyk, M. Gutowska, K. Piotrowski, B. Dąbrowski, J. Appl. Phys. *94* (2003) 1873–1876.

[89] A. Szewczyk, M. Gutowska, B. Dabrowski, T. Plackowski, N.P. Danilova, Y.P. Gaidukov, Phys. Rev. B 71, 224432 (2005) 1–7.

[90] M. Koubaa, W. Cheikhrouhou-Koubaa, A. Cheikhrouhou, L. Ranno, Physica B Condens Matter 403 (2008) 4012–4019.

[91] M. Koubaa, W.C.R. Koubaa, A. Cheikhrouhou, J Alloys Compd 479 (2009) 65–70.

[92] K. McBride, N. Partridge, S. Bennington-Gray, S. Felton, L. Stella, D. Poulidi, Mater Res Bull 88 (2017) 69–77.

[93] R. Atanasov, E. Brinza, R. Bortnic, R. Hirian, G. Souca, L. Barbu-Tudoran, I.G. Deac, Magnetochemistry 9 (2023).

[94] H. Zhang, Y. Wang, H. Wang, D. Huo, W. Tan, J Appl Phys 131 (2022).

[95] W. Zhong, W. Chen, W.P. Ding, N. Zhang, A. Hu, Y.W. Du, Q.J. Yan, J Magn Magn Mater 195 (1999) 112–118.

[96] L. Malavasi, M.C. Mozzati, S. Polizzi, C.B. Azzoni, G. Flor, Chemistry of Materials 15 (2003) 5036–5043.

[97] S. Roy, Y.Q. Guo, S. Venkatesh, N. Ali, 9547 (2001).

[98] S.B. Kansara, D. Dhruv, B. Kataria, C.M. Thaker, S. Rayaprol, C.L. Prajapat, M.R. Singh, P.S. Solanki, D.G. Kuberkar, N.A. Shah, Ceram Int 41 (2015) 7162–7173.

[99] M. Wali, R. Skini, M. Khlifi, E. Dhahri, E.K. Hlil, J Magn Magn Mater 394 (2015) 207–211.

[100] S. Das, T.K. Dey, J Phys D Appl Phys 40 (2007) 1855–1863.

[101] N. Sethulakshmi, I.A. Al-Omari, K.G. Suresh, M.R. Anantharaman, Appl Phys Lett 104 (2014).

[102] B. Alzahrani, M. Hsini, S. Hcini, M. Boudard, A. Dhahri, M.L. Bouazizi, J Low Temp Phys 200 (2020) 26–39.

[103] N. Mechi, S. Hcini, B. Alzahrani, M. Boudard, A. Dhahri, J. Supercond Nov Magn (2019).

[104] S.C. Maatar, R. M'Nassri, W.C. Koubaa, M. Koubaa, A. Cheikhrouhou, J Solid State Chem 225 (2015) 83–88.

[105] F. Ayadi, F. Saadaoui, W. Cheikhrouhou-Koubaa, M. Koubaa, A. Cheikhrouhou, L. Sicard, S. Ammar, IOP Conf Ser Mater Sci Eng 28 (2012).

[106] S.Das,T.K.Dey, J.Phys. Condens. Matter 18 (2006) 7629.

[107] I. Walha, M. Smari, T. Mnasri, E. Dhahri, J Magn Magn Mater 454 (2018) 190–195.

[108] V.A. Ryzhov, A. V. Lazuta, V.P. Khavronin, P.L. Molkanov, Y.M. Mukovskii, J. Phys. Condes. Matter. 26 (2014).

[109] J.B. Yang, M.S. Kim, T.F. Creel, H. Zhao, X.G. Chen, W.B. Yelon, W.J. James, Perovskite Materials - Synthesis, Characterisation, Properties, and Applications (2016) 261–280.

[110] M.H. Phan, T.L. Phan, S.C. Yu, N.D. Tho, N. Chau, Phys Status Solidi B Basic Res 241 (2004) 1744–1747.

[111] M.S.Khalil, Materials Sciences and Engineering A 352 (2003) 64-70.

[112] C. Li, B. Lei, Z. Luo, S. Han, Z. Liu, D. Zhang, C. Zhou, Advanced Materials 17 (2005) 1548–1553.

[113] Meenakshi, A. Kumar, R.N. Mahato, Physica B Condens Matter 511 (2017) 83–88.

[114] E.J.W. Verwey, E.L. Heilmann, J Chem Phys 15 (1947) 174–180.

[115] A. Vedrtnam, K. Kalauni, S. Dubey, A. Kumar, AIMS Mater Sci 7 (2020) 800–835.

[116] M. Bohra, S. Prasad, N. Kumar, D.S. Misra, S.C. Sahoo, N. Venkataramani, R. Krishnan, Appl Phys Lett 88 (2006) 1–4.

[117] E.V. Gopalan, I.A. Al-Omari, D.S. Kumar, Y. Yoshida, P.A. Joy, M.R. Anantharaman, Appl Phys A Mater Sci Process 99 (2010) 497–503.

[118] P. Poddar, J. Gass, D.J. Rebar, S. Srinath, H. Srikanth, S.A. Morrison, E.E. Carpenter, J Magn Magn Mater 307 (2006) 227–231.

[119] M.A. Islam, A.K.M.A. Hossain, Heliyon 9 (2023) e15106.

[120] H. Mamiya, N. Terada, T. Furubayashi, H.S. Suzuki, H. Kitazawa, J Magn Magn Mater 322 (2010) 1561–1564.

[121] E. Oumezzine, S. Hcini, M. Baazaoui, E.K. Hlil, M. Oumezzine, Powder Technol 278 (2015) 189–195.

[122] M.A. Hamad, H.R. Alamri, J Electron Mater 51 (2022) 3359–3363.

[123] M.K. Manglam, M. Kar, J Alloys Compd 899 (2022) 163367.

[124] Y. Zare, I. Shabani, Materials Science and Engineering: C 60 (2016) 195–203.

[125] G. Barrera, P. Tiberto, P. Allia, B. Bonelli, S. Esposito, A. Marocco, M. Pansini, Y. Leterrier, (2019).

[126] V. Gopalan, Al-Omari I, Kumar D, Yoshida Y, Joy P, Anantharaman M, Appl Phys A 99 (2010): 497–503.

…..ᘓ*ᘓ…..

# Chapter 2

# Experimental Methods and Characterisation Techniques

## Objectives

An overview of the different types of experimental procedures used for the synthesis of nanoparticles perovskites, ferrites and nanocomposites is presented. The characterisation techniques employed to analyse the structural, compositional, magnetic, magnetocaloric (MCE), and dielectric properties of the nanomagnetic materials are detailed.

## 2.1 Introduction

The various synthesis techniques and analytical tools employed in the present investigation are detailed in this chapter. We have synthesised three types of nanomagnetic materials: perovskites, ferrites and nanocomposites. Perovskite materials were synthesised by sol-gel auto combustion method. The modified sol-gel method is used to synthesise the ferrite materials. The nanocomposites were synthesised by the ion-exchange reduction method. A comprehensive description of the different sophisticated analytical techniques such as X-Ray Diffraction (XRD), Rietveld Analysis, Scanning Electron Microscopy (SEM), Field Emission Scanning Electron Microscopy (FESEM), Energy Dispersive X-ray spectroscopy (EDAX), Fourier Transform Infrared Spectroscopy (FTIR) and High Resolution Transmission Electron Microscopy (HRTEM) for the structural characterisation of the samples is detailed. The magnetic properties of the nanomagnetic materials were analysed employing Vibrating Sample Magnetometer (VSM), and the temperature dependence of the magnetisation was studied by ZFC-FC measurement using a Physical Property Measurement System (PPMS) instrument and a SQUID magnetometer. The temperature dependent dielectric properties of the materials were investigated by employing an LCR meter.

## 2.2 Experimental Techniques for the synthesis of nanoparticles

Synthesis procedures play a vital role in deciding the various physical, chemical and magnetic properties of the nanomagnetic materials. The nanomaterials are usually synthesised by two main approaches: the top-down approach and the bottom-up approach[1]. In a top-down approach, the bulk materials are divided to produce nanostructured materials. Top-down approaches include mechanical milling, laser ablation, etching, and sputtering. In a bottom-up approach, the nanostructures are built up from basic atoms and molecules controlling the reaction parameters. Some examples of bottom-up approaches are the sol-gel method, hydrothermal

method, chemical co-precipitation method, and solid-state synthesis method etc .[1–5].

According to the different scientific processes involved, the synthesis techniques are also classified into physical and chemical methods. The physical processes involve only changes in the physical state, such as size, shape, and phase of the matter. Condensing gaseous metal vapours into nanoparticles is an example. Most of the physical methods belong to the top-down technique. Chemical process belongs to the bottom-up technique. Compared to the other synthesis techniques, chemical methods possess several advantages, including easy control over particle size and composition, quick and simple preparation, and various possibilities to modify the surface state and overall homogeneity [6].

The sol-gel method is widely used in the synthesis of materials, especially metal oxides, ceramics, and nanomaterials, at relatively low temperatures[7,8]. When compared to conventional ceramic powder processes, sol-gel processing is largely motivated by the possibility of improved homogeneity and uniformity. Hence, in the present investigation, we have employed the sol-gel auto combustion method for perovskite samples and a modified sol-gel combustion method for the ferrite samples.

### *2.2.1 Sol-gel auto combustion method for the synthesis of perovskites*

The sol-gel method is a wet chemical method used for fabricating ceramics and organic-inorganic hybrids. The sol–gel process generally involves a solution system that undergoes a transition from a liquid *sol* to a solid *gel* phase. Fibres, porous or dense materials, thin film coatings, ultrafine or spherically shaped powders and highly porous aerogel materials are some of the advanced materials that may be made utilising the sol-gel approach[8–11]. The different steps involved in the sol-gel process are:

1. Preparation of metal salt solution
2. Hydrolysis and polycondensation of alkoxide or nitrate precursors followed by hypercritical drying of the gel.
3. Gelation
4. Aging
5. Drying under ambient temperature[12].

The sol-gel auto combustion method is a popular variation of the traditional sol-gel process used to synthesise ferrites, nanoscale metal oxides, and advanced ceramic materials[13–15]. The advantages of this synthesis technique include good chemical homogeneity, high product purity and crystallinity, fine particle size, narrow particle size distribution and absence of multiple steps. In the sol-gel method, it is easy to control stoichiometry and to introduce dopants to the final products and to prepare highly reactive nanosized powder at lower calcination temperatures and shorter reaction times [16,17]. The main feature of this method is that the heat required to initiate the chemical reaction is provided by the reaction itself, not by an external source[18]. The nitrate and acetate base compounds, which are easily soluble in distilled water, are used as the raw materials for this synthesis method. The nitrate salts of are preferred as precursors because they provide a low-temperature, water-soluble supply of $NO_3^-$ oxidant for synthesis[19] In the preset investigation we have employed this sol-gel autocombustion approach to synthesise cobalt substituted lanthanum sodium manganite $La_{0.5}Na_{0.5}Co_xMn_{1-x}O_3$ (x=0,0.1,0. 3,0.5,0.7,0.9 and 1) We have used metal nitrates of lanthanum, sodium, manganese and cobalt dissolved in water as the precursor solution .An organic fuel, such as glycine, urea, or citric acid, can be used to help in the combustion process. Here we have used citric acid is used as the fuel. This method can also be called citrate-nitrate combustion process, in which citric acid acts as a fuel and metal nitrates are used as the metal oxidant. We have additionally added ethylene glycol which lead to the formation of an organic ester; the esterification reaction forms the bond between the complexant and the

ethylene glycol. Ethylene glycol acts as a gelating agent [20]. All the precursor solutions of the raw materials were dissolved/prepared separately and finally, they were mixed under continuous stirring and kept on a magnetic stirrer with heating. The metal nitrate solution turned thicker and formed a gel after constant stirring for 4–6 hours. Auto ignition takes place as time advances, resulting in the production of a flame, and generates a huge amount of different gases, $CO_2$, $NO_2$ etc. Finally, the mixed solution is burned to form powder. The detailed procedure is explained in chapter 3.

Compared to the other synthesis methods of perovskite manganites, which require a longer sintering time, our approach forms a perovskite phase after sintering for shorter duration of time.

### *2.2.2 Modified sol-gel auto combustion method for synthesis of ferrites*

In this thesis, we have used a modified sol-gel auto combustion method to synthesise ferrite nanoparticles. In this method, the stoichiometric amount of metal nitrate is dissolved separately in deionized water. The prepared aqueous solutions of metal nitrates were mixed well using a magnetic stirrer continuously for 10 minutes. The citric acid dissolved in water was added to the metal nitrate solution in a molar ratio of 1:1 to the metal nitrates. 3M citric acid was added to the metal nitrate solution and stirred with heating at 80°C for half an hour. Then, it is placed on a hot plate, and the subsequent heating causes the gel to burn in a self-propagating combustion process, producing a residue powder. Finally, a powder of nanoparticles will be obtained. Compared to the conventional sol-gel auto combustion method, in our modified method, the metal nitrate solution is directly transferred to a hot plate without the formation of a gel. The gel is formed when the solution is heated on the hot plate and then undergoes auto combustion. The novelty of this method is that it is an easy and simple synthesis technique to prepare ferrite nanomaterials in bulk. In contrast to the traditional sol-gel auto combustion approach, our ferrite

synthesis process does not transform the metal salt solution into a gel. After adding citric acid to the well-agitated metal salt solution, it is immediately moved to the hot plate to undergo combustion to form nano powder. By adopting this modified sol-gel synthesis procedure we have synthesised two ferrite series: $Cu_{1-x}Co_xFe_2O_4$ and $Cu_{1-x}Zn_xFe_2O_4$ for different x values. The detailed procedure is given in chapter 5 and chapter 6.

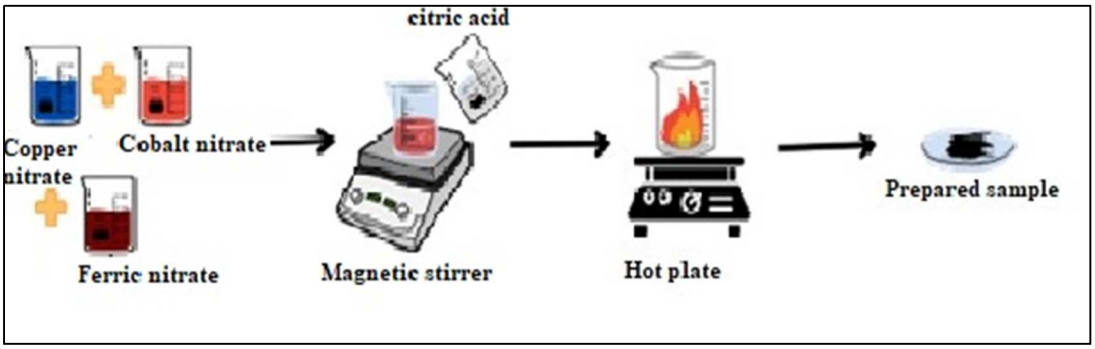


**Figure 2.1.** Schematic of Sol-gel synthesis of ferrites

### *2.2.3 Ion exchange reduction method for synthesis of magnetic nanocomposites*

Metal nanoparticles were found to be highly unstable because of their high surface reactivity. One extremely interesting method for reducing this stability issue is the production of metal nanoparticles in a host matrix, forming a metal nanocomposite. The multifunctional nature of the nanocomposite is attributed to the complementary characteristics of the metal nanoparticles and the host matrix. Polymers are considered to be a good host matrix for composite materials[21]. Various advanced polymer composites have been developed, employing a wide range of inclusions, such as metals, semiconductors, carbon nanotubes, and magnetic nanoparticles. Mesoporous ion exchange resins are polymeric substances with a large surface area and have a large number of functional groups at the pore surface, which can load a variety of metal ions. They are characterised by permanent percolated

porosity formed by phase separation occurring during polymerization. These metal ions are subsequently reduced in the matrix to form metal polymer nanocomposites.

A resin or polymer that serves as a medium for ion exchange is known as an ion exchange resin or an ion exchange polymer. It is an insoluble matrix (or support structure) fabricated from an organic polymer substrate, which is normally in the form of small (0.25–0.5 mm radius) microbeads, typically white or yellowish. Ion exchange resin beads IRC-120 are shown in Fig.2.2.

**Figure 2.2**. Ion-exchange resin beads

As the beads are typically porous, there is a large surface area on and inside them. The process is called ion exchange because the trapping of ions occurs along with the release of other ions. There are different types of ion-exchange resin. Most commercial resins are made of polystyrene sulfonate. Bead-shaped ion exchange resins are made of functionalized polystyrene with a three-dimensional porous polymer matrix, which is cross-linked with divinylbenzene. The sulfonic acid group is used to functionalize strongly acidic resins (gel type), whereas carboxylic acid groups are used to functionalize the weakly acidic resins (macroporous) (Fig. 2.3 and Fig. 2.4). We can use a conventional ion exchange mechanism to load polymer matrix with metal cations because of the presence of functional groups in them. Some important resins are SRC-120 (Amberlite IRC-120) and WRC-50 (Amberlite

IRC-150). Both these resins are 8% cross-linked polymers of polystyrene and divinylbenzene, which have exchangeable $H^+$ ions associated with their respective functional groups.

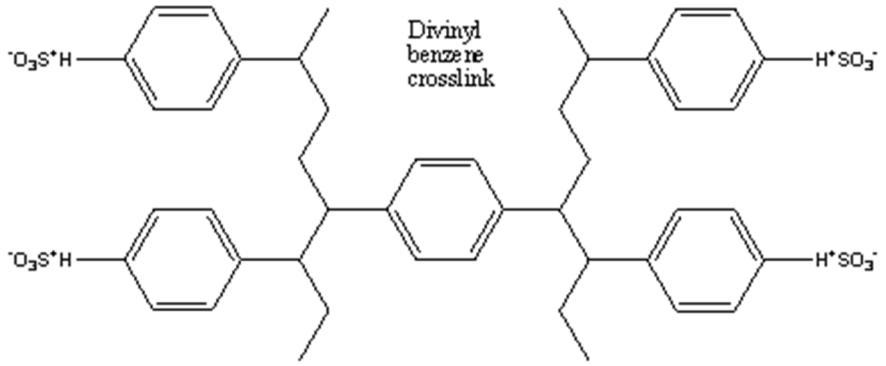


**Figure 2.3.** Strongly Acidic Cation (SAC) exchange resin

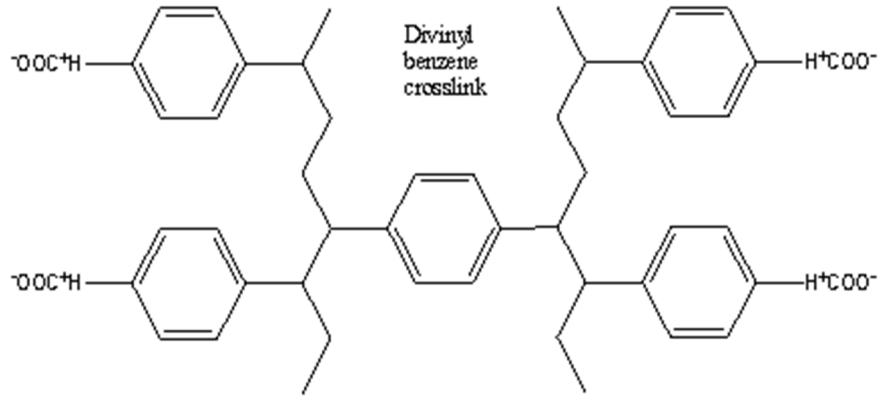


**Figure 2.4**. Weakly Acidic Cation (WAC) exchange resin

We have used Strongly Acidic Cation Exchange Resin SRC-120 (Amberlite IRC120) as the polymer matrix to synthesise the metal nanocomposites. The precursors used for the synthesis of cobalt nanocomposites are metallic salts, sodium borohydride ($NaBH_4$) and SRC-120 (Amberlite IRC120). The metal ions are exchanged with the $H^+$ ions in the resin. Further reduction of metal ions to metal inside the polymer matrix occurs with the addition of $NaBH_4$. A dilute solution of

$NaBH_4$ is added dropwise to the resin. Metal ions are reduced to metal particles by the reduction reaction. Thus, metal particles are expected to be trapped within the interstitial channels of polymer beads. The detailed experimental procedure is described in Chapter 8.

## 2.3 Structural Characterisation

### *2.3.1 X-ray Diffraction Analysis*

The X-ray Diffraction (XRD) is the most widely used analytical tool for the structural characterisation, providing information about the phases present in the material as well as crystallographic parameters of powder nanoparticles and thin films [22].

The working of XRD is based on the elastic scattering of X-ray photons by atoms in a periodic lattice. The schematic diagram of an XRD diffractometer is shown in Fig. 2.5.

X-ray diffractometers consist mainly of three basic elements:

1. X-ray source- X-ray Tube
2. The sample and sample holder
3. X-ray detector

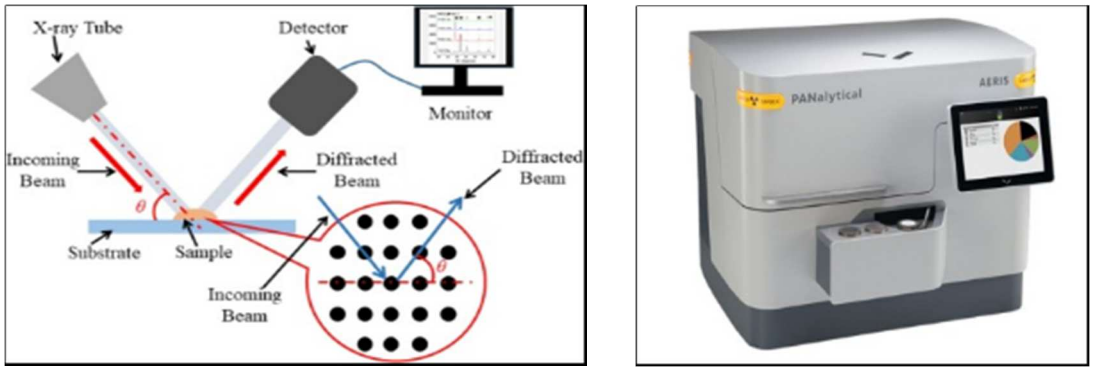


**Figure 2.5.** Schematic diagram of X-ray diffractometer

A cathode ray tube produces X-rays by heating a filament to produce electrons, by applying a voltage to accelerate the electrons toward a target, and bombarding the target material with electrons. Characteristic X-ray spectra are produced when electrons have sufficient energy to dislodge the inner shell electrons of the target material. These spectra consist of several components, the most common being $K_\alpha$ and $K_\beta$. $K_\alpha$ consists, in part, of $K_{\alpha 1}$ and $K_{\alpha 2}$. $K_{\alpha 1}$ has a slightly shorter wavelength and twice the intensity of $K_{\alpha 2}$. The specific wavelengths are characteristic of the target material (Cu, Fe, Mo, Cr). To generate monochromatic X-rays needed for diffraction, filtering is necessary by foils or crystal monochromators. Copper is generally used as the target material for single-crystal diffraction, with Cu $K_\alpha$ radiation = 1.5418 Å. These X-rays are collimated and directed to incident on the sample. The intensity of the reflected X-rays is recorded by rotating the sample and detector. The constructive interference occurs and a peak in intensity is obtained when the geometry of the incident X-rays impinging on the sample satisfies the Bragg Equation. A detector records and processes this X-ray signal and converts the signal to a count rate, which is then transferred to a device such as a printer or computer monitor as output. The geometry of an X-ray diffractometer is such that the sample rotates in the path of the collimated X-ray beam at an angle $\theta$ while the X-ray detector is mounted on an arm to collect the diffracted X-rays and rotates at an angle of $2\theta$. The instrument used to maintain the angle and rotate the sample is termed a *goniometer*. Each peak or reflection in the diffraction pattern is of different intensities which corresponds to X-rays diffracted from a specific set of planes in the specimen. The intensity is usually expressed in arbitrary units. The positions of the peaks in an X-ray diffraction pattern depend on the crystal structure of the material. The intensities of diffracted beams are measured and the intensity versus $2\theta$ graph can be plotted. A reference figure for the XRD pattern is shown in Fig. 2.6.

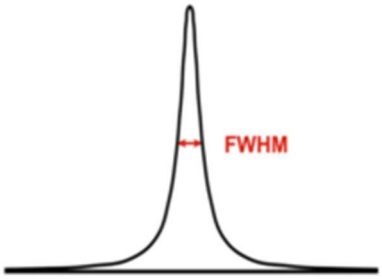


**Figure 2.7.** FWHM of a peak

The crystallite size, *D* can be estimated by employing the Scherrer equation by utilizing the full width at half maximum, β, obtained from the XRD pattern[22,23].

$$D = \frac{0.9\lambda}{\beta Cos\theta} \tag{2.2}$$

The lattice parameter can also be estimated from the (h k l) planes identified from the XRD pattern.

The XRD pattern of the samples in the present work has been recorded with a Bruker D8 Advance X-ray Diffractometer using Cu $K_\alpha$ radiation ($\boldsymbol{\lambda}$=1.5406Å) with a step size of 0.04° in a range from 2θ=20° to 90°.

***Rietveld Refinement***

Rietveld refinement is a software technique used for performing the structural refinement to characterise the crystalline material using X-ray diffraction data or neutron diffraction data. It evaluates the material properties like lattice parameters, unit cell volume and space groups by utilizing the diffraction data of peak reflections as a function of angles. H.M. Rietveld discovered the Rietveld technique, which modifies a theoretical line profile to fit a measured profile using least least-squares approach[24]. A reference pattern of Rietveld refinement is shown in Fig. 2.8.

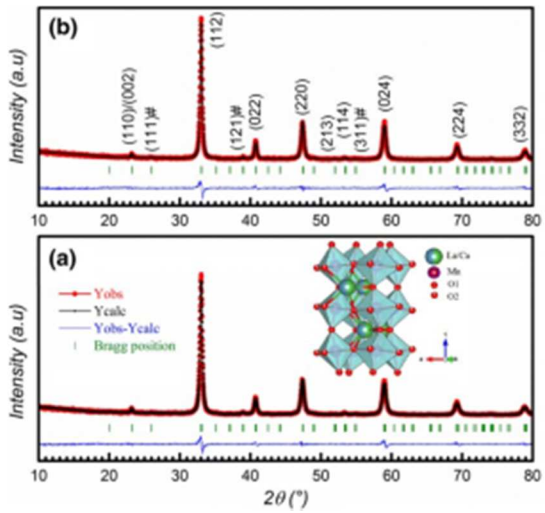


**Figure 2.8.** Reference pattern of Rietveld refinement. [25]

The Rietveld refinement was first applied to neutron diffraction data with reflection positions expressed in terms of Bragg angle 2θ, then he extended this method to X-ray powder diagrams to refine the crystal structure if a satisfactory function was used to describe the peak profile. Apart from the structural refinement, this method is often employed for measures like x-ray energy or neutron time of flight [26]. The theoretical profile is adjusted to match the measured profile by varying the refinement parameters like scale factors, fundamental lattice vectors, the angle between them, occupancy and positions of ions, peak profile variables (u, v, w), and preferred orientation factor. The basic principle of profile refinement to obtain best fit is to minimise a function M, defined by equation 2.3, which is the difference between the calculated profile $Y_{cal}$ and observed data $Y_{obs}$ with respect to the parameters [24].

$$M = \sum_i w_i \left( Y_i^{obs} - \frac{1}{c} Y_i^{cal} \right)^2 \tag{2.3}$$

where $w_i$ is the statistical weight and c is the scaling factor such that $Y_{cal} = cY_{obs}$.

The R-factor is a measure of refining quality. The weighed profile R-factor (Rwp), which is derived directly from the square root of the quantity to be minimised, is the most widely used discrepancy index, which is described by

$$R_{wp} = \left( \frac{\sum W_i \left( Y_i^{obs} - Y_i^{cal} \right)^2}{\sum W_i \left( Y_i^{obs} \right)^2} \right)^{1/2} \quad (2.4)$$

The other refined parameters are defined by

$$\chi^2 = \left( \frac{R_{wp}}{R_{exp}} \right)^2 \quad (2.5)$$

$$\mathrm{R_{pattern}}, R_p = \frac{\sum \left( Y_i^{obs} - Y_i^{cal} \right)}{\sum Y_i^{obs}} \quad (2.6)$$

$$\mathrm{R_{expected}}, \quad R_{exp} = \left( \frac{N - P + C}{\sum W_i \left( Y_i^{obs} \right)^2} \right)^{1/2} \quad (2.7)$$

The goodness of fit ($\chi^2$) and refined profile values $R_p$ and $R_{wp}$ are employed to evaluate the quality of fit. A good fit is judged by the ($\chi^2$) value being near to one and the $R_p$ and $R_{wp}$ values being near to 10%[26]. During the least square refinement, the following parameters are changed: (i) lattice parameter (a, b, c, α, β, γ) (ii) atomic positions (x, y, z) (iii) atomic site occupancy (iv)atomic thermal vibrational parameter (isotropic or anisotropic) (v)parameters from Cagliotti formula (u,v,w) (vi) preferred orientation (vii) background function (viii) 2θ Zero correction (ix) overall scale factor (x) overall isotropic temperature parameters. The input values required for the refinement are (i) starting and ending of 2θ value, (ii) step in which the experimental techniques 2θ is measured, (iii) wavelength and (iv) initial values of all the parameters that can be adjusted. The Rietveld refinement is an advantageous tool for the refinement of structural and magnetic phases.

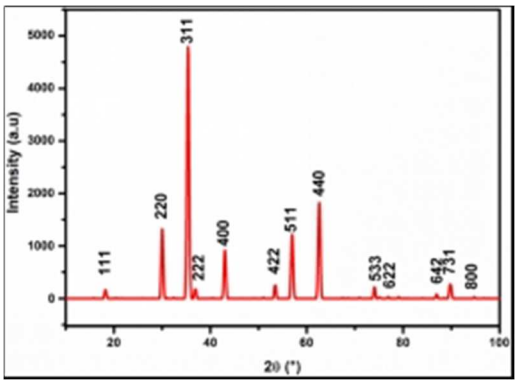


**Figure 2.6.** XRD pattern.

The intensity of the diffracted rays from the crystal planes will be recorded in accordance with Bragg's law which is given by

$$2dSin\theta = n\lambda \qquad (2.1)$$

where $\lambda$ is the wavelength of X-rays used, which is 1.5406Å, $\theta$ is the diffraction angle, $d$ is the interplanar spacing, and $n$ is the order of interference[22]. The Bragg equation is then solved for an appropriate value of λ to determine the $d$-spacing of each peak.

The different planes in the X-ray diffraction pattern are indexed by different analytical techniques. Once all $d$-spacings have been determined, the $d$'s of the unknown to those of known materials can be compared with automated search/match routines. Since each mineral has a unique set of $d$-spacings, matching these $d$-spacings provides an identification of the unknown sample. The $d$-spacings of the diffraction peaks can be compared with the International Centre for Diffraction Data (ICDD), which maintains a database of powder diffraction patterns, the Powder Diffraction File (PDF), for hundreds of thousands of inorganic compounds, including the $d$-spacings (related to angle of diffraction) and relative intensities of observable diffraction peaks. Patterns may be experimentally determined or computed based on crystal structure and Bragg's law.

### 2.3.2 Transmission Electron Microscopy (TEM)

Transmission Electron Microscopy (TEM) has emerged as an essential instrument in materials research due to the high lateral spatial resolution (better than 0.2 nm). It is also capable of providing clear and magnified sample images as well as crystallographic information through diffraction. This technique utilizes a highly energetic electron beam, which interacts with matter to generate information on a particular material. Consequently, TEM is a straightforward technique for visualising the shapes and sizes of the nanoparticles.

The spatial information in the signal is magnified by as little as 50 times to as much as a factor of $10^6$, accompanying the signal transmission. The key to the unique capabilities associated with TEM analysis is the incredible range of magnification, which is made possible by the small wavelength of incident electrons. Diffraction mode and imaging mode are the two primary techniques of sample observation that it offers. The schematic diagram of a TEM instrument is displayed in Fig. 2.9.

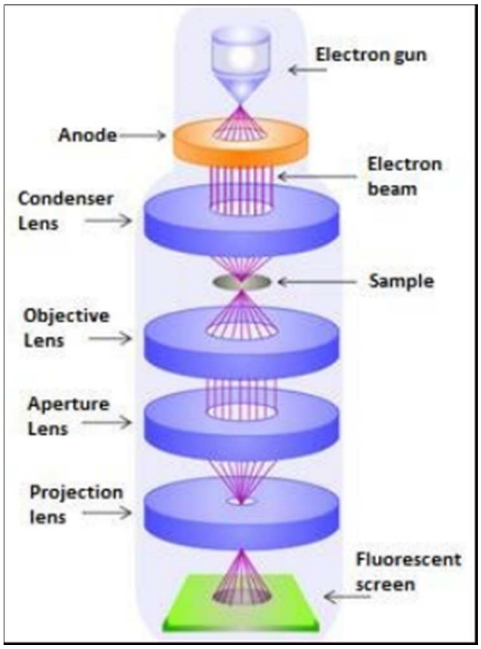


**Figure 2.9.** Schematic diagram of TEM

An electron gun generates the electron beam, which is then typically accelerated by an anode at a voltage of between 100 - 400 kV. The electron beam is subsequently focused by the electromagnetic lenses. When they are passed through a very thin sample, some are dispersed, lost, or transmitted. The information about the structure of the sample is enlarged as the transmitted electron travels through the objective lens. The projection lens expands the electron beam, and thereafter, the image is then recorded on a specialised photographic film or projected onto a fluorescent screen[27]. However, various factors such as spherical and chromatic aberration, which are caused by flaws in lenses, limit the resolving power of the TEM.

Atomic resolutions in the images of the nanoparticles are provided by a High Resolution Transmission Electron Microscope (HRTEM). These can be seen in the photographs as lattice fringes, which indicate the crystallinity of the sample. The *d*-spacing can be determined from the lattice fringe and compared to crystallographic data to identify the plane of growth. The information about the crystal can be obtained from the selected area electron diffraction (SAED). The diffracted electrons converge at the back focal plane of the objective lens. At this plane, electrons that satisfy Bragg's law form a pattern of bright spots (for crystalline materials) or rings (for polycrystalline/nanocrystalline materials). Amorphous materials show a diffuse halo instead of spots and rings. The HRTEM analysis of the ferrite sample and perovskite sample was performed by JEOL JEM 2100 High Resolution Transmission Electron Microscope at an operating voltage of 200 kV.

### *2.3.3 Scanning Electron Microscopy (SEM)*

Scanning electron microscopy is a distinctive, unique tool for the analysis of the surface morphology and structural characteristics of a solid sample. While scanning, electrons interact with the atoms of the sample to produce signals that provide information about its composition, surface topography, and shape and size of the particles. The resolution of SEM approaches a few micrometers to nanometers

and it can work at easily adjustable magnifications ranging from 10X to 30000X, providing a magnified image. In the majority of the applications, measurements are gathered over a selected region of the surface of the sample, and a two dimensional image is created to show the spatial variations in the external morphology, crystalline structure and chemical composition. When a high-energy electron beam interacts with materials, it will produce backscattered electrons, Auger electrons, secondary electrons, and X-rays. The ejected secondary electrons are detected, and these signals contain information about the topography of the sample under investigation. The schematic diagram of the instrumentation of a scanning electron microscope is shown in Fig. 2.10.

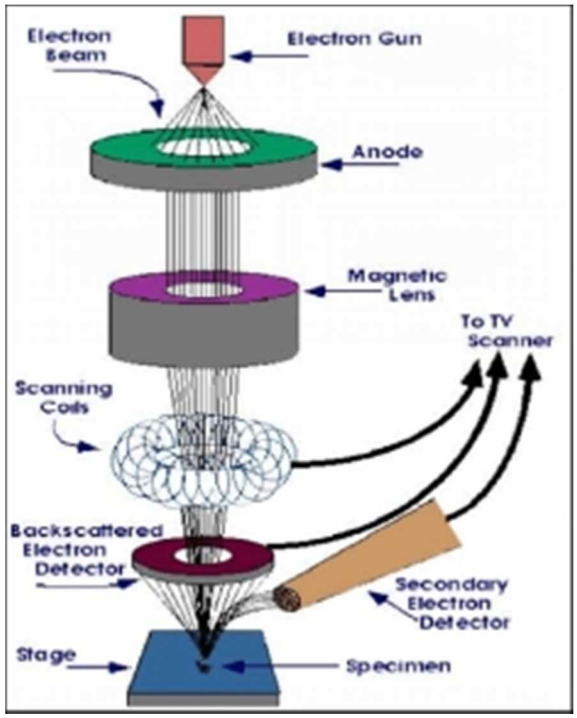


**Figure 2.10.** Schematic diagram of a Scanning Electron Microscope [28].

A tungsten filament is a suitable source for the generation of electron beams in SEM. These beams have been accelerated using an anode. The optical aperture includes lenses for the production of the narrow electron beam. The beam scans the

specimen surface with scan coils. A detector is used to collect the electrons emitted from the surface through the scanning beam action. The specimen image could be observed through a screen. The image is formed by the signal acquisition developed from the interactive specimen and the electron beam. Condenser lenses are the top lenses, and they are frequently used in the same manner as a single lens. The focal length is decreased, and the divergence is increased by increasing the current flowing through the condenser lens. As a result, the lens passes less beam current to the subsequent lens in the chain. After that, the beam reaches the final lens-aperture combination. The beam is ultimately focused onto the sample surface of the sample by the final lens. The secondary electrons are captured by a detector and produce an electrical signal. Once this signal has been amplified, it can be converted into a video scan image that can be viewed on a monitor or a digital image that can be captured and processed further. The two dimensional map of the signal yields a SEM image. The elemental topography and surface morphology are the main applications of SEM.

The SEM analysis of the samples in this work was carried out by Jeol 6390LA/ OXFORD XMX N from STIC, Cochin University of Science and Technology. Kochi. Field Emission Scanning Electron Microscopy (FESEM) provides a wide range of information from the sample surface with higher magnification and significantly larger energy range than SEM. FESEM makes use of a field emission gun that generates highly focused high and low energy electron beams, greatly enhancing spatial resolution and enabling work to be carried out at low potential. This reduces the effect of charging on non-conductive specimens and prevents damage to samples that are sensitive to electron beams. An ultra-high vacuum is required to work with an FESEM. FESEM imaging of one of the synthesized samples was carried out by Carl Zeiss – Sigma Field Emission Scanning Electron Microscope.

### 2.3.4 Energy Dispersive X-ray Spectroscopy (EDAX)

EDAX is one of the most useful analytical tools used to determine the elemental composition of the sample. It is always connected to a SEM/TEM instrument connected to the vacuum. The electrons in the inner shell of the atoms that compose the sample are expelled when the electron beam is made to fall on the sample. This process leaves a hole in the inner shell; the electron from a higher energy shell fills this hole, emitting characteristic X-rays from the sample under investigation. The energy of the X-rays depends on the difference between the inner shell where the hole is created and the outer shell from which the electron is filled. The elements contained in the sample can be identified by measuring the energy of the X-rays emitted by the sample. To detect X-rays released from the sample as a result of the electron beam radiating it, a SEM further needs an X-ray detector, a pulse processor and a computer. The elemental stoichiometry of the sample can be estimated from the EDAX measurements.

SEM -EDAX measurements of synthesised samples were carried out with 'Jeol 6390LA/ OXFORD XMX N' and EDAX by Bruker- QUANTAX 200 WITH X-FLASH 6I 100.

### 2.3.5 Fourier Transform Electron Microscopy (FTIR)

Fourier Transform Infrared Spectroscopy is an efficient analytical technique for the characterisation and identification of chemical bonds and functional groups in the structure of chemical compounds. Infrared spectroscopy is concerned mainly with molecular vibrations, as transitions between individual rotational states can be measured only in the infrared region of small molecules in the gas phase[29]. The analysis by FTIR is extended to gas, liquid and solid samples. A schematic diagram of an FTIR spectrometer is shown in Fig. 2.11.

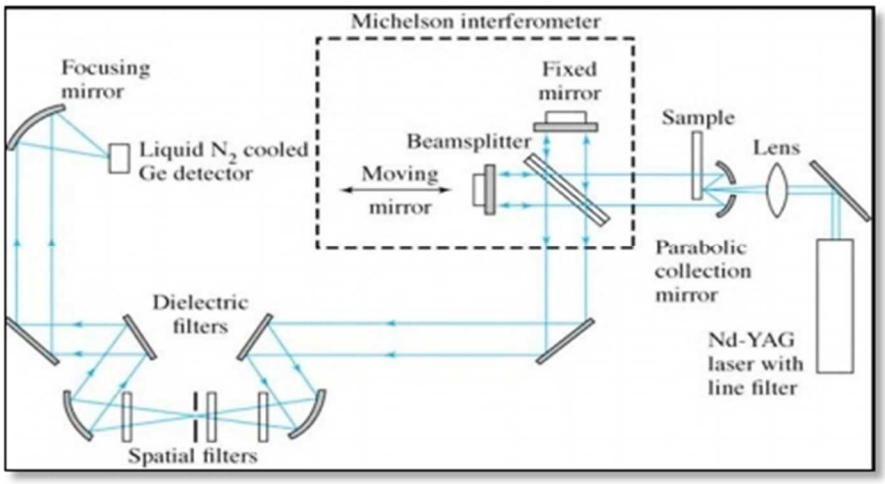


**Figure 2.11.** Schematic diagram of FTIR spectrometer

An infrared spectrometer essentially consists of a source of continuous IR radiation, an interferometer for resolving the infrared radiation into its component wavelengths and a detector. An interferometer consists of a beam splitter, a fixed mirror, and a moving mirror. A collimated beam of IR radiation from a source is directed into the interferometer and enters a beam splitter. The IR beam is split at the beam splitter; and half of it is transmitted to the fixed mirror, and the remaining half is reflected to the moving mirror. The reflected beams from these two mirrors are recombined at the beam splitter. An interference pattern is generated due to the changes in the relative position of the moving mirror and the fixed mirror[30]. When the mirror is moved with constant velocity, the intensity of radiation reaching the detector varies in a sinusoidal manner to produce an interferogram. The signals are converted to a spectrum with computer software that applies a Fourier transform to the interferogram.

The FTIR spectrum of our samples was recorded with SHIMADZU IR Spirit FTIR spectrometer in the range 400 $cm^{-1}$ to 4000 $cm^{-1}$ at the DST-FIST laboratory of Vimala College, Thrissur, Kerala.

## 2.4 Differential Scanning Calorimetry (DSC)

Differential Scanning Calorimetry is the most important thermoanalytic technique that measures the characteristic of a material as a function of temperature and time. In this technique, the difference in the amount of heat required to increase the temperature of a sample and reference is measured as a function of temperature. In DSC, both the sample and reference are maintained at the same temperature throughout the experiment. A schematic diagram of the working of a differential scanning calorimeter is shown in Fig. 2.12.

DSC works based on the principle that when the sample undergoes a physical transformation, such as phase transitions, more or less heat will need to flow to it than to the reference to maintain both at the same temperature. The energy changes or heat capacity changes involved in these transitions can be detected by DSC with great sensitivity.

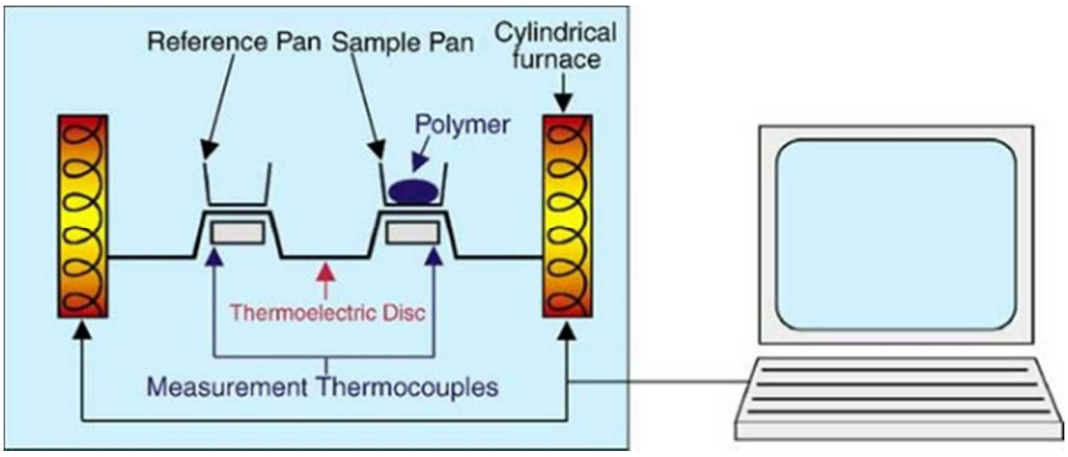


**Figure 2.12.** Schematic Diagram of the working of a DSC. [31]

The specific heat capacity of lanthanum sodium manganite perovskite samples was measured by DSC Netzsch DSC 204 F1 Heat flux DSC.

## 2.5 Magnetic Characterisation

Magnetic characterisation needed for the investigation includes three measurements: Magnetisation curves (M-H curves), Zero field cooled and Field cooled (ZFC-FC) curves, and Magnetisation isotherms for magnetocaloric effect measurements. We have carried out these measurements using three instruments: Vibrating Sample Magnetometer (VSM), SQUID Magnetometer, and Physical Property Measurement System (PPMS).

### *2.5.1 Vibrating Sample Magnetometry (VSM)*

A Vibrating Sample Magnetometer (VSM) is an instrument used to measure the magnetic properties of a material based on Faraday's laws of electromagnetic induction. It was originally put forth by Simon Foner in 1959 at Lincoln Laboratory, MIT[32]. According to Faraday's laws of induction, a changing magnetic field can produce an electric field, and the information about the change in magnetic flux is provided by these electrical signals.

The amplitude of the alternating electromagnetic field produced in the detection coils by the oscillating magnetic field of the moving sample is directly proportional to the magnetic moment of the sample. A lock-in amplifier, which is exclusively sensitive to signals at the vibration frequency, is typically used to amplify the small alternating emf. A reference signal at the vibration frequency can be sent to the lock–in amplifier by an optical, magnetic, or capacitive sensor that is connected to the drive system. Foner describes other alternative detection coil arrangements, all using balanced pairs of coils that cancel signals as a result of variations in the applied field [33]. The schematic diagram of a vibrating sample magnetometer is shown in Fig. 2.13 [34]

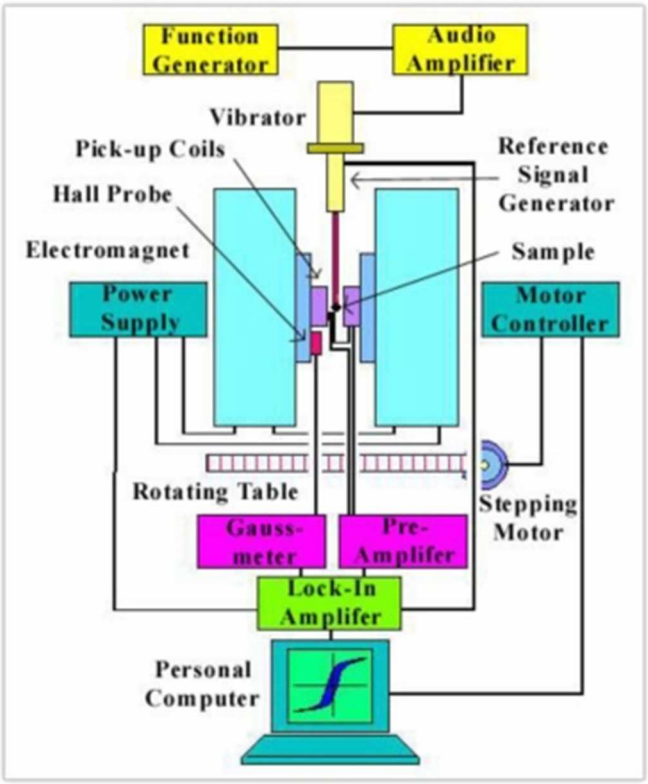


**Figure 2.13.** Schematic diagram of a vibrating sample magnetometer

The VSM is operated by driving an oscillator to which a sample rod is attached at a specified frequency and fixed amplitude. The magnetic sample is mounted on a sample holder and placed between the poles of an electromagnet. The sample is then vibrated sinusoidally with the help of a vibration drive unit. As the magnetised sample moves through the pickup coils, an emf is induced according to Faraday's law of induction. The induced emf is then fed into the lock-in amplifier through a differential amplifier to record the magnetic moment of the sample. The high signal-noise ratio can be produced through signal processing with a lock-in amplifier. The pickup coils are designed to remove signals from the applied dc field and ensure a linear response throughout the vibration. When the constant magnetic field varies over a specific range, a magnetisation versus magnetic field graph is obtained. VSMs are incredibly versatile devices that can be constructed using superconducting magnets for larger applied fields and ordinary electromagnets for

moderate fields. It is possible to create coil sets that can sense magnetic moments along two orthogonal axes, enabling vector measurements. Furthermore, a very broad range of temperatures can be achieved by using both cryogenic and high temperature conditions. The magnetisation curves (M-H curves ) at different temperatures of some samples in the present investigation were recorded with the Lakeshore VSM 7410 from SAIF, IIT Madras.

### *2.5.2 SQUID Magnetometer*

A SQUID (Superconducting Quantum Interface Device) is a highly sensitive device used to measure very low field magnetic moments. It is a device made up of two superconductors separated by thin insulating layers to form two Josephson junctions. It is typically used to get magnetic measurements at low temperatures and high magnetic fields. The geometry of a SQUID magnetometer is shown in Fig. 2.14.

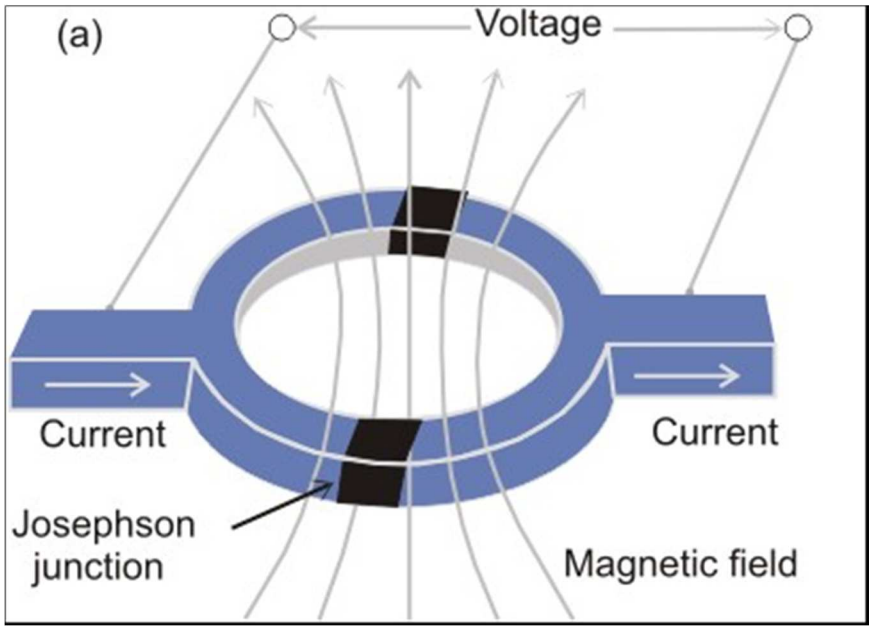


**Figure 2.14.** Schematic diagram of a SQUID magnetometer.

In commercial systems, the applied magnetic field is provided by a superconducting magnet and the sample is placed in a temperature-controlled environment. Due to the presence of two Josephson junctions, the electrons in a SQUID device move continuously in both directions. When a steady bias current is applied to the SQUID device, the voltage oscillates with the change in phase at the two junctions. The sample is continuously moved through the detection coil set through a transport mechanism and the amplified signal is subsequently recorded. The absolute value of the magnetic moment of the sample is obtained by fitting these data to a dipole model and calibrated against a traceable standard. The magnetic characteristic of the sample is then examined by varying the temperature or the applied magnetic field. The superconducting magnet needs to be isolated from the variable temperature sample environment and maintained at liquid helium temperatures, which requires significant engineering expertise to create a reliable instrument. The SQUID amplifier and transformer must also be configured to minimize the interference from the superconducting magnet. FC-ZFC measurements of some of the samples in our investigation is carried out using SQUIID equipment.

### *2.5.3 Physical Property Measurement System (PPMS)*

The PPMS was used to measure the electrical and thermal responses of the samples in a range of magnetic fields and at various temperatures. A PPMS system is a fully automated variable temperature and magnetic field system with multiple measurements, such as electrical property, magnetic property, electric transport properties, and specific heat measurement. The temperature range of the PPMS utilised to gather the data is between 1.8 K and 400 K, and the magnetic field range is up to 90kOe. A PPMS instrument is shown in Fig. 2.15.

**Figure 2.15.** Physical Property Measurement System (PPMS)

A PPMS uses a combination of a superconducting magnet system and a two-stage pulse tube cryocooler to control temperature and measure physical properties of a material. The superconducting magnet system provides an external magnetic field up to ±16 T and the cryocooler creates a low vibration environment in the temperature range 1.9 K- 400 K. Low-temperature magnetisation isotherm measurements and ZFC-FC measurements were carried out with a Physical Property Measurement System. A typical magnetisation isotherm curve is shown in Fig. 2.16.

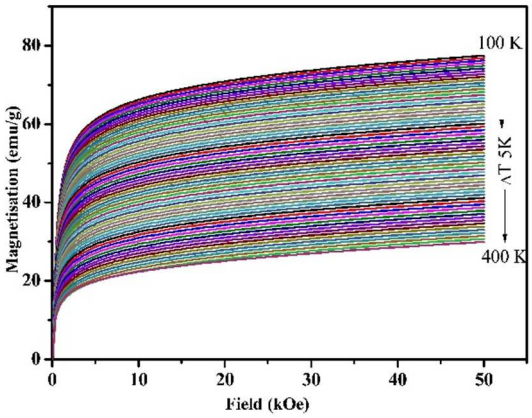


**Figure 2.16.** Typical magnetisation isotherm curves

In this thesis, the magnetisation measurements like M-H curves , FC-ZFC measurements and magnetisation isotherms of the samples were carried out by the PPMS instruments at CIF, PPMS-9 and P935A (Cryo Dewar) and the PPMS instrument from Sultan Qaboos University.

***Field Cooled (FC) and Zero Field Cooled (ZFC) measurements***

Temperature dependent magnetisation measurements such as Zero Field Cooled and Field Cooled curves (ZFC-FC curves), are used to analyse various magnetic interactions. In ZFC measurements, the sample is cooled to an extremely low temperature close to 5K in the absence of a magnetic field. It is cooled from very high temperatures, normally much above $T_B$ (Blocking temperature) for super paramagnets and $T_c$ (Curie temperature) for ferromagnets. When the temperature of the samples reaches the lowest value, a small magnetic field is applied. Thereafter, magnetization values are recorded upon heating the sample at a constant rate. The magnetisation of each particle is oriented to minimise the total energy due to anisotropy and applied field under ZFC conditions at low temperature. As temperature increases, the thermal fluctuations enable the magnetisation to rotate in the direction of the applied field, and the net magnetisation increases to a maximum value at a temperature $T_{max.}$ As the temperature is further increased, the thermal agitation starts to compete with the aligning effect of the applied magnetic field, resulting in a reduction in net magnetization as per Curie's law. In FC measurements, the sample is cooled to a lower temperature in the presence of a magnetic field and magnetic moments are recorded on heating the sample. In the FC conditions, the magnetic moments are again blocked at lower temperatures, but this time, they are partially aligned along the direction of the field rather than being randomly oriented [35]. A typical ZFC-FC curve is shown in Fig. 2.17.

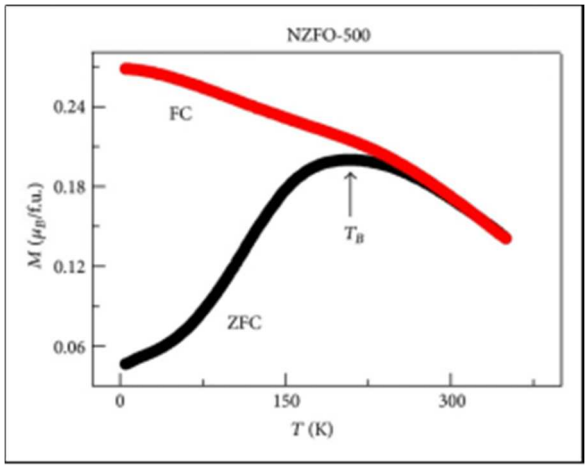


**Figure 2.17.** ZFC-FC curve

The applied magnetic field in both ZFC and FC measurements should be less than the anisotropy field to detect competent magnetic interactions. Additionally, the divergence of FC and ZFC curves can be explained that in ZFC, the spin corresponding to each particle tend to align with different crystalline axis and will be frozen in that state at low temperature whereas in FC, spins corresponding to each particle align with easy crystalline axis that is closest to the applied field direction and remain frozen in that direction at low temperatures[36]. FC and ZFC measurements are considered to be beneficial as they are one of the most sensitive methods for the study of magnetic behaviour at the nanoregime.

## 2.6 Magnetocaloric Characterisation

The MCE characteristic values of a material are isothermal magnetic entropy change ($\Delta S_m$) and adiabatic temperature change ($\Delta T_{ad}$) (described in chapter 1). In the present work, MCE is evaluated as isothermal magnetic entropy change $\Delta S_m$ indirectly from magnetisation isotherms. The different steps involved in this MCE measurement are detailed below.

a) Measuring the field dependent magnetisation curves (M-H curves), the nature of the magnetic behaviour of the sample can be evaluated.

b) Next, by recording the ZFC-FC or M-T measurements, one can determine the exact value of the transition temperature.

c) After fixing the transition temperature, isothermal magnetisation curves can be recorded in the vicinity of the transition temperature.

d) The isothermal magnetic entropy change can be estimated from the area under the magnetisation isotherms. Multiplying the area between two successive isotherms by the reciprocal of the temperature difference between the isotherms indicates the numerical value of magnetic entropy change $\Delta S_m$ (Refer. Equation 1.19).

$$\Delta S_m = \frac{1}{\Delta T}\int_{H1}^{H2}(M_{i+1}(T_{i+1}, H_{i+1}) - M_i(T_i, H_i))dH \qquad (2.4)$$

From the magnetic entropy change we can indirectly measure $\Delta T_{ad}$ from isothermal magnetic entropy change $\Delta S_m$ and the specific heat capacity measurements $\Delta C_H$ using the equation

$$\Delta C_H = C(T, H) - C(T, 0) = T\frac{\delta \Delta S_m}{\delta T} \qquad (2.5)$$

For a second order magnetic phase transition (SOMT), the specific heat capacity is independent of magnetic field, the adiabatic temperature change ($\Delta T_{ad}$) can be determined by employing equation (2.5).

## 2.7 Dielectric Characterisation

The dielectric constant of the sample can be determined by recording the capacitance of the material as a function of temperature. To find the dielectric constant of samples at room temperature, first, the powdered samples are changed into very thin pellets (1mm thickness and 10mm diameter) by using a pelletizer. The capacitance, loss factor, dielectric constant, impedance, and ac conductivity of the pellet were measured with frequencies ranging from 4 Hz to 8 MHz. A temperature controller controls the sample temperature, and the temperature on the sample is

sensed by an Iron-Constantan (Fe-K) thermocouple on the sample. A dielectric cell was employed for the electrical measurements and the LCR meter in which the sample is kept. The outer view of the IM3536 LCR meter and the dielectric cell is shown in Fig. 2.18.

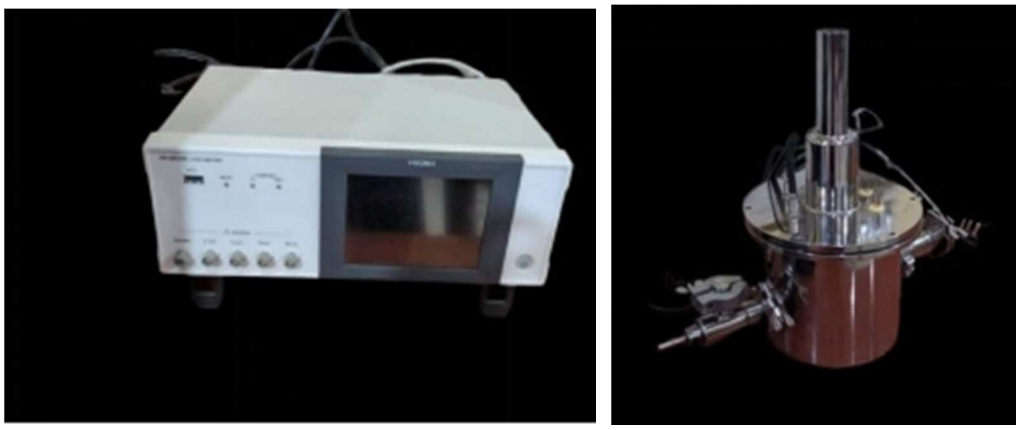

**Figure 2.18.** Outer view of HIOKI IM3536 LCR meter

The cell is made up of mild steel with a cylindrical stem having provisions for fixing various attachments such as electrical connections and vacuum gauges. Pellets are mounted on the sample holder consisting of two copper disc electrodes in between the pelletized samples are loaded for the electrical conductivity and dielectric measurements. The sample holder can be heated using a temperature-controlled heater.

The dielectric constant measurements of the samples at low and high frequencies, *viz*, from 100 Hz to 8 MHz were carried out by a HIOKI IM3536LCR meter which is automated and controlled by a virtual instrumentation package called LCR Meter Application Software. Temperature variation studies have also been carried out.

The dielectric constant of the sample can be calculated using the equation,

$$\varepsilon_r = \frac{C\,d}{\varepsilon_0 A} \tag{2.6}$$

where, $d$ is the thickness of the pellet, $C$ is the capacitance measured by LCR meter, $A$ is the area of the sandwiched structure and $\varepsilon_0$ is the absolute permittivity of air.

The theory used for the evaluation of ac conductivity from dielectric constant values is described as follows. Any capacitor when charged under an ac voltage will have a loss current due to ohmic resistance or impedance by heat absorption.

The ac conductivity for a parallel plate capacitor of area of cross section $A$ and separation $d$, is given by the relation

$$\sigma_{ac} = \frac{J}{E} \tag{2.7}$$

Here, $J$ is the current density and $E$ is the field density. But we know that the electric field vector

$$E = \frac{D}{\varepsilon} \tag{2.8}$$

where $\varepsilon$ is the complex permittivity of the material and $D$ is the displacement vector of the dipole charges. Also, the electric field intensity ($E$) for a parallel plate capacitor is the ratio of the potential difference between the plates of the capacitor (V) and the distance between the plates (d).

$$E = \frac{V}{d} \tag{2.9}$$

Since the current density $$J = \frac{dq}{dt} \tag{2.10}$$

and q is given by $$\frac{Q}{A} = \frac{V\varepsilon}{d}\ , \tag{2.11}$$

where $Q$ is the charge in coulombs due to a potential difference of $V$ volts between two plates of the capacitor.

$$J = \frac{dq}{dt} = \frac{d}{dt}\left(\frac{V\varepsilon}{d}\right) = \frac{\varepsilon}{d}\frac{dV}{dt} \tag{2.12}$$

$$J = \frac{\varepsilon}{d}\frac{dV}{dt} = \frac{\varepsilon}{d}Vj\omega \tag{2.13}$$

Substituting for $E$ and $J$ from equations (2.12) and (2.13) we get

$$\sigma_{ac} = \frac{J}{E} = \varepsilon j\omega \tag{2.14}$$

Considering $\varepsilon$ as a complex entity of the form $\varepsilon^* = \varepsilon' - j\varepsilon''$ and neglecting the imaginary term in the conductivity, we can write

$$\sigma_{ac} = \omega\varepsilon'' \tag{2.15}$$

But the loss factor or dissipation factor in any dielectric is given by the relation

$$tan\delta = \frac{\varepsilon''(\omega)}{\varepsilon'(\omega)} \tag{2.16}$$

Hence, from the dielectric loss and dielectric constant, ac conductivity of these samples can be evaluated using the relation

$$\sigma_{ac} = 2\pi f tan\delta\varepsilon_0\varepsilon_r \tag{2.17}$$

where $f$ is the frequency of the applied field and tanδ is the loss factor.

The ac electrical conductivity of powder samples was calculated utilizing the dielectric parameters. The ac conductivity is calculated by using the relation. After obtaining capacitance and dielectric loss from the instrument, LCR Meter Application Software first calculates the dielectric constant and then evaluates the ac conductivity.

The dielectric measurements of the sample in our study were carried out with HIOKI IM3536LCR meter at Vimala College, Thrissur, Kerala.

## REFERENCES

[1] N. Abid, A.M. Khan, S. Shujait, K. Chaudhary, M. Ikram, M. Imran, J. Haider, M. Khan, Q. Khan, M. Maqbool, Adv Colloid Interface Sci 300 (2022) 102597.

[2] V.M. Arole, S. V Munde, JAAST:Material Science (Special Issue 1 (2014) 2–89.

[3] A.B. Djurisic, Y.Y. Xi, Y.F. Hsu, W.K. Chan, Recent Pat Nanotechnol, (2007) 121–128.

[4] S. Enache, M. Dragan, A. Soare, D. Ion-Ebrasu, A. Zaulet, M. Varlam, K. Petrov, Bulgarian Chemical Communications 50 (2018) 127–132.

[5] Y.B. Kannan, R. Saravanan, N. Srinivasan, K. Praveena, K. Sadhana, Journal of Materials Science: Materials in Electronics 27 (2016) 12000–12008.

[6] R. Massart, E. Dubois, V. Cabuil, E. Hasmonay, J Magn Magn Mater 149 (1995) 1–5.

[7] A.H. Ashour, A.I. El-Batal, M.I.A.A. Maksoud, G.S. El-Sayyad, S. Labib, E. Abdeltwab, M.M. El-Okr, Particuology 40 (2018) 141–151.

[8] A. Hussain, T. Abbas, S.B. Niazi, Ceram Int 39 (2013) 1221–1225.

[9] Z.N. Kayani, M. Iqbal, S. Riaz, R. Zia, S. Naseem, Materials Science- Poland 33 (2015) 515–520.

[10] A. Rostamnejadi, H. Salamati, P. Kameli, H. Ahmadvand, J Magn Magn Mater 321 (2009) 3126–3131.

[11] L.L. Hench, J.K. West, Chem Rev 90 (1990) 33–72.

[12] R.C. Kambale, P.A. Shaikh, C.H. Bhosale, K.Y. Rajpure, Y.D. Kolekar, Smart Mater Struct 18 (2009) 0–7.

[13] B.G. Toksha, S.E. Shirsath, S.M. Patange, K.M. Jadhav, Solid State Commun 147 (2008) 479–483.

[14] M. Saleem, D. Varshney, RSC Adv 8 (2018) 1600–1609.

[15] M. George, A. Mary John, S.S. Nair, P.A. Joy, M.R. Anantharaman, J Magn Magn Mater 302 (2006) 190–195.

[16] A.S. Mukasyan, P. Epstein, P. Dinka, Proceedings of the Combustion Institute 31 (2007) 1789–1795.

[17] A.C.F.M. Costa, M.R. Morelli, R.H.G.A. Kiminami, Journal of Materials Synthesis and Processing 9 (2001) 347–352.

[18] A.M. Balagurov, I.A. Bobrikov, M.S. Maschenko, D. Sangaa, V.G. Simkin, Crystallography Reports 58 (2013) 710–717.

[19] S. Vivekanandhan, M. Venkateswarlu, N. Satyanarayana, Mater Lett 58 (2004) 2717–2720.

[20] E. Veena Gopalan, I.A. Al-Omari, K.A. Malini, P.A. Joy, D. Sakthi Kumar, Y. Yoshida, M.R. Anantharaman, J Magn Magn Mater 321 (2009) 1092–1099.

[21] B.D. Cullity, S.R. Stock, Elements of Xray Diffraction, Prentice-Hall, New York (2001).

[22] J.C. Woolley, Introduction to Solid State Physics, Second edition John Wiley and Sons (1957).

[23] H.M. Rietveld, J Appl Crystallogr 2 (1969) 65–71.

[24] S. Ben Moumen, Y.G.M. Chettab, D.M.M. Amjoud, S.F.L. Hajji, Journal of Materials Science: Materials in Electronics (2019).

[25] B.H. Toby, Powder Diffr 21 (2006) 67–70.

[26] C.F. Escalante Sierra, ucentral.edu.co., 9 (2019) 10.

[27] A. V Crewe, Science, 154 (1966) 3750.

[28] A.A. Ismail, F.R. van de Voort, J. Sedman, Techniques and Instrumentation in Analytical Chemistry 18 (1997) 93–139.

[29] Z. Raheem, Choice Reviews Online 35 (1998) 35-3308-35–3308.

[30] G.A. Bogaert, L. Goeman, D. De Ridder, M. Wevers, J. Ivens, A. Schuermans, Eur Urol 46 (2004) 641–646.

[31] S. Foner, Review of Scientific Instruments 30 (1959) 548–557.

[32] B.D.Cullity, C.D.Graham, Introduction to Magnetic Materials, John Wiley and Sons, Inc. Hoboken, N.J (2009).

[33] T. Thomson, Magnetic Properties of Metallic Thin Films, 2013.

[34] G. Barrera, P. Tiberto, P. Allia, B. Bonelli, S. Esposito, A. Marocco, M. Pansini, Y. Leterrier, Appl. Sci. 9 (2019) 212.

[35] T. Realization, M. Applications, L.M. Thesis, (2014).

…..ര*ര…..

# Chapter 3

# Synthesis, Structural, Magnetic and Dielectric Properties of Cobalt Substituted Lanthanum Sodium Manganite ($La_{0.5}Na_{0.5}Co_xMn_{1-x}O_3$)

## Objectives

The synthesis, structural, and magnetic properties of cobalt-substituted lanthanum sodium manganite $La_{0.5}Na_{0.5}Co_xMn_{1-x}O_3$ (x=0, 0.1, 0.3, 0.5, 0.7, 0.9 and 1) nanoparticles synthesized by sol-gel auto combustion method are elucidated.

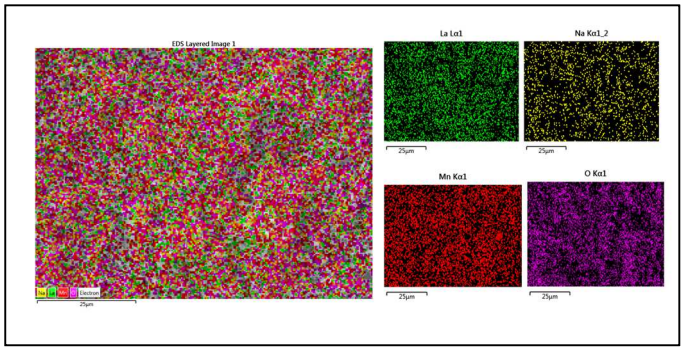

## 3.1 Introduction

Lanthanum perovskite manganites have attracted immense interest in recent research on account of their fascinating magnetic field-induced properties like magnetocaloric effect, colossal magneto resistance, spin, charge and orbital ordering, ferromagnetic ordering, canted antiferromagnetic, simple antiferromagnetic, and electronic phase separation. In addition to the magnetic behaviour, the strong interaction between charge, magnetic, and lattice degrees of freedom often results in metal–insulator transitions occurring concurrently with structural or magnetic transitions. Numerous investigations have been carried out on the magnetic and transport properties of rare-earth manganites, especially lanthanum manganites[1–5]. The doping or substitution of ions in the lattice can affect the $Mn^{3+}$–$O^{2-}$-$Mn^{4+}$ double exchange inside the perovskite manganite, thereby modifying the magnetic properties, Curie temperature $T_c$, etc. The perovskite compound $LaMnO_3$ with an orthorhombic crystal structure is an AFM insulator with Mn ions in the $3^+$ valence state and super exchange (SE) coupling between $Mn^{3+}$ sites mediated by an $e_g$ electron. It is possible to dope/substitute both the La site and Mn site of $LaMnO_3$. The substitution of divalent or monovalent ions at the La site in lanthanum manganite ($La_{1-x}B_xMnO_3$ (B=Sr, Ca, Na) results in the mixed valence of $Mn^{3+}$ and $Mn^{4+}$ with the electronic configuration $(3d^4, t_{2g}^3, \uparrow e_g^1, S = 2)$ , $\left(3d^4, t_{2g}^3, \uparrow e_g^0, S = {}^3/_2\right)$ , where $Mn^{4+}$ lacks an $e_g$ electron, and hence the itinerant hole may hop to $Mn^{3+}$. There have been numerous studies on the magnetic, electrical, magnetocaloric, and magnetoresistance properties and hyperthermia applications of monovalent or divalent substituted lanthanum manganites [6–17].

The sodium substitution in the A site of lanthanum manganites introduces the mixed valence state of $Mn^{3+}/Mn^{4+}$ pairs, which contributes to ferromagnetism in manganites. The conversion rate of $Mn^{3+}$ to $Mn^{4+}$ and, hence, hole density in monovalent substitution is twice that for the equivalent concentration of divalent substitution. Several reports have explored the applications of lanthanum sodium

manganite, including its use in hyperthermia, quantum computing, spintronics, and magnetic refrigeration [18–24]. The literature review suggests that the higher substitution of Na in the La site contributes to the magnetic interaction by double exchange interaction as well as the induced vacancies in the La or O sites, which play an important role in the magnetic ordering and, hence an enhanced magnetocaloric effect[25]. Among the sodium-rich compositions, in $La_xNa_{1-x}MnO_3$ perovskites, the highest magnetocaloric effect near room temperature in lanthanum sodium manganite has been reported for a fifty percent substitution of sodium $La_{0.5}Na_{0.5}MnO_3$[18].

Since we are interested in the near room temperature magnetocaloric properties, we have taken $La_{0.5}Na_{0.5}MnO_3$ as the basic perovskite system for the study in the present work. The doping at the Mn site in $La_{0.5}Na_{0.5}MnO_3$, is important when compared to that in La site because B-site doping with *3d* ions would interrupt the ferromagnetic ordering of the Mn network, which leads to changes in the electrical and magnetic properties of the manganites. Although cobalt differs from manganese in terms of electron configuration and spin states, cobalt shows multiple valence and spin states ($Co^{3+}/Co^{4+}$) like manganese. The investigations on the cobalt substitution at the Mn site of lanthanum manganites ($LaMnO_3$) have been extensively studied [26–29]. However, the reports on the cobalt substitution in the Mn site of lanthanum sodium manganite ($La_xNa_{1-x}MnO_3$) are not available in the literature so far. In this work, Co is substituted in the Mn site of $La_{0.5}Na_{0.5}MnO_3$, to obtain a series of samples as $La_{0.5}Na_{0.5}Mn_{1-x}Co_xO_3$ (for x=0, 0.1, 0.3,0.5, 0.7, 0.9, 1). Due to the multiple spin states of cobalt, the substitution of Mn by Co can modify the magnetic properties and ordering temperature. The aim is to examine the impact of the substitution of cobalt in lanthanum sodium manganite ($La_{0.5}Na_{0.5}Co_xMn_{1-x}O_3$) samples on their structural and magnetic properties. Attempts are also made to probe the effect of sintering on tuning the different structural and magnetic characteristic properties of the samples.

## 3.2 Synthesis and Characterisation

The samples belonging to the series $La_{0.5}Na_{0.5}Co_xMn_{1-x}O_3$ (x=0, 0.1, 0.3, 0.5, 0.7, 0.9 and 1) were synthesized by the sol-gel auto-combustion method. Stoichiometric ratios of lanthanum nitrate ($LaNO_3.6H_2O$), sodium nitrate ($NaNO_3.H_2O$), cobalt nitrate ($CoNO_3.6H_2O$), and manganese nitrate $Mn(NO_3)_2$ were dissolved in 50 mL of deionized water separately. The metal nitrate solution was stirred well using a magnetic stirrer. Citric acid ($C_6H_8O_7$) was added to this solution in the molar ratio of 2:1 with metal nitrates while continuously stirring the solution. Ethylene glycol was added to this solution as a fuel after 20 minutes. The solution was stirred well at 60°C until it became a black colored gel with the evolution of gases. The highly viscous gel was then placed on a hot plate, and the subsequent heating caused the gel to burn in a self-propagating combustion process, producing a very fine powder. The powder was ground, and powder samples of cobalt substituted lanthanum sodium manganites were obtained. The parent sample $La_{0.5}Na_{0.5}MnO_3$ and $La_{0.5}Na_{0.5}Co_xMn_{1-x}O_3$ samples were prepared by the above method, by varying the concentrations of cobalt, x=0, 0.1, 0.3, 0.5, 0.7, 0.9 and 1 (by taking the required molar concentration of cobalt nitrate). All the powder samples were sintered at 1000°C for 6 hours in a furnace. Both the as-prepared (unsintered) and sintered powder samples are probed for different characteristics. The parent sample $La_{0.5}Na_{0.5}MnO_3$ is labeled as LNMO, while the cobalt substituted samples ($La_{0.5}Na_{0.5}Co_xMn_{1-x}O_3$ ) are labeled as LNCMO1, LNCMO3, LNCMO5, LNCMO7, LNCMO9, and LNCO for x=0.1, x=0.3, x=0.5. x=0.7, x=0.9 and x=1 respectively.

The structural characterisation of the sample was carried out by XRD , Rietveld refinement, TEM, SEM, and FTIR. EDAX measurements were performed for the compositional analysis. The magnetic properties of the samples were studied by employing the field dependent magnetisation curves at room temperature. The dielectric properties of LNMO were studied in a temperature range of 303 K- 350 K using an LCR meter with a dielectric cell.

## 3.3 Results and Discussion

### Structural Characterisation

#### 3.3.1 *XRD Analysis*

X-ray Diffraction analysis is used to identify the crystal structure and evaluate the lattice parameters of the as prepared and sintered $La_{0.5}Na_{0.5}Co_xMn_{1-x}O_3$ samples.

**a) *XRD Analysis* of as prepared samples.**

The XRD pattern of as prepared (unsintered) $La_{0.5}Na_{0.5}Co_xMn_{1-x}O_3$ (x=0, 0.1, 0.3, 0.5, 0.7, 0.9 and 1) samples is shown in Fig. 3.1.

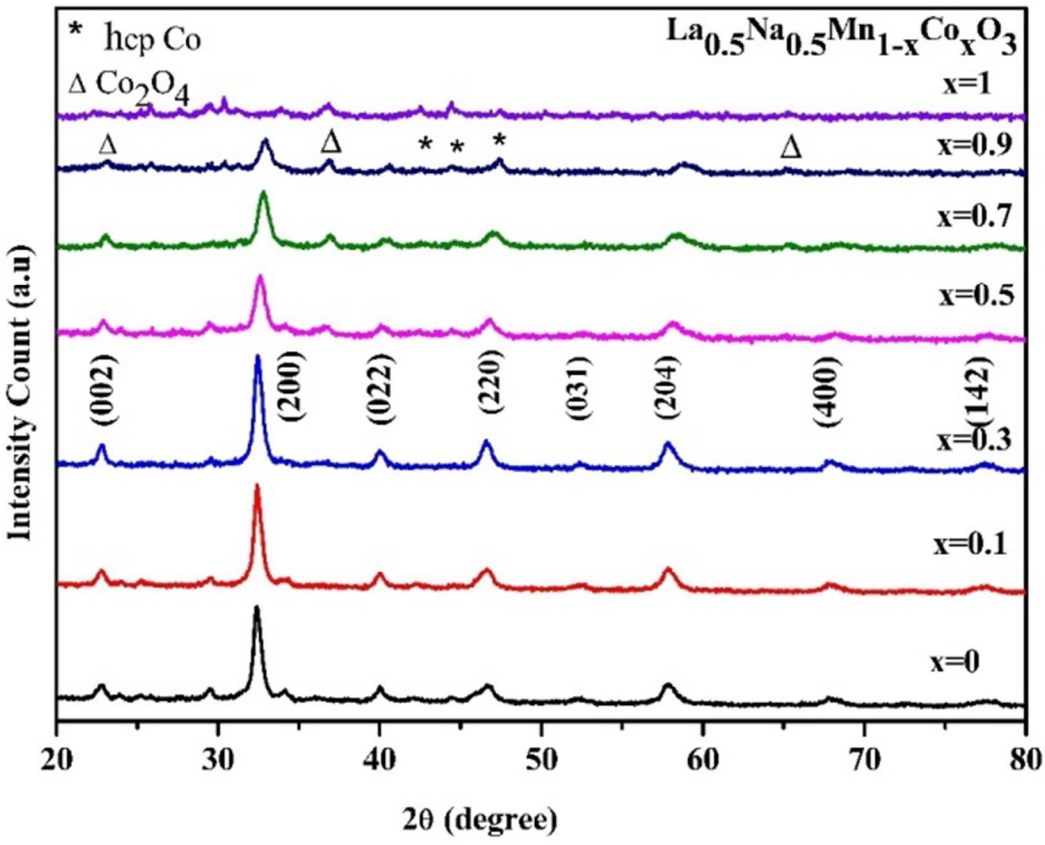


**Figure. 3.1** XRD pattern of as prepared $La_{0.5}Na_{0.5}Co_xMn_{1-x}O_3$ samples

The crystal planes indexed in the XRD patterns are consistent with those of the orthorhombic structure of lanthanum manganites. However, the single-phase perovskite structure is identified for the Mn- rich samples x=0, 0.1, and 0.3 ($x \leq 0.3$), and the crystalline perovskite phases are not identified for the other samples with $x > 0.3$. For the samples with cobalt concentration $x>0.3$, additional peaks of cobalt metal nanoparticles and cobalt oxide $Co_2O_4$ have been observed. The intensity of XRD peaks diminishes with increasing cobalt concentration, and it is the lowest for the cobaltite sample LNCO (x=1) when compared to other samples. This may be because the synthesis conditions are not optimum for the complete structure formation of cobalt rich samples in the as prepared $La_{0.5}Na_{0.5}Co_xMn_{1-x}O_3$ series. The XRD patterns of lanthanum sodium manganite $La_{0.5}Na_{0.5}MnO_3$(LNMO) and lanthanum sodium cobaltite, $La_{0.5}Na_{0.5}CoO_3$ (LNCO), are separately shown in Fig. 3.2 and Fig. 3.3, respectively.

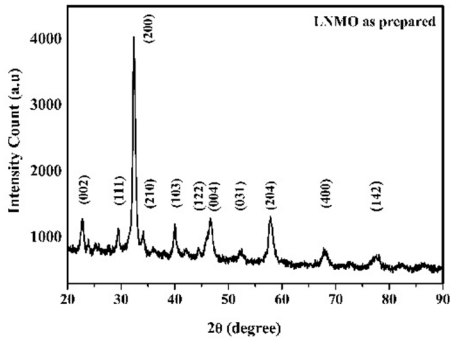


**Figure. 3.2.** XRD pattern of LNMO

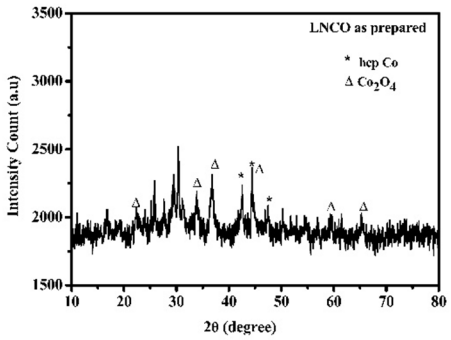


**Figure. 3.3.** XRD pattern of LNCO

The XRD pattern of the as prepared sample LNMO ($La_{0.5}Na_{0.5}MnO_3$, x=0) shown in Fig. 3.2 reveals that the crystal planes are consistent with the orthorhombic structure. While the XRD pattern of the LNCO(x=1) sample shown in Fig. 3.3 depicts that the orthorhombic perovskite phase was not formed in the cobalt rich sample LNCO, some other peaks corresponding to $Co_2O_4$ and cobalt metal were observed. The enlarged view of the main peaks of the XRD patterns in as-prepared samples $La_{0.5}Na_{0.5}Co_xMn_{1-x}O_3$ reveals a shift and reduced intensity with an increase in cobalt concentration, which is shown in Fig. 3.4.

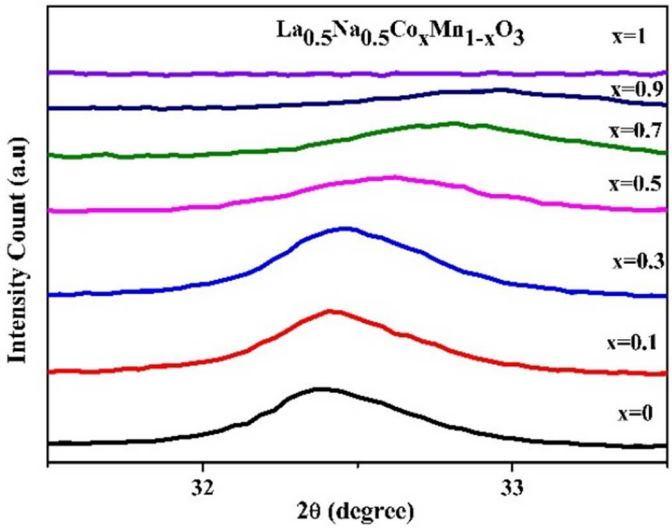


**Figure. 3.4**. Shift for main peak (200) in the XRD of $La_{0.5}Na_{0.5}Co_xMn_{1-x}O_3$

The partial incorporation of Co in the Mn site and the diminished intensity of the peak are attributed to the incomplete structural phase formation in cobalt rich samples.

### *Rietveld Refinement*

X-ray diffraction data of as prepared LNCMO samples were refined with Fullprof Suit software. Since the reports on cobalt substituted lanthanum sodium manganite are not available in the literature, the refined values of lattice parameters and unit cell volume are compared with those of lanthanum sodium manganite nanoparticles and lanthanum cobaltite nanoparticles. The Rietveld refined patterns of these $La_{0.5}Na_{0.5}Co_xMn_{1-x}O_3$ (x=0, 0.1, and 0.3) samples are displayed in Fig. 3.5. The structural parameters refined by Rietveld software are listed in Table 3.1

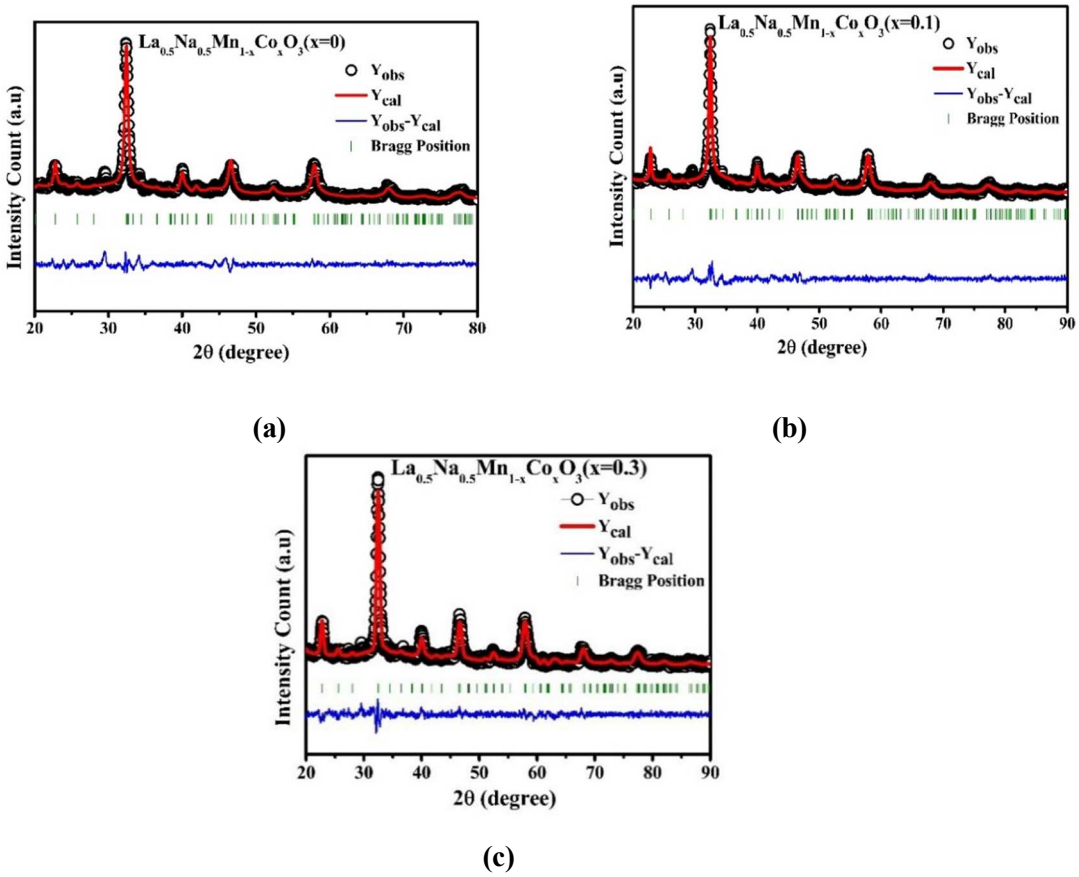


**Figure. 3.5.** Rietveld refined patterns of as prepared $La_{0.5}Na_{0.5}Co_xMn_{1-x}O_3$ (a) x=0 (b) x=0.1 and (c) x=0.3

**Table 3.1.** Refined structural parameters of as prepared samples

| Structural parameters | Compositions x | | |
|---|---|---|---|
| | **0** | **0.1** | **0.3** |
| **Lattice parameter a (Å)** | 5.5208 | 5.5207 | 5.5117 |
| **b (Å)** | 5.3817 | 5.3678 | 5.4943 |
| **c (Å)** | 7.799 | 7.805 | 7.809 |
| **V (Å$^3$)** | 231.72 | 231.29 | 236.47 |
| **$R_{Bragg}$** | 4.12 | 4.78 | 5.07 |
| **$R_{wp}$** | 26.8 | 27.1 | 24.3 |
| **$R_e$** | 17.33 | 17.80 | 17.72 |
| **($\chi^2$)** | 2.39 | 2.33 | 1.89 |

The refined parameters listed in Table. 3.1 depicts that the XRD data have been refined for the best fit with the least difference for the as prepared $La_{0.5}Na_{0.5}Co_xMn_{1-x}O_3$ samples (x=0, 0.1, and 0.3) in the orthorhombic symmetry. For all the other samples for x > 0.3 in the $La_{0.5}Na_{0.5}Co_xMn_{1-x}O_3$ series, the crystalline perovskite phase was not identified and the refinement using the Rietveld technique could not be carried out due to the incomplete phase formation.

***b) XRD Analysis of sintered samples***

$La_{0.5}Na_{0.5}Co_xMn_{1-x}O_3$ (x=0 to 1) samples were sintered to achieve perovskite phase formation in cobalt-rich samples. The XRD pattern of the sintered $La_{0.5}Na_{0.5}Co_xMn_{1-x}O_3$ (x=0 to 1) samples is shown in Fig. 3.6.

The XRD patterns of all the sintered samples exhibited a typical perovskite structure with a double-peaking nature for the main peaks. The presence of the most intense peak at 2θ positions of 32.8° and 58.3° in the XRD patterns of sintered $La_{0.5}Na_{0.5}Co_xMn_{1-x}O_3$ samples indicates that they are crystallised in the trigonal system with rhombohedral symmetry (JCPDS Card No. 50-0298) which shows an entirely different pattern when compared to the as-prepared sample (Fig.3.1). Some additional peaks of α-$MnO_2$ are present in the XRD pattern of LNMO. As the cobalt concentration increases, the peaks at 2θ positions of 32.8°, 40.2°, 58.3°, and 68.8° become more intense and sharper for cobalt rich samples, such that the double peaks are clearly seen. For samples with x > 0.5, some additional peaks are observed around 2θ positions of 36°, 44°, and 49°, indicating the presence of sodium cobalt oxide. These peaks are absent in the XRD patterns of the samples for x < 0.5. The diffraction peaks of sodium cobalt oxide are more intense for the concentration x=0.5 compared to the other samples. Similar lattice distortion for the x = 0.5 sample in B site substituted lanthanum manganite has been observed in the reports [30].

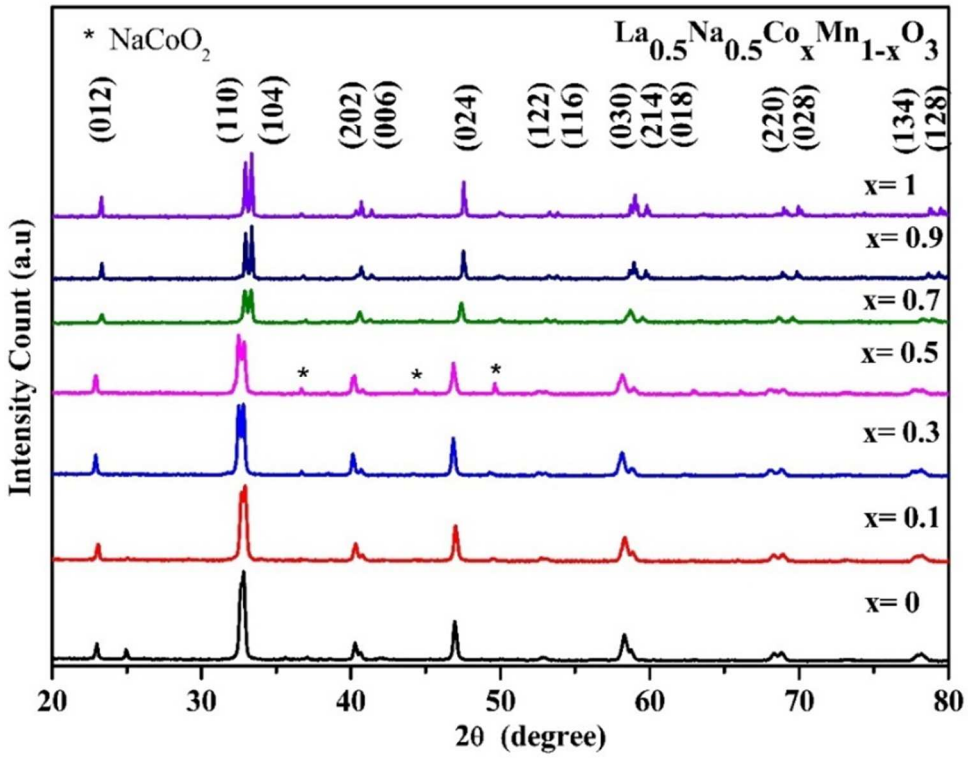


**Figure. 3.6.** XRD patterns of sintered $La_{0.5}Na_{0.5}Co_xMn_{1-x}O_3$ samples

The XRD patterns of the samples with x=0 (LNMO) and x=1 (LNCO) are shown in Fig.3.7(a) and Fig.3.7(b) respectively. It can be observed from Fig. 3.7 that the sintered sample $La_{0.5}Na_{0.5}MnO_3$ (LNMO) crystallized in a less distorted rhombohedral symmetry of $R\bar{3}c$ space group with JCPDS Card No. 50-0298 [31] while the as prepared LNMO sample exhibited an orthorhombic symmetry (Fig.3.2). But some peaks of α-$MnO_2$ with less intensity are observed in the XRD pattern of the sintered LNMO sample. The impurity phases of $MnO_2$ are reported in some research work on lanthanum sodium manganite [32]. In contrast, the XRD pattern of LNCO reveals that the peaks at 32° and 58° split into sharp and intense ones which is similar to the reported behavior of cobaltite with JCPDS (48-0123)[33]. It is also noted that these peaks could not be identified in the XRD pattern of as prepared LNCO (Fig.3.3).

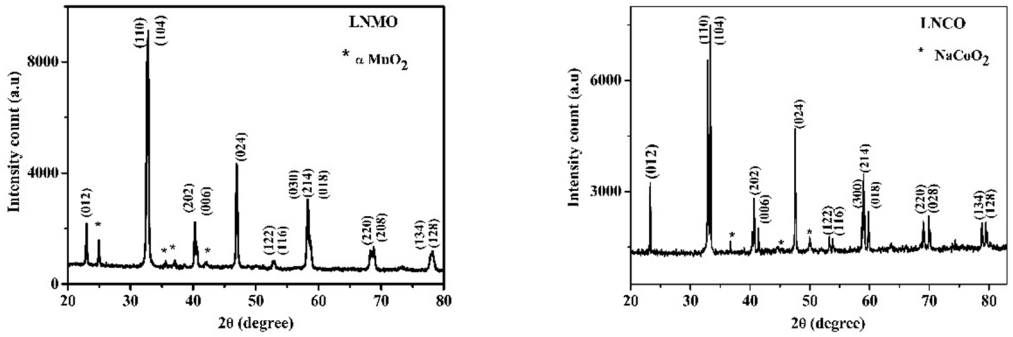


(a) LNMO (b) LNCO

**Figure. 3.7.** XRD pattern of (a) (LNMO) and (b) (LNCO)

The enlarged view of the most intense peak shift with an increase in cobalt concentration is shown in Fig. 3.8, which indicates a structural modification of the samples with cobalt substitution. The peak shift towards the lower 2θ values has been observed for x=0.3 and 0.5 samples. This may be due to the sodium volatility in these samples. On sintering the samples at high temperatures, sodium volatility can induce vacancies in the La or O site for higher concentrations of Na. These vacancies can affect the average radius of the A site, which could lead to lattice distortion[18]. For samples with x > 0.5 in $La_{0.5}Na_{0.5}Co_xMn_{1-x}O_3$, the diffraction angle of the most intense peak (110), ((104) shifts to higher 2θ values indicating a lattice contraction with the substitution of $Co^{3+}$ with a lower ionic radius (0.61Å) for larger $Mn^{3+}$ ion (0.64Å), which confirms the incorporation of $Co^{3+}$ ions into the lattice. Similar observations were reported in Lanthanum cobaltite[34]. The rhombohedral symmetry is found to be increased in the cobalt rich samples due to the charge ordering and reduced distortion of $MnO_6$ octahedra, which is absent in the as prepared samples (Fig. 3.1). Evidently, a structural transition from orthorhombic to rhombohedral symmetry can be observed when the $La_{0.5}Na_{0.5}Co_xMn_{1-x}O_3$ samples were sintered at 1000°C for 6 hours.

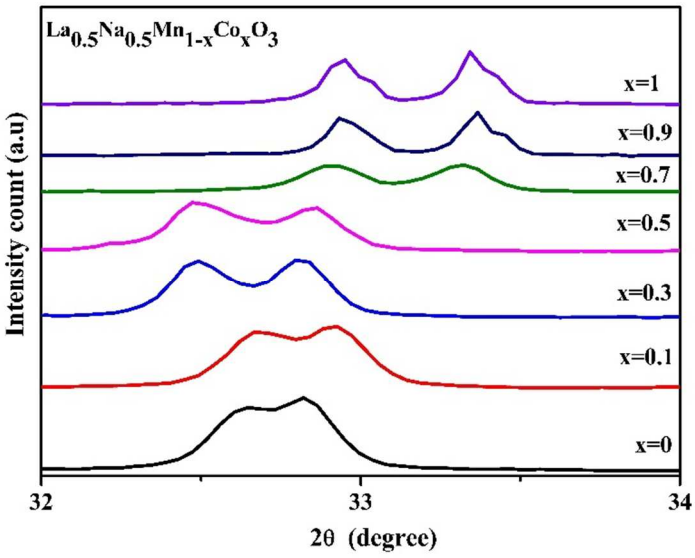


**Figure. 3.8.** 2θ shift of the most intense peak towards a higher angle for $La_{0.5}Na_{0.5}Co_xMn_{1-x}O_3$

### *Rietveld Refinement*

The Rietveld refined pattern and crystal structure of the LNMO sample drawn with Vesta software are shown in Fig. 3.9. (a) and (b) respectively.

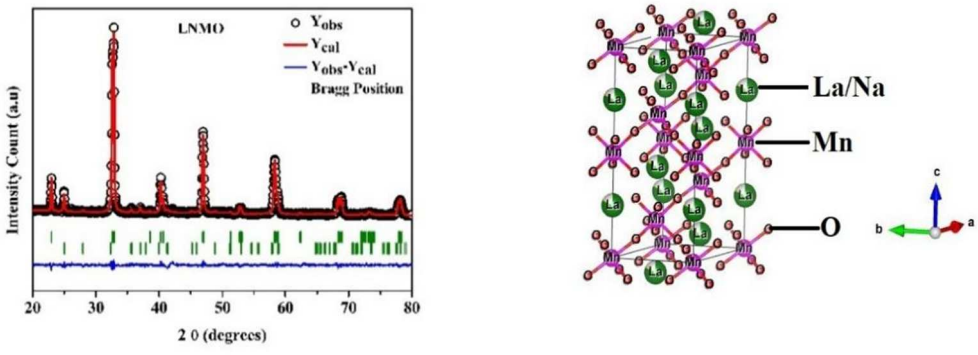


(a) (b)

**Figure. 3.9** Rietveld patterns of sintered (a) LNMO (b) Crystal structure of LNMO

The refined pattern of the LNMO sample reveals that the best fit with the least difference was obtained for the LNMO samples. It is also observed that nanoparticles crystallise in the rhombohedral symmetry with the $R\bar{3}c$ space group (Space group No. 167)[31]. The crystal structure drawn by Vesta software depicts that the LNMO sample crystallises in the rhombohedral symmetry. In this structure, La/Na atoms are represented in green colour, Mn in violet colour and oxygen atoms in black colour. The Rietveld refined pattern of other samples $La_{0.5}Na_{0.5}Co_xMn_{1-x}O_3$ (x=0.1,0.3,0.5, 0.7, 0.9 and 1) in this series is shown in Fig. 3.10. The refined XRD patterns indicate that all the LNCMO samples crystallize in the rhombohedral symmetry with the $R\bar{3}c$ space group. The best fit is obtained for the sintered LNCMO samples except for LNCMO5 (x=0.5). The refined XRD pattern of LNCMO5 is largely distorted with more intense peaks of the impurity phase of sodium cobalt oxide.

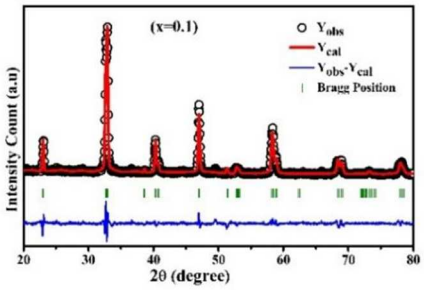


LNCMO1

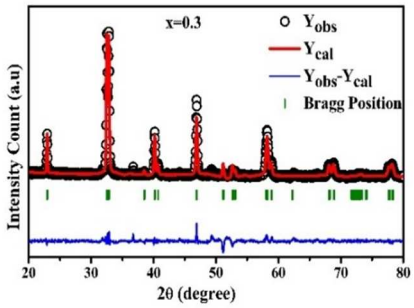


LNCMO3

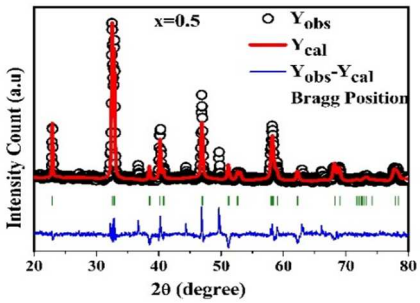


LNCMO5

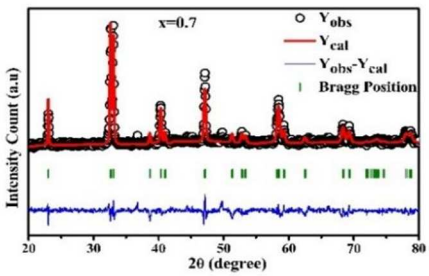


LNCMO7

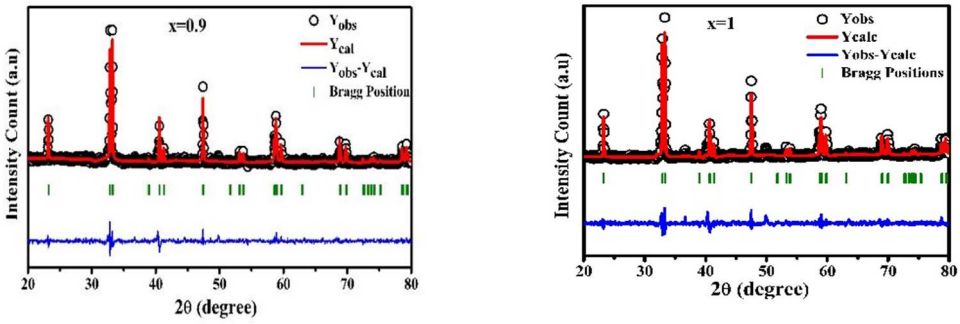


LNCMO9 LNCO

**Figure. 3.10**. Rietveld patterns of sintered $La_{0.5}Na_{0.5}Co_xMn_{1-x}O_3$ samples (x=0.1, 0.3. 0.5, 0.7, 0.9 and 1). *The black circles represent the observed values, red solid lines represent the calculated data, blue solid lines represent the difference between the observed data and calculated data, and the vertical bars represent the Bragg positions.*

The structural parameters of $La_{0.5}Na_{0.5}Co_xMn_{1-x}O_3$ (x=0, 0.1, 0.3, 0.5, 0.7, 0.9, and 1) samples refined by Rietveld software are listed in Table 3.2.

**Table 3.2.** The refined structural parameters of $La_{0.5}Na_{0.5}Co_xMn_{1-x}O_3$ samples.

| **Composition x** | **0** | **0.1** | **0.3** | **0.5** | **0.7** | **0.9** | **1** |
|---|---|---|---|---|---|---|---|
| ***Lattice parameter a(Å)*** | 5.489 | 5.486 | 5.505 | 5.505 | 5.489 | 5.455 | 5.444 |
| ***c(Å)*** | 13.320 | 13.286 | 13.297 | 13.28 | 13.208 | 13.121 | 13.095 |
| ***V(Å$^3$)*** | 347.619 | 346.285 | 348.948 | 348.647 | 344.717 | 338.131 | 336.113 |
| $R_{Bragg}$ | 2.22 | 2.89 | 4.88 | 2.75 | 4.48 | 7.52 | 3.55 |
| $R_{wp}$ | 12.2 | 21.4 | 21.9 | 23.6 | 29.3 | 24.1 | 23.7 |
| $R_e$ | 8.74 | 10.32 | 10.66 | 11.74 | 16.79 | 14.7 | 12.76 |
| $(\chi^2)$ | 1.96 | 4.30 | 4.21 | 4.03 | 3.05 | 2.69 | 3.45 |

Table 3.2 illustrates that the lattice parameters *a* and *c* decrease for the initial composition of cobalt x=0.1 and then increase. The unit cell volume also varies similarly to that of the lattice parameters *a* and *c*. The variation of lattice parameters

*a, c* with unit cell volume (*V*) with concentration of cobalt (x) in sintered LNCMO samples is also displayed in Fig. 3.11.(a), Fig. 3.11.(b) respectively.

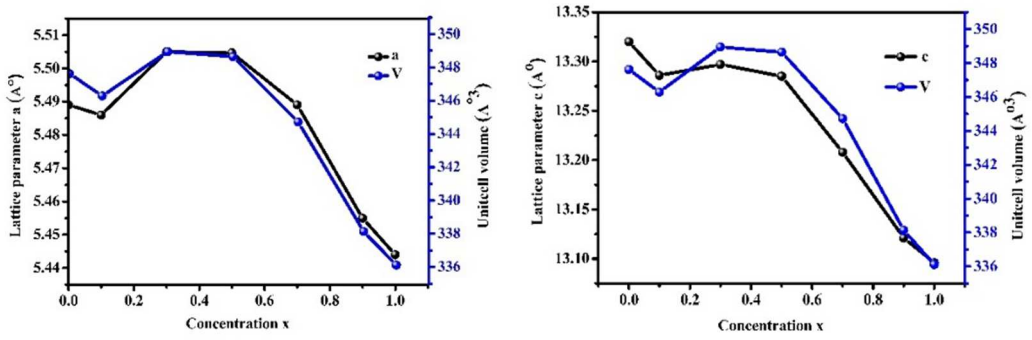


(a) (b)

**Figure. 3.11.** (a) Variation of lattice parameter *a* and unit cell volume *V* with concentration of cobalt (b) Variation of lattice parameter *c* and unit cell volume *V* with x

With the substitution of cobalt for Mn in LNMO, the high spin $Mn^{3+}$ (0.645 Å) is replaced by high spin $Co^{3+}$ (0.61 Å), and as a result, the lattice parameter *a* decreases initially for x=0.1. The lattice parameter increases for x=0.3 and 0.5 samples due to the volatility of sodium for the Mn rich samples, which is confirmed later by the EDAX spectrum. The increase in lattice parameters for the Mn rich samples, x=0.3 and x=0.5, can be due to the sodium volatility, which creates cation vacancy in the La/Na sites. The substitution of $Na^{+}$ in the La site introduces $Mn^{4+}$ ions to maintain charge neutrality. However, if Na is lost by volatilisation during the synthesis process, the number of $Mn^{4+}$ ions decreases. This increases the $Mn^{3+}/Mn^{4+}$ ratio, which indicates that the number of $Mn^{3+}$ ions with a large ionic radius is more significant than the $Mn^{4+}$ ions and, hence, a lattice expansion. $Mn^{3+}$ is known to be more Jahn-Teller active, which can increase lattice distortions and have a negative impact on the structural stability of the samples. So, the sodium volatility can cause oxygen deficiency in these samples and result in a distortion of the $MnO_6$ octahedra[35]. In the cobalt-rich samples, $Co^{3+}$ has undergone a charge transfer mechanism shown by equation (3.1), and hence the concentration of $Mn^{4+}$ (0.53 Å) and $Co^{2+}$ (0.65 Å) increases.

$$Mn^{3+} + Co^{3+} \rightarrow Mn^{4+} + Co^{2+} \quad (3.1)$$

The $Mn^{4+}$ and $Co^{2+}$ with larger ionic radius replace the $Co^{3+}$ ion with smaller ionic radius. The increase in number of $Co^{2+}$ increases the octahedral distortion with substitution of cobalt. So, the lattice parameters *a* and *c* decrease with cobalt substitution. The variation of unit cell volume with an increase in cobalt substitution can be due to two possibilities[35,36]. The first case is the transition of larger $Mn^{3+}$ ions to smaller $Mn^{4+}$ ions as per equation (3.1), and the second is the distortion of $MnO_6$ octahedra due to the increase of $Mn^{4+}$. In the present work, this can be due to the distortion of the $MnO_6$ octahedra caused by the volatility of sodium for the x=0.3 and 0.5 samples. As cobalt concentration increases, for the samples with x > 0.5, a less distorted rhombohedral symmetry is achieved which can be due to the observed decrease in the sodium volatility in these concentrations (Refer EDAX measurement).The structural analysis confirms that the samples in the $La_{0.5}Na_{0.5}Co_xMn_{1-x}O_3$ series form a complete phase after sintering at 1000°C for 6 hours. According to published research, the synthesis of perovskite lanthanum manganites involved sintering for 48–72 hours. However, in the present work on the synthesis of cobalt substituted lanthanum sodium manganite, the samples were sintered for only six hours which is a relatively shorter duration.

### *3.3.2 Transmission Electron Microscopy (TEM)*

Transmission Electron Microscope (HRTEM) measurements of a typical as prepared sample, $La_{0.5}Na_{0.5}Co_{0.3}Mn_{0.7}O$ (LNCMO3, x=0.3), is carried out. The crystallite size was estimated from the TEM image. The crystal planes are identified from the HRTEM images and Selected Area Electron Diffraction (SAED) pattern. The SAED pattern confirmed the crystalline nature of the synthesized particles. As shown in the TEM images, most of the particles crystallised in the nano range. The estimated average crystallite size of the particle is 15.8 nm from the histogram. The TEM image, histogram, diffraction pattern, and SAED pattern of as prepared LNMO

are shown in Fig. 3.12 (a), (b), (c), and (d), respectively. The crystal planes (002) corresponding to the orthorhombic structure are seen in Fig. 3.12 (c).

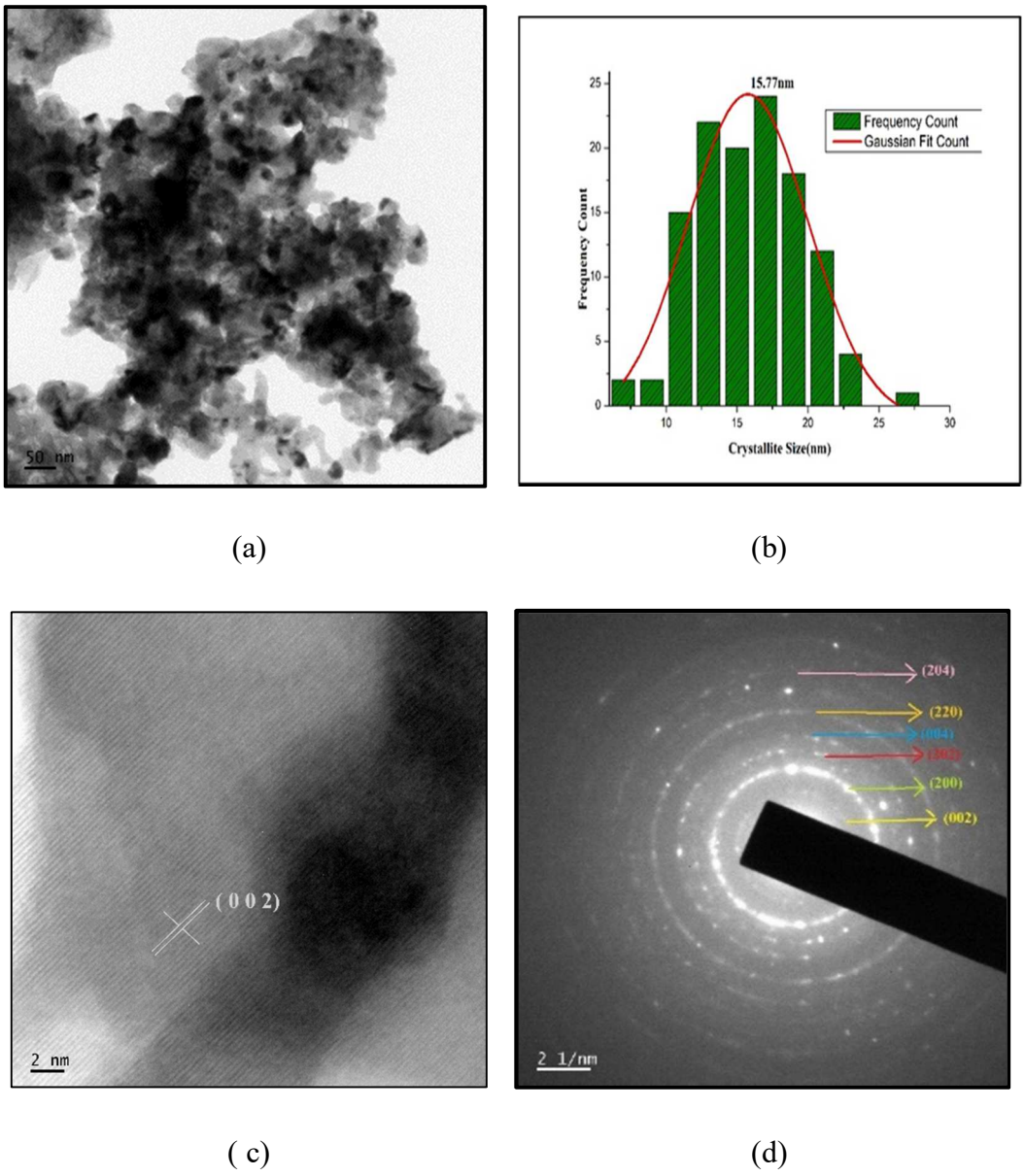


**Figure. 3.12.** (a) The TEM image, (b) Histogram (c) HRTEM (d) SAED pattern of as prepared LNMO

TEM images of a typical sintered sample of LNMO (x=0) are displayed in Fig. 3.13. The average crystallite size estimated from the TEM image is 58.3 nm. Fig.3.13 (b) reveals that most of the particles crystallize in the 50 nm- 60 nm range. Moreover, the associated HRTEM images shown in Fig. 3.13(c) reveal a distinctive spacing of 2.94 Å which can be indexed as the (012) lattice planes of LNMO belonging to rhombohedral symmetry.

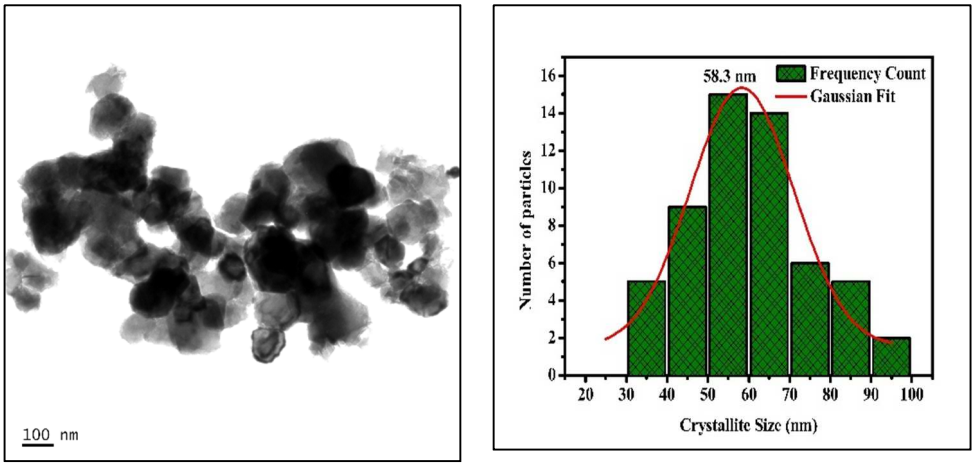


**Figure.3.13.** (a) TEM (b) HRTEM (c) Histogram (d) SAED pattern of sintered LNMO.

The SAED pattern shown in Fig. 3.13 (d) depicts the crystalline behaviour of the sintered LNMO particles. It can be observed that the crystallite size of the LNMO sample increased with sintering at higher temperatures.

### *3.3.3 Scanning Electron Microscopy (FESEM) and EDAX*

The morphology of the $La_{0.5}Na_{0.5}Co_xMn_{1-x}O_3$ (x=0.3) from the as prepared series has been examined by FESEM micrograph, which is shown in Fig. 3.14. A uniform morphology and the formation of larger agglomerates of smaller particles can be observed from the micrograph displayed in Fig. 3.14 (a) and (b) . The SEM images reveal that the porosity is found to be reduced on sintering the nanoparticles at 1000°C.

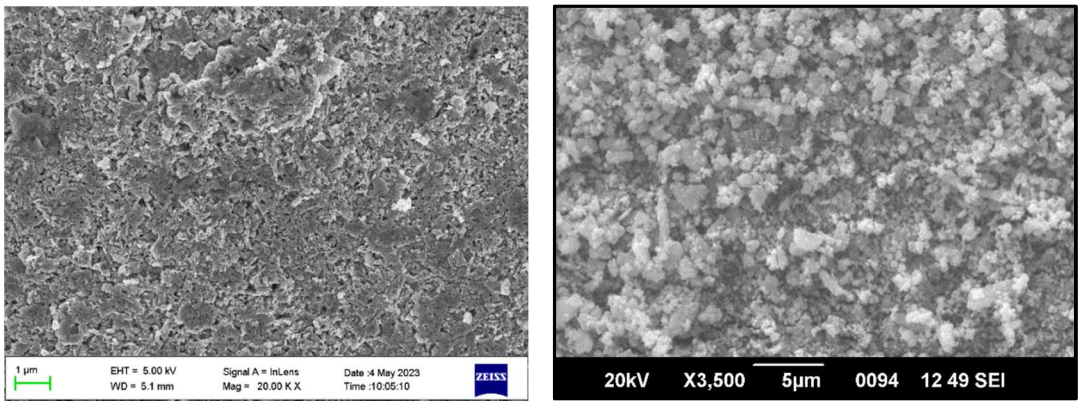


**Figure. 3.14**.SEM micrographs of (a) as prepared LNMO (b) sintered LNMO nanoparticles.

### *EDAX Measurements*

EDAX measurements of a typical as prepared sample and all the sintered samples were carried out. All of the observed peaks in the EDAX spectrum of both as prepared and sintered sample can be associated with the native elements of the compound LNCMO, including lanthanum (La), sodium (Na), manganese (Mn), cobalt (Co), and oxygen (O). Initially, the stoichiometry of the sample, $La_{0.5}Na_{0.5}MnO_3$ (LNMO), of both as prepared and sintered samples is compared from their EDAX spectrum displayed in Fig. 3.15. The Stoichiometric ratio of La/Na

and La/Mn was estimated from the spectrum and is listed in Table 3.3. The estimated La/Na and La/Mn stoichiometry of the as prepared are 0.9 (expected 1) and 0.47 (expected 0.5) respectively. However, the estimated stoichiometry of the sintered sample reveals a sodium-deficient structure as the experimental La/Na ratio is 1.21 instead of 1, while the La/Mn ratio is in exact agreement with the theoretical value. The EDS mapping of LNMO shown in Fig. 3.15 (c) exhibits a uniform distribution of corresponding elements La, Na, Mn and O.

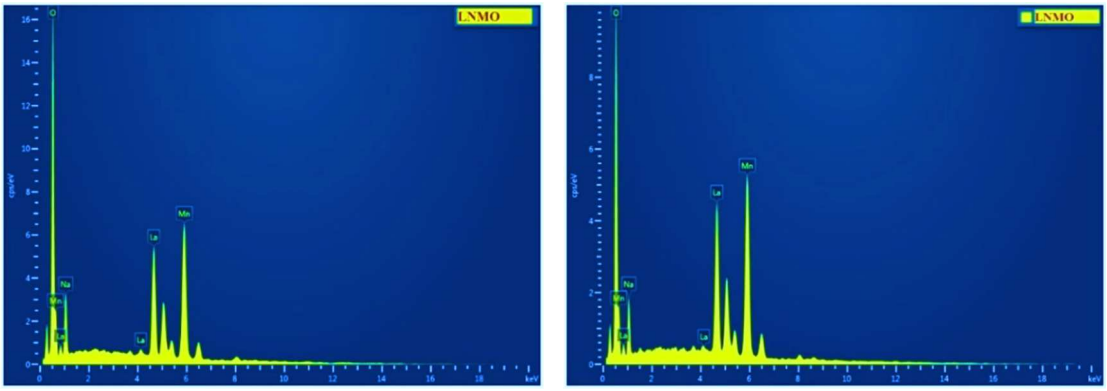


(a) As prepared LNMO (b) Sintered LNMO

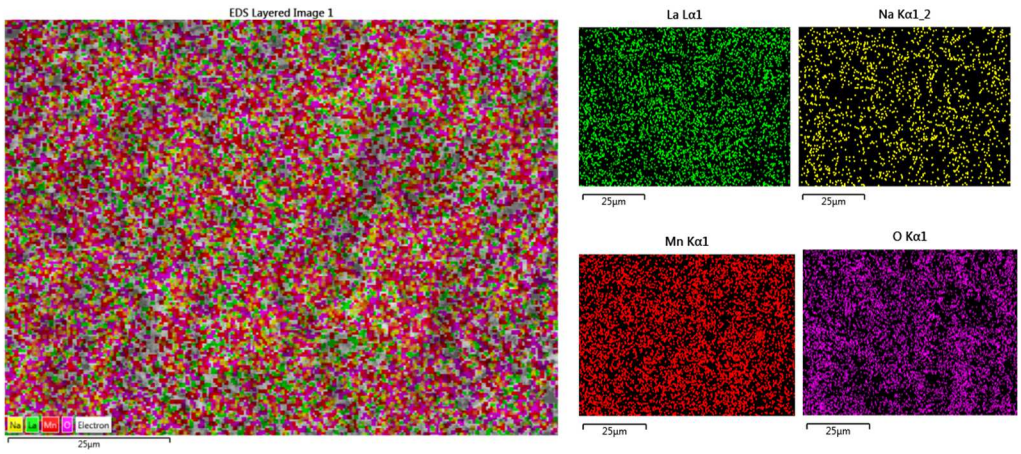


(c) Elemental Mapping

**Figure.3.15.** EDAX spectrum of as-prepared (a) LNMO (b) sintered LNMO samples ( c) Elemental Mapping of LNMO.

**Table 3.3.** Estimated and Theoretical Stoichiometry of as prepared $La_{0.5}Na_{0.5}MnO_3$ samples.

| $La_{0.5}Na_{0.5}MnO_3$ | Stoichiometry Ratio | | | | Estimated Stoichiometry |
|---|---|---|---|---|---|
| | La/Na | | La/Mn | | |
| | Experimental | Theoretical | Experimental | Theoretical | |
| **As prepared** | 0.9 | 1 | 0.47 | 0.5 | $La_{0.45}Na_{0.55}MnO_3$ |
| **Sintered** | 1.21 | 1 | 0.5 | 0.5 | $La_{0.5}Na_{0.41}MnO_3$ |

The compositional analysis of all the sintered $La_{0.5}Na_{0.5}$ $Mn_{1-x}Co_xO_3$ (LNCMO) samples was evaluated by the EDAX spectrum displayed in Fig. 3.16. The theoretical and experimental values of stoichiometric ratios are displayed in Table 3.4. The estimated stoichiometric ratio displayed in the table shows that for the samples $x < 0.5$, the expected stoichiometric ratio of La/Na (1) is not obtained, and loss of sodium is observed in these samples. It may be due to the volatilisation of sodium in the Mn rich samples on sintering at high temperatures. The sodium volatility in Mn rich samples can also be evident from the XRD spectrum. In the XRD spectrum shown in Fig. 3.8, the observed $2\theta$ shift to the lower region for $x < 0.5$ is consistent with the estimated stoichiometric ratio from the EDAX spectrum. For the sample with x=0.7, the estimated values of the La/Na ratio agree well with the theoretical value, indicating low levels of sodium volatilisation. But for Co rich samples (x=0.9 and x=1), the La/Na ratio is found to be less than the expected value, which may be due to the oxygen deficiency and presence of sodium cobalt oxide in these samples. An impurity phase of sodium cobalt oxide is observed in the cobalt rich samples ($x > 0.5$) which is clear from the XRD pattern of the sintered samples shown in Fig. 3.6. The stoichiometric ratio of Mn/Co is in good agreement with the theoretical value in all samples indicating the incorporation of cobalt in Mn site.

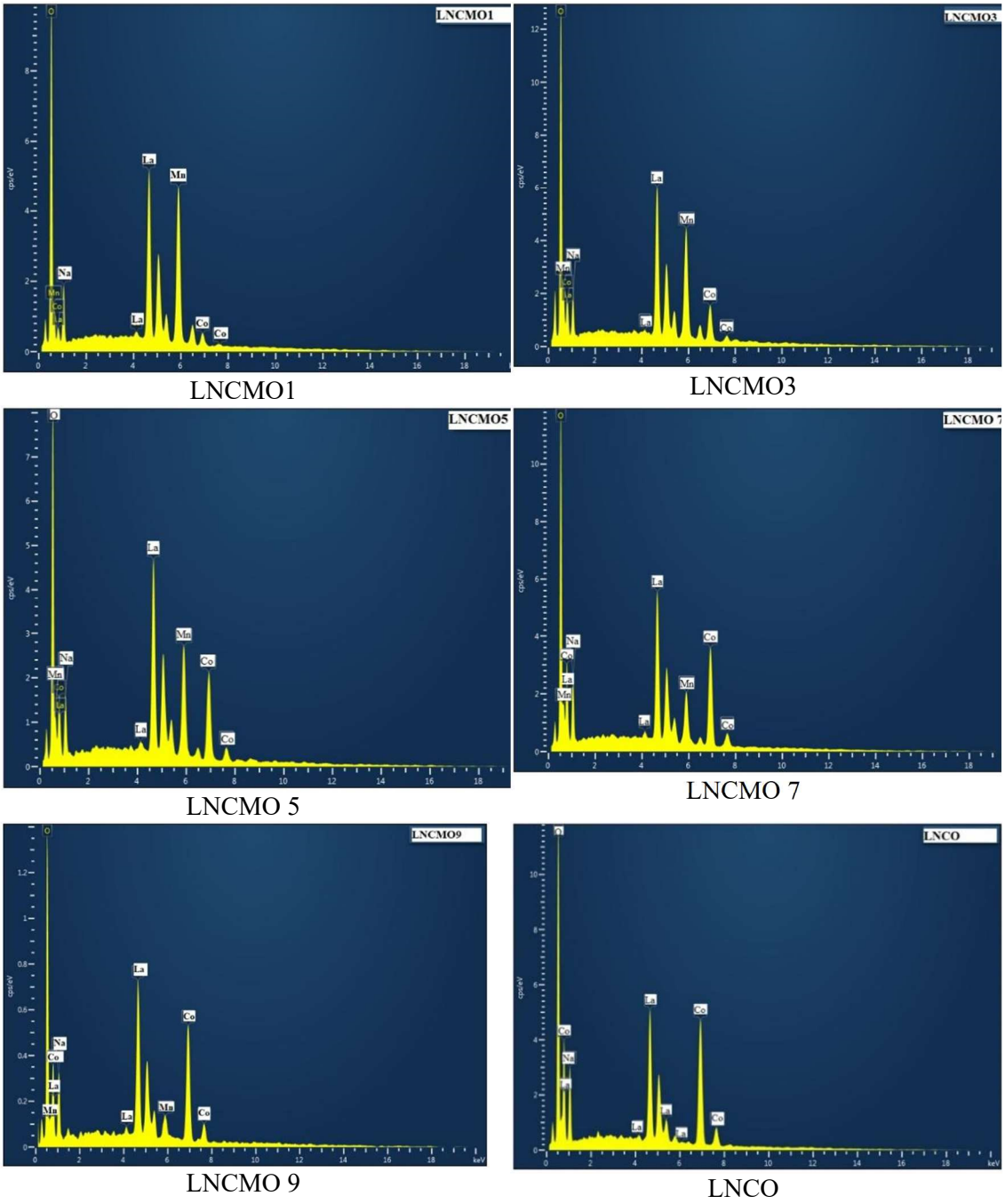


**Figure. 3.16.** EDAX spectrum of sintered $La_{0.5}Na_{0.5}Mn_{1-x}Co_xO$ (x=0.1, 0.3, 0.5, 0.7, 0.9 & 1) samples.

**Table 3.4.** Estimated and Theoretical Stoichiometry of $La_{0.5}Na_{0.5}Mn_{1-x}Co_x$ samples.

| Sample | La/Na | | Mn/Co | | La/Mn | |
|---|---|---|---|---|---|---|
| | **Exp.** | **Theo.** | **Exp.** | **Theo.** | **Exp.** | **Theo.** |
| $\mathbf{La_{0.5}Na_{0.5}Co_{0.1}Mn_{0.9}O_3}$ | 1.36 | 1 | 9.71 | 9 | 0.68 | 0.55 |
| $\mathbf{La_{0.5}Na_{0.5}Co_{0.3}Mn_{0.7}O_3}$ | 1.64 | 1 | 2.28 | 2.33 | 0.87 | 0.71 |
| $\mathbf{La_{0.5}Na_{0.5}Co_{0.5}Mn_{0.5}O_3}$ | 1.42 | 1 | 0.97 | 1 | 1.08 | 1 |
| $\mathbf{La_{0.5}Na_{0.5}Co_{0.7}Mn_{0.3}O_3}$ | 1.04 | 1 | 0.39 | 0.42 | 1.79 | 1.67 |
| $\mathbf{La_{0.5}Na_{0.5}Co_{0.9}Mn_{0.1}O_3}$ | 0.84 | 1 | 0.15 | 0.11 | 4.88 | 5 |
| $\mathbf{La_{0.5}Na_{0.5}CoO_3}$ | 0.79 | 1 | - | - | 0.49 | 0.5 |

Exp.*-Experimental value, Theo.** -Theoretical value

### *3.3.4 Fourier Transform Infrared (FTIR) Spectroscopy*

The functional groups of the active components are identified based on the peak value of the FTIR spectra recorded in the wavenumber range 4000 $cm^{-1}$ - 400 $cm^{-1}$ and structural formation is confirmed in the as prepared and sintered $La_{0.5}Na_{0.5}Co_xMn_{1-x}O$ (LNCMO) samples. FTIR spectra of as prepared and sintered LNCMO samples are displayed in Fig.3.17 and Fig.3.18 respectively.

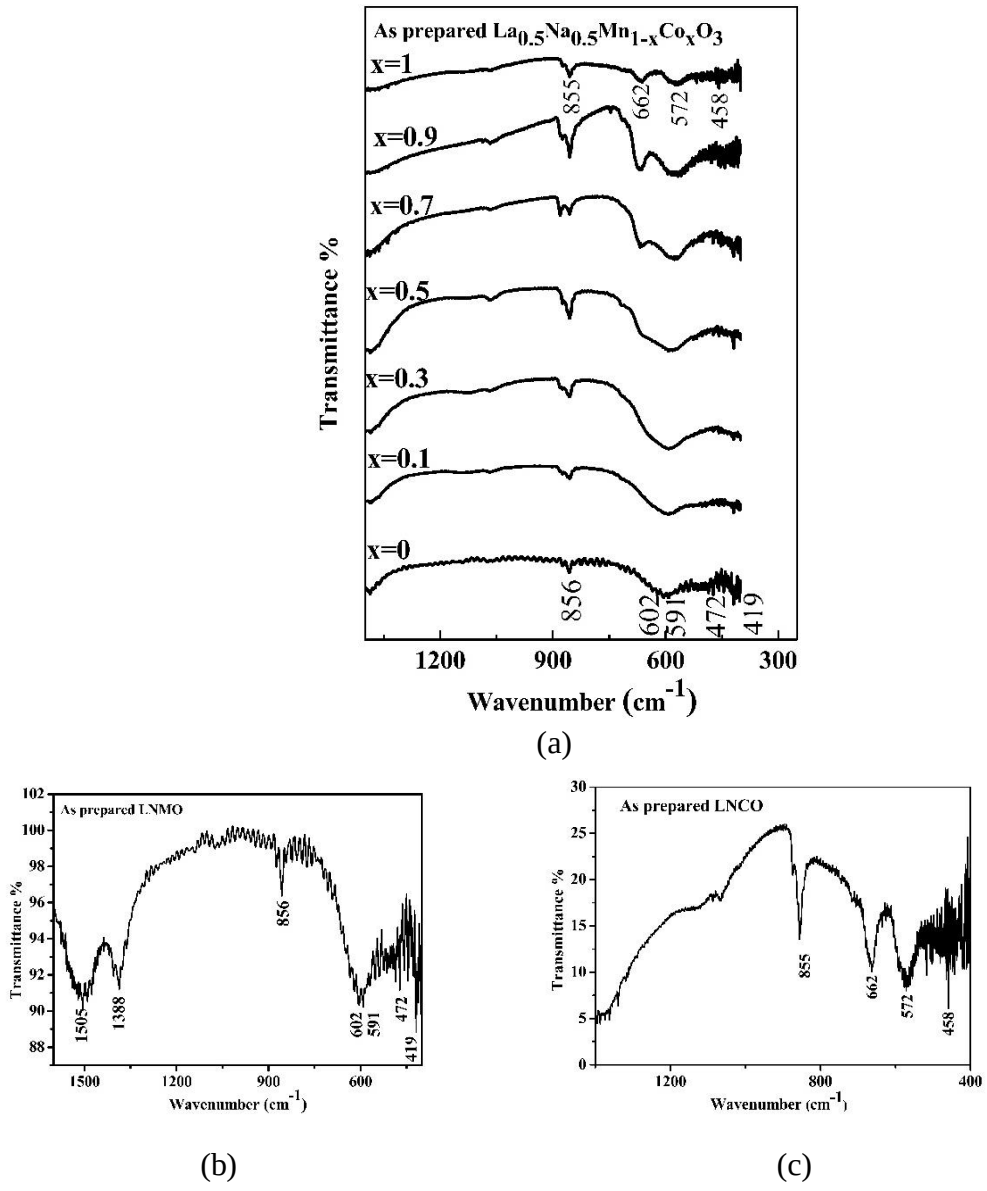


**Figure.3.17.** FTIR spectrum of as prepared (a) $La_{0.5}Na_{0.5}Co_xMn_{1-x}O_3$ (x=0-1) (b) LNMO (c ) LNCO

In the FTIR spectrum of the as-prepared LNCMO sample shown in Fig.3.17 (a), the bands around 856 $cm^{-1}$ correspond to the Mn–O stretching vibrations due to the perovskite structure of LNMO. The absorption peak around 472 $cm^{-1}$ in the FTIR spectrum of as-prepared LNMO shown in Fig. 3.17 (b) is associated with La-O

stretching vibrations. The bands around 602 $cm^{-1}$ corresponding to the absorption peaks of the Mn-O bond disappear gradually when the cobalt concentration increases, and a band near 662 $cm^{-1}$ associated with Co-O stretching vibrations appears in the cobalt-rich samples. The bands around 591 $cm^{-1}$ shift to the lower wavenumber region with an increase in cobalt concentration. The absence of the stretching mode of La-O around 472 $cm^{-1}$ and the vibrating mode of Co-O around 419 $cm^{-1}$ indicates the incomplete phase formation in the as prepared cobalt rich samples.

FTIR spectrum of sintered LNCMO samples confirms the rhombohedral symmetry for the cobalt-rich samples as the characteristic peaks are dominant in these samples. The FTIR spectrum of LNCMO samples shown in Fig. 3.18 (a) reveals that the band around 600 $cm^{-1}$ corresponds to the asymmetric stretching of the Mn-O-Mn bonds associated with the $MnO_6$ octahedra, which is the vibration characteristic of the $ABO_3$ perovskite structure. It was reported that the broadening of the 600 $cm^{-1}$ band and/or the appearance of a band around 550 $cm^{-1}$ and 410 $cm^{-1}$ corresponds to Mn–O (metal–oxygen) stretching and are the characteristics of a lanthanum manganite crystallised in rhombohedral structure with lower symmetry[37]. In our study, the band of lanthanum manganite at 550 $cm^{-1}$ is shifted to a lower frequency region and located at 522 $cm^{-1}$ in the FTIR spectrum of LNMO (Fig.3.18 b) due to the incorporation of Na in the La site and the distortion of $MnO_6$. According to the reports, the absorption peaks around 486 $cm^{-1}$ indicate the characteristic peaks of LNMO [31]. The absorption peaks around 486 $cm^{-1}$, 622 $cm^{-1}$, and 861 $cm^{-1}$ in the FTIR spectrum of LNMO indicate the vibration of the La-O bond, which are the characteristic peaks of $LaNaMnO_3$[31]. As the cobalt concentration increases, these peaks get weakened, and the peak at 602 $cm^{-1}$ becomes dominant due to Co-O bonding.

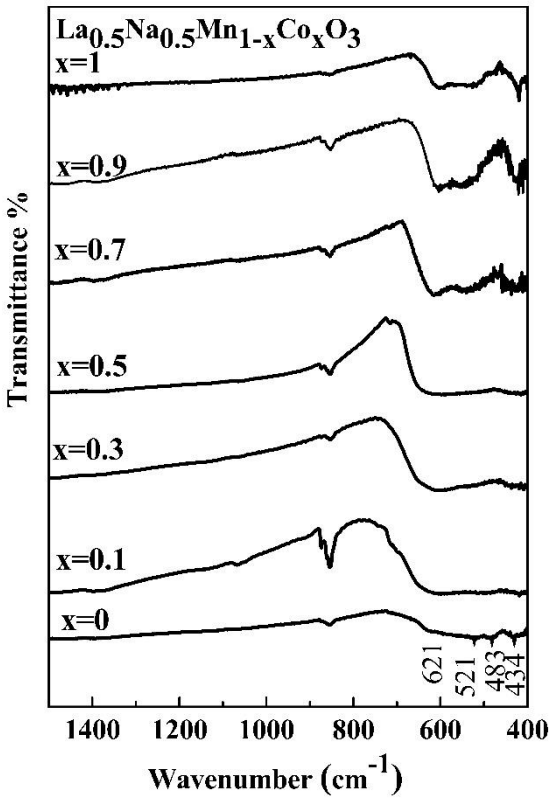


(a)

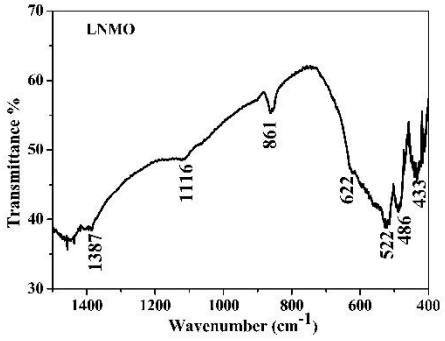


(b)

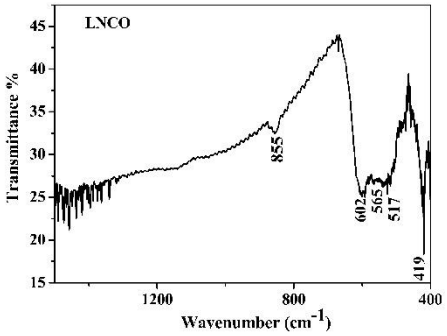


(c )

**Figure.3.18.** FTIR spectrum of sintered (a) $La_{0.5}Na_{0.5}Co_xMn_{1-x}O_3$ (x=0-1) samples (b) LNMO (c ) LNCO

In the spectrum shown in Fig. 3.18.(b) a shoulder near 565 $cm^{-1}$ corresponds to the asymmetric stretching $\nu_1$ mode of the B-O bond of the $BO_6$ octahedra, which appears in the cobalt rich samples usually observed in lanthanum cobaltites [38,39]. So, the rhombohedral structure of the sintered LNCMO samples is confirmed from the FTIR spectrum. As the concentration of cobalt increases, the appearance of a band around 419 $cm^{-1}$, the stretching mode of Co-O bonding, confirms the incorporation of Co into the Mn site. The small peak at 1116 $cm^{-1}$ indicates the stretching mode of the Mn-O-Mn bonds associated with the octahedron $MnO_6$ [9]. The absorption bands at 1387 $cm^{-1}$ in the FTIR spectra of the LNMO sample correspond to the asymmetric stretching mode of $CO_3^{2-}$ indicates the presence of carbonates which arise due to surface oxygen and $CO_2$ from the environment. The bands at 1387 $cm^{-1}$ correspond to the traces of carbonates present in the as prepared LNMO sample as the residue of the sol-gel combustion process is observed to be diminished in the FTIR spectra of the sintered sample [37].

### *3.3.5 Magnetic Characterisation*

The magnetic properties of as prepared and sintered $La_{0.5}Na_{0.5}Mn_{1-x}Co_xO_3$ samples were examined by field-dependent magnetisation at room temperature.

a) **As prepared samples**.

The evolution of hysteresis loops (M-H) of as prepared $La_{0.5}Na_{0.5}Mn_{1-x}Co_xO_3$ (x=0 to 1) samples at room temperature is shown in Fig.3.19. It is observed from the figure that the field dependent magnetisation curves of as prepared samples exhibit a paramagnetic behaviour at room temperature for the sample with x=0 and x=0.1. The as prepared LNMO sample exhibits a paramagnetic behavior at room temperature.

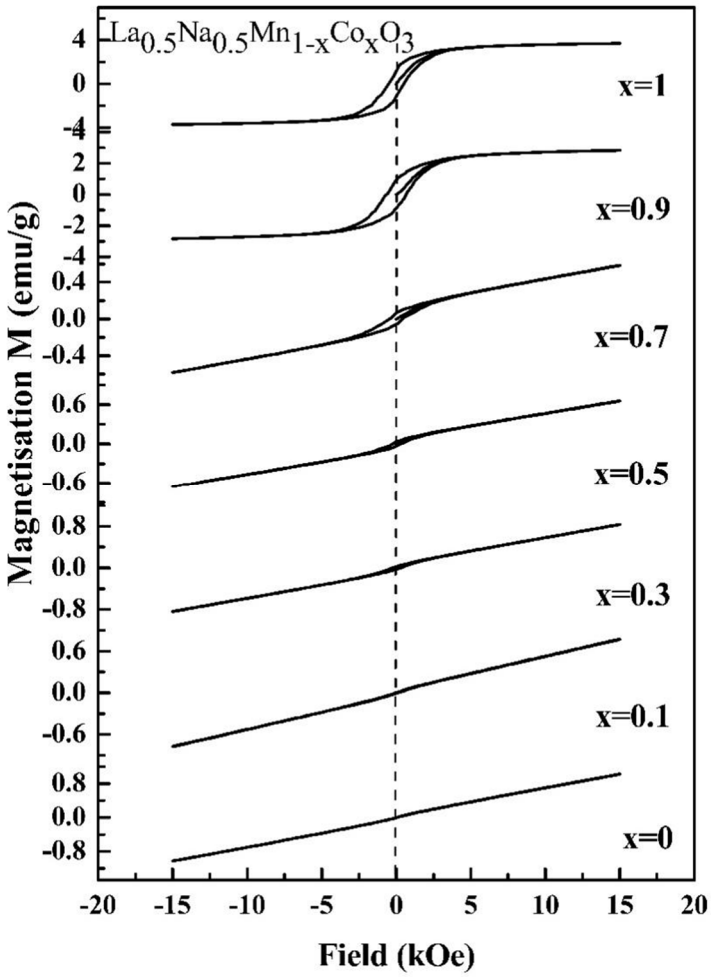


**Figure 3.19.** M-H curves of as prepared $La_{0.5}Na_{0.5}Mn_{1-x}Co_xO_3$ samples

It can be observed that as the cobalt concentration increases, the magnetic hysteresis loop develops gradually in the M-H curves at room temperature. So, the magnetic behaviour changes from paramagnetic to ferromagnetic at room temperature with cobalt substitution. The ferromagnetic behavior of cobalt rich samples ($x > 0.5$) can be due to the presence of cobalt metal nanoparticles. The presence of cobalt nanoparticles is also evident from the XRD of as prepared LNCO sample in which the peaks of cobalt nanoparticles are marked (Fig.3.3). The magnetic parameters obtained from the M-H curves of as prepared samples at room

temperature are listed in Table. 3.5. It is clear from Table 3.5 that the increase in magnetisation and coercivity with the increase in cobalt concentration is owing to the intrinsic magnetic property of cobalt.

**Table 3.5.** Magnetic parameters of as prepared $La_{0.5}Na_{0.5}Mn_{1-x}Co_xO_3$

| Sample | $M_{max}$ (emu/g) | $H_c$ (Oe) | $M_r$ (emu/g) | Magnetic Behaviour @300K |
|---|---|---|---|---|
| **LNMO** | 1.03 | 3 | 0 | Paramagnetic |
| **LNCMO1** | 0.77 | 55 | 0.007 | Paramagnetic |
| **LNCMO3** | 0.83 | 300 | 0.03 | - |
| **LNCMO5** | 0.64 | 241 | 0.04 | - |
| **LNCMO7** | 0.58 | 452 | 0.07 | - |
| **LNCMO9** | 2.81 | 615 | 0.9 | Ferromagnetic |
| **LNCO** | 3.7 | 506 | 1 | Ferromagnetic |

The M-H curves of the sintered sample at room temperature are displayed in Fig.3.20. It is clear from the figure that the sintered LNMO (x=0) sample gets highly magnetised at low fields and saturated at high fields, indicating the ferromagnetic behavior at room temperature with a saturation magnetisation of 20.7 emu/g. It exhibits a low value of a coercive field of 30 Oe and a remanent magnetisation of 0.75 emu/g near room temperature. The low value of coercivity and remanent magnetisation is due to the superparamagnetic phase of the LNMO sample. The monovalent substitution of $Na^+$ in La sites of lanthanum manganite plays a significant role in the conversion of $Mn^{3+}$ ions to $Mn^{4+}$ ions. Significantly, in the higher sodium substituted lanthanum manganite, the manganese exists in the mixed valence states of $Mn^{3+}$ and $Mn^{4+}$ [25]. The ferromagnetic behavior of the LNMO sample is attributed to the presence of Jahn Teller active $Mn^{3+}(4\mu_B)$ ions rather than

the $Mn^{4+}$ ions with a lower magnetic moment ($3\mu_B$), as well as the double exchange interaction between $Mn^{3+}$ -O- $Mn^{4+}$[23].

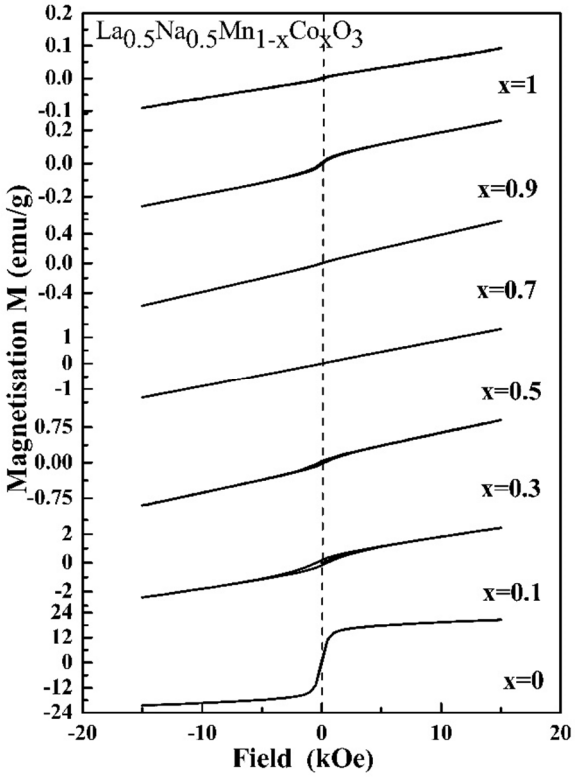


**Figure. 3.20.** M-H curves of sintered $La_{0.5}Na_{0.5}Mn_{1-x}Co_xO_3$ samples

The room temperature M-H curve depicts that the magnetic behaviour of the cobalt substituted samples changes from ferromagnetic to paramagnetic at room temperature, even with a small percentage of Co substitution for Mn. Fig.3.20 depicts a small hysteresis loop for the samples $x < 0.5$, completely paramagnetic behaviour for x=0.5 and x=0.7 samples and again a small hysteresis loop appeared for the samples $x > 0.7$. The hysteresis loop for the cobalt rich samples, LNCMO9 and LNCO is due to the coercivity of the cobalt. The magnetisation increases with an applied field for all samples, and the sample x = 0 attains saturation magnetisation at 15 kOe. When cobalt is substituted in the B site, the samples do not attain saturation magnetisation even at 15 kOe. The non-saturating behaviour of these

samples at higher external fields can be explained by the dominance of antiferromagnetic super exchange interactions of $Mn^{4+}$- $Mn^{4+}$[40], $Co^{3+}$-O-$Co^{2+}$ and which is the characteristic magnetic behaviour of lanthanum cobaltite perovskite materials. The magnetic parameters estimated from the room temperature magnetisation curves of the $La_{0.5}Na_{0.5}Mn_{1-x}Co_xO_3$ samples are listed in Table 3.6.

**Table 3.6.** Magnetic parameters of sintered $La_{0.5}Na_{0.5}Mn_{1-x}Co_xO_3$ at room temperature.

| Sample | $M_{max}$ (emu/g) | $H_c$ (Oe) | $M_r$ (emu/g) | Magnetic Behaviour @300K |
|---|---|---|---|---|
| **LNMO** | 20.7 | 30 | 0.75 | Ferromagnetic |
| **LNCMO1** | 2.42 | 410 | 0.19 | Antiferromagnetic |
| **LNCMO3** | 1 | 214 | 0.04 | Antiferromagnetic |
| **LNCMO5** | 1.31 | - | 0.007 | Paramagnetic |
| **LNCMO7** | 0.57 | - | - | Paramagnetic |
| **LNCMO9** | 0.26 | 75 | 0.006 | Antiferromagnetic |
| **LNCO** | - | - | - | Paramagnetic |

The variation of maximum magnetisation shown in Fig. 3.21 indicates that it is maximum for the x=0 sample, then it decreases abruptly even for the initial concentration of cobalt. For the cobalt substituted manganite system, generally, the Co ions are randomly distributed in the Mn site, destroying the double exchange interaction between $Mn^{3+}$-O-$Mn^{4+}$. With the cobalt substitution in LNMO, charge ordering according to equation (3.1) reduces the double exchange interaction, and the presence of mixed valence states of Mn and Co results in a rapid decrease in saturation magnetisation [30,41,42]. Among the LNCMO samples, the magnetisation is maximum for the LNMO sample due to the double exchange interaction. For the initial concentration of cobalt for x<0.5, increase in the sodium volatilisation decreases the number of $Mn^{4+}$ ions and double exchange interaction resulting in the

reduction in magnetisation. However, in the case of cobalt -rich samples (x>0.5) also, we observed a reduction in magnetisation. As more $Mn^{3+}$ ions are replaced by $Co^{3+}$ ions, the double exchange interaction decreases along with the increase in antiferromagnetic interaction between $Co^{3+}$- $Co^{2+}$ resulting in the observed magnetic behaviour of the samples. So, in this $La_{0.5}Na_{0.5}Mn_{1-x}Co_xO_3$ samples, LNMO (x=0) exists in both superparamagnetic and ferromagnetic phases, while the cobalt substituted samples exist in ferromagnetic/paramagnetic phases at room temperature. A phase coexistence including a ferromagnetic cluster, an antiferromagnetic cluster, and superparamagnetic-like spins is reported in lanthanum sodium manganite when cobalt is substituted [36].

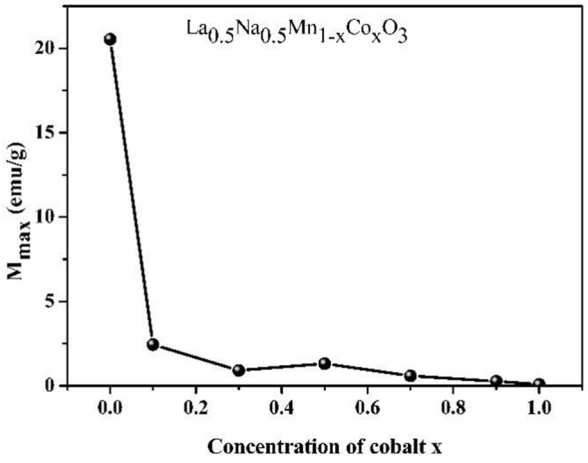


**Figure. 3.21.** Variation of maximum magnetisation with x of sintered $La_{0.5}Na_{0.5}Mn_{1-x}Co_xO_3$

The room temperature magnetisation curves reveal that the coercivity is observed to be small for $La_{0.5}Na_{0.5}Mn_{1-x}Co_xO_3$ (x=0), and is increased for samples with x=0.1 and x=0.3. (Table 3.6). With further increase in the cobalt substitution, coercivity decreases to a value nearly zero indicating the paramagnetic behaviour for x > 0.5 samples.

The M-H curves of the samples recorded before and after sintering, shown in Figs. 3.19 and. 3.20, respectively are compared to study the effect of sintering on the magnetic properties of these samples. It has been observed that the Mn-rich samples

in the as prepared series are paramagnetic in nature at room temperature while the Co-rich samples show ferromagnetic behaviour. However, the sintered samples exhibited a ferromagnetic to paramagnetic change in magnetic behaviour with an increase in cobalt concentration at room temperature. This can be attributed to the structural phase formation of the $La_{0.5}Na_{0.5}Mn_{1-x}Co_xO_3$ samples on sintering at high temperatures. As the cobalt substituted samples (x=0.1 to 1) exhibit paramagnetic behaviour at room temperature, there can be a magnetic transition below room temperature. M-T measurements can be employed to investigate further magnetic properties at lower temperatures (Refer Chapter 4).

### *3.3.6 Dielectric Characterisation*

The dielectric properties are crucial for applications involving electrical devices because they quantify the capacity of a substance to hold electric charges. The literature suggests that there are numerous research works on the magnetic properties of cation substituted lanthanum manganites, whereas only a few reports are on the dielectric properties of lanthanum manganites. R. Majumder *et. al.* reported the low value of the dielectric constant of sodium doped lanthanum manganite synthesised by a flux method[31]. M. A. A. Bally *et al*. reported a high value of the real part of the dielectric constant at lower temperatures and a metallic transition near room temperature for $La_{0.7}Ca_{0.2}Pb_{0.1}CoO_3$ [43] I. A. Abdel-Latif *et. al.* reported the frequency and temperature dependent dielectric properties of $Nd_{0.6}Sr_{0.4}Mn_xCo_{1-x}O_3$ composites. S.E.L. Kossi *et al*. reported the enhanced dielectric properties of strontium doped lanthanum manganite [44]. According to the literature review, the lanthanum manganite and cobaltite exhibit dielectric properties. So, we have investigated the dielectric properties of the synthesised sintered $La_{0.5}Na_{0.5}Mn_{1-x}Co_xO_3$ samples. The frequency and temperature dependent dielectric measurements are probed to check the transition, if any, exhibited by the LNMO sample near and above room temperatures. The frequency-dependent dielectric properties of the

sintered $La_{0.5}Na_{0.5}MnO_3$ were measured in a frequency range of 100 Hz to 8 MHz by an LCR meter at different temperatures above room temperature. The dielectric constant was estimated by employing the formula [45].

$$\varepsilon_r = \frac{C\,d}{\varepsilon_0 A} \tag{3.2}$$

where C is the capacitance of the parallel plate capacitor, d is the thickness of the dielectric medium, A is the area of the plate, and $\varepsilon_0$ is the permeability of free space.

The ac conductivity ($\sigma_{ac}$) defines the ability of a material to conduct an electrical current when an alternating field is applied. Any capacitor, when charged under an AC voltage will have a loss current due to ohmic resistance or impedance by heat absorption. $\sigma_{ac}$ is given by the relation.

$$\sigma_{ac} = \frac{J}{E} \tag{3.3}$$

where, J is the current density and E is the electric field. It can also be calculated from the loss factor (tanδ), and dielectric constant ($\varepsilon_r$) using the relation [46]

$$\sigma_{ac} = 2\pi f tan\delta\varepsilon' \tag{3.4}$$

where f is the frequency of the applied field and $\varepsilon'$ is the real part of the dielectric constant or dielectric permittivity given by

$$\varepsilon' = \varepsilon_0\varepsilon_r. \tag{3.5}$$

The loss factor or dissipation factor in any dielectric material is given by the relation

$$tan\delta = \frac{\varepsilon''}{\varepsilon'} \tag{3.6}$$

where $\varepsilon''$ is the imaginary part of the dielectric constant.

The variation of capacitance and dielectric constant with frequency and temperature of the sintered LNMO sample is shown in Fig 3.22 and Fig. 3.23, respectively.

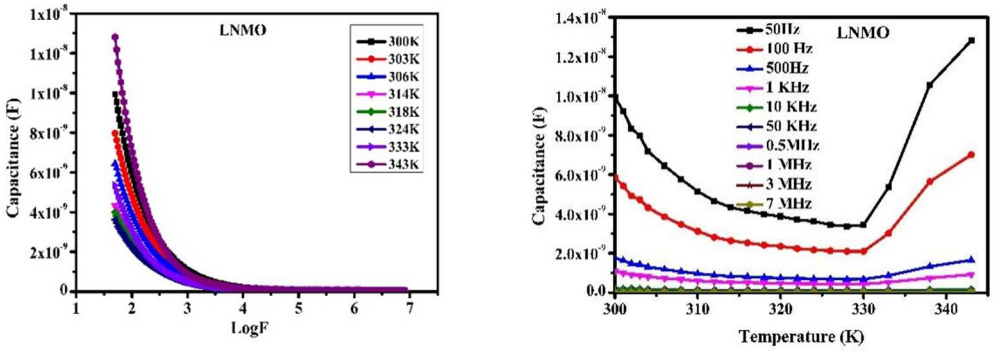


(a) (b)

**Figure 3.22.** (a) Variation of capacitance with (a) LogF (b) Temperature for $La_{0.5}Na_{0.5}MnO_3$

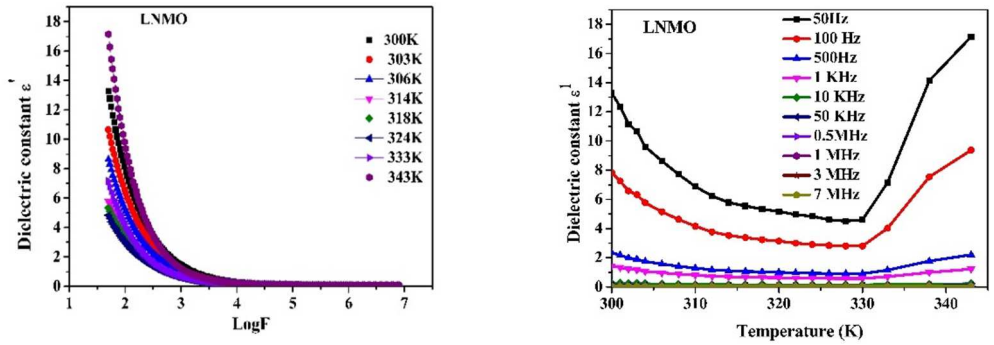


(a) (b)

**Figure 3.23.** Variation of dielectric constant with (a) LogF (b) Temperature for $La_{0.5}Na_{0.5}MnO_3$

It is clear from the figure that the capacitance and dielectric constant decrease with an increase in frequency. At the lower frequencies of 100 Hz, the sample exhibits a maximum value of dielectric constant, and then it decreases at higher frequencies, which is a characteristic behaviour of ferromagnetic material. The dielectric constant decreases sharply from 100Hz to 3MHz and thereafter decreases slowly with frequency while it shows almost frequency-independent behaviour at high-frequency regions [45]. The maximum value of the dielectric constant at low frequencies is due to the bulk polarization of the sample. The variation of dielectric constant with frequency can be explained based on space-charge polarization and

Maxwell-Wagner interfacial polarization [47]. According to this model, dielectric material has well-conducting grains separated by high resistive grain boundaries. When an electric field is applied, space charge accumulates at the grain boundaries, and voltage drops mainly at the boundaries. According to the Maxwell-Wagner model, space charge polarisation arises because of the inhomogeneous dielectric structure of the materials[48]. The grain boundaries are more effective at lower frequencies, whereas grains perform better at higher frequencies.

The LNMO sample exhibits frequency independent behaviour at higher frequencies, which can be due to the charge carriers that cause distinct polarization mechanisms. The dielectric constant of any material is affected by the dipolar, electronic, ionic, and interfacial polarizations. Dipolar and ionic polarizations are effective to the dielectric constant at low frequencies, whereas electronic polarization contributes more at higher frequencies[49]. The frequency-independent behaviour of dielectric permittivity is attributed to the absence of space charge polarization[50]. In the present work, the LNMO sample exhibited a maximum value of the dielectric constant of 17 at 343 K and at room temperature, its value is 13. This value of the dielectric constant is greater than the reported value of lanthanum sodium manganite [31]. Norah Alhokbany *et.al.* reported the dielectric properties of lanthanum strontium cobaltite with a low value of dielectric constant [2]. Materials with low values of dielectric constant can be used in printed circuit board materials [51] . It can also be used for high-frequency applications in electric circuits to minimise dielectric losses.

A significant variation of dielectric loss with temperature has been observed at lower frequencies, which is displayed in Fig. 3.24.

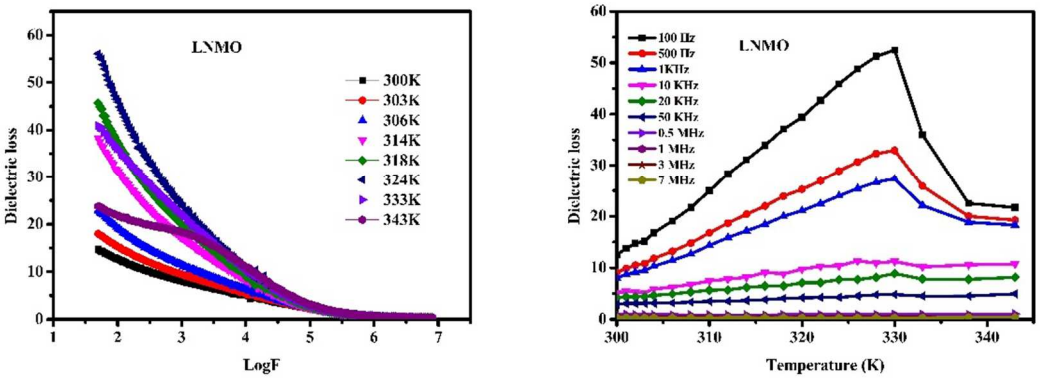


(a) (b)

**Figure 3.24.** Variation of Dielectric loss with (a) Log F (b) Temperature for $La_{0.5}Na_{0.5}MnO_3$.

. The dielectric loss has been measured in a frequency range of 100 Hz to 8 MHz at temperatures from 300 K to 350 K. It was observed that the dielectric loss decreases rapidly at lower frequency ranges and shows a frequency independent behaviour at higher frequencies. This variation of dielectric loss with frequency indicates the dielectric dispersion.

The ac conductivity measured as a function of frequency and temperature is shown in Fig 3.25.

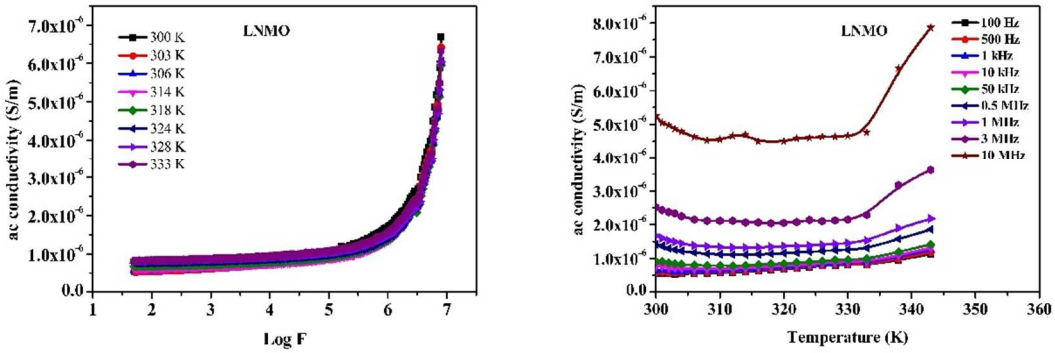


(a) (b)

**Figure 3.25.** Variation of ac conductivity with (a) Log F (b) Temperature for $La_{0.5}Na_{0.5}MnO_3$

It is observed from the figure that the ac conductivity increases with an increase in frequency. On increasing the frequency of the applied field, the hopping carriers increase and thereby increase the conductivity of the material. This variation of ac conductivity with frequency may also be explained by the Koop's phenomenological theory[52]. In all the variations of dielectric characteristics like dielectric constant, ac conductivity, and dielectric loss with the temperature, a variation is observed at a particular temperature around 330 K. This temperature suggests a phase transition associated with the sample. A similar type of phase transition near room temperature is reported to be associated with ferromagnetic to paramagnetic phase transition or metal to insulator phase transition in lanthanum manganites[53].

## 3.4. Conclusion

Cobalt substituted lanthanum sodium manganite $La_{0.5}Na_{0.5}Mn_{1-x}Co_xO_3$ (x=0-1) has been synthesised by the sol-gel auto-combustion method. Compared to other perovskite manganite materials, the LNCMO samples in the present work were sintered only for 6 hours at 1000°C which is relatively a very short duration. Structural investigation of the as prepared and sintered $La_{0.5}Na_{0.5}Mn_{1-x}Co_xO_3$ samples was carried out by X-ray diffraction, Rietveld refinement, FTIR spectrum and TEM images. The as prepared samples crystallised in the orthorhombic structure, and the phase formation was not complete in the cobalt rich (x>0.5) as prepared samples. The sintered samples crystallised in the rhombohedral symmetry and the best fit with the least difference was obtained for these samples using Rietveld refinement. The lattice parameter decreased from $a = 5.489$ Å to 5.444 and $c = 13.320$ Å to 13.095 Å when Mn was substituted with Co in lanthanum sodium manganite. HRTEM measurements confirmed the nanocrystalline behaviour of the synthesised particles. The stoichiometric ratio of La/Na was consistent with the theoretical value for the as prepared samples, whereas, in the sintered samples, the Mn-rich (x < 0.5) samples exhibit volatilisation of Na, resulting in a La/Na ratio, which exceeds the theoretical value. The incorporation of $Mn^{3+}$ for $Co^{3+}$ in the B lattice has been confirmed in all the samples from the EDAX spectrum. Magnetic

properties of the as-prepared and sintered samples have been investigated by the M-H curves. In the as prepared $La_{0.5}Na_{0.5}Mn_{1-x}Co_xO_3$ , Mn rich samples ($x< 0.5$) exhibits a paramagnetic behaviour while cobalt-rich samples show high magnetisation value with a small hysteresis loop due to the presence of cobalt nanoparticles. In the sintered series of samples, LNMO ($x = 0$) exhibits superparamagnetic behaviour with a significant magnetisation and low values of remanence and coercivity at room temperature. In the cobalt substituted sintered samples LNCMO, Mn rich samples are found to be less magnetic than LNMO while Co rich samples are mostly paramagnetic at room temperature. The temperature-dependent dielectric measurements of LNMO samples show a phase transition associated with the sample at 330 K. The LNMO sample can be used in electric circuits and printed circuit board materials due to its low dielectric constant. It is observed from the structural and magnetic properties that all the sintered samples in the $La_{0.5}Na_{0.5}Mn_{1-x}Co_xO_3$ form a complete phase as that of perovskite manganite. So, further investigations of the temperature-dependent magnetic characteristics and magnetocaloric properties of $La_{0.5}Na_{0.5}Mn_{1-x}Co_xO_3$ samples have been conducted in the sintered samples.

## REFERENCES

[1] M. Saleem, D. Varshney, RSC Adv 8 (2018) 1600–1609.

[2] N. Alhokbany, S. Almotairi, J. Ahmed, S.I. Al-Saeedi, T. Ahamad, S.M. Alshehri, J King Saud Univ Sci 33 (2021) 101419.

[3] G. Venkataiah, V. Prasad, P. Venugopal Reddy, J Alloys Compd 429 (2007) 1–9.

[4] S.S. Shah, K. Hayat, S. Ali, K. Rasool, Y. Iqbal, Mater Sci Semicond Process 90 (2019) 65–71.

[5] N.S. Rogado, J. Li, A.W. Sleight, M.A. Subramanian, Advanced Materials 17 (2005) 2225–2227.

[6] I. Zeydi, A. Zaidi, J. Dhahri, E.K. Hlil, J Magn Magn Mater 471 (2019) 529–536.

[7] Y. Kalyana Lakshmi, G. Venkataiah, M. Vithal, P. Venugopal Reddy, Physica B Condens Matter 403 (2008) 3059–3066.

[8] D.T. Morelli, A.M. Mance, J. V. Mantese, A.L. Micheli, J Appl Phys 79 (1996) 373–375.

[9] A.O. Turky, M.M. Rashad, A.M. Hassan, E.M. Elnaggar, M. Bechelany, Physical Chemistry Chemical Physics 19 (2017) 6878–6886.

[10] M. Koubaa, W.C.R. Koubaa, A. Cheikhrouhou, J Alloys Compd 479 (2009) 65–70.

[11] K. Laajimi, M. Khlifi, E.K. Hlil, M.H. Gazzah, J. Dhahri, J Magn Magn Mater 491 (2019) 165625.

[12] I. Walha, M. Smari, T. Mnasri, E. Dhahri, J Magn Magn Mater 454 (2018) 190–195.

[13] M. Suemitsu, T. Nakagawa, Y. Hirayama, S. Seino, T.A. Yamamoto, J Alloys Compd 551 (2013) 195–199.

[14] M.W. Shaikh, D. Varshney, Mater Chem Phys 134 (2012) 886–898.

[15] M.Z. Ahsan, P.M.A. Ahsan, M.A. Islam, F.C. Asif, Results Phys 15 (2019) 102600.

[16] C.P. Reshmi, S. Savitha Pillai, K.G. Suresh, M.R. Varma, Solid State Sci 19 (2013) 130–135.

[17] A.S. Khan, M.F. Nasir, A. Humayun, Physica B Condens Matter 550 (2018) 1–8.

[18] N. Sethulakshmi, I.A. Al-Omari, K.G. Suresh, M.R. Anantharaman, Appl Phys Lett 104 (2014).

[19] L. Malavasi, M.C. Mozzati, S. Polizzi, C.B. Azzoni, G. Flor, Chemistry of Materials 15 (2003) 5036–5043.

[20] M. V. Kuznetsov, I.P. Parkin, D.J. Caruana, Y.G. Morozov, Mendeleev Communications 16 (2006) 36–38.

[21] D. Varshney, N. Dodiya, J Mater Res 29 (2014) 1183–1198.

[22] S.B. Kansara, D. Dhruv, B. Kataria, C.M. Thaker, S. Rayaprol, C.L. Prajapat, M.R. Singh, P.S. Solanki, D.G. Kuberkar, N.A. Shah, Ceram Int 41 (2015) 7162–7173.

[23] M.H. Phan, T.L. Phan, S.C. Yu, N.D. Tho, N. Chau, Phys Status Solidi B Basic Res 241 (2004) 1744–1747.

[24] A. Jerbi, A. Krichene, N. Chniba-Boudjada, W. Boujelben, Physica B Condens Matter 477 (2015) 75–82.

[25] N. Sethulakshmi, I.A. Al Omari, M.R. Anantharaman, Bulletin of Materials Science 38 (2015) 1545–1552.

[26] J.B. Goodenough, A. Wold, R.J. Arnott, N. Menyuk, Physical Review 124 (1961) 373–384.

[27] J.B. Yang, M.S. Kim, T.F. Creel, H. Zhao, X.G. Chen, W.B. Yelon, W.J. James, Perovskite Materials, Chapter 3, Intech Open, (2016)

[28] S.K. Estemirova, V.Y. Mitrofanov, S.A. Uporov, R.I. Gulyaeva, J Magn Magn Mater 502 (2020) 166593.

[29] M. Oumezzine, O. Peña, T. Guizouarn, R. Lebullenger, J Magn Magn Mater 324 (2012) 2821–2828.

[30] A. Kumar1, C.V.T. and A.D. Thakur1, Apply. Phy.A, 3 (2024) 0–12.

[31] R. Majumder, M.A.R. Sarker, M.M. Hossain, M.E. Hossain, D. Shen, A.K.M.S. Reza, M.H. Kabir, Journal of Scientific Research 11 (2019) 195–207.

[32] S. Roy, Y.Q. Guo, S. Venkatesh, N. Ali, J.Phy.Condens. Matter, 13 9547 (2001) 9547

[33] V.A. Ferby, A.M.E. Raj, M. Bououdina, Appl Phys A Mater Sci Process 126 (2020) 1–8.

[34] R. Tetean, I.G. Deac, E. Burzo, A. Bezergheanu, J Magn Magn Mater 320 (2008) 179–182.

[35] M. Wali, R. Skini, M. Khlifi, E. Dhahri, E.K. Hlil, J Magn Magn Mater 394 (2015) 207–211.

[36] N. Gayathri, A. Raychaudhuri, S. Tiwary, R. Gundakaram, A. Arulraj, C. Rao, Phys Rev B Condens Matter Mater Phys 56 (1997) 1345–1353.

[37] A. Gholizadeh, A. Gholizadeh, Journal of Advanced Materials and Processing 3 (2015) 71–83.

[38] M.B. Bellakki, C. Madhu, T. Greindl, S. Kohli, P. McCurdy, V. Manivannan, Rare Metals 29 (2010) 491–500.

[39] G. Pecchi, C. Campos, M.G. Jiliberto, Y. Moreno, O. Peña, J Mater Sci 43 (2008) 5282–5290.

[40] M.A. Gdaiem, S. Ghodhbane, A. Dhahri, J. Dhahri, E.K. Hlil, J Alloys Compd 681 (2016) 547–554.

[41] O. Toulemonde, F. Studer, B. Raveau, Solid State Commun 118 (2001) 107–112.

[42] J.M.D. Coey, M. Viret, S. Von Molnár, Adv Phys 48 (1999) 167–293.

[43] M.A.A. Bally, M.Z. Ahsan, M.A. Islam, M.K. Alam, F.A. Khan, AIP Adv 10 (2020).

[44] S. EL Kossi, C. Rayssi, A.H. Dhahri, J. Dhahri, K. Khirouni, J Alloys Compd 767 (2018) 456–463.

[45] B.C. Babu, V. Naresh, B.J. Prakash, S. Buddhudu, Ferroelectrics, Letters Section 38 (2011) 114–127.

[46] E. Veena Gopalan, K.A. Malini, S. Saravanan, D. Sakthi Kumar, Y. Yoshida, M.R. Anantharaman, J Phys D Appl Phys 41 (2008).

[47] N. Rezlescu, E. Rezlescu, Physica Status Solidi (a) 23 (1974) 575–582.

[48] M. Raghasudha, D. Ravinder, P. Veerasomaiah, Materials Sciences and Applications 04 (2013) 432–438.

[49] I.A. Abdel-Latif, A.M. Ahmed, H.F. Mohamed, S.A. Saleh, J.A. Paixão, K.A. Ziq, M.K. Hamad, E.G. Al-Nahari, M. Ghozza, S. Allam, J Magn Magn Mater 457 (2018) 126–134.

[50] S. Mohanty, R.N.P. Choudhary, R. Padhee, B.N. Parida, Ceram Int 40 (2014) 9017–9025.

[51] J. Balde, G. Messner, Circuit World 14 (1987) 11–14.

[52] C.G. Koops, Physical Review 83 (1951) 121–124.

[53] K. Yi, Q. Tang, Z. Wu, X. Zhu, Nanomaterials 12 (2022) 1–20.

…..ര*ര…..

# Chapter 4

# Tuning the Magnetocaloric Properties of $La_{0.5}Na_{0.5}MnO_3$ and $La_{0.5}Na_{0.5}Co_xMn_{1-x}O_3$ Nanoparticles

## Objectives

The magnetocaloric properties of the perovskite Lanthanum Sodium Manganite ($La_{0.5}Na_{0.5}MnO_3$) and cobalt-substituted Lanthanum Sodium Manganite nanoparticles ($La_{0.5}Na_{0.5}Co_xMn_{1-x}O_3$) are investigated using the calculated $\Delta S_m$ characteristic values from magnetic isotherms recorded around the transition temperature. The critical behaviour of the magnetic transition is analysed using the Arrott plot, the Kouvel-Fischer approach and critical isotherm.

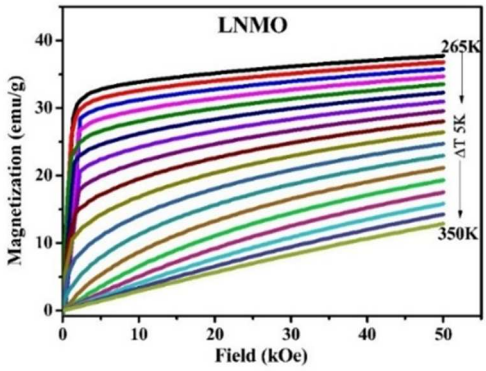


S. Bhaskaran, Laveena Varghese, V S Sharon, K A Malini, E Veena Gopalan, Probing the Near Room Temperature Magnetocaloric Properties and Critical Behaviour in Sol-gel Synthesized Lanthanum Sodium Manganite Nanoparticles, J Alloys Compd, (2025),184097. https://doi.org/10.1016/j.jallcom.2025.184097

## 4.1 Introduction

Magnetic refrigeration based on the magnetocaloric effect is becoming an emerging technology to replace conventional gas compression refrigeration as it is environmentally friendly, compact and highly efficient[1]. The magnetocaloric effect (MCE) is an intrinsic thermodynamic property of magnetic material arising because of the coupling of magnetic sublattice with the magnetic field. When a magnetic field is applied to a ferromagnetic material, the magnetic moments are aligned in the direction of the applied field, resulting in a decrease in magnetic spin entropy accompanied by an increase in lattice entropy. Inversely the adiabatic demagnetisation increases the magnetic spin entropy, which results in a decrease in lattice entropy and causes the system to cool down. The potential magnetocaloric materials are characterized by large isothermal magnetic entropy change, $\Delta S_m$, and large adiabatic temperature change $\Delta T_{ad}$ over a wide temperature range[2,3]. Significant relative cooling power (RCP) and high magnetic entropy change values at low external magnetic fields are features of a potential magnetocaloric material for room-temperature magnetic refrigerant applications. [4,5]. These properties are typically found to be enhanced at or near magnetic transition temperature ($T_c$) where the ordering results in a rapid reduction in magnetisation which can manifest as a large magnetic entropy change.

The nature of magnetic transition also plays an important role in deciding the working temperature of magnetic refrigerant materials. Even though a giant MCE has been exhibited mostly by materials with the first-order magnetic transitions, the associated undesirable intrinsic thermal and magnetic hysteresis inevitability results in low energy efficiency during cooling cycles, limiting the practical applications of these materials. It is noteworthy that the second order transition is typically spread over a large temperature range, which is preferable for active magnetic refrigerants, whereas the first order transition can focus the magnetocaloric effect over a small temperature range[6]. Apart from the magnetic refrigerant applications magnetic

materials with large MCE have gathered considerable attention for antimicrobial properties in biomedical applications[7] and magnetic hyperthermia applications[8,9].

Magnetocaloric materials exhibiting large MCE near room temperature are usually desired in room-temperature magnetic refrigerant technology. Hence, to obtain an MCE near room temperature, a magnetic material with an ordering temperature near room temperature will be the most suitable choice. Perovskite-type manganese oxide materials with an $ABO_3$ structure exhibiting large MCEs are expected to be good candidates for magnetic refrigeration at various temperatures because of the magnetic properties like large saturation magnetisation and tunable Curie temperature. The double exchange/super exchange mechanism between mixed valence states of Mn ions and the strong spin-lattice coupling underlie the magnetism in a manganite. The doping or substitution of cations in the A lattice can affect the $Mn^{3+}$ –$O^{2-}$ -$Mn^{4+}$ double exchange inside the perovskite manganite, thereby causing changes in the Curie temperature $T_c$, the maximum magnetic entropy change $\Delta S_m$ and the relative cooling efficiency. The ferromagnetic to paramagnetic (FM to PM) transition, which occurs at high temperatures normally accompanied by the metal-insulator transition in doped manganite, is a promising feature for an MCE material [10]. Among the manganite perovskite materials, lanthanum manganite with the $ABO_3$ structure and its compounds exhibit a large MCE near room temperature, which can be comparable with gadolinium [11–14]. The monovalent substitution in the A site of lanthanum manganites introduces the mixed valence state of $Mn^{3+}$/$Mn^{4+}$ pairs, which contributes to ferromagnetism in manganites. The conversion rate of $Mn^{3+}$ to $Mn^{4+}$ and, hence, hole density in monovalent substitution is twice that for the equivalent concentration of divalent substitution. The higher substitution of Na in the La site contributes to the magnetic interaction by the double exchange interaction and the induced vacancies in the La or O sites play an important role in the magnetic ordering.

Many researchers have investigated the magnetocaloric properties of divalent ion substituted lanthanum manganite[6,13]. However, there are only a few reports on the study of the MCE properties of monovalent sodium substitution in the A site of lanthanum manganite. The review of the literature survey suggests that the Curie temperature can be modified by monovalent Na doping in the A site of lanthanum manganite [15–17]. F. Ayadi *et al*. reported a maximum entropy change $\Delta S_m$ of 1.93 $Jkg^{-1}K^{-1}$ in a magnetic field of 2T at 350 K in $La_{0.7}Sr_{0.2}Na_{0.1}MnO_3$[16]. M. Koubaa *et al*. reported a $\Delta S_m$ of 2.26 $Jkg^{-1}K^{-1}$ in a magnetic field of 2T in $La_{0.75}Ba_{0.1}Na_{0.15}MnO_3$[19]. S.Choura Maatar *et al.* reported a $\Delta S_m$ of 2.3 $Jkg^{-1}K^{-1}$ in a magnetic field of 2T at 330 K in $La_{0.8}Na_{0.2}MnO_3$[17]. Sethulakshmi *et al*. reported a maximum magnetic entropy change of 1.5 $Jkg^{-1}K^{-1}$ near room temperature in a magnetic field of 5T [19]. The literature shows that the critical magnetic behaviour analysis using modified Arrott's plot Kouvel Fischer approach and critical isotherm analysis can result in a better understanding of MCE near the magnetic ordering temperature[20–24].

In the present work, the MCE properties of the monovalent sodium substituted (in A site) Lanthanum manganite (LNMO) and the series $La_{0.5}Na_{0.5}Mn_{1-x}Co_xO_3$ (x=0, 0.1, 0.3, 0.5, 0.7, 0.9 & 1) (LNCMO) in which the trivalent cobalt ion is substituted for manganese ion in the B site of lanthanum sodium manganite are investigated. The synthesis, structural and magnetic properties of the samples are described in Chapter 3. In this chapter, the MCE properties of the as-prepared pristine and sintered LNMO and $La_{0.5}Na_{0.5}Mn_{1-x}Co_xO_3$ (LNCMO) samples are compared. A theoretical understanding of the temperature dependent magnetic phase transitions observed in the samples is carried out for appropriate samples, and attempts are made to corroborate the results with the temperature dependent magnetic properties. MCE properties of the parent sample $La_{0.5}Na_{0.5}MnO_3$ (LNMO) and cobalt substituted $La_{0.5}Na_{0.5}Mn_{1-x}Co_xO_3$ (LNCMO) samples are presented here as different sections. The different steps involved in the MCE characterisation of the samples are detailed in Chapter 2. (Section 2.5.4).

## 4.2 Magnetocaloric properties of Lanthanum Sodium Manganite *($La_{0.5}Na_{0.5}MnO_3$ -LNMO)*

The MCE characteristics of the parent sample $La_{0.5}Na_{0.5}MnO_3$ (LNMO) are investigated in detail for the as prepared and sintered cases as it exhibited good structural and magnetic characteristics. As an initial step, ZFC-FC measurements have been performed in a temperature range of 10 K to 400 K to determine the transition temperature. Followed by the temperature-dependent measurements, the magnetisation isotherms will be recorded in the vicinity of the observed transition temperature. The characteristic property of MCE, isothermal magnetic entropy change, is estimated from the magnetic isotherms at different temperatures using the equation (1.20).

### *4.2.1 ZFC-FC Measurements*

The magnetic properties of the $La_{0.5}Na_{0.5}MnO_3$, LNMO, samples (as prepared and sintered) are studied from the temperature-dependent magnetisation curves (M-T) in Field Cooled and Zero Field Cooled conditions under an applied magnetic field of 100 Oe. The ZFC and FC curves of the as prepared LNMO sample are displayed in Fig. 4.1, and its derivative plot is shown in the inset of the figure. The temperature-dependent magnetisation curves were recorded in zero field cooling (ZFC) and field cooling (FC) in a temperature range of 2 K – 300 K for as prepared LNMO samples. In general, in the ZFC measurement, the sample was cooled from 300K to 5K without any applied field. Then, reaching 5K, magnetisation was measured upon warming in a desired applied field. In FC measurements, the sample was cooled from 300 K to 5 K with an applied magnetic field, and magnetic measurements were taken as same as in ZFC measurements.

The temperature-dependent magnetisation curve of LNMO (as prepared), shown in Fig.4.1, reveals that a maximum magnetisation value has been observed at low temperatures and decreases with an increase in temperature. It is evident from the ZFC-FC curve of as-prepared LNMO that, compared to the ZFC curve, the

magnetisation has a rapid increase with the application of an external dc magnetic field (FC curve). Furthermore, the FC curve shows a steep decrease in magnetisation when the temperature rises, which cannot be observed in the case of the ZFC curve, even though a peak corresponding to maximum magnetisation is noticeable towards 135 K in the ZFC curve. The bifurcation of the FC and ZFC curves in this region indicates the superparamagnetic behaviour of the LNMO sample below its blocking temperature. The smaller coercivity value and the moderate magnetisation of this sample agree with the chance of blocking temperature near 155 K. The blocking temperature is estimated from the inflexion point of the derivative plot of -(ZFC-FC). Although the sample has a paramagnetic behaviour at room temperature (Fig. 3.19 in chapter 3) it has an increasing magnetisation at lower temperatures and a transition around 155 K which can correspond to a superparamagnetic phase.

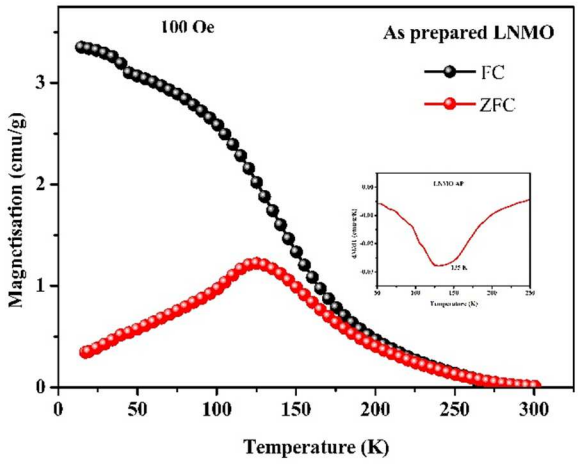


**Figure 4.1.** ZFC-FC curves of $La_{0.5}Na_{0.5}MnO_3$ (As prepared)

The ZFC-FC magnetisation of the sintered LNMO sample shown in Fig.4.2 depicts a significant decrease in the magnetic moment at higher temperatures, attributed to a ferromagnetic (FM) to paramagnetic (PM) phase transition. The ZFC curve attains a maximum magnetisation value at 276 K, followed by a steep decrease in magnetisation, indicating a very sharp transition. It is observed that at lower

temperatures, ZFC magnetisation values are lower than FC values, indicating that the applied field enhances the FM response. The divergence of $M_{FC}$ and $M_{ZFC}$ curves below $T_c$ is typically exhibited by the perovskite manganites [25]. In ferromagnets, the absolute value of the derivative of magnetisation with respect to temperature $\left|\frac{dM}{dT}\right|$ is a minimum at $T_c$ (Curie Temperature) [18]. The $\left|\frac{dM}{dT}\right|$ versus temperature graph of the LNMO sample shown in the inset displays a minimum value at 324 K, which corresponds to the transition temperature $T_c$ at which the sample exhibits a ferromagnetic to paramagnetic transition.

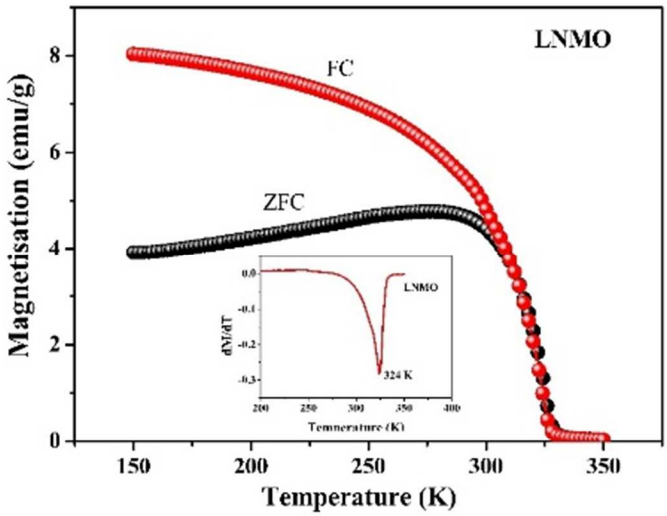


**Figure 4.2** ZFC-FC curves of sintered $La_{0.5}Na_{0.5}MnO_3$

The peak corresponds to the maximum magnetisation in the ZFC curve can be due to the presence of the superparamagnetic clusters associated with the sample. The blocking temperature is identified at 304 K from the derivative plot of –(ZFC-FC) curve of the LNMO sample, which confirms the presence of superparamagnetic clusters near the transition temperature. The magnetic properties, coercivity $H_c$ (30 Oe), saturation magnetisation $M_s$ (20.6 emu/g), and remanence $M_r$ (0.75 emu/g) estimated from the hysteresis loop described in Chapter 3 agree well with the room temperature superparamagnetic behaviour of the LNMO sample.

### 4.2.2 *Magnetisation Isotherm Curves*

The magnetisation isotherms of LNMO samples (as prepared and sintered) were recorded to study the magnetocaloric properties in the temperature range of 150 K–300 K. It is observed from the magnetisation isotherms of the as-prepared LNMO sample shown in Fig.4.3. that the magnetisation increases at low field levels at lower temperatures without being saturated even at a higher magnetic field of 50 kOe, which is attributed to a weak ferromagnetic behaviour. As temperature increases, the ferromagnetic behaviour diminishes, and linear dependency of magnetisation with magnetic field is found to be dominant, which shows that the material is paramagnetic at room temperature.

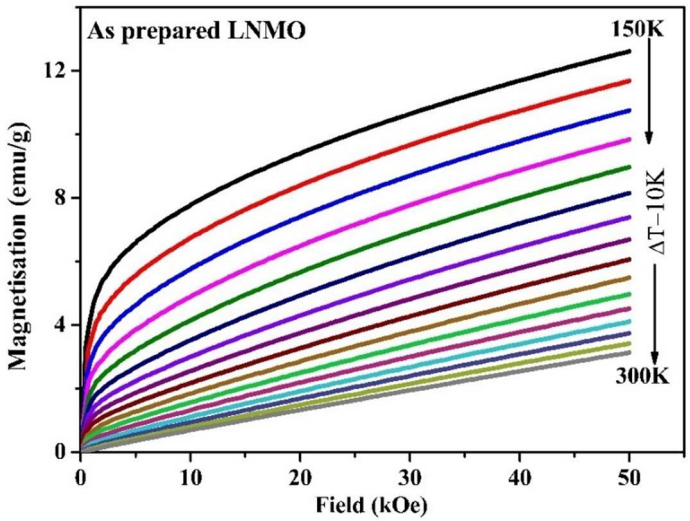


**Figure 4.3.** Magnetisation Isotherms of as prepared $La_{0.5}Na_{0.5}MnO_3$.

The magnetisation isotherms of the sintered LNMO sample are shown in Fig.4.4. Since the estimated Curie temperature was around 324 K, the isotherms were taken in a temperature range of 265 K – 350 K in steps of 5 K. It is evident from the figure that the magnetisation exhibits a nonlinear behaviour with a sharp increase at low field for $T < T_c$. The magnetisation increases with the applied fields around the magnetic transition and approaches saturation at higher field values, exhibiting a ferromagnetic behaviour. This is attributed to the rotation of magnetic domains under

the application of magnetic fields, which get polarised completely along the direction of the field[20]. For temperatures $T > T_c$, the thermal energy becomes strong enough to overcome the exchange interactions that keep the magnetic moments aligned. Consequently, the magnetisation decreases significantly with an almost linear behaviour, corresponding to the paramagnetic state (PM) and follows Curie Weiss Law.

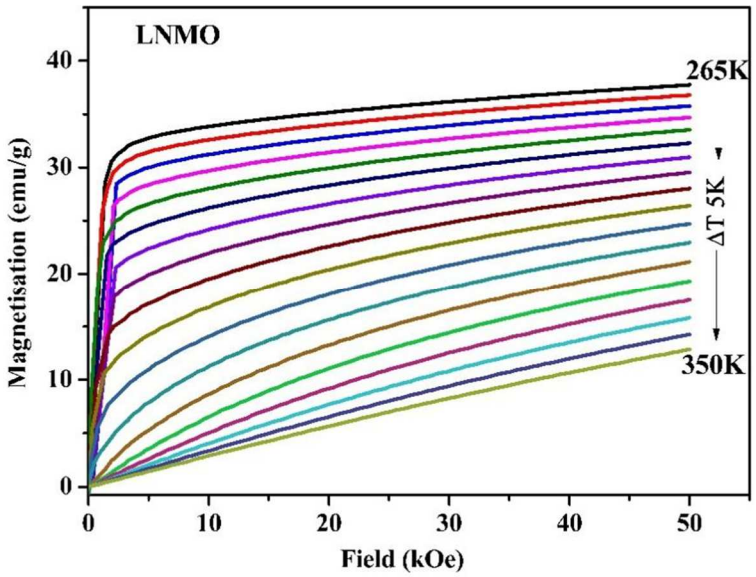


**Figure 4.4.** Magnetisation isotherms of sintered $La_{0.5}Na_{0.5}MnO_3$.

The sintered LNMO sample with excellent structural properties is expected to exhibit large MCE near room temperature due to its considerable increase in magnetisation observed at a high magnetic field (50 kOe) and a decrease in magnetisation with temperature near $T_c$. Consequently, magnetisation isotherms can be employed to investigate the magnetocaloric characteristics of LNMO samples near the transition temperature under an applied magnetic field of 50 kOe.

### 4.2.3 Magnetic entropy change ($-\Delta S_m$)

The MCE properties of a magnetic material can be investigated employing theoretical and experimental approaches. It can be experimentally evaluated by employing magnetisation measurements or calorimetric measurements. Generally, the MCE characteristics can be evaluated either from the variation of adiabatic temperature in the presence of a magnetic field or from the magnetic entropy change $\Delta S_m$ from M-H isotherms at different temperatures (Chapter 1, Section 1.5).

The magnetic entropy change under different magnetic fields can be evaluated by equation (4.1).

$$\Delta S_{m\left(\frac{T_1+T_2}{2}\right)} = \frac{1}{T_2-T_1}\left\{\int_0^{H_{max}} M(T_2,H)dH - \int_0^{H_{max}} M(T_1,H)dH\right\} \quad (4.1)$$

According to equation (4.1), the entropy change from magnetisation isotherms can be calculated by multiplying the area between two adjacent M-H curves with the reciprocal of temperature difference (ΔT). The magnetic entropy changes $\Delta S_m$ are estimated for both as prepared LNMO sample and the sintered sample from the magnetisation (M-H) isotherms at different applied fields.

The magnetic entropy change for the as-prepared LNMO sample has been estimated in the temperature range of 150 K to 300 K at different applied magnetic fields and are shown in Fig.4.5. The negative sign of the estimated $\Delta S_m$ shows that heat is released when the magnetic field is changed adiabatically[14]. It is observed that the $\Delta S_m$ increases with the applied magnetic field, and a maximum value of 0.487 J/kg/K is observed at 155 K in an applied field of 50 kOe. The entropy change of 0.487 J/kg/K for the as prepared sample is an appreciable value when we consider the fact that the sample is unsintered and possesses a good crystalline structure.(Chapter 3, Section 3.3.1).

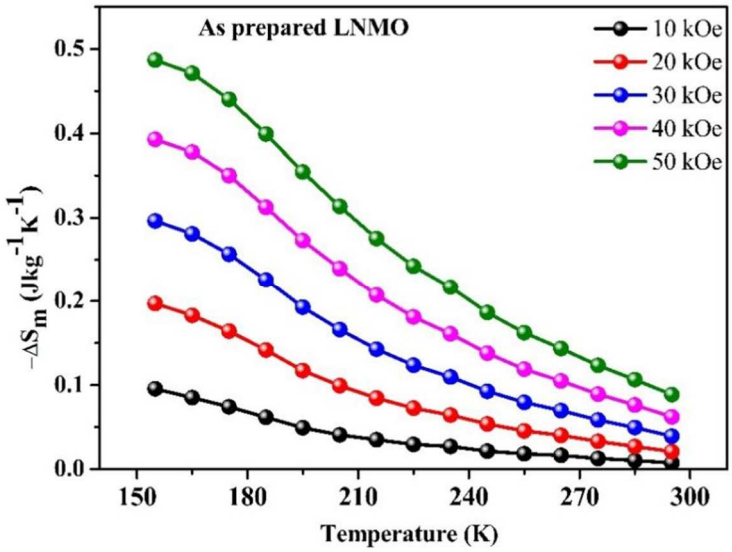


**Figure 4.5.** Variation of $-\Delta S_m$ with temperature of as prepared $La_{0.5}Na_{0.5}MnO_3$.

The behaviour of magnetic entropy change ($-\Delta S_m$) as a function of temperature for several applied magnetic fields for the sintered LNMO samples are shown in Fig. 4.6. The graph depicts that an extremum of variation of magnetic entropy can be detected in the vicinity of a magnetic transition due to a change of the magnetic order in the material. Generally, the strong magnetic entropy change in perovskite materials is caused by the large variation in magnetisation near the ordering temperature. As a result, near the ordering temperature, magnetisation decreases more abruptly, which causes a substantial change in magnetic entropy[26]. The observed magnetic entropy change at 20 kOe, 30 kOe, and 40 kOe is 1.126 J/kg/K, 1.566 J/kg/K, and 1.9726 J/kg/K, respectively. A significant entropy change is observed for the as prepared LNMO, even for a small magnetic field of 20 kOe. These values are comparable to those of magnetic refrigerant materials that have been reported[19]. The maximum entropy change of 2.344 J/kg/K is observed at 317.5K at an applied field of $\Delta H$ =50 kOe for sintered LNMO, which is greater than the reported values of the magnetocaloric properties of lanthanum sodium manganite with the same composition near room temperature[19].

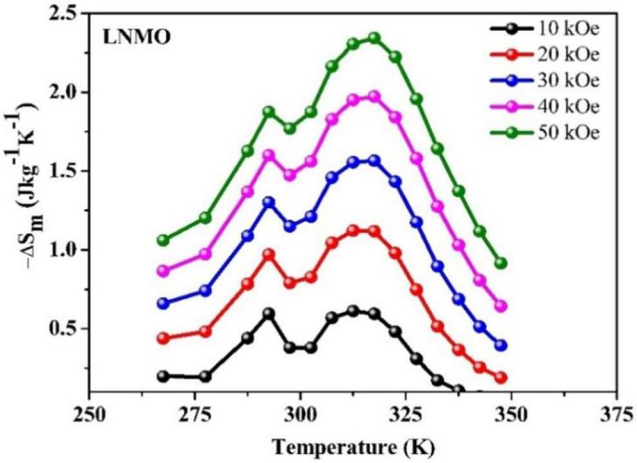


**Figure 4.6.** Variation of $-\Delta S_m$ with the temperature of sintered $La_{0.5}Na_{0.5}MnO_3$.

The reported values of magnetic ordering temperature and magnetic entropy change near room temperature exhibited by some alkaline earth-doped/substituted lanthanum manganites at $\Delta H$ = 5T and 2T are summarised in Table 4.1. It can be observed that we have obtained a maximum entropy change of 2.344 J/kg/K, which is a relatively good value for room-temperature magnetic refrigerant applications.

**Table 4.1.** Summary of the magnetic entropy change at $T_c$ for some alkaline earth doped lanthanide manganites.

| Compound | T (K) | ΔH(T) | $\Delta S_m$ (J/kg/K) | Ref |
|---|---|---|---|---|
| $La_{0.5}Na_{0.5}MnO_3$ | 317.5 | 5(50kOe) | 2.34 | Present work |
| $La_{0.5}Na_{0.5}MnO_3$ | 312.5 | 2(20kOe) | 1.12 | Present work |
| $La_{0.5}Na_{0.5}Co_{0.1}Mn_{0.9}O_3$ | 222.5 | 5 | 1.6 | Present work |
| $La_{0.5}Na_{0.5}Co_{0.1}Mn_{0.9}O_3$ | 212.5 | 2 | 0.727 | Present work |
| $La_{0.67}Sr_{0.33}Mn_{0.9}Ni_{0.1}O_3$ | 290 | 5 | 3.00 | [4] |
| $La_{0.8}Na_{0.2}MnO_3$ | 330 | 2 | 2.3 | [17] |
| $La_{0.8}Ca_{0.2}MnO_3$ | 230 | 2 | 3.2 | [17] |
| $La_{0.67}Ba_{0.33}Mn_{0.975}Ni_{025}O_3$ | 328 | 5 | 2.78 | [27] |
| $La_{0.67}Ba_{0.33}MnO_3$ | 292 | 5 | 1.48 | [27] |
| $Pr_{0.5}Na_{0.05}Sr_{0.45}MnO_3$ | | 2 | 1.6 | [28] |
| $Pr_{0.5}K_{0.05}Sr_{0.45}MnO_3$ | | 2 | 1.66 | [28] |

Variation of maximum magnetic entropy change of sintered LNMO with the magnetic field is displayed in Fig. 4.7 (a). The magnetic entropy change increases linearly with an increase in the magnetic field, suggesting that a significantly larger magnetic entropy change is to be expected at higher magnetic fields. A detailed investigation of the field dependence of entropy change of LNMO has been performed as $\Delta S_m$ increases with the applied field to probe the magnetic transition.

The magnetic field dependence of $\Delta S_m$ of materials with a second order phase transition can be approximated by the power law[29],

$$\Delta S_m = \mathrm{a}\ H^n \tag{4.2}$$

where $a$ is constant and $n$ is the local exponent related to the critical exponents β and δ at $T_c$ by the relation[30],

$$n(T_c) = 1 + \frac{1}{\delta}\left(1 - \frac{1}{\beta}\right) \tag{4.3}$$

The value of $n$ can be calculated by the slope of the power law fitting of $\Delta S_m$ versus H plot on log-log scale by employing the formula

$$n = \frac{d\log(\Delta S_m)}{d\log H} \tag{4.4}$$

Magnetic entropy change as a function of the magnetic field graph in the log-log scale of the LNMO sample fitted with linear function is shown in Fig.4.7(b).

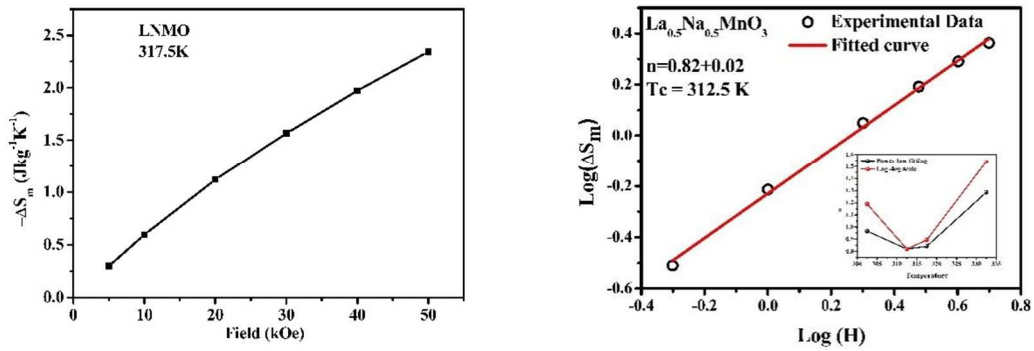


(a) (b)

**Figure 4.7.** (a) Variation of maximum $\Delta S_m$ with an applied field of $La_{0.5}Na_{0.5}MnO_3$. near $T_c$ (b) Power law fitting of $\Delta S_m$ versus Field graph in log-log scale.

The value of the local exponent, *n*, is determined from the slope of the graph and is found to be 0.82±0.02. The value of *n* is estimated by power law fitting of entropy change versus field at different temperatures and also by the linear fitting of entropy change versus field in log-log scale. The estimated value of *n* by fitting the graph in log-log scale matches the reported values [21,31]. The variation of *n* with temperature at a high field of 50 kOe is shown in the inset of Fig. 4.7 (b). At low temperatures, the value of *n* is around 1 (1.18) and shows a dip at $T_c$ = 312.5, (*n* = 0.82) then approaches 2 (1.54) at higher fields. The value of *n* around 2 at T >$T_c$ indicates the sample is in the paramagnetic region, which is a consequence of Curie-Weiss law[22]. Similar observations have been reported in some research papers [32]. The variation of *n* around 1, at T < $T_c$ indicates the ferromagnetic nature of the sample and the minimum value of *n* (0.82) observed at T= $T_c$ confirms that the exchange interaction agrees with the Mean-Field Theory. The expected value of *n* at $T_c$ for the Mean-field approximation is 2/3. The difference in this *n* value is attributed to the presence of local inhomogeneity[21,33] and superparamagnetic clusters near $T_c$ [34]. The superparamagnetic behaviour can be confirmed by the identification of the blocking temperature from the ZFC curve at 304.5 K.

### 4.2.4 Indirect calculation of adiabatic temperature change ($\Delta T_{ad}$)

The adiabatic temperature change ($\Delta T_{ad}$) refers to the temperature change, when a material is adiabatically demagnetised. The adiabatic temperature change associated with the magnetic entropy change is given by

$$\Delta T_{ad}\,(T,\Delta H) = -\int_{H1}^{H2}\left(\frac{T}{C(T,H)}\right)_H\left(\frac{\partial M(T,H)}{\partial T}\right)_H\,dH \qquad (4.5)$$

A second order phase (SOPT) transition material shows lower dependence of specific heat on the magnetic field compared to the first order transition material (FOPT) [30].So for a second order transition material, considering the field independence equation (1.16) can be further written as

$$\Delta T_{ad} = \frac{T}{C\,(T)}\Delta S_m \qquad (4.6)$$

where $C(T)$represents the specific heat capacity, which is considered as independent of magnetic field variations. Equation (4.6) describes the indirect measurement of adiabatic temperature by calorimetric measurement[35].

The changing magnetic field produces a magnetic entropy change, which results in a heat transfer in the system. The specific heat capacity, which governs the amount of heat transferred, associated with the applied magnetic field is related to the magnetic entropy change by the equation [36],

$$\Delta C_H = C(T,H) - C(T,0) = T\frac{\delta \Delta \mathrm{Sm}}{\delta T} \qquad (4.7)$$

$\Delta C_H$ is calculated from the magnetic entropy change values at different temperatures by employing equation (4.7). The change in specific heat capacity, $\Delta C_H$, of the LNMO sample as a function of temperature is shown in Fig. 4.8.

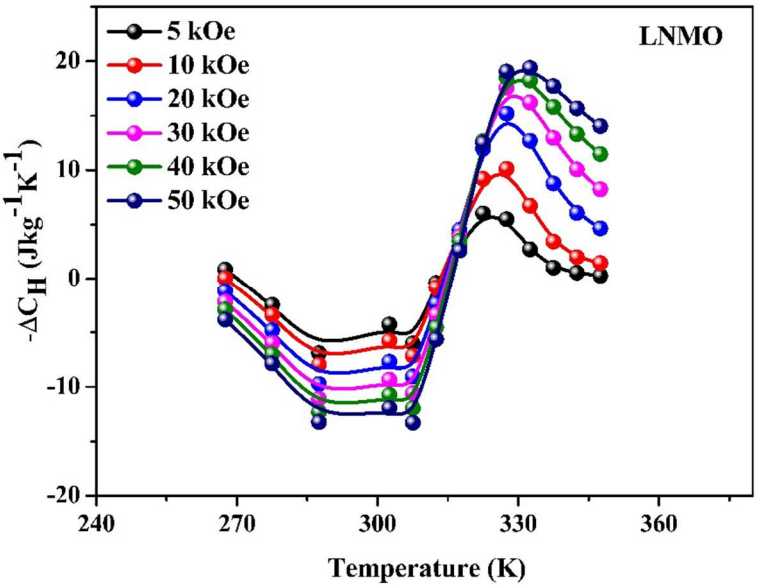


**Figure 4.8.** Variation of $\Delta C_H$ with temperature of $La_{0.5}Na_{0.5}MnO_3$.

It exhibits a peak for minima and a peak for maxima, and it crosses over from minimum to maximum near transition temperature identified as 317 K. The sum of the positive and negative parts of heat capacity represents the magnetic contribution to the total heat capacity, which influences the cooling and heating of a magnetic refrigerator. Consequently, the change in heat capacity is advantageous and provides quantitative information which is useful for the design of a magnetic refrigerator[22]. Hence, the second-order phase transition is characterised by a discontinuity in $\Delta C_H$ near the transition temperature as shown in Fig. 4.8 [32] which again confirms the ferromagnetic to paramagnetic magnetic transition in the LNMO sample according to Mean Field Theory. The maximum and minimum values of $\Delta C_H$ observed at 50 kOe are 19.5 J/kg/K and -13.55 J/kg/K, respectively, comparable to the reported value[23].

Specific heat capacity without applying a magnetic field was measured in the temperature range 253 K -353 K with a maximum value of C of 1443 J/kg, and that at an applied magnetic field of 50 kOe had been estimated indirectly. Since ($\Delta C_H$) will be the difference between the two, the specific heat capacity values in an applied

magnetic field of 50 kOe are determined from these using the specific heat capacity values without a magnetic field as per equation (4.7). The graph showing the variation of specific heat capacity with and without a magnetic field and temperature is shown in Fig. 4.9.

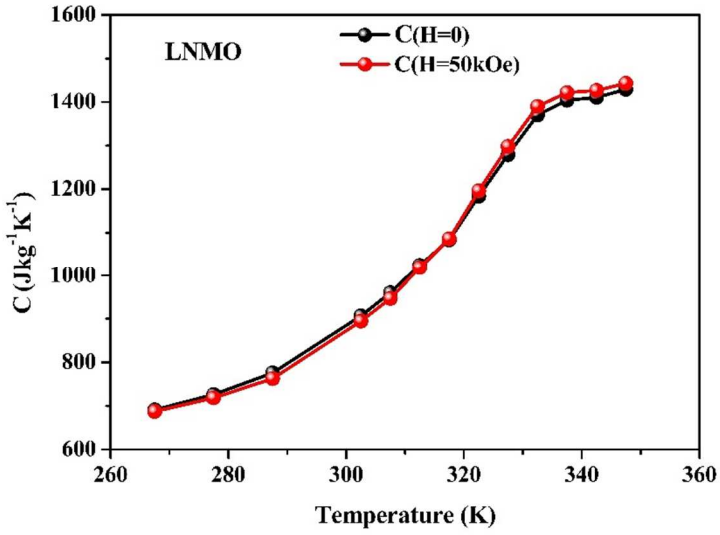


**Figure 4.9.** Variation of specific heat capacity of $La_{0.5}Na_{0.5}MnO_3$. in the presence and absence of a magnetic field

It was observed from the figure that there is no remarkable difference between the specific heat capacity with and without an applied magnetic field. Hence, the adiabatic temperature change ($\Delta T_{ad}$) for a second order transition material can be estimated from the specific heat measurements by employing equation (4.6)[36]. The adiabatic temperature change has been calculated at different temperatures and the variation of $\Delta T_{ad}$ with temperature is shown in Fig. 4.10.

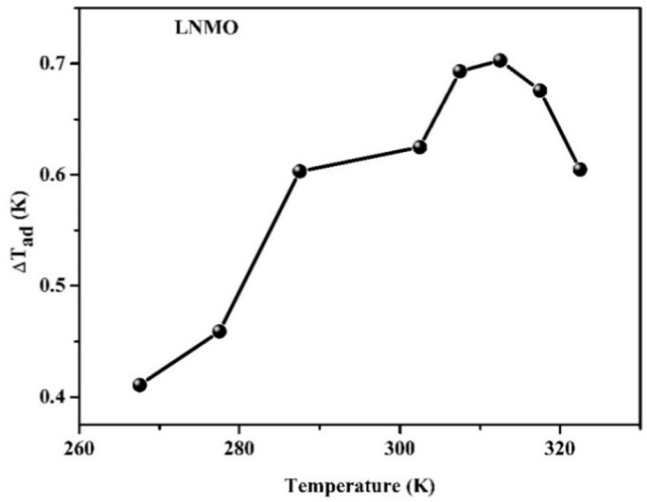


**Figure 4.10.** Variation of $\Delta T_{ad}$ with temperature for $La_{0.5}Na_{0.5}MnO_3$.

The linear variation of $\Delta T_{ad}$ with temperature around room temperature is a promising result regarding the MCE applications of the sample. The maximum adiabatic temperature change $\Delta T_{ad}$ estimated from the specific heat capacity versus temperature curve is 0.7K in an applied field of 50 kOe at a temperature of 312.5 K. An increase in adiabatic temperature change with an increase in temperature near the room temperature and preferably at an ordering temperature of 312.5 K is a favourable condition for a potential magnetic refrigerant material. A material can store and release significant heat energy during magnetisation and demagnetisation if its specific heat is higher. So, the change in heat capacity and magnetic entropy plays an important role in designing a magnetic refrigerant material in manganites [22,36].

### *4.2.5 Relative cooling Power (RCP)*

The magnetic cooling efficiency, also known as relative cooling power (RCP), is another important indicator for evaluating magnetocaloric materials. The cooling power per unit volume corresponds to the amount of heat transferred between the cold and hot sinks in the ideal refrigeration cycle. RCP is related to $\Delta S_m$ by the equation

$$RCP = \Delta S_m \times \delta T_{FWHM} \quad (4.8)$$

where, $\delta T_{FWHM}$ is the full width at half maximum of the $\Delta S_m$ vs. $T$ curves. The RCP of the LNMO sample is estimated at different applied magnetic fields, and the variation of RCP with field is shown in Fig. 4.11. The relative cooling power increases with the applied field, and a maximum value has been observed at 50 kOe.

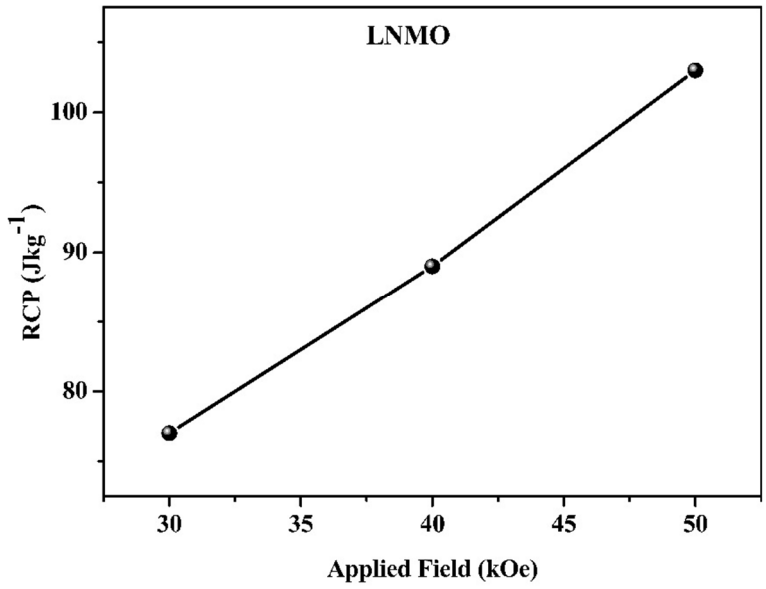


**Figure 4.11.** Variation of RCP with magnetic field for $La_{0.5}Na_{0.5}MnO_3$.

The estimated value of RCP for maximum entropy changes 2.344 J/kg/K at an applied field of 50 kOe is 105.75 J/kg for the LNMO sample. Hence, the synthesised LNMO sample exhibits an appreciable entropy change and RCP near room temperature. As per the observed values of the maximum $\Delta S_m$ (2.344 J/kg/K), $\Delta T_{ad}$ (0.7K), and $RCP$ (105.75 J/kg), the LNMO sample can be a promising potential material for magnetic refrigerant application near room temperature.

Since the sintered LNMO sample showed enhanced magnetocaloric properties near room temperature, a detailed theoretical analysis of the critical behaviour of the sample near the ordering temperature is carried out.

### *4.2.6 Analysis of Critical Behaviour in LNMO*

It is shown from the specific heat capacity measurements and field dependence of magnetic entropy change that the sample LNMO exhibits a second order magnetic transition from ferromagnetic to paramagnetic behaviour. So, it can be characterised by the critical exponents $\beta$, $\gamma$ and $\delta$ which relate the spontaneous magnetisation, initial susceptibility and critical magnetisation isotherm respectively. The critical exponents describe the behaviour of physical properties near the Curie temperature and are defined by the Arrott- Noakes equations of state. [40]

$$M_s(T) = M_0(-\varepsilon)^{\beta} \quad \varepsilon \geq 0 \tag{4.9}$$

$$\chi^{-1}(T) = \frac{H_0}{B_0}(\varepsilon)^{\gamma} \quad \varepsilon \leq 0 \tag{4.10}$$

$$M = DH^{1/\delta} \quad \varepsilon = 0 \tag{4.11}$$

where $\varepsilon = 1 - \frac{T}{T_c}$ $M_0$, $H_0$ and D are the critical amplitudes and remain constant. The spontaneous magnetisation and inverse of magnetic susceptibility are determined by the linear extrapolation from the $M^{1/\beta}$ and $(H/M)^{1/\gamma}$ plot. The best values of $\beta$, $\gamma$ are obtained by fitting $M_s(T)$ and $\chi^{-1}(T)$ data using equations (4.9) and (4.10). The magnetocaloric study provides a powerful tool to probe the magnetic transition[36]. The critical behaviour of the magnetic phase transition in the LNMO sample was investigated in terms of the critical exponents.

The materials in ferromagnetism are classified into four universality classes based on the types of interactions and critical exponents. Mean Field Theory (long range interactions) *$\beta$=0.5, $\gamma$=1,* 3D Heisenberg model (short range interactions) *$\beta$=0.365, $\gamma$=1.336*, 3D Ising model (short range interactions) *$\beta$=0.325, $\gamma$=1.241* and Tri critical mean field (short range interactions) *$\beta$=0.25, $\gamma$=1* are the four types of universality classes in ferromagnetism. Various techniques like Modified Arrott Plots (MAP), Kouvel Fischer approach and critical isotherm analysis were employed on magnetic isotherms to estimate critical exponents.

**Arrott Plots**

Arrott plots are an easy method to determine the presence of ferromagnetic order in a material. It is a plot between the square of magnetisation $M^2$ and inverse susceptibility (H/M) at several temperatures. For a ferromagnetic system exhibiting long-range interactions, Mean Field Theory (MFT) suggests that the free energy *G* is expanded in the even powers of M according to Landau theory as [35].

$$G = G_0 + \frac{1}{2}A(T)M^2 + \frac{1}{4}B(T)M^4 + \cdots - \mu_0 HM, \tag{4.12}$$

where *A(T)* represents magnetoelastic coupling and *B(T)* is the electron condensation energy. For minimum energy, *dG/dM =0*, results in the relation

$$\frac{H}{M} = A(T) + B(T)M^2 \tag{4.13}$$

At $T\text{-}T_c$, A(T)=0, and A(T) can be rewritten as $A(T) = a\left(\frac{T-T_c}{T_c}\right) = a\varepsilon$

$$\frac{H}{M} = a\varepsilon + bM^2 \tag{4.14}$$

It means that for the magnetic interactions in the ferromagnetic system exactly follow the Mean Field Theory, ($M^2$ versus $H/M$) curves, the Arrott plots, around the transition temperature are parallel straight lines and ($M^2$ versus $H/M$) curve at $T_c$ passes through the origin[37]. In the Arrott plots, if the curves are not parallel and the curve at $T_c$ does not pass through the origin, the exchange interaction does not exactly follow the MFT. In such cases, the Modified Arrott Plot (MAP) technique is used to estimate critical exponents by employing the Arrott- Noakes equations of state[37].

$$\left(\frac{H}{M}\right)^{1/\gamma} = a\varepsilon + bM^{1/\beta} \tag{4.15}$$

Arrott plots ($M^2$ versus $H/M$) are constructed according to mean field theory taking $\beta$=0.5 and $\gamma$=1 from magnetic isotherms to confirm the nature of the phase transition observed in the LNMO nanoparticles. It has been noted that Arrott plots of the LNMO sample shown in Fig.4.12 approaches a linear behaviour parallel to one another at higher fields with a decrease in temperature. Magnetic isotherm at 315 K passes through the origin, which is known to be the critical isotherm at the transition temperature. So, the Arrott plots of the LNMO sample obey the criteria of mean field theory and it can be shown that the FM interactions in the LNMO samples responsible for magnetisation are long range. According to the Banerjee criterion, if the slope of $M^2$ versus $H/M$ curves is positive, the magnetic transition is of second order from the ferromagnetic (FM) to the paramagnetic (PM) phase and if the slope is negative, it corresponds to a first order transition from PM to FM [38]. In our work, the Arrott plots of the LNMO sample exhibit a positive slope at $T \geq T_c$, which is attributed to a second-order magnetic phase transition from ferromagnetic to paramagnetic phases.

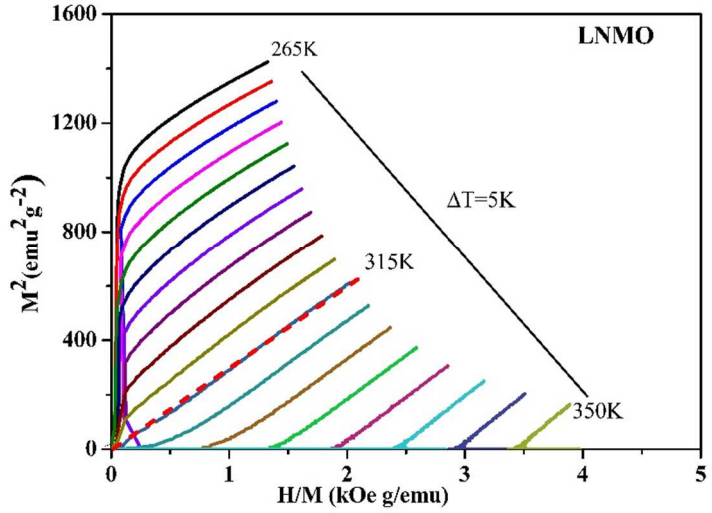


**Figure 4.12.** $M^2$-H/M curves of $La_{0.5}Na_{0.5}MnO_3$ at an applied field of 50 kOe

**Kouvel Fischer Approach**

Kouvel Fischer approach is another method to estimate critical exponents more accurately from the Arrott plots. The spontaneous magnetisation ($M_{sp}$) and inverse susceptibility ($\chi^{-1}$) have been determined from the Arrott plots by the intercepts of the line at the higher magnetic field with $M^{1/\beta}$ below and with $(H/M)^{1/\gamma}$ above $T_c$, respectively. The critical exponents associated with spontaneous magnetisation $M_s$ below $T_c$ and initial inverse susceptibility above $T_c$ respectively were estimated more accurately from the Arrott plots by employing Kouvel Fisher (KF) equations (4.16) and (4.17) on magnetisation isotherms near the transition temperature[24].

$$\frac{M_{sp}(T)}{dM_{sp}(T)/dT} = \frac{T-Tc}{\beta} \tag{4.16}$$

$$\frac{\chi^{-1}(T)}{d\chi^{-1}/_{dT}} = \frac{T-Tc}{\gamma} \tag{4.17}$$

According to these equations, the obtained temperature-dependent spontaneous magnetisation $M_{sp}$ and initial inverse susceptibility data were used to construct $\frac{M_{sp}(T)}{dM_{sp}(T)/dT}$ vs temperature and $\frac{\chi^{-1}(T)}{d\chi^{-1}/_{dT}}$ vs temperature straight line graphs with slope 1/β and 1/γ respectively are displayed in Fig.4.13. The intercepts on the temperature axis indicate the transition temperature $T_c$. The experimental values of $\beta$ and $\gamma$ estimated from the graph are found to be 0.43 ± 0.13 and 1.00 ± 0.03 respectively. The estimated values of $T_c$ corresponding to the KF approach using equations (4.16) and (4.17) are 313.5 K and 313.3 K respectively. It is noteworthy that the estimated critical exponents by employing the KF method are in good agreement with the theoretical values of $\beta$ (0.5) and $\gamma$ (1.00) according to Mean Field Theory and the corresponding estimated $T_c$ are 313.5 K and 313.3 K.

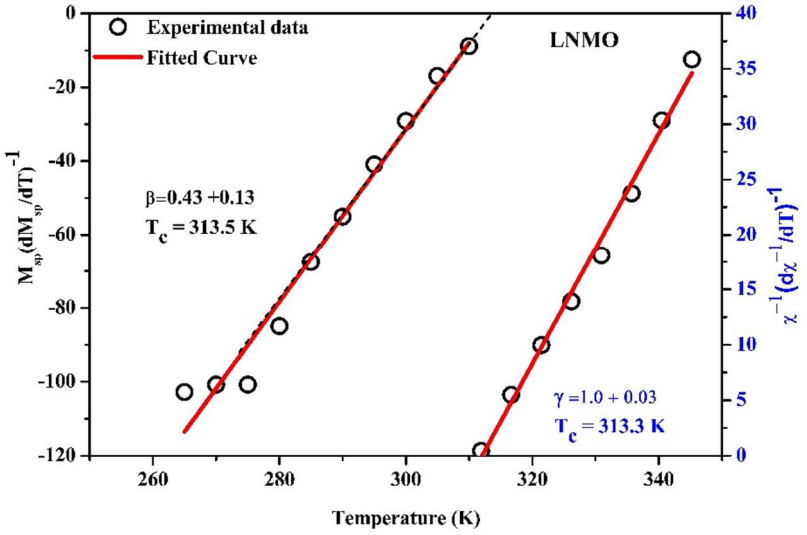


**Figure 4.13.** Kouvel-Fisher plots of $La_{0.5}Na_{0.5}MnO_3$.

## Critical Isotherm Analysis

The other critical exponent $\delta$ can be determined from the Log-Log plot of magnetisation M and magnetic field H of the critical magnetic isotherm at 315 K, displayed in Fig.4.14. The slope of the M-H curve in the log-log scale indicates the value of $\delta$, which is estimated as 2.85.

According to the statistical theory, the critical exponents $\beta$, $\gamma$ and $\delta$ are related by a hypothesis known as Widom scaling relation given by [39]

$$\delta = 1 + \frac{\gamma}{\beta} \tag{4.18}$$

The estimated value of $\delta$ using the scaling relation is 3.353. The critical exponent $\delta$ is estimated from the M-H curves in log-log scale using equation (4.11) as 2.85. The estimated values of $\delta$, 3.35 and 2.85 are close to the expected value ($\delta$ =3) for the Mean Field Theory. As the estimated value of $\delta$ using the critical isotherm is closer to the theoretical value, we have adopted this method to estimate the critical exponent δ rather than the Widom scaling relation. The magnetisation isotherms were measured in a temperature interval of 5 K. So, the critical isotherm

may not be exactly at 315 K. This may also be the reason for the small variation of $\delta$ from the theoretical value.

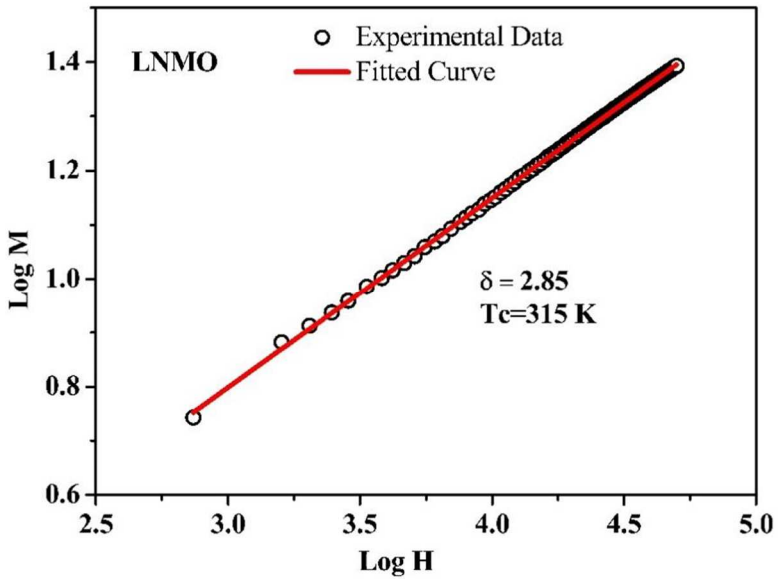


**Figure 4.14.** M-H curves of $La_{0.5}Na_{0.5}MnO_3$ in a log-log scale.

The estimated values of critical exponents $\beta$, $\gamma$ and $\delta$ from Arrott plots again confirmed that the magnetic phase transition is a second-order transition. The Curie temperature determined from the first derivative of the magnetisation versus temperature curve differs from that obtained through Arrott plots. This may be because the magnetic entropy change is maximum in the vicinity of the ordering temperature rather than at the ordering temperature. In the present work, the maximum magnetic entropy change of 2.344 J/kg/K has been observed at 317.5 K for an applied field of 50kOe rather than 324 K. A similar behaviour has been reported in other research papers[40]. The method of determining the ordering temperature in LNMO, which employs Arrott plots instead of the minimum of the dM/dT curve, is more accurate and accounts for the temperature difference[41].

The magnetocaloric properties of the as-prepared and sintered LNMO samples were investigated by the magnetic isotherms (M-H), and a maximum

magnetic entropy change $\Delta S_m$ of 2.344 J/kg/K was observed for LNMO samples at an applied field of 50 kOe at 317.5K. An adiabatic temperature change $\Delta T_{ad}$ of 0.7K is estimated indirectly from the specific heat capacity values. The relative cooling power of the LNMO sample is found to be 105.75 J/kg. The Arrott plots, Kouvel Fischer plots and critical isotherm analysis confirmed the second-order magnetic phase transition of the LNMO samples. According to the observed values of the magnetocaloric parameters, the lanthanum sodium manganite nanoparticles synthesised by the novel sol-gel auto-combustion method in the present work can be a promising material for magnetic refrigeration applications around room temperature.

## 4.3 MCE Properties of Cobalt substituted Lanthanum Sodium Manganite $La_{0.5}Na_{0.5}Mn_{1-x}Co_xO_3$ (LNCMO)

The MCE properties of nearly fifty percent sodium-substituted lanthanum manganite LNMO samples have been examined, and a maximum magnetic entropy change of 2.344 J/kg/K is observed at 317.5 K for an applied field of 50 kOe. The literature survey reveals that the substitution of Co for Mn in manganite materials can reduce the transition temperature. However, the sample $La_{0.5}Na_{0.5}MnO_3$ exhibits the maximum magnetic entropy change near room temperature; cobalt is substituted for Mn in the present work to tune the transition temperature to room temperature. The magnetocaloric properties of $La_{0.5}Na_{0.5}Co_xMn_{1-x}O_3$ (x=0.1,0.3,0.7) samples were studied from the magnetisation isotherms.

### *4.3.1 ZFC-FC Measurements*

The temperature dependent magnetisation measurements (ZFC-FC) of as prepared and sintered cobalt substituted $La_{0.5}Na_{0.5}Mn_{1-x}Co_xO_3$ samples were recorded under various dc magnetic fields according to their maximum magnetisation values. ZFC-FC measurements of as prepared $La_{0.5}Na_{0.5}Mn_{1-x}Co_xO_3$ (x=0.3 and 0.9) were recorded under an applied magnetic field of 200 Oe. The ZFC-

FC curves of as-prepared samples x=0.3 and x=0.9 are shown in Fig. 4.15 and 4.16, respectively.

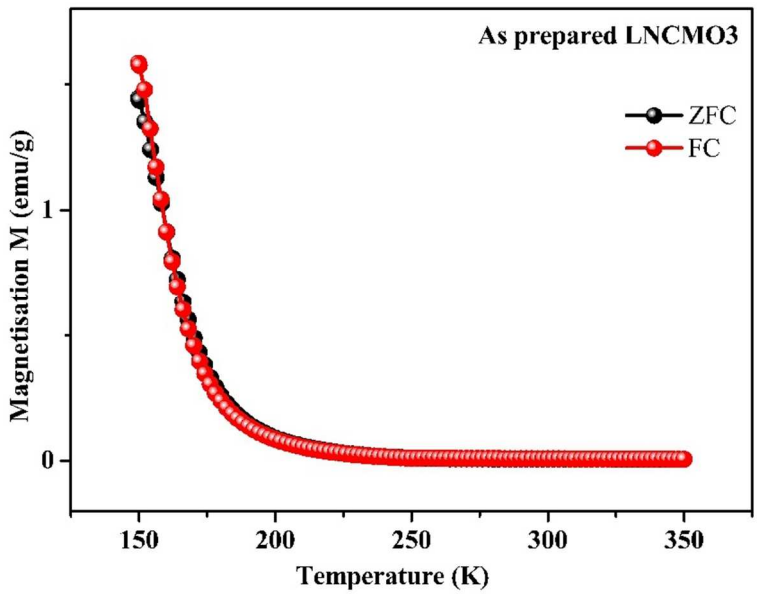


**Figure 4.15.** ZFC-FC curves of as prepared $La_{0.5}Na_{0.5}Mn_{0.7}Co_{0.3}O_3$

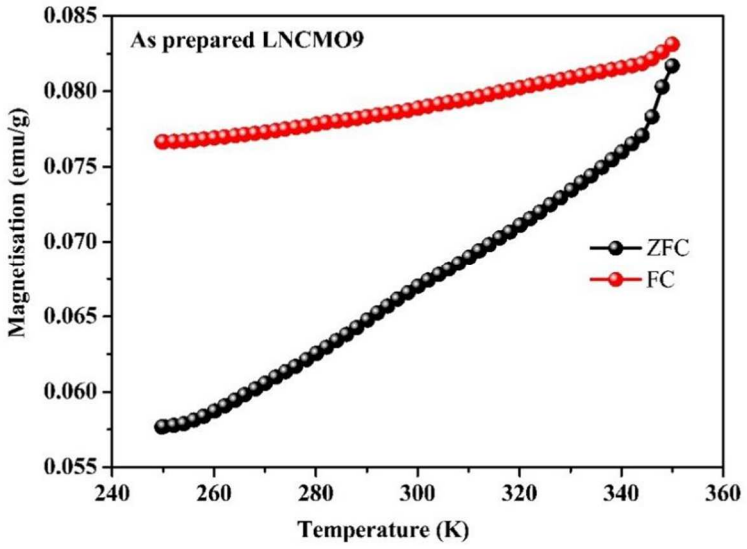


**Figure 4.16.** ZFC-FC curves of as prepared $La_{0.5}Na_{0.5}Mn_{0.1}Co_{0.9}O_3$

It was observed from the ZFC-FC curves that they show different patterns for the two as prepared samples (x=0.3 and x=0.9). For the x=0.3 sample (Fig.4.15), the ZFC magnetisation value shows a maximum value at 150 K and then decreases with an increase in temperature. For the x=0.3 sample, the variation of ZFC and FC magnetisation with temperature is in the same manner; no significant transition can be found in the measured temperature range. A minimum value of dM/dT is observed at 158 K from the derivative plot of the FC curve. For the x=0.9 sample, both the ZFC and FC magnetisation increase with temperature and no significant transition was observed in the measured temperature range. From the ZFC-FC curves of as prepared samples, a better result was obtained for the x=0 sample. Since the structural properties and magnetic characteristics were not suited for MCE materials, our further investigation concerning the MCE properties was restricted to the sintered samples ($La_{0.5}Na_{0.5}Mn_{1-x}Co_xO_3$ for x=0.1, 0.3 and 0.7) with good structural and compositional properties.

The temperature dependent magnetisation properties of the sintered ($La_{0.5}Na_{0.5}Mn_{1-x}Co_xO_3$ for x=0.1, 0.3 and 0.7*)* samples have been studied. The behaviour of magnetisation as a function of temperature in the ZFC and FC conditions for the sample with x=0.1 is shown in Fig. 4.17. As the room temperature magnetisation of this sample was low, a high magnetic field of 5000 Oe was applied for ZFC-FC measurements. It can be observed that the magnetisation decreases with temperature. The derivative plot of magnetisation with the temperature of (x=0.1) gives a minimum at 211 K, which corresponds to its Curie temperature $T_c$.

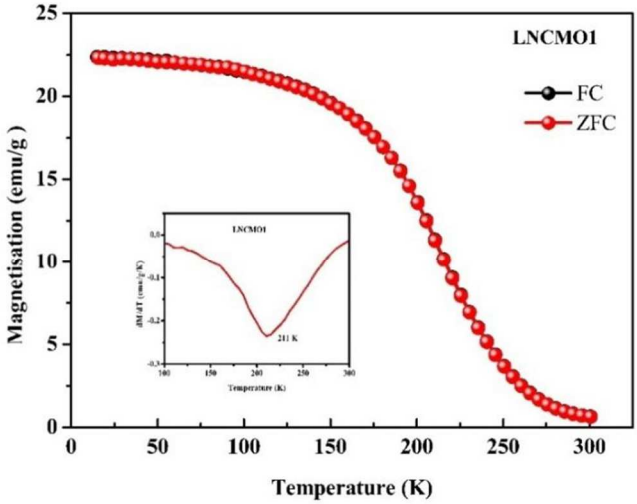


**Figure.4.17.** ZFC-FC curves of $La_{0.5}Na_{0.5}Mn_{0.9}Co_{0.1}O_3$ (x=0.1).

A magnetic transition from ferromagnetic to paramagnetic was observed for the $La_{0.5}Na_{0.5}Mn_{0.9}Co_{0.1}O_3$, LNCMO1 sample. Fig. 4.17 reveals that the ZFC and FC curves almost coincide for the $La_{0.5}Na_{0.5}Mn_{1-x}Co_xO_3$ (x=0.1) sample. Kumar and Banerjee reported that the difference between the ZFC and FC curves decreases with the increase in applied field, and at higher fields, they almost coincide[42].

The ZFC-FC curves of $La_{0.5}Na_{0.5}Mn_{0.7}Co_xO_3$ (LNCMO3) measured in the temperature range 220 K – 350 K under an applied field of 200 Oe are shown in Fig. 4.18 (x=0.3). Fig.4.18 shows that the sample attains a high magnetisation value at a lower temperature 220K and the magnetisation decreases gradually with increase in temperature. The ZFC and FC curves of LNCMO3 exhibit a similar variation of magnetisation within this temperature range. No noticeable divergence between the ZFC-FC curves is seen in the graph. The transition temperature of the LNCMO3 sample is not in the measured temperature range and it can possibly be below 220 K. ZFC-FC curves of $La_{0.5}Na_{0.5}Mn_{0.3}Co_{0.7}O_3$ (LNCMO7) sample have been recorded in the temperature range of 50 K-250 K under an applied dc magnetic field of 1000 Oe and are displayed in Fig. 4.19.

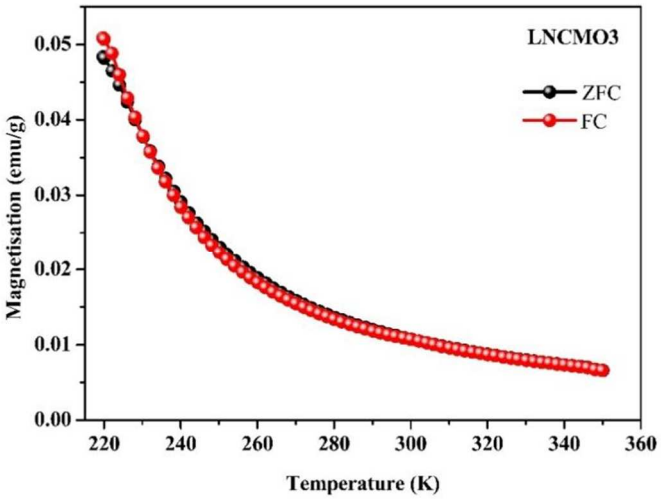


**Figure 4.18** ZFC-FC curves of $La_{0.5}Na_{0.5}Mn_{0.7}Co_{0.3}O_3$.

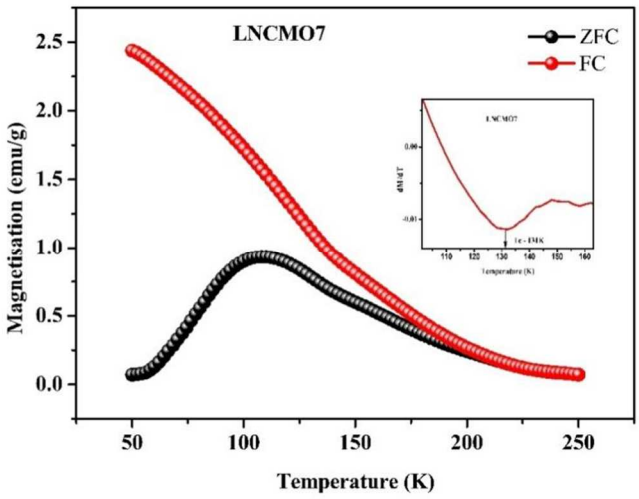


**Figure 4.19.** ZFC-FC curves of $La_{0.5}Na_{0.5}Mn_{0.3}Co_{0.7}O_3$.

It can be observed from Fig.4.19 that the magnetisation of the samples decreases with increasing temperature. Moreover, the ZFC magnetisation curve exhibits a maximum at 107 K and the magnetisation decreases at low temperatures. A prominent divergence in the ZFC curve is more obvious from Fig. 4.19, which is observed in several perovskite cobaltites. So, the first derivative of magnetisation (dM/dT) of the ZFC curve is plotted as a function of temperature, and a minimum is

observed from the derivative plot at 130 K indicating the freezing temperature points to the spin glass behaviour of the sample. The observed freezing temperature at 130 K in the ZFC-FC curves of LNCMO7 is associated with the spin glass behaviour of the sample. It was reported that the cobalt-rich samples of cobalt-substituted lanthanum manganite exhibit spin glass behaviour due to the antiferromagnetic interactions. This is because of the increase of $Mn^{4+}$ content, which decreases the double exchange interaction between $Mn^{3+}/Mn^{4+}$ and the increase of antiferromagnetic interaction with cobalt substitution[28].

From the ZFC-FC curves of sintered LNCMO7, it was observed that the variation of the magnetisation with temperature is similar for as prepared $La_{0.5}Na_{0.5}MnO_3$(LNMO, x=0) sample. The temperature dependent zero field magnetisation of these two samples shows a characteristic maximum, which is the signature of the freezing/blocking temperature of a spin glass/superparamagnetic system[43,44]. In the ZFC curve of as prepared LNMO sample, the peak corresponds to a blocking temperature, revealing the superparamagnetic behaviour, whereas in the sintered LNCMO7 sample, the peak in the ZFC curve is around the freezing temperature corresponding to the spin glass behaviour. Furthermore, it is evident that the peak in the ZFC curve is located very close to the FC curve in the as prepared LNMO, while it is far from the FC curve for the LNCMO7 sample. As the magnetisation of $La_{0.5}Na_{0.5}Mn_{1-x}Co_xO_3$ samples decreases with cobalt substitution, a large magnetic field was applied while recording ZFC-FC measurements. The ZFC-FC curves of sintered LNCMO1 and LNCMO3 samples reveal that the samples exhibit high magnetisation values at lower temperatures and the magnetisation is found to decrease at higher temperatures. It is observed that the transition temperature decreases with cobalt substitution. The value of $T_c$ decreases from 324 K to 211 K even with the initial substitution of cobalt and reaches 130 K when x changes from 0 to 0.7.

### *4.3.2 Magnetisation Isotherm Curves*

The magnetisation isotherms of the $La_{0.5}Na_{0.5}Mn_{1-x}Co_xO_3$ (x=0.1, 0.3, and 0.7) were recorded in the vicinity of their respective Curie temperature, and the M-H isotherms are displayed in Fig. 4.20, 4.21 and 4.22, respectively.

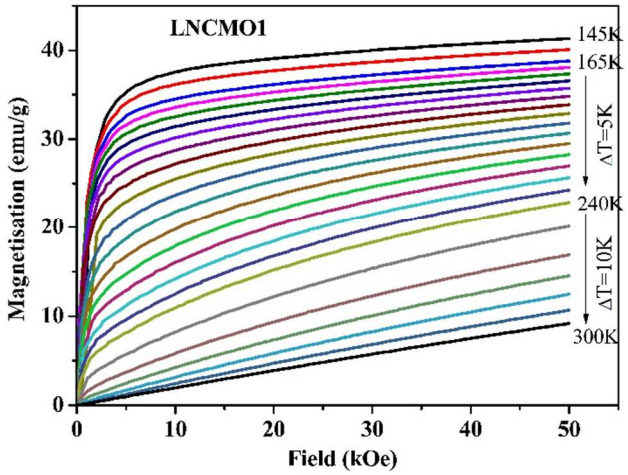


**Figure 4.20**. M-H isotherms of $La_{0.5}Na_{0.5}Mn_{0.9}Co_{0.1}O_3$

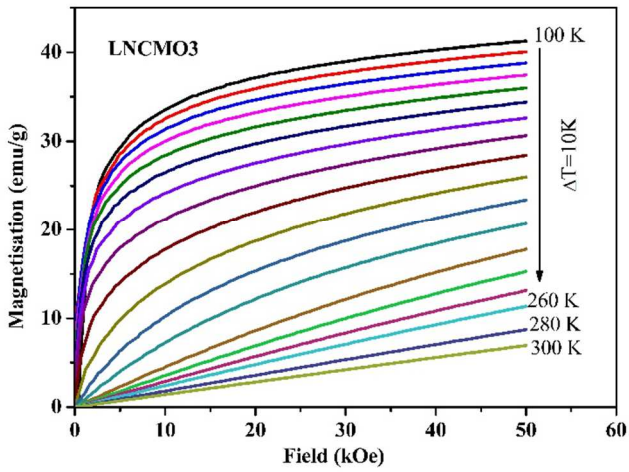


**Figure 4.21.** M-H isotherms of $La_{0.5}Na_{0.5}Mn_{0.7}Co_{0.3}O_3$

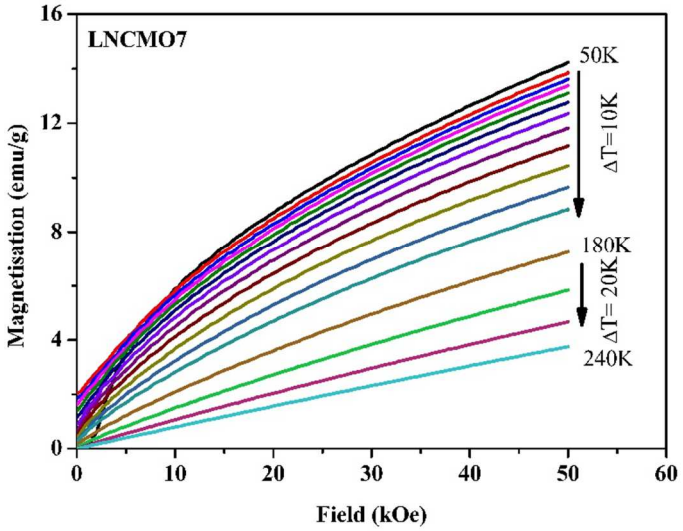


**Figure 4.22.** M-H isotherms of $La_{0.5}Na_{0.5}Mn_{0.3}Co_{0.7}O_3$

M-H isotherms of the samples x=0.1, 0.3 and 0.7 reveal a ferromagnetic to paramagnetic transition with temperature rise. However, it is noted that the maximum magnetisation of these samples decreases with the concentration of cobalt (Refer Chapter 3). The M-H isotherms of the samples x=0.1 and x=0.3 show the same magnetic behaviour, whereas the sample x=0.7 exhibits an entirely different pattern. It is observed that the $La_{0.5}Na_{0.5}Mn_{1-x}Co_xO_3$ samples exhibit a decrease in ferromagnetic behaviour with the substitution of cobalt in the Mn site of lanthanum sodium manganite nanoparticles. This is attributed to the antiferromagnetic interaction between $Mn^{4+}$- $Mn^{4+}$ ions rather than the double exchange interaction between $Mn^{3+}$- $Mn^{4+}$ ions. For the cobalt rich sample LNCMO7, the magnetisation isotherms shown in Fig. 4.22 depict that the magnetisation is not saturated even at a higher magnetic field of 50 kOe. This is because the antiferromagnetic interaction between $Mn^{4+}$- $Mn^{4+}$ dominates and leads to the spin glass behaviour of the sample.

### 4.3.3 Magnetic entropy change ($-\Delta S_m$)

The entropy change $-\Delta S_m$ was estimated from the magnetisation (M-H) isotherms at different applied fields for the samples (x=0.1, 0.3 and 0.7) in the $La_{0.5}Na_{0.5}Mn_{1-x}Co_xO_3$ series and is plotted as a function of temperature and are shown in Fig.4.23, Fig.4.24 and Fig.4.25 respectively.

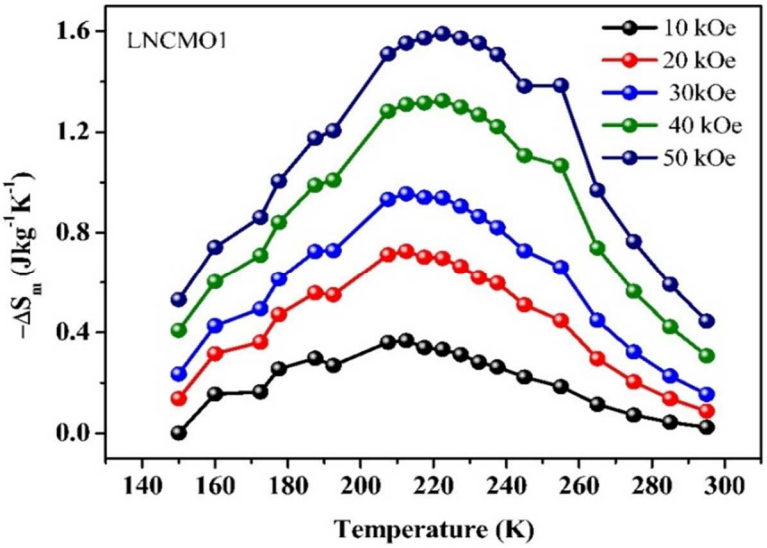


**Figure 4.23.** Variation of $-\Delta S_m$ with temperature $La_{0.5}Na_{0.5}Mn_{0.9}Co_{0.1}O_3$

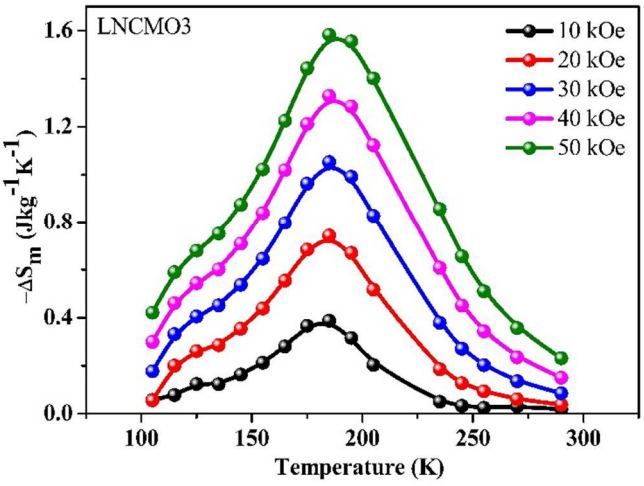


**Figure 4.24.** Variation of $-\Delta S_m$ with temperature $La_{0.5}Na_{0.5}Mn_{0.7}Co_{0.3}O_3$

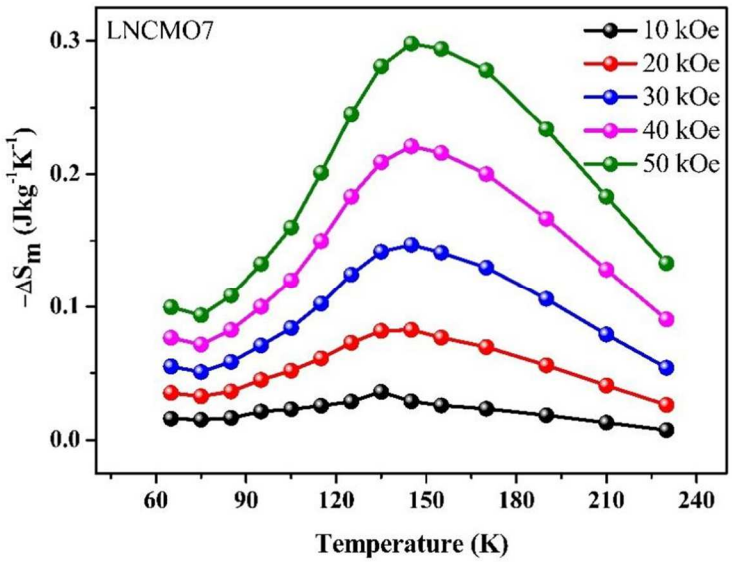


**Figure 4.25.** Variation of $-\Delta S_m$ with temperature $La_{0.5}Na_{0.5}Mn_{0.3}Co_{0.7}O_3$

Fig.4.23 depicts that the estimated maximum entropy change, $-\Delta S_m$, at 20 kOe, 30 kOe and 40 kOe is 0.727 J/kg/K, 0.956 J/kg/K and 1.316 J/kg/K respectively. The magnetic entropy change is enhanced with the applied magnetic field and the estimated maximum value of 1.591 J/kg/K is obtained for 50 kOe at a temperature of 222.5 K. The temperature at which maximum entropy change is recorded changes from 212.5 K to 222.5 K when the field increases from 20 kOe to 50 kOe. It is observed that the initial substitution of $Mn^{3+}$ by $Co^{3+}$ (x=0.1) in the LNMO sample reduces the transition temperature from 312.5 K to 212 K; similar behaviour is reported in cobalt substituted lanthanum manganites[45].

The behaviour of magnetic entropy change of LNCMO3 (x=0.3) as a function of temperature displayed in Fig.4.24, reveals the field dependence of entropy change. It is noteworthy that the peak temperature at which the magnetic entropy change is maximum does not vary with the applied field. The MCE properties of $La_{0.5}Na_{0.5}Mn_{1-x}Co_xO_3$ samples are listed in Table 4.2.

**Table 4.2.** MCE summary of LNCMO samples

| MCE Summary of LNCMO Samples | | | | |
|---|---|---|---|---|
| **Sample** | Applied Field | $\Delta S_m^{max}$ (J/kg/K) | $T_c$ (K) | $T_{peak}$ (K) |
| **LNMO AP** | 10 kOe | 0.1039 | 135K | 155 |
| | 20 kOe | 0.1012 | | 155 |
| | 30 kOe | 0.098 | | 155 |
| | 40 kOe | 0.0952 | | 155 |
| | 50 kOe | 0.487 | | 155 |
| **LNMO** | 10 kOe | 0.612 | 324 | 312.5 |
| | 20kOe | 1.122 | | 312.5 |
| | 30 kOe | 1.566 | | 317.5 |
| | 40 kOe | 1.972 | | 317.5 |
| | 50 kOe | 2.344 | | 317.5 |
| **LNCMO1** | 10 kOe | 0.368 | 211 | 212.5 |
| | 20 kOe | 0.727 | | 212.5 |
| | 30 kOe | 0.956 | | 212.5 |
| | 40 kOe | 1.316 | | 222.5 |
| | 50 kOe | 1.591 | | 222.5 |
| **LNCMO3** | 10 kOe | 0.366 | - | 185 |
| | 20kOe | 0.743 | | 185 |
| | 30 kOe | 1.052 | | 185 |
| | 40 kOe | 1.328 | | 185 |
| | 50 kOe | 1.583 | | 185 |
| **LNCMO7** | 10kOe | 0.029 | 130 | 135 |
| | 20 kOe | 0.082 | | 145 |
| | 30 kOe | 0.147 | | 145 |
| | 40kOe | 0.221 | | 145 |
| | 50 kOe | 0.298 | | 145 |

The maximum values of estimated $\Delta S_m$ are 0.366 J/kg/K, 0.743 J/kg/K, 1.052 J/kg/K, 1.328 J/kg/K, and 1.583 J/kg/K under an applied magnetic field of 10 kOe, 20 kOe, 30 kOe, 40 kOe and 50 kOe, respectively. A maximum magnetic entropy change of 1.583 J/kg/K has been observed for 50 kOe at 185 K for the LNCMO3 (x=0.3) sample. Fig.4.25 depicts that the maximum value of $-\Delta S_m$ of x=0.7 sample enhances from 0.029 J/kg/K to 0.298 J/kg/K when the applied magnetic field increases from 10 kOe to 50 kOe. It is observed that the sample exhibits a maximum entropy change of 0.298 J/kg/K at 145 K. The peak temperature remains at 145 K for the LNCMO7 sample even though the applied magnetic field rises.

The variation of $-\Delta S_m$ with cobalt substitution at different applied magnetic fields is shown in Fig. 4.26. It is observed from Fig. 4.26 that the magnetic entropy change is found to be maximum for the parent element, LNMO. The maximum value of $-\Delta S_m$, 2.344 J/kg/K, is exhibited by the LNMO sample in an applied magnetic field of 50 kOe. With the cobalt substitution, $-\Delta S_m$ decreases from 2.344 J/kg/K for (x=0) to 0.298 J/kg/K for (x=0.7) at 50 kOe.

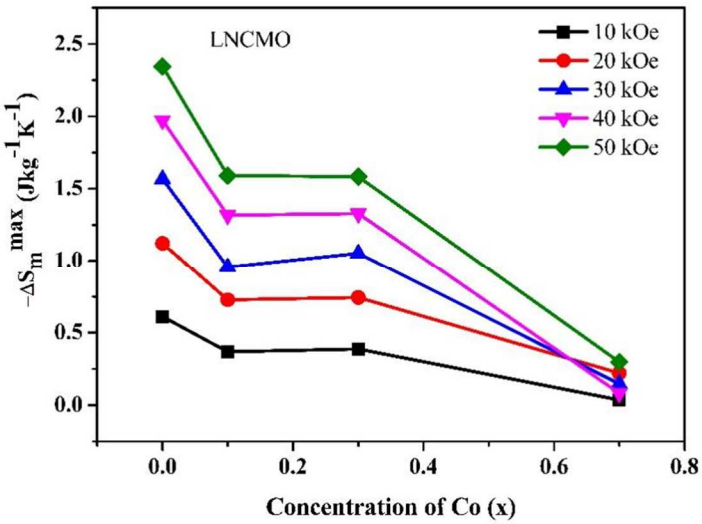


**Figure 4.26.** Variation of $-\Delta S_m$ with cobalt substitution in $La_{0.5}Na_{0.5}Mn_{1-x}Co_xO_3$.

We have investigated the magnetocaloric properties of cobalt substituted lanthanum sodium manganite in the present work which has not been reported so far. The parent sample, LNMO, of the synthesised series $La_{0.5}Na_{0.5}Mn_{1-x}Co_xO_3$ exhibits the largest magnetic entropy change of 2.344 J/kg/K at 317.5 K. It is found that the cobalt substituted samples also show a noticeable change in magnetic entropy; however, this change decreases as the cobalt concentration increases. It is evident from our work that the transition temperature decreases even for a small concentration of cobalt substitution for Mn, as reported in the literature. Even though the magnetic entropy change decreases with the cobalt substitution, a transition broadening is observed in the magnetic entropy curve. A practical magnetic refrigerator performs well in a wide range of temperatures. The peak temperature ($T_{peak}$) at which the entropy change is maximum shifts to a higher temperature region with the increase in applied magnetic field for x=0 and x=0.1 samples in the $La_{0.5}Na_{0.5}Mn_{1-x}Co_xO_3$ series. This can be explained on the basis of Griffith's phase, where short range interactions take place due to the presence of FM clusters in the paramagnetic regime[20]. However, for the other two concentrations, x=0.3 and x=0.7, the peak position is found to be a constant. It is also evident from Table 4.3 that the maximum entropy change is observed at a temperature above the transition temperature. This is attributed to the fact that FM cluster size development is promoted above $T_c$ when a stronger magnetic field is applied. Consequently, the MCE significantly enhances as the applied magnetic field increases[5].

### *4.3.4 Relative Cooling Power (RCP)*

The relative cooling power of the LNCMO1, LNCMO3 and LNCMO7 samples is estimated from their respective magnetic entropy curves. The estimated value of RCP using equation (4.8) for maximum entropy changes 2.344 J/kg/K at an applied field of 50 kOe is 105.75 J/kg for the LNMO sample. As the cobalt concentration increases, a transition broadening is observed, even though the entropy change decreases and hence RCP increases for the initial concentrations of cobalt

substitution (x=0.1 and x=0.3).The variation of RCP of LNCMO samples with cobalt concentration at 50 kOe magnetic field is shown in Fig. 4.27. Even though the entropy change in the cobalt substituted samples is less than the LNMO sample, maximum relative cooling power is exhibited by the x=0.1 sample at a 50 kOe magnetic field due to the transition broadening, which is observed in cation-substituted lanthanum manganite.

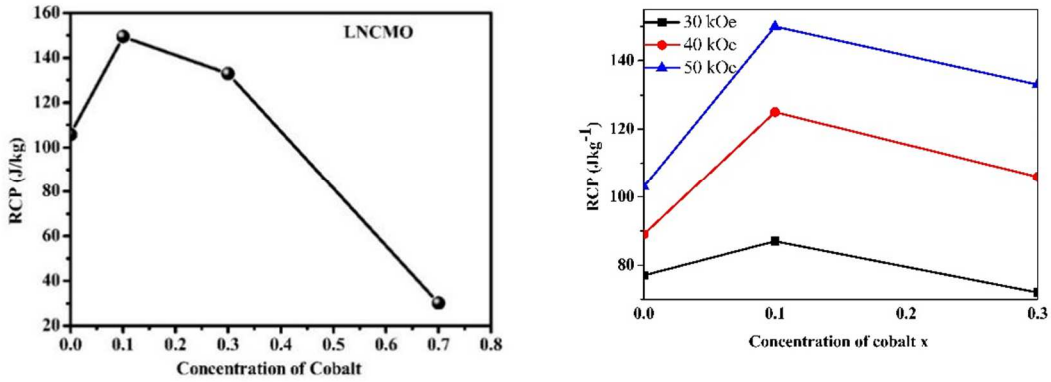


**Figure 4.27.** Variation of RCP with the magnetic field in $La_{0.5}Na_{0.5}Mn_{1-x}Co_xO_3$

It can be concluded that a small amount of cobalt substitution in lanthanum sodium manganite can enhance the magnetic cooling efficiency.

### *4.3.5 Specific Heat Capacity Measurements*

The change in heat capacity and change in magnetic entropy are characteristic properties of a material that can be tuned precisely in manganites for MCE based specific applications through cation engineering[36]. The change in heat capacity of the LNCMO samples is estimated indirectly by employing equation (4.7). The variation of the specific heat capacity as a function of temperature of the samples x=0.1, x=0.3, and x=0.7 is shown in Figs. 4.28, 4.29, and 4.30, respectively.

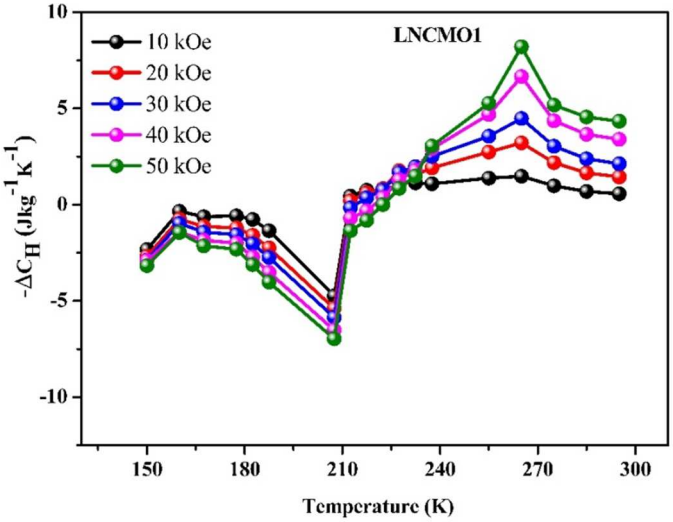


**Figure 4.28.** Variation of $\Delta C_H$ of $La_{0.5}Na_{0.5}Mn_{0.9}Co_{0.1}O_3$ with temperature

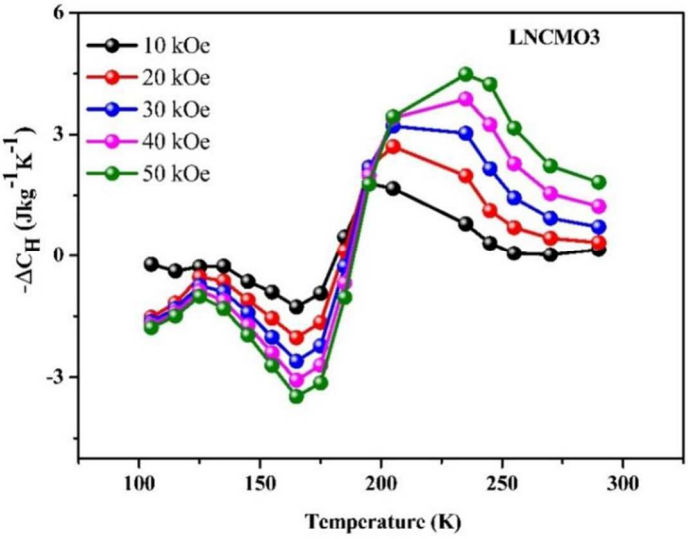


**Figure 4.29.** Variation of $\Delta C_H$ of $La_{0.5}Na_{0.5}Mn_{0.7}Co_{0.3}O_3$ with temperature

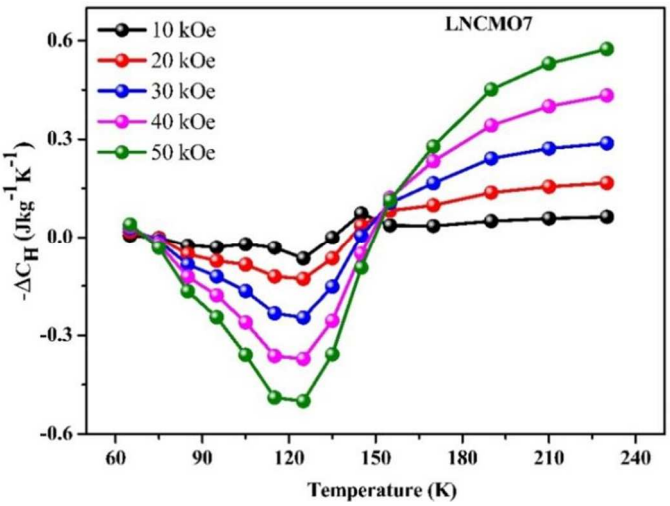


**Figure 4.30.** Variation of $\Delta C_H$ of $La_{0.5}Na_{0.5}Mn_{0.3}Co_{0.7}O_3$ with temperature.

The figures of specific heat variation with temperature exhibits a peak corresponding to minima and maxima, and it crosses over from minimum to maximum near Tc. The second order phase transition is characterised by a discontinuity in $\Delta C_H$ near the transition temperature[32] in LNCMO again confirms the nature of the magnetic transition in the LNCMO sample. However, the variation of $\Delta C_H$ with temperature of the LNCMO7 sample differs from that of the LNCMO1 and LNCMO3 samples due to the presence of antiferromagnetic superexchange interaction. To probe into the details of the nature of magnetic transition in the LNCMO samples (LNCMO1, LNCMO3 and LNCMO7), the critical behaviour analysis is carried out.

### *4.3.6 Critical Behaviour Analysis*

The ZFC-FC curves and the specific heat capacity measurements of the LNCMO samples indicate a second order magnetic phase transition in these samples. So, the nature of the magnetic phase transition in the $La_{0.5}Na_{0.5}Mn_{1-x}Co_xO_3$ samples was examined from the Arrott's plots, Kouvel Fischer approach and the critical isotherm analysis. Arrott plots $M^2$ versus $H/M$ are constructed from magnetic isotherms to explain the nature of the phase transition observed in the LNCMO nanoparticles.

The Arrott plots of the LNCMO1 displayed in Fig.4.31 show that it consists of parallel lines with a positive slope at higher fields. The positive slope of Arrotts plots of the LNCMO1 sample reveals that it has undergone a second-order magnetic transition. It can also be observed that the isotherm that passes through the origin corresponds to a temperature of 225 K, which is very close to the transition temperature of 222.5 K obtained from the $\Delta S_m$ curves. So, the interactions associated with the samples can be approximated to the Mean Field Theory, which can be examined with the estimation of critical exponents.

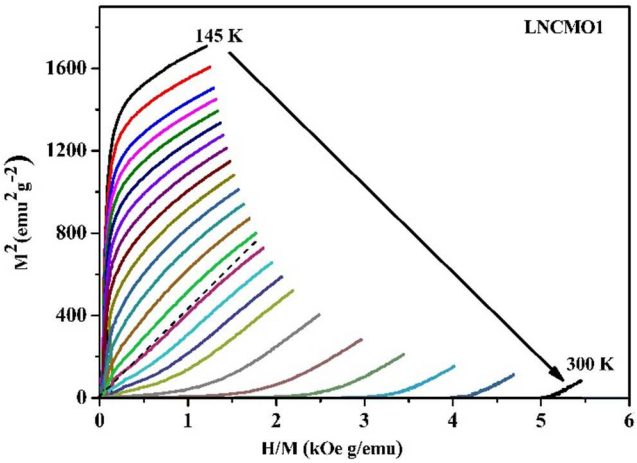


**Figure 4.31.** Arrott Plots of $La_{0.5}Na_{0.5}Mn_{0.9}Co_{0.1}O_3$

Arrott plots of LNCMO3 shown in Fig.4.32 depict that instead of the parallel line in the higher fields, it exhibits an upward curve different from that of the x=0.1 sample. The positive slope of the curves results in a second-order transition associated with the sample. However, the curved shapes of the lines show that the exchange interactions do not follow the long range interactions associated with MFT. The isotherm that passes through the origin of this sample corresponds to 185 K. These results agree with the transition temperature of 185 K obtained from the magnetic entropy curve. But in the case of the LNCMO7, the Arrott plots of $La_{0.5}Na_{0.5}Mn_{0.3}Co_{0.7}O_3$ shown in Fig.4.33 differ from that of the other two samples, x=0.1 and x=0.3. It reveals that the LNCMO7 sample does not undergo an FM to PM

second-order magnetic transition according to Mean Field Theory as the interactions belong to short range [23]. It is consistent with the results obtained from the ZFC-FC curves and magnetisation isotherms of the sample that the superexchange antiferromagnetic interactions between $Mn^{4+}$-$Mn^{4+}$ are present in the sample LNCMO7.

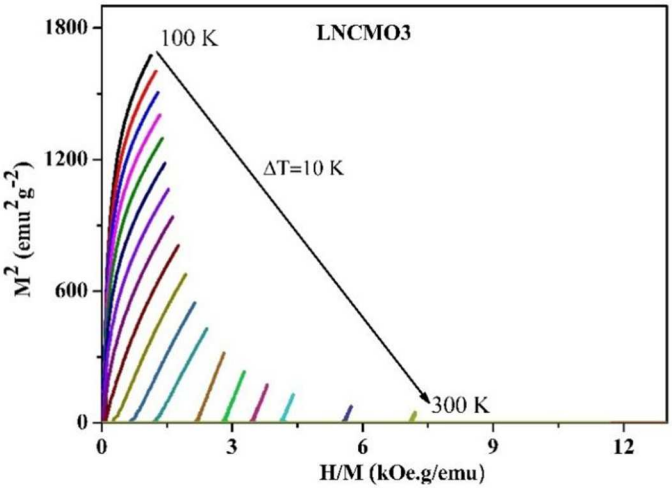


**Figure. 4.32.** Arrott Plots of $La_{0.5}Na_{0.5}Mn_{0.7}Co_{0.3}O_3$

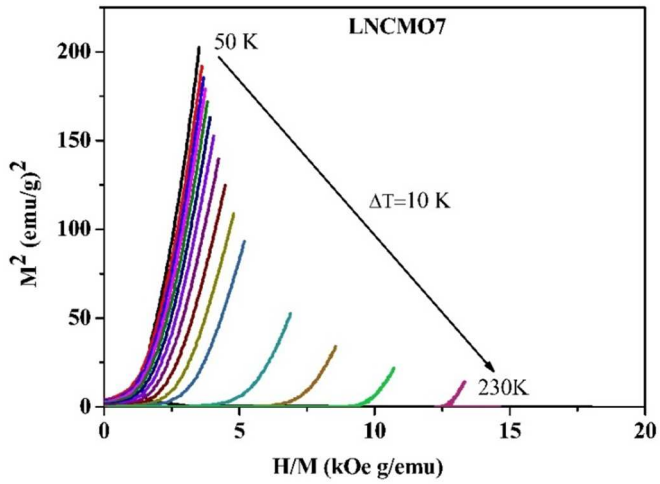


**Figure 4.33.** Arrott Plots of $La_{0.5}Na_{0.5}Mn_{0.3}Co_{0.7}O_3$

So, it can be concluded from the Arrott Plot analysis that the LNCMO1 exhibits a second order magnetic transition following MFT, whereas the samples

LNCMO3, LNCMO7 do not follow the exchange interactions according to MFT. Hence Kouvel Fischer approach and critical isotherm analysis was carried out only in LNCMO1 sample.

The critical exponents $\beta$, $\gamma$ and $\delta$ of LNCMO1 sample are examined as it undergoes a second order transition. The critical exponents $\beta$ and $\gamma$ are estimated using the Kouvel-Fischer method for LNCMO1 sample. Kouvel Fischer plot and critical isotherms plotted in the log-log scale of the LNCMO1 sample are shown in Fig. 4.34 and 4.35 respectively. The estimated values of $\beta$ and $\gamma$ from the KF approach are 0.301 ± 0.111 and 1.273 ± 0.027, respectively. The other exponent δ estimated directly from the critical isotherm at 225 K is 3.225 ± 0.005. However, these values do not match with the values of the critical exponents $\beta=0.5$ and $\gamma=1$ for the long interactions associated with the Mean Field Theory. This is close to the theoretical values $\beta = 0.325$ and $\gamma = 1.241$ with the 3D Ising model. This is owing to the reduction of the double exchange interaction between $Mn^{3+}$-$Mn^{4+}$ and the presence of superexchange interaction with the substitution of cobalt for Mn in lanthanum sodium manganite. Hence the cobalt substitution is found to disturb the long range interactions in the sample.

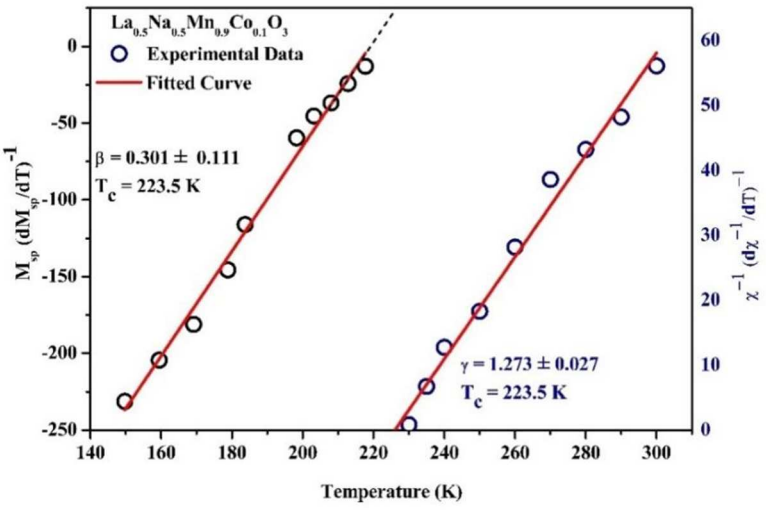


**Figure 4.34.** Kouvel-Fisher plots of $La_{0.5}Na_{0.5}Mn_{0.9}Co_{0.1}O_3$.

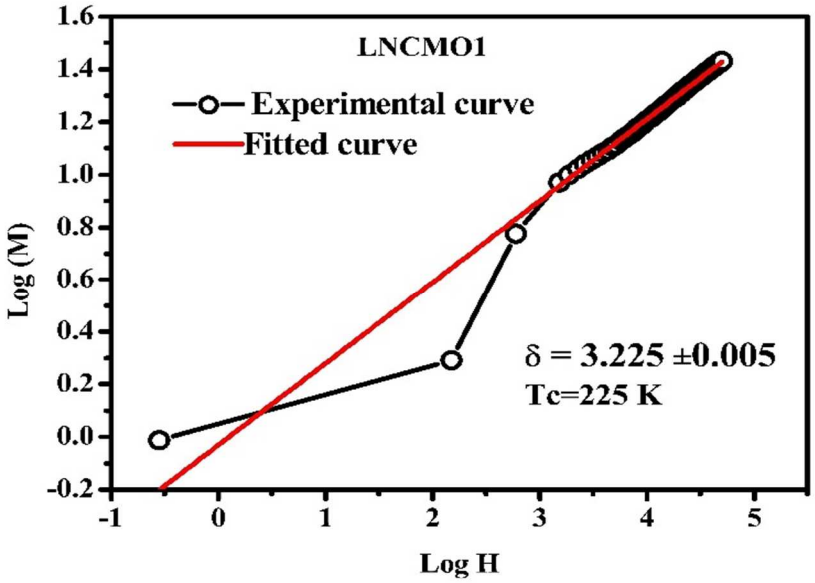


**Figure 4.35.** M-H curves of $La_{0.5}Na_{0.5}Mn_{0.9}Co_{0.1}O_3$ in log-log scale.

The investigation of magnetocaloric properties of the $La_{0.5}Na_{0.5}Mn_{1-x}Co_xO_3$ samples identified a magnetic refrigerant material, $La_{0.5}Na_{0.5}MnO_3$ (LNMO), near room temperature. However, the literature suggests that the MCE properties have applications beyond magnetic cooling, such as magnetic hyperthermia and biomedical applications[7,46]. Since the LNMO sample exhibits an appreciable magnetic entropy change near room temperature, we extended our investigation of the LNMO sample in the hyperthermia applications. The in vitro cytotoxicity measurements are performed on the LNMO sample to check the biocompatibility of the sample.

## 4.4 Biocompatibility and In Vitro Cytotoxicity of LNMO

Magnetic hyperthermia in cancer treatment employs magnetic nanoparticles and localised heat generation to focus on cancer cells selectively. In this technique, biocompatible magnetic nanoparticles are injected into the body, and they accumulate at the tumour site. These nanoparticles typically consist of soft magnetic materials with a narrow hysteresis curve. When these nanoparticles are accumulated

in the tumour, an alternating magnetic field induces rapid oscillation the nanoparticles, resulting in heat generation through hysteresis loss. The heat generation by the magnetic nanoparticles raises the temperature in the tumour region, leading to localised hyperthermia. For apoptotic cell death, this localised hyperthermia aims to achieve a temperature between 42°C and 45°C [46]. In cancer treatment, magnetic hyperthermia has attracted immense attention due to its key advantage that it selectively targets the tumour cells, while the surrounding healthy surrounding tissues are less damaged. This can be examined by the invitro cytotoxicity measurements of the sample. In the present work, as the LNMO sample exhibits a maximum magnetic entropy change in the desired temperature region (42°C - 45°C), the in vitro cytotoxicity measurements were performed on this sample for different concentrations.

The test compound was studied for short term in vitro cytotoxicity using rat spleen cells. Viable cell suspension ($1x10^6$ cells in 0.1 ml) was added to tubes containing various concentrations of the test compound, and the volume was made up to 1 ml using RPM media. Control tubes contained only cell suspension (without additives). These tubes were incubated for 3h at 37°C. At the end of incubation, the cell suspension in the tubes was mixed with 0.1 ml l% trypan blue and kept for 2-3 minutes and loaded on a haemocytometer. Dead cells take up the blue colour of trypan blue, while live cells do not take up the dye. The number of stained cells was counted separately.

$$\%\ Cytotoxicity = \frac{No.of\ dead\ cells}{No.of\ live\ cells + No.of\ dead\ cells} \times\ 100$$

The percentage of cytotoxicity in cell death with the concentration of LNMO sample is shown in Fig. 4.36

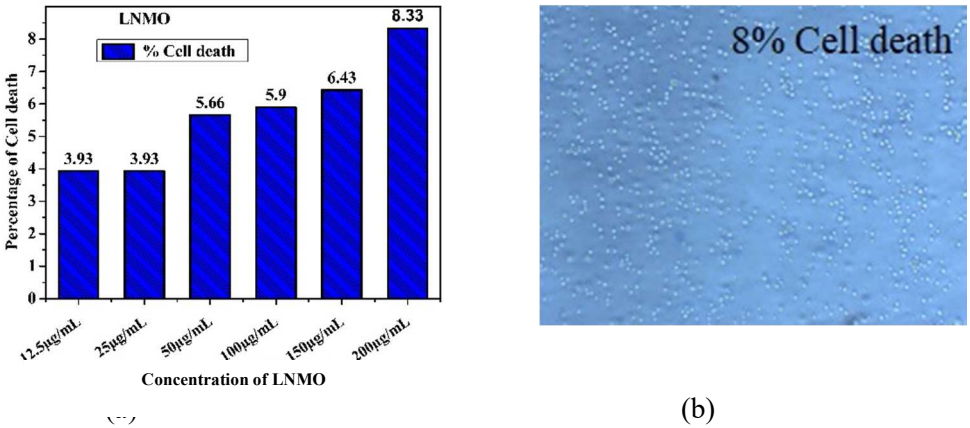


**Figure 4.36. (a)** Percentage of cytotoxicity against normal cell death with concentration of LNMO (b) Optical microscope image of 8% normal cell death after incubation with 200 µg/mL of LNMO

The short-term in vitro cytotoxicity of the LNMO sample against tumor cells was studied using Dalton's Lymphoma Ascites cells (DLA). The tumour cells aspirated from the peritoneal cavity of tumour-bearing mice were washed thrice with PBS or a normal cell line. Cell viability was determined by the trypan blue-exclusion method. Viable cell suspension ($1X10^6$ cells in 0.1ml) was added to tubes containing various concentrations of the test compounds, and the volume was made up to 1 ml using phosphate-buffered cell line (PBS). The control tube contained only cell suspension. These assay mixtures were incubated for 3 hours at 37°C. Further cell suspension was mixed with 0.1 ml of l% trypan blue and kept for 2-3 minutes and loaded on a hemocytometer- Dead cells take up the true colour of trypan blue, while live cells do not take up the dye. The number of stained and unstained cells was counted separately. The fluctuation of cancer cell cytotoxicity (%) with sample concentration is shown in Fig. 4.37. The LNMO sample exhibited 28.8% cytotoxicity against tumour cells at 200 µg/mL, making it a biocompatible anticancer medication.

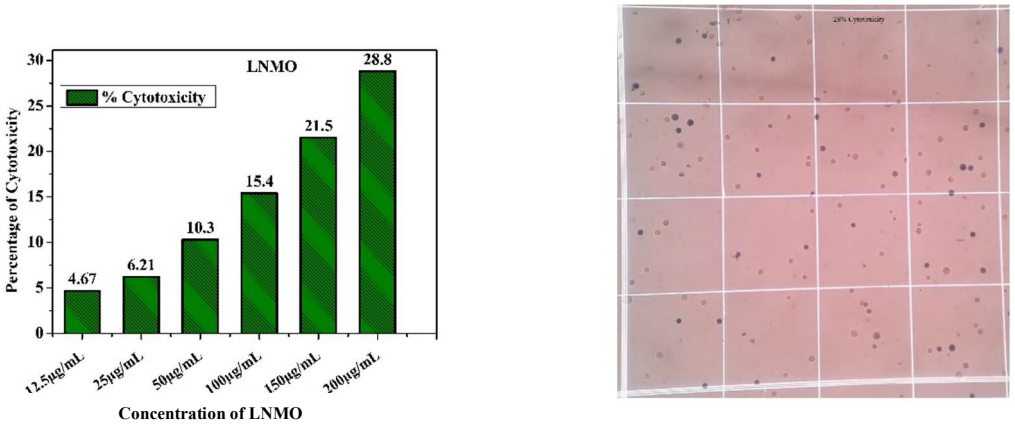


(a) (b)

**Figure 4.37**. a) Percentage of cytotoxicity against tumour cells with concentration of LNMO b) Optical microscope image of 28.8% tumour cell death after incubation of 200 μg/mL of LNMO.

## 4.5 Conclusion

The magnetocaloric properties and nature of magnetic phase transition of $La_{0.5}$ $Na_{0.5}$ $Mn_{1-x}Co_xO_3$ (x=0, 0.1, 0.3 and 0.7) samples have been investigated in this chapter. The transition temperature was determined from the ZFC-FC curves under different applied magnetic fields according to their magnetisation. The transition temperature varies from 324 K to 130 K with the substitution of cobalt in lanthanum sodium manganite. The magnetic isotherms were recorded in the vicinity of the transition temperature for these samples. Magnetic entropy change $|\Delta S_m|$ has been estimated from the magnetic isotherms, and it is found to be a maximum of 2.344 J/kg/K for the $La_{0.5}Na_{0.5}MnO_3$ (LNMO) sample and is found to increase with applied magnetic field. So, the field dependence of $|\Delta S_m|$ has been investigated, and the value of the local exponent $n$ is consistent with that of a second order magnetic transition for LNMO. An adiabatic temperature change of 0.7 K is estimated indirectly from the estimated specific heat capacity values. The calculated value of RCP for maximum entropy changes 2.344 J/kg/K at an applied field of 50kOe is 105.75 J/kg for the LNMO sample. A maximum entropy change $|\Delta S_m|$ of 1.591 J/kg/K , 1.583 J/kg/K and 0.298 J/kg/K is obtained for $La_{0.5}Na_{0.}5Mn1_{-x}Co_xO_3$ for x=0.1, 0.3 and 0.7 (LNCMO1, LNCMO3 and LNCMO7) samples respectively at an

applied field of 50kOe. Even though the $|\Delta S_m|$ values decreased with increase in cobalt concentration, the RCP attains a maximum for the LNCMO1 sample, and then it decreases with cobalt substitution. In the critical behaviour analysis, the positive slope of the $M^2$ vs. $\frac{M}{H}$ in Arrott plots and Kouvel Fischer plots confirmed the second order magnetic phase transition of the LNMO samples. The critical exponents $\beta$, $\gamma$ and $\delta$ of the LNMO sample, 0.43, 1.00, and 2.82, respectively, are consistent with the Mean field theory, which confirms the long-range interaction in an FM-PM transition. For the other samples LNCMO1, LNCMO3 and LNCMO7, the results of critical behaviour analysis does not match with the theory of long range interactions according to Mean Field Theory. Based on the investigations of the magnetocaloric properties of lanthanum sodium manganite perovskite nanoparticles, it can be concluded that the parent sample LNMO is a promising material for magnetic refrigerant applications near room temperature. The increase in the relative cooling power of the initially substituted sample LNCMO1 can also be chosen as a refrigerant material. The cytotoxicity measurement of the sample LNMO on normal cells (8% cell death) confirmed the biocompatibility of the samples while 29% of cell death was obtained for tumour cells. The combination of these properties with the material's magnetocaloric characteristics near room temperature highlights its potential for biomedical applications like hyperthermia treatment of cancer/tumour cells.

**REFERENCES**

[1] V.K. Pecharsky, K.A. Gschneidner, J Magn Magn Mater 200 (1999) 44–56.

[2] V.K. Pecharsky, V.K. Pecharsky, K.A. Gschneidner, K.A. Gschneidner, A.O. Pecharsky, A.M. Tishin, Phys Rev B Condens Matter Mater Phys 64 (2001) 1444061–14440613.

[3] F. Zhang, K. Westra, Q. Shen, I. Batashev, A. Kiecana, N. van Dijk, E. Brück, J Alloys Compd 906 (2022) 164337.

[4] C.P. Reshmi, S. Savitha Pillai, K.G. Suresh, M.R. Varma, Solid State Sci 19 (2013) 130–135.

[5] S.K. Estemirova, V.Y. Mitrofanov, S.A. Uporov, R.I. Gulyaeva, J Magn Magn Mater 502 (2020) 166593.

[6] I. Walha, M. Smari, T. Mnasri, E. Dhahri, J Magn Magn Mater 454 (2018) 190–195.

[7] C.O. Ehi-Eromosele, J.A.O. Olugbuyiro, A. Edobor-Osoh, A.A. Adebisi, O.A. Bamgboye, J. Ojeifo, Journal of Biomimetics, Biomaterials and Biomedical Engineering 37 (2018) 117–127.

[8] S. Pandey, A. Quetz, A. Aryal, I. Dubenko, D. Mazumdar, S. Stadler, N. Ali, International Journal of Hyperthermia 33 (2017) 779–784.

[9] A.O. Ayaş, E. Seçilmiş, A. Ekicibil, J Mol Struct 1231 (2021).

[10] M. Oumezzine, O. Peña, T. Guizouarn, R. Lebullenger, J Magn Magn Mater 324 (2012) 2821–2828.

[11] M. Phan, S. Yu, N.H. Hur, Appl. Phys. Lett, 3 (2005) 10–13.

[12] S. Das, T.K. Dey, J Alloys Compd 440 (2007) 30–35.

[13] M. Iqbal, M.N. Khan, A.A. Khan, N. Zafar, J Alloys Compd 769 (2018) 766–776.

[14] K. Laajimi, M. Khlifi, E.K. Hlil, M.H. Gazzah, J. Dhahri, J Magn Magn Mater 491 (2019) 165625.

[15] S.B. Kansara, D. Dhruv, B. Kataria, C.M. Thaker, S. Rayaprol, C.L. Prajapat, M.R. Singh, P.S. Solanki, D.G. Kuberkar, N.A. Shah, Ceram Int 41 (2015) 7162–7173.

[16] F. Ayadi, F. Saadaoui, W. Cheikhrouhou-Koubaa, M. Koubaa, A. Cheikhrouhou, L. Sicard, S. Ammar, IOP Conf Ser Mater Sci Eng 28 (2012).

[17] S.C. Maatar, R. M'Nassri, W.C. Koubaa, M. Koubaa, A. Cheikhrouhou, J Solid State Chem 225 (2015) 83–88.

[18] M. Koubaa, W.C.R. Koubaa, A. Cheikhrouhou, J Alloys Compd 479 (2009) 65–70.

[19] N. Sethulakshmi, I.A. Al-Omari, K.G. Suresh, M.R. Anantharaman, Appl Phys Lett 104 (2014).

[20] H. Biswal, V. Singh, R. Nath, J.R. Sahu, Mater Res Bull 133 (2021) 111030.

[21] A. Mleiki, R. M'nassri, W. Cheikhrouhou-Koubaa, A. Cheikhrouhou, E.K. Hlil, J Alloys Compd 727 (2017) 1203–1212.

[22] S. Vadnala, S. Asthana, J Magn Magn Mater 446 (2018) 68–79.

[23] S. Tillaoui, A. El Boubekri, A. Essoumhi, M. Sajieddine, E.K. Hlil, R. Moubah, M. Sahlaoui, A. Razouk, H. Lassri, Materials Science and Engineering: B 266 (2021) 115052.

[24] J.S. Kouvel, M.E. Fisher, Physical Review 136 (1964).

[25] Meenakshi, A. Kumar, R.N. Mahato, J Magn Magn Mater 448 (2018) 60–65.

[26] M.H. Phan, H.X. Peng, S.C. Yu, N. Hwi Hur, J Magn Magn Mater 290-291 PA (2005) 665–668.

[27] D.T. Morelli, A.M. Mance, J. V. Mantese, A.L. Micheli, J Appl Phys 79 (1996) 373–375.

[28] A. Jerbi, A. Krichene, N. Chniba-Boudjada, W. Boujelben, Physica B Condens Matter 477 (2015) 75–82.

[29] H. Oesterreicher, F.T. Parker, J Appl Phys 55 (1984) 4334–4338.

[30] V. Franco, J.S. Blázquez, A. Conde, Appl Phys Lett 89 (2006) 6–9.

[31] V. Franco, J.S. Blazquez, B. Ingale, A.Conde, annurev.matsci., 42 (2012) 305-342.

[32] S. Datta, S. Guha, S.K. Panda, M. Kar, Appl Phys A Mater Sci Process 127 (2021) 1–10.

[33] T.-L. Phan, P. Zhang, T.D. Thanh, S.C. Yu, J Appl Phys 115 (2014).

[34] M. Iqbal, M.N. Khan, A.A. Khan, N. Zafar, J Alloys Compd 769 (2018) 766–776.

[35] V.K. Pecharsky, K.A. Gschneidner, J Appl Phys 86 (1999) 565–575.

[36] M. Földeàki, R. Chahine, T.K. Bose, J Appl Phys 77 (1995) 3528–3537.

[37] A. Arrott, J.E. Noakes, Phys Rev Lett 19 (1967) 786–789.

[38] B.K. Banerjee, Physics Letters 12 (1964) 16–17.

[39] B. Simon, Phase Transitions and Collective Phenomena, Chapter 3, Cambridge University Press (1997) 39-43.

[40] N. Sethulakshmi, I.A. Al-Omari, K.G. Suresh, M.R. Anantharaman, Appl Phys Lett 104 (2014).

[41] A. Ben Hassine, S. Hcini, A. Dhahri, M.L. Bouazizi, E.K. Hlil, M. Oumezzine, J Mol Struct 1142 (2017) 102–109.

[42] L. Kumar, P. Kumar, S.Srivastava, M.Kar, J.Supercond. Nov.Magn 27(7) (2014).

[43] C.R. Sankar, P.A. Joy, Phys Rev B Condens Matter Mater Phys 72 (2005) 1–4.

[44] A. Rostamnejadi, H. Salamati, P. Kameli, H. Ahmadvand, J Magn Magn Mater 321 (2009) 3126–3131.

[45] M.A. Gdaiem, S. Ghodhbane, A. Dhahri, J. Dhahri, E.K. Hlil, J Alloys Compd 681 (2016) 547–554.

[46] A.B. Tewari, R. Sharma, D. Sharma, Results in Engineering 20 (2023) 101537.

…..ର*ର…..

# Chapter 5

# Synthesis, Structural and Magnetic Properties of Cobalt substituted Copper Ferrite Nanoparticles $Cu_{1-x}Co_xFe_2O_4$

## Objectives

The synthesis, structural, and magnetic properties of cobalt-substituted copper ferrite nanoparticles ($Cu_{1-x}Co_xFe_2O_4$) are detailed. The structural analysis was performed by different techniques and the magnetic properties of the samples at room temperature and at a lower temperature have been studied and compared.

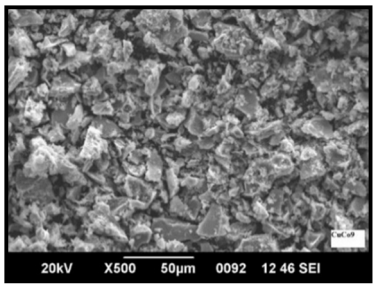


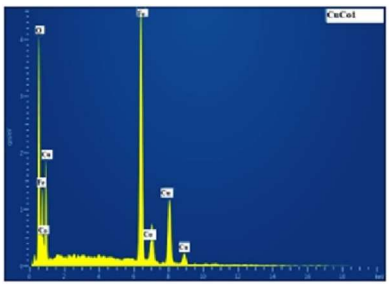

*S. Bhaskaran, I.A. Al-Omari, E.V. Gopalan, On the enhanced coercive field and anisotropy observed in cobalt substituted copper ferrite nanoparticles prepared by a modified sol-gel method, J Alloys Compd 884 (2021) 161095. https://doi.org/10. 1016/J.JALLCOM.2021.161095.*

## 5.1 Introduction

Transition metal oxides are being studied extensively in nanostructures due to their wide applications such as magnetic sensors, actuators, magnetic tape, magnetic fluids, microwave devices [1–5]. Among the transition metal oxides, numerous works are being carried out in ferrite nanoparticles because of their important physical, chemical and electrical properties[6–8]. $CuFe_2O_4$ is one of the important candidates of ferrite groups, which has been under focus due to the structural transformation and reduction of crystal symmetry known as Jahn-Teller distortion [9,10]. Generally, copper ferrite crystallises into a spinel structure, which may exist in two symmetries, tetragonal for T < 427°C (space group *I*41/*amd*) and cubic space group *Fd*3*m* at *T* > 700 K (427°C) for T > 427°C. A phase transition is observed in $CuFe_2O_4$ between these two structures, which can be explained by Jahn-Teller distortion. This is because the oxygen environment of copper ion becomes distorted, the orbital degeneracy of electronic states is removed, and the total energy of the system is reduced [10]. Properties of nano ferrites can be tailored and improved by the incorporation of suitable cations into the spinel lattice. The transition metal substitution in $Cu_{1-x}B_xFe_2O_4$ (B-Mn, Zn, Ni, Co, Mg) plays an important role in the electrical, magnetic, and optical properties of $CuFe_2O_4$ nanoparticles[11–14]**.** It is identified from the literature that the saturation magnetization *($M_s$)* of bulk copper ferrite is 33.4 emu/g.The difference in the value of $M_s$ of the bulk and nanostructured (24.73 emu/g) copper ferrite is because of the size and Jahn Teller distortion appearing in the nanoparticles[9]. The dependence of $M_s$ on the nanoparticle size in copper ferrite is due to surface spins, which prevent the inner core spins of the nanoparticle from aligning with the field. As a result, the saturation magnetisation $M_s$ and remanent magnetisation ($M_r$) decrease for smaller particles and increase for larger particles [9].

$CuFe_2O_4$ and $CoFe_2O_4$ are two ferrite systems that show varied structural, magnetic and electrical properties. The remarkable properties of cobalt, like high

coercivity, moderate saturation magnetisation, strong magneto crystalline anisotropy, good mechanical hardness and chemical stability, can suitably be exploited by substituting cobalt for copper in $CuFe_2O_4$**.** It is identified from the literature that there are investigations on the properties of substitution of $Co^{2+}$ for $Cu^{2+}$ in $CuFe_2O_4$ and their applications in the field of biotechnology [15,16]. It has been reported that cobalt doped copper ferrite nanoparticles and their nanocomposites with carbon nanotubes synthesized by the microemulsion method are excellent materials having photocatalytic properties [17]. The antibacterial properties of copper substituted cobalt ferrite have been investigated [18,19]**.** The electrical and magnetic properties of $Cu_{1-x}Co_x$ $Fe_2O_4$ nanoparticles has also been reported by several researchers [20–22]. The magnetocaloric properties (MCE) of substituted copper and cobalt ferrite have also been investigated recently [23,24].

The substitution of cobalt for copper in $CuFe_2O_4$ can alter the structural properties of $CuFe_2O_4$ as they exhibit two different structures. Among the various synthesis methods, sol-gel auto combustion method is chosen for the synthesis of nano ferrites in the present study as it is a well-known method to produce good quality, crystalline, homogenous nano-powder samples and is also cost-effective [8]. The $Cu_{1-x}Co_xFe_2O_4$ samples, which are reported to be hard magnetic materials, exhibit the evolution of magneto crystalline anisotropy[25]. There are only a few reports on the study of magneto crystalline anisotropy of $Cu_{1-x}Co_xFe_2O_4$ nanoparticles even though many researchers have investigated the biomedical, photocatalytic and technological applications of $Cu_{1-x}Co_xFe_2O_4$ nanoparticles[26]. Hence, a study on a series of cobalt substituted copper ferrite nanoparticles emphasising the evolution of the anisotropy characteristics can help understand the magnetism in ferrites. In the present chapter, structural and magnetic properties of the cobalt substituted copper ferrite nanoparticles, $Cu_{1-x}Co_x$ $Fe_2O_4$ (x=0, 0.1, 0.2, 0.3, 0.4, 0.5, 0.7, 0.8, 0.9 and 1) are investigated. It is also envisaged to carry out the MCE characterisation of these materials.

## 5.2 Synthesis and characterisation

The cobalt substituted copper ferrite nanoparticles with molecular formula $Cu_{1-x}Co_xFe_2O_4$ (x=0, 0.1, 0.2, 0.3, 0.4, 0.5, 0.7, 0.8, 0.9 and 1) have been synthesized by a modified sol-gel auto combustion method (Chapter 2. Section 2.2.3). Cobalt nitrate Co $(NO_3)_2.6H_2O$, copper nitrate Cu $(NO_3)_2.3H_2O$, iron nitrate Fe $(NO_3)_3.9H_2O$ and citric acid ($C_6H_8O_7$) are the precursors used to synthesize $Cu_{1-x}Co_xFe_2O_4$ nanoparticles. The metal nitrates in the stoichiometric ratio are dissolved separately in deionized water and stirred well to get a metal nitrate solution. The stoichiometric amount of citric acid is added to the metal nitrate solution in the molar ratio 1:1 and is stirred for half an hour using a magnetic stirrer. Then, the solution is shifted to a hot plate and is heated. It is observed that the solution is first turned to black coloured gel and then ultimately underwent auto combustion to yield a black coloured powder. Powder samples of cobalt substituted copper ferrite nanoparticles are obtained. The samples are labelled as CuFe, CuCo1, CuCo2, CuCo3, CuCo4, CuCo5, CuCo6, CuCo7, CuCo8 CuCo9 and CoFe respectively, for the concentrations x=0, 0.1, 0.2, 0.3, 0.4, 0.5, 0.6, 0.7, 0.8, 0.9 and 1.

The structural characterisation of the $Cu_{1-x}Co_xFe_2O_4$ samples has been carried out by X-ray diffraction technique, Rietveld Analysis, TEM and FTIR spectroscopy. The magnetic characterisation of the samples was carried out by Vibration Sample Magnetometry (VSM) at room temperature and a lower temperature of 5 K.

## 5.3 Results and Discussion

### Structural Characterisation

#### *5.3.1 XRD Analysis*

The XRD patterns of $CuFe_2O_4$ nanoparticles sintered at 800°C, $CoFe_2O_4$, and $Cu_{1-x}Co_xFe_2O_4$ (x= 0.1 to 0.9) are shown in Fig.5.1(a) and Fig.5.1 (b) and Fig.5.2, respectively. The XRD pattern of $CuFe_2O_4$ reveals that it exhibits a tetragonal

structure while it changes to a cubic structure with the substitution of cobalt ($Cu_{1-x}Co_xFe_2O_4$).

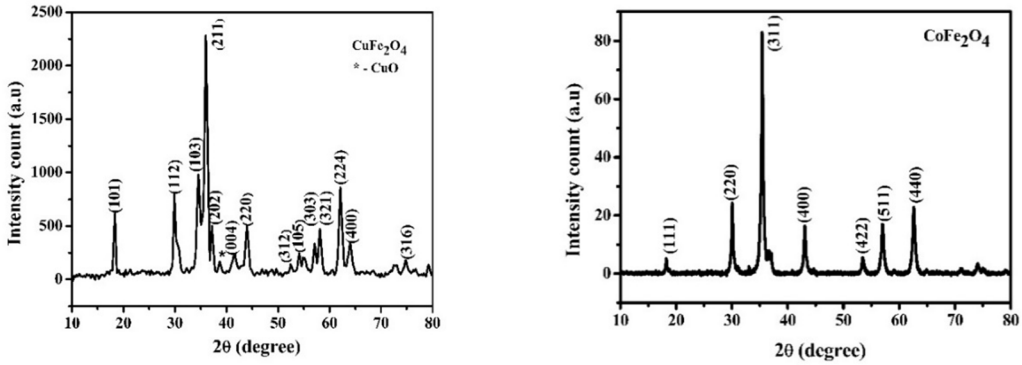


**(a)** $CuFe_2O_4$ (b) $CoFe_2O_4$

**Figure 5.1.** XRD pattern of (a) $CuFe_2O_4$ (b) $CoFe_2O_4$

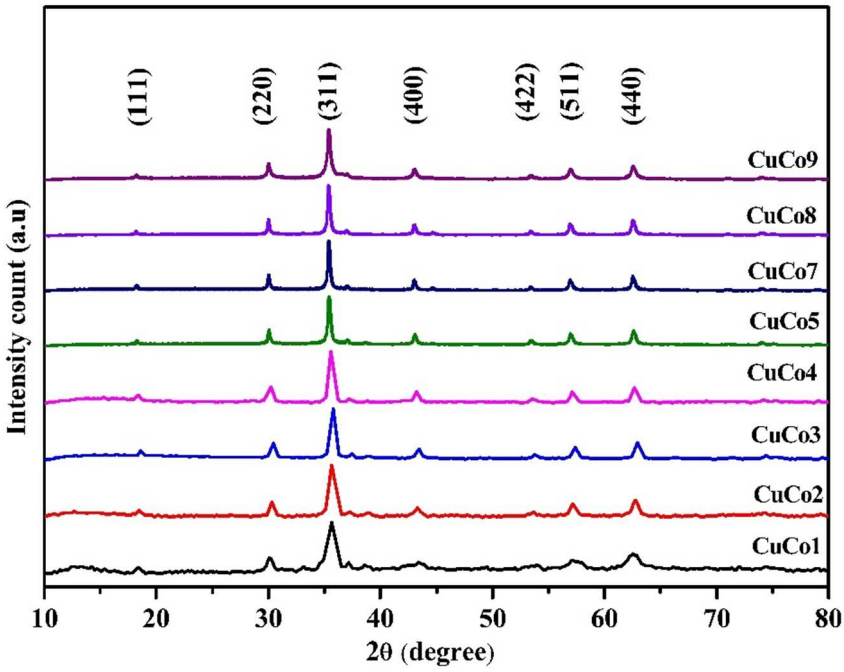


**Figure 5.2.** XRD pattern of $Cu_{1-x}Co_xFe_2O_4$ (x=0.1 -1) nanoparticles

It is observed from the XRD pattern that the peaks of $CuFe_2O_4$ sample are consistent with the peaks of the body-centred tetragonal structure with I41/amd space group (JCPDS No. 34-0425), and an additional peak of CuO has been observed [27]. The XRD patterns of $Cu_{1-x}Co_xFe_2O_4$ samples in Fig. 5.2 revealed that all peaks are indexed to pure cubic phase with *fd3m* space group. The diffraction peaks corresponding to (220), (311), (400), (422), (511), and (440) crystal planes exhibited the face-centered cubic crystal and are in good agreement with JCPDS-00-001-1121[20]. When $Cu^{2+}$ is substituted with $Co^{2+}$ in $CuFe_2O_4$, the crystal structure changes from tetragonal to cubic symmetry. The structural change can be observed even for the initial substitution of cobalt, $Cu_{0.9}Co_{0.1}Fe_2O_4$, which is crystallised in a cubic structure.

The average crystallite size *D* of the samples was calculated by employing the Scherrer formula[28]. The estimated crystallite size of $Cu_{1-x}Co_xFe_2O_4$ samples varied from 18 nm to 34 nm with cobalt substitution. The lattice parameter values of tetragonal structured $CuFe_2O_4$ and cubic structured $Cu_{1-x}Co_xFe_2O_4$ nanoparticles were calculated using equations (5.1) and (5.2), respectively.

$$\frac{1}{d^2} = \frac{h^2}{a^2} + \left[\frac{k^2}{a^2} + \frac{l^2}{c^2}\right] \tag{5.1}$$

$$\frac{1}{d^2} = \frac{h^2+k^2+l^2}{a^2} \tag{5.2}$$

X-ray density is calculated by employing the formula

$$d_x = \frac{8M}{Na^3} \tag{5.3}$$

where *M* is the molecular weight and *N* is the Avogadro number.

The structural parameters, such as crystallite size and lattice constant, are listed in Table 5.1.

**Table 5.1.** Structural parameters of $Cu_{1-x}Co_xFe_2O_4$ samples from XRD analysis

| X | Crystallite size | Lattice Constant | Xray density | Structure |
|---|---|---|---|---|
| | nm | Å | g/cm$^3$ | |
| **0** | 18 | c=8.693, a=5.816 | 4.842 | Tetragonal |
| **0.1** | 13 | 8.398 | 5.455 | Cubic |
| **0.2** | 20 | 8.349 | 5.439 | Cubic |
| **0.3** | 23 | 8.315 | 5.495 | Cubic |
| **0.4** | 24 | 8.363 | 5.391 | Cubic |
| **0.5** | 32 | 8.397 | 5.313 | Cubic |
| **0.7** | 34 | 8.403 | 5.281 | Cubic |
| **0.8** | 33 | 8.407 | 5.265 | Cubic |
| **0.9** | 29 | 8.398 | 5.261 | Cubic |
| **1** | 26 | 8.396 | 5.265 | Cubic |

The values of lattice constants *a* and *c* of the tetragonal structured $CuFe_2O_4$ nanoparticle obtained from XRD are *a=5.816 Å* and *c=8.693 Å*. The ratio *c/a*>1 for $CuFe_2O_4$, which indicates that most of the $Cu^{2+}$ ions were located in the octahedral site[10]. Hence, the synthesised $CuFe_2O_4$ sample is an inverse spinel. The structural formula of inverse spinel $CuFe_2O_4$ is given by $(Cu_xFe_{1-x})[Cu_{1-x}Fe_{1+x}]O_4$, where the inversion parameter $x \approx 0$ [29] reveals that half of the $Fe^{3+}$ ions are in tetrahedral A sub-lattice, while $Fe^{3+}$ ions statistically occupy the octahedral B sub-lattice $Fe^{3+}$ ions and $Cu^{2+}$ ions occupy the octahedral B sub-lattice. The experimental values of lattice constants *a* and *c* of the tetragonal $CuFe_2O_4$ sample obtained are in good agreement with the values reported in the literature [10]. For the other samples with $x > 0$, as the lattice constants *a=b=c,* they crystallize in the cubic spinel structure. The substitution of cobalt in copper ferrite replaces the $Cu^{2+}$ ions from the octahedral site to the tetrahedral site. Further increase in cobalt concentration replaces the $Fe^{3+}$ ions from the tetrahedral lattice to the octahedral lattice when $Cu^{2+}$ takes the positions in the tetrahedral lattice and hence results in a structural transition.

### *Rietveld Analysis*

The Rietveld refined patterns of typical samples (x=0.5, x=0.8, and x=1) in $Cu_{1-x}Co_xFe_2O_4$ samples are shown in Fig.5.3. Best fit with the least difference is obtained for these samples, and the refined structural parameters are shown in Table 5.2.

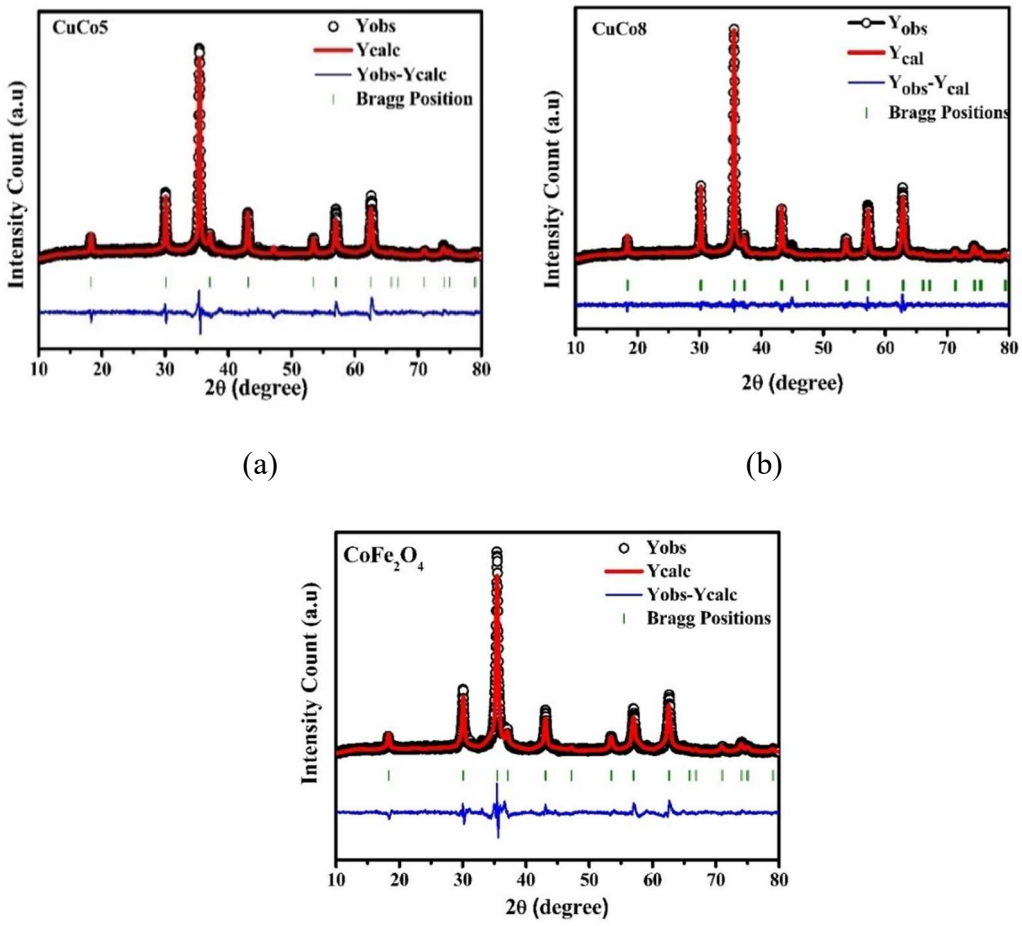


**Figure. 5.3.** Rietveld refined patterns of (a) CuCo5, (b)CuCo8, and (c) $CoFe_2O_4$.

**Table 5.2** Refined structural parameters of CuCoFe samples.

| **Sample** | **CuCo5** | **CuCo8** | **$CoFe_2O_4$** |
|---|---|---|---|
| **Structure** | Cubic | Cubic | Cubic |
| **Lattice constant a (Å)** | 8.398 | 8.364 | 8.397 |
| **Unit cell volume V(Å)$^3$** | 592.276 | 585.26 | 592.089 |
| **$R_{wp}$** | 27.3 | 16.5 | 29.1 |
| **$R_{exp}$** | 13.94 | 11.83 | 12.91 |
| **$R_{Bragg}$** | 3.12 | 1.7 | 1.54 |
| **$\chi^2$** | 3.84 | 1.95 | 5.10 |

The variation of crystallite size and lattice constant with cobalt concentration is shown in Fig. 5.4 and Fig. 5.5, respectively. The crystallite size increases with the concentration of cobalt and reaches a maximum at x=0.8; thereafter, it decreases due to the cation redistribution in the A and B sites.

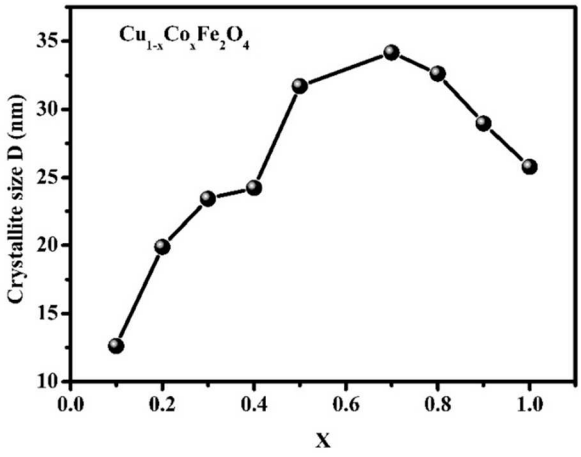


**Figure 5.4.** Variation of crystallite size with x in $Cu_{1-x}Co_xFe_2O_4$

It is observed from Fig. 5.5 that the lattice constant decreases for the initial concentrations of cobalt and increases thereafter. The decreasing nature of the lattice

constant for the initial concentrations of x is due to the structural transitions from tetragonal structure to cubic. In the parent compound, copper ferrite, most of the $Cu^{2+}$ ions occupy the octahedral site, while the initial substitution of cobalt replaces the larger $Cu^{2+}$ ions by $Fe^{3+}$ ions in the octahedral site, resulting in a decrease of lattice constant for samples with x=0.1 to 0.3. The further increase of *a* is due to the incorporation of smaller $Cu^{2+}$ (0.72Å) ions by larger $Co^{2+}$ ions (0.74Å) in the lattice. As it approaches $CoFe_2O_4$, the value of the lattice constant decreases. It may be attributed to the redistribution of cobalt ions in the tetrahedral and octahedral lattices. The lattice constant will be affected by the site occupation of $Fe^{3+}$ and $Co^{2+}$, which is known to vary with the different synthesis processes [30,31]. The lattice constant of $CoFe_2O_4$ (8.396 Å) is in good agreement with the reported value of 8.394 Å [30] .

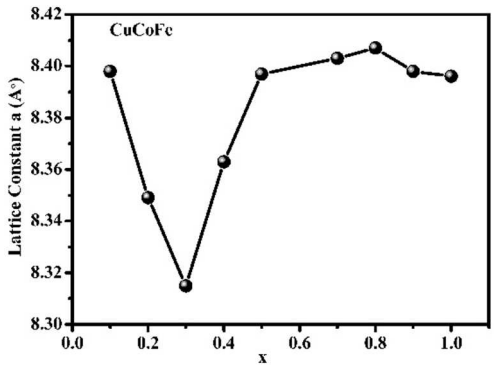


**Figure 5.5.** Variation of lattice constant with x in $Cu_{1-x}Co_xFe_2O_4$

The tetragonal distortion of the octahedral site of $CuFe_2O_4$ is due to the Jahn-Teller effect found with the octahedral site cation ($Cu^{2+}$) having a high spin state. The $Cu_{1-x}Co_xFe_2O_4$ crystallises in the cubic structure even with the initial concentration of cobalt substitution for x=0.1. When $Co^{2+}$ is substituted in $CuFe_2O_4$, $Cu^{2+}$ replaces $Fe^{3+}$ at the tetrahedral site, and it reduces the Jahn-Teller distortion. This is due to the site preference of $Co^{2+}$, which leads to the transfer of $Fe^{3+}$ from the A site to the B site and results in a structural distortion from tetragonal to cubic. Lattice contraction for the initial compositions for $x < 0.3$ and thereafter a lattice expansion has been observed in $Cu_{1-x}Co_xFe_2O_4$ samples. Similar structural

properties have been reported in cobalt-substituted copper ferrite nanoparticles[32]. The cobalt substitution in copper ferrite has modified its structure, cation distribution, and lattice parameter.

### *5.3.2. FTIR Spectroscopy*

The FTIR spectra of $Cu_{1-x}Co_xFe_2O_4$ samples recorded in the frequency range 400-4000 $cm^{-1}$ are shown in Fig. 5.6. The absorption and the vibrational bands formed in the nanocrystalline particles are identified from the FTIR spectrum.

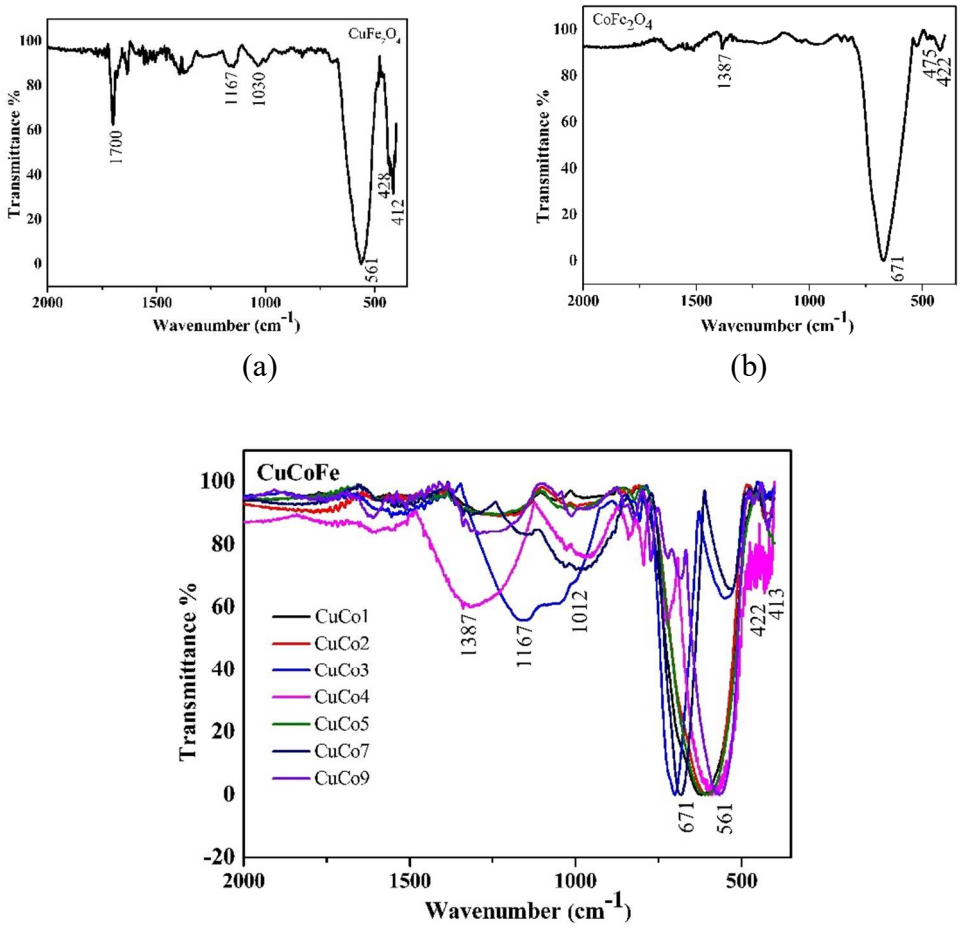


**Figure 5.6.** FTIR spectrum of $Cu_{1-x}Co_xFe_2O_4$

According to Waldron, ferrites can be regarded as continuously connected crystals, in which the atoms are linked to all of their nearest neighbors by ionic, covalent, or Vander Waals forces[33]. The metal ions in ferrites are arranged in two distinct sub-lattices, known as the tetrahedral (A-site) and octahedral (B-site), depending on the geometry of the oxygen nearest neighbors. In general, the IR spectra of spinel ferrite consist of two strong absorption bands, $\nu_2$ (330-400 $cm^{-1}$) attributed to the octahedral metal-oxygen bond and $\nu_1$ (540-600 $cm^{-1}$) associated with the stretching vibration of the tetrahedral metal-oxygen bond (Fe-O) [5]. It can be observed from Fig. 5.9.(a) that the band around 428 $cm^{-1}$ is associated with the stretching vibrations of Cu ions in the octahedral site and the band around 561 $cm^{-1}$ corresponds to the stretching vibrations of the tetrahedral Fe-O bond [34,35]. The stretching vibrations around 475 $cm^{-1}$ shown in Fig. 5.9 (b) reveal the Co ions in the octahedral sites[7]. The strong band at 671 $cm^{-1}$ indicates the presence of the stretching vibrations of M-O bond within the octahedral sites of the spinel structure, specifically the dominant Fe-O bands in the octahedral position of cobalt ferrite tetrahedral complexes. The existence of $\nu_1$ and $\nu_2$ bands confirms the formation of spinel ferrite structure. The substitution of cobalt in copper ferrite shifts the absorption band to a large frequency region. The shift in the position of the absorption band can also be due to the cation redistribution or migration among tetrahedral and octahedral sites with the substitution of cobalt [5]. In addition to the above-mentioned characteristic bands for the spinel structure, a few low intensity peaks due to the auto-combustion synthesis process are observed. The IR bands in the frequency range 860-1012 $cm^{-1}$ are associated with M-O organic linkages and the peak at 1700 $cm^{-1}$ is assigned to the carbonyl (C═O) group of citrate complexes[36].

### *5.3.3 Transmission Electron Microscopy (TEM)*

TEM measurements of a typical sample, CuCo8, in the $Cu_{1-x}Co_xFe_2O_4$ series have been carried out and is shown in Fig. 5.7. The crystallite size estimated from the TEM image is found to be 10.33 nm and is smaller than that estimated from the

XRD (33 nm). The nano behaviour of the particle is confirmed by the TEM image. Almost spherical shape of the $Cu_{0.2}Co_{0.8}Fe_2O_4$ particles is observed from the TEM image. A notable homogeneity in the shape and size in the synthesised samples is observed.

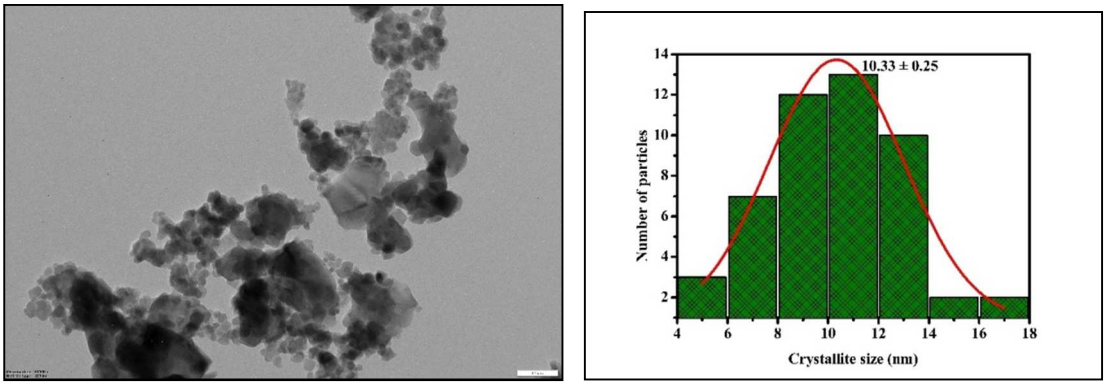


(a) (b)

**Figure 5.7.** (a) TEM images of $Cu_{0.2}Co_{0.8}Fe_2O_4$ (b) Histogram

### *5.3.4. Scanning Electron Microscopy (SEM) and EDAX Spectrum*

The morphology of the samples has been studied from the SEM images, which are shown in Fig. 5.8 Flake-like appearance has been observed for cobalt substituted copper ferrite which is characteristic of the sol-gel auto-combustion synthesis technique. Grain boundaries are distinct in all compositions, indicating that the grains are fully developed.

Elemental analysis is carried out by EDAX for $Cu_{1-x}Co_xFe_2O_4$ samples are shown in Fig.5.9. The stoichiometry of the compositions determined from the EDAX spectrum are compared with the theoretical values and listed in Table 5.3. It is observed that the stoichiometry estimated is in good agreement with the experimental value.

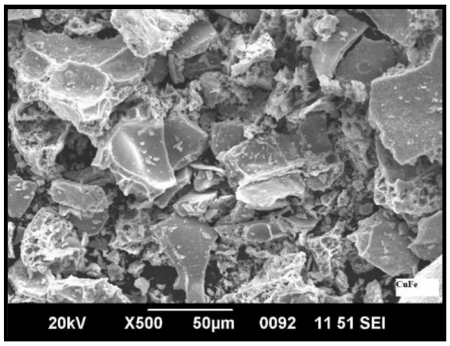


(a) $CuFe_2O_4$

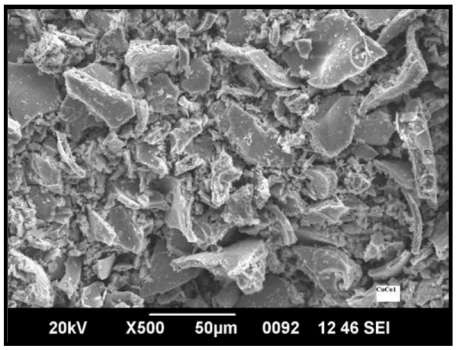


(b) $Cu_{0.9}Co_{0.1}Fe_2O_4$

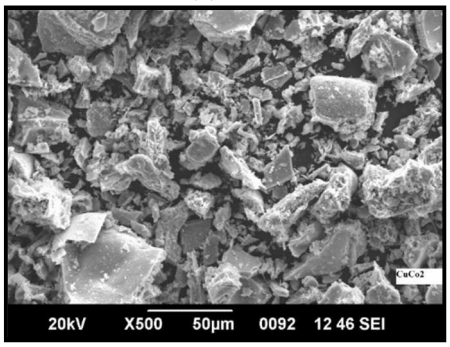


(c) $Cu_{0.8}Co_{0.2}Fe_2O_4$

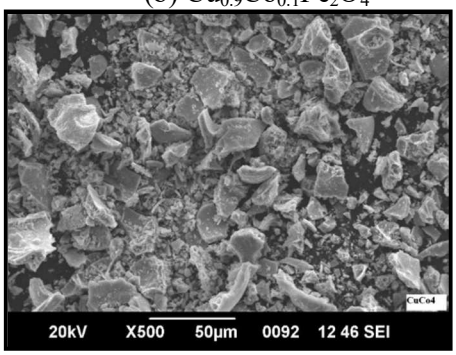


(d) $Cu_{0.6}Co_{0.4}Fe_2O_4$

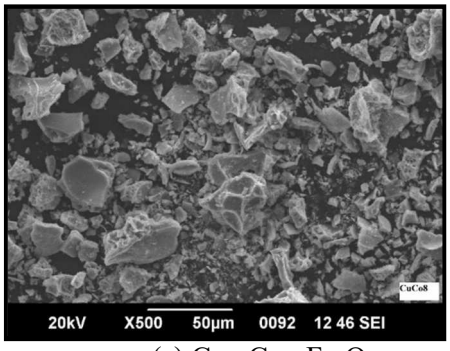


(e) $Cu_{0.2}Co_{0.8}Fe_2O$

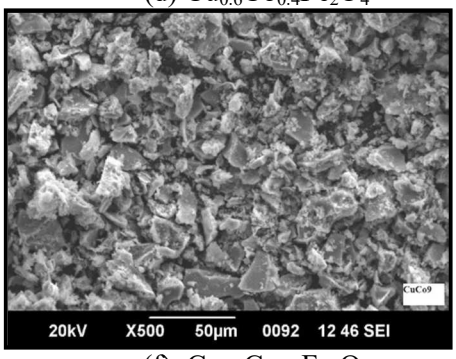


(f) $Cu_{0.1}Co_{0.9}Fe_2O_4$

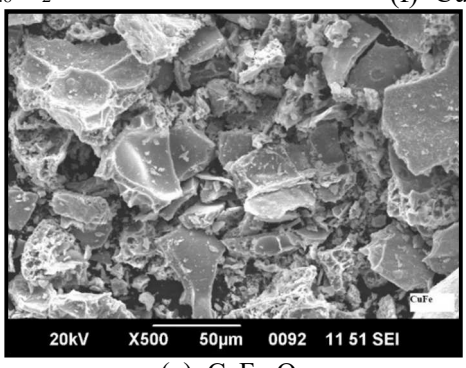


(g) $CoFe_2O_4$

**Figure 5.8.** SEM images of $Cu_{1-x}Co_xFe_2O_4$

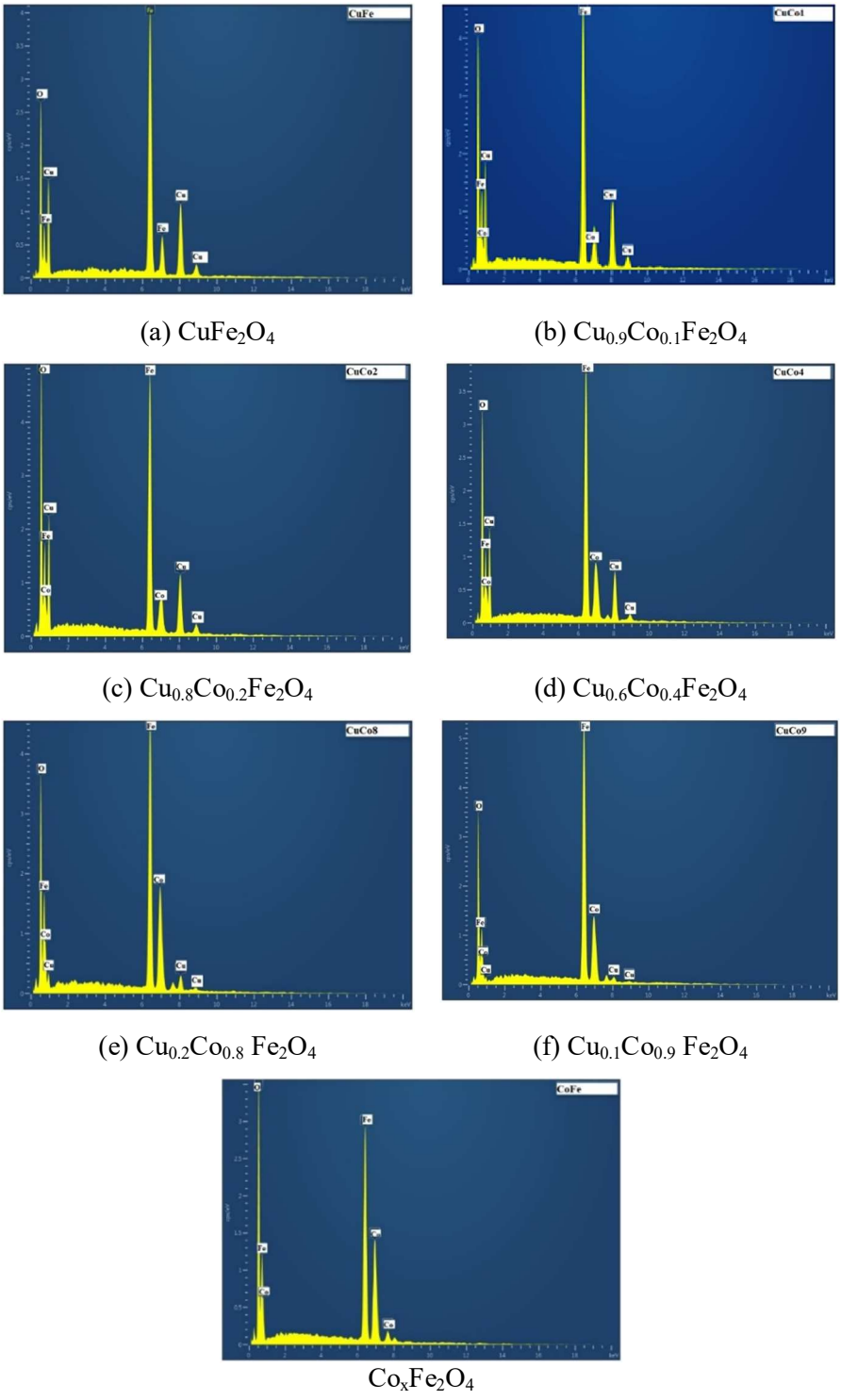


(a) $CuFe_2O_4$ (b) $Cu_{0.9}Co_{0.1}Fe_2O_4$

(c) $Cu_{0.8}Co_{0.2}Fe_2O_4$ (d) $Cu_{0.6}Co_{0.4}Fe_2O_4$

(e) $Cu_{0.2}Co_{0.8}$ $Fe_2O_4$ (f) $Cu_{0.1}Co_{0.9}$ $Fe_2O_4$

$Co_xFe_2O_4$

**Figure 5.9.** EDAX spectrum of $Cu_{1-x}Co_xFe_2O_4$

**Table 5.3.** Estimated stoichiometry from EDAX measurements

| Sample | Stoichiometric Ratio Cu:Fe / Co:Fe* | | Stoichiometric Ratio Cu:Co | | Stoichiometric Composition |
|---|---|---|---|---|---|
| | Calculated | Experimental | Calculated | Experimental | |
| **$CuFe_2O_4$** | 0.5 | 0.476 | - | - | $Cu_{0.95}Fe_2O_4$ |
| **$Cu_{0.9}Co_{0.1}Fe_2O_4$** | 0.45 | 0.452 | 9 | 10.79 | $Cu_{0.904}Co_{0.084}Fe_2O_4$ |
| **$Cu_{0.8}Co_{0.2}Fe_2O_4$** | 0.4 | 0.394 | 4 | 3.7 | $Cu_{0.788}Co_{0.212}Fe_2O_4$ |
| **$Cu_{0.6}Co_{0.4}Fe_2O_4$** | 0.3 | 0.343 | 1.5 | 1.63 | $Cu_{0.598}Co_{0.367}Fe_{1.75}O_4$ |
| **$Cu_{0.2}Co_{0.8}Fe_2O_4$** | 0.1 | 0.100 | 0.25 | 0.24 | $Cu_{0.19}Co_{0.81}Fe_2O_4$ |
| **$Cu_{0.1}Co_{0.9}Fe_2O_4$** | 0.05 | 0.03 | 0.11 | 0.10 | $Cu_{0.09}Co_{0.91}Fe_3O_4$ |
| **$CoFe_2O_4$ *** | 0.5 | 0.514 | - | - | $CoFe_{1.95}O_4$ * |

**In the case of $CoFe_2O_4$, Co: Fe ratio is considered*

The estimated stoichiometry indicates that the $Co^{2+}$ ions have been incorporated into the $Cu^{2+}$ lattice site.

## Magnetic Characterisation

### *5.3.5 M-H Curves*

Magnetic measurements were carried out by Vibration Sample Magnetometer for all the samples at 300 K and 5 K. The M-H curves of $Cu_{1-x}Co_xFe_2O_4$ at 300 K and 5 K are shown in Fig.5.10 and Fig. 5.11 respectively.

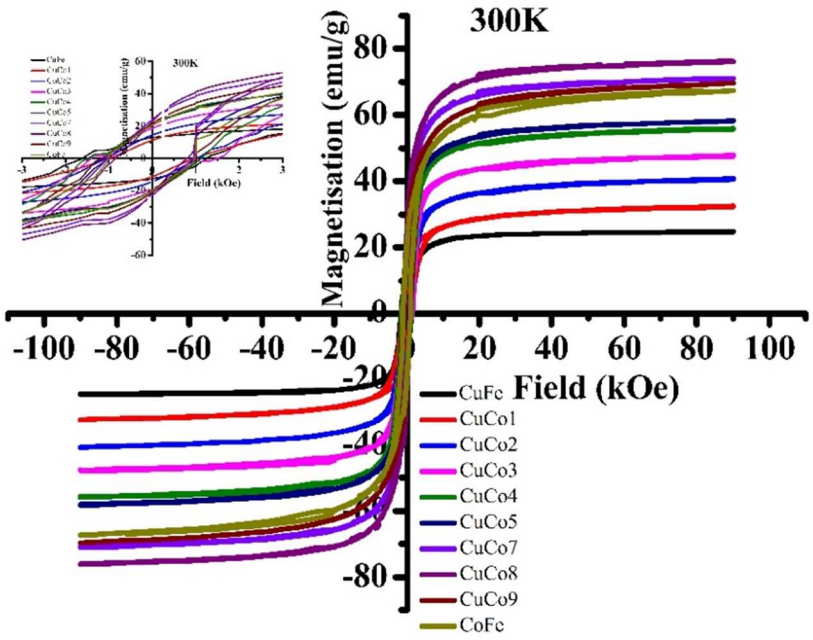


**Figure 5.10.** The M-H curves of $Cu_{1-x}Co_xFe_2O_4$ at 300K

The magnetisation curves of $Cu_{1-x}Co_xFe_2O_4$ indicate that the moments get highly magnetised at low fields and saturated at higher fields, which is attributed to the ferromagnetic behaviour at 300 K. The inset of the M-H curves shown in Fig. 5.10 displays the coercivity and remanence of the particles at room temperature. The M-H loop can be divided into two parts: loops at a low field below 3 kOe and loops at a high field above 3 kOe. The inset of Fig.5.10 represents the magnetisation loops below 3 kOe, revealing that the loop is elliptical in shape below 3 kOe. This suggests that the M-H curve at a low applied field can be explained by employing Rayleigh's law defined by [37]

$$M = \chi_0 H + \frac{1}{2}\eta H^2 \tag{5.5}$$

where, $\chi_0$ and η are the initial susceptibility and Rayleigh's constant, respectively. The first term of the equation (5.5) describes the magnetisation at low fields due to reversible magnetisation and the high field magnetisation can be explained by the second term. The elliptical shape of the loop changes above 4 kOe. Rayleigh loop

applies to the magnetisation caused by the application of a weak magnetic field, near the demagnetised state, which is characteristic of a ferromagnetic material.

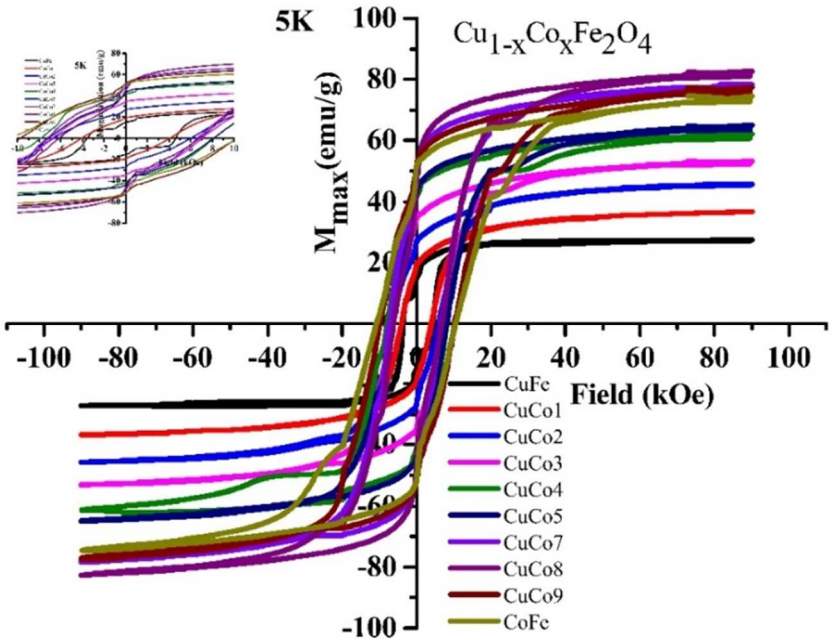


**Figure 5.11.** The M-H curves of $Cu_{1-x}Co_xFe_2O_4$ at 5K

The M-H curves of $Cu_{1-x}Co_xFe_2O_4$ at 5 K shown in Fig. 5.11 indicate the ferromagnetic behaviour of the nanoparticles with high coercivity. It may be due to the high coercivity, saturation magnetisation, and anisotropy of cobalt, which dominates at lower temperature in all CuCoFe samples. The coercivity and remanence can be observed from the inset of Fig. 5.11. It can be observed that the saturation behaviour decreases with the cobalt substitution at a lower temperature of 5 K. The magnetisation of the samples at the lower temperature 5 K can also be explained by Rayleigh's law. The inset of Fig. 5.11 reveals that the elliptical shape of the M-H loop changes above 10 kOe. This is attributed to the high coercivity of the nanoparticles at 5K.

**Table 5.4.** Magnetic parameters $M_{max}$, $H_c$, $M_r$ and $M_r/M_s$ of $Cu_{1-x}Co_xFe_2O_4$ samples

| x | $M_{max}$ (emu/g) | | $H_c$(Oe) | | $M_r$(emu/g) | | $M_r/M_{max}$ | |
|---|---|---|---|---|---|---|---|---|
| | **5 K** | **300 K** | **5 K** | **300 K** | **5 K** | **300 K** | **5 K** | **300 K** |
| **0** | 27.35 | 24.73 | 1632 | 1361 | 12.2 | 10.2 | 0.447 | 0.413 |
| **0.1** | 36.76 | 32.44 | 4055 | 945 | 19.7 | 11.4 | 0.536 | 0.352 |
| **0.2** | 45.79 | 40.71 | 6286 | 1065 | 27.1 | 14.5 | 0.592 | 0.357 |
| **0.3** | 53.2 | 47.7 | 6846 | 1118 | 34.4 | 18.6 | 0.65 | 0.39 |
| **0.4** | 62.08 | 55.89 | 7166 | 1200 | 41.2 | 20.3 | 0.664 | 0.364 |
| **0.5** | 64.9 | 58.2 | 7601 | 1027 | 44.0 | 20.7 | 0.68 | 0.36 |
| **0.7** | 78.3 | 71.0 | 7286 | 979 | 49.6 | 24.4 | 0.63 | 0.34 |
| **0.8** | 82.53 | 76.13 | 6326 | 829 | 37.8 | 10.7 | 0.459 | 0.141 |
| **0.9** | 77.5 | 69.6 | 10374 | 1152 | 50.4 | 28.4 | 0.65 | 0.41 |
| **1** | 74.65 | 67.49 | 10442 | 1200 | 45.6 | 21.3 | 0.610 | 0.315 |

It is observed from Table 5.4 that the saturation magnetisation values increases with the concentration of cobalt. This can be explained based on Neel's two sub-lattice models. According to this model, the magnetic moment per formula in Bohr magneton $n_B$ is

$$\boldsymbol{n_B} = M(B) - M(A) \tag{5.6}$$

where *M(A)* and *M(B)* are the magnetisation of the sublattices A and B

The variation of saturation magnetisation with concentration of cobalt is shown in Fig.5.12. The saturation magnetisation is maximum for x=0.8 among this series of $Cu_{1-x}Co_xFe_2O_4$ samples and its values are 76.13 emu/g and 82.53 emu/g at 300 K and 5 K respectively. The increase in saturation magnetisation was attributed to the higher magnetic moment of the $Co^{2+}$ ion ($3\mu_B$) as compared to its substituted

counterpart, the $Cu^{2+}$ ion (1 $\mu_B$). As described earlier, $Co^{2+}$ substitution in $CuFe_2O_4$ transfers $Fe^{3+}$ ions from the tetrahedral to the octahedral site, which in turn increases the magnetic moment of the B sublattice. The magnetic moment of the B sublattice is increased sequentially with the increase in cobalt substitution, resulting in an increase in net magnetisation of the samples. The magnetic moment $n_B$ estimated by employing equation (5.6) is also maximum (3.2 $\mu_B$) at 300K and (3.5 $\mu_B$) at 5 K for concentration=0.8.

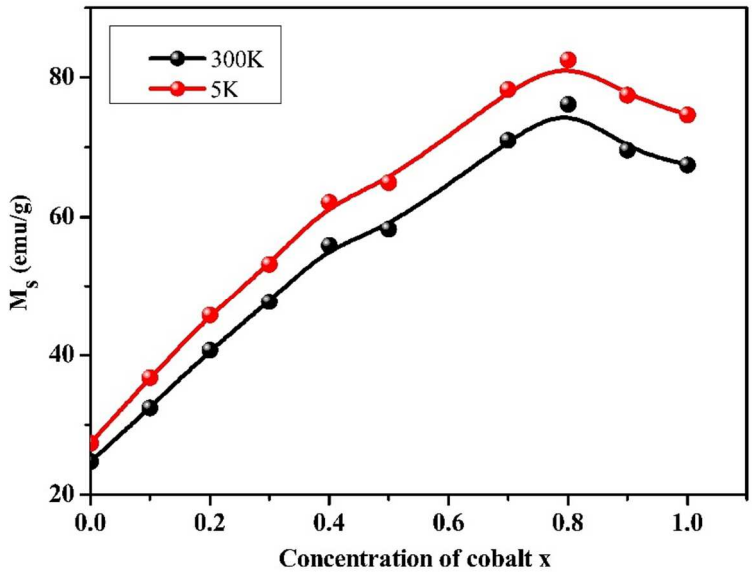


**Figure 5.12.** Variation of saturation magnetisation with x in $Cu_{1-x}Co_xFe_2O_4$

It is observed from Fig. 5.13 that the value of $M_s$ increases with crystallite size. Obviously, the initial $M_s$ of 24.73 emu/g for 18 nm particles gradually increases to 76.13 emu/g for the 33 nm particles. The dependence of $M_s$ on the crystallite size is due to the reduced surface contribution[38]. The increase in crystallite size leads to an increase in the magnetic domain size in the nanocrystalline materials, which enhances the saturation magnetisation.

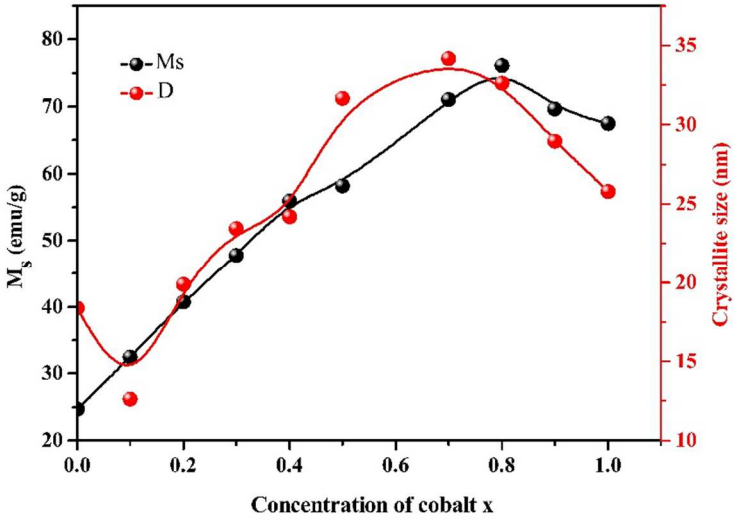


**Figure 5.13.** Variation of $M_s$ and crystallite size with x in $Cu_{1-x}Co_xFe_2O_4$

It can be observed from Table. 5.4 that there is no appreciable temperature dependence of $H_c$ and $M_r/M_s$ for $CuFe_2O_4$ as compared to $Cu_{1-x}Co_xFe_2O_4$ samples. The variation of coercivity with the concentration of cobalt in CuCoFe at 300 K and 5K is shown in Fig. 5.14 (a). $H_c$ values of $Cu_{1-x}Co_xFe_2O_4$ samples increase gradually and become maximum for CuCo4 (x=0.4) (7166 Oe) at a lower temperature of 5 K and then decrease. At the lower temperature, 5K, x=1 shows the maximum value of $H_c$ (10442Oe) since $CoFe_2O_4$ is a prominent material with a higher value of coercive field. The same pattern of variation is observed for $H_c$ values at room temperature also. Many researchers reported that the coercive field is maximum for a crystallite size of 20-30nm. The maximum observed value of $H_c$ at low temperatures in this work is greater than the reported value of $H_c$ of $CoFe_2O_4$ [39]. The enhanced value of $H_c$ reveals that it is a hard ferrite. The increase in the coercive field with the substitution of cobalt can be correlated with the strengthening of the A-B interaction. However, the $CoFe_2O_4$ sample(x=1) attained the maximum value of coercive field 10442 Oe at 5K, which is 8.7 times greater than the values of $H_c$, 1200 Oe at 300 K. The comparison of the value of $H_c$ at 5 K and 300 K shows a significant increase at a

lower temperature for $Cu_{1-x}Co_xFe_2O_4$ samples due to the enhanced coercivity of cobalt at lower temperatures.

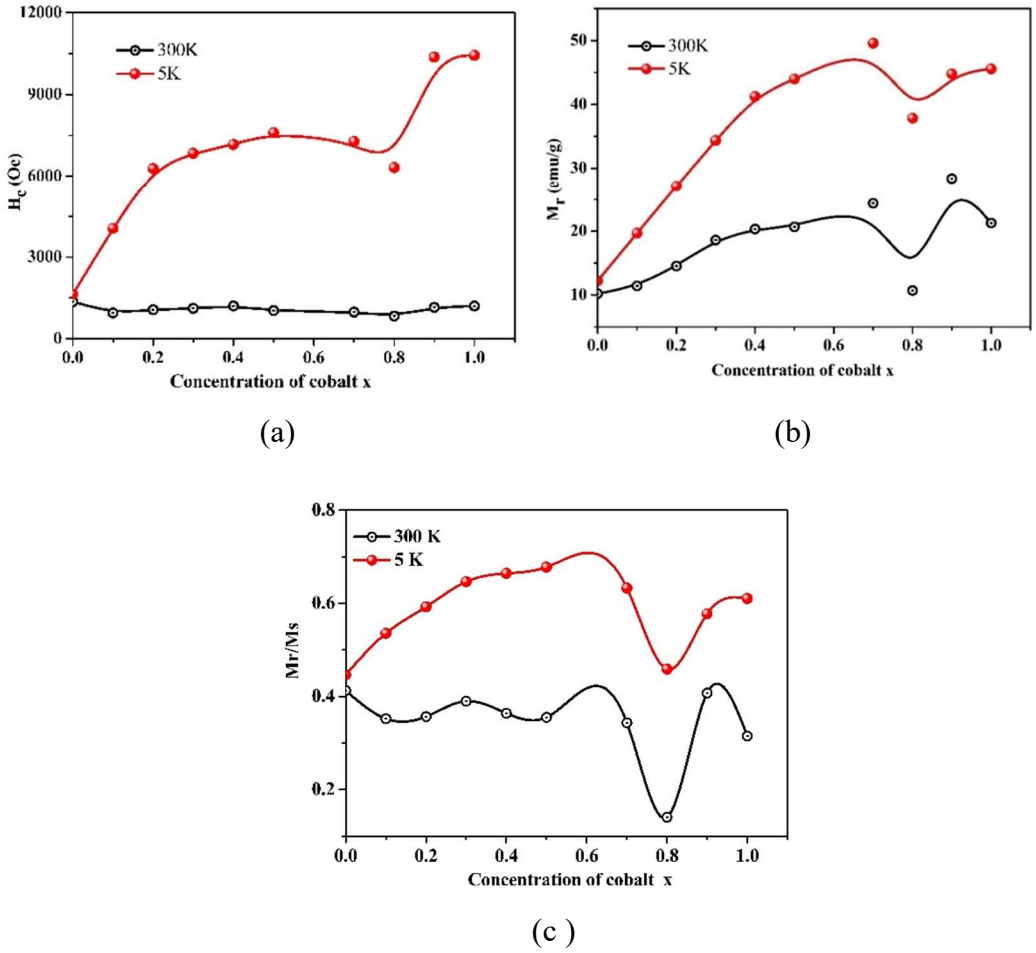


**Figure. 5.14.** Variation of (a) $H_c$ (b) $M_r$ (c) $M_r/M_s$ with x in $Cu_{1-x}Co_xFe_2O_4$ at 300 K and 5K.

The variation of remanent magnetisation of $Cu_{1-x}Co_xFe_2O_4$ samples is shown in Fig.5.14 (b). It is observed from the figure that $M_r$ increases with the concentration of cobalt and reaches a maximum value for x=0.7 at both 5K and 300K, and moreover, there is a noticeable decrease in $M_r$ for x=0.8 at 300 K and 5 K.

The variation of the remanence ratio with x at 300 K and 5 K is shown in Fig. 5.14 (c). At a lower temperature 5K, the remanence ratio, $M_r/M_s$ increases with

cobalt concentration, and it is greater than 0.5. According to the Stoner-Wohfarth model, at low temperatures, the nanoparticles exhibit cubic anisotropy if $M_r/M_s > 0.5$. The remanence ratio revealed that $Cu_{1-x}Co_xFe_2O_4$ nanoparticles exhibit cubic anisotropy at a lower temperature 5 K. Moreover, it is observed that the value of $M_r/M_s$ is less than 0.5 at room temperature for $Cu_{1-x}Co_xFe_2O_4$ samples. In the sol-gel synthesised $Cu_{1-x}Co_xFe_2O_4$ samples, as the values of $M_r/M_s$ are close to 0.5 the particles can be regarded as randomly oriented noninteracting particles that rotate coherently [26].

The other important magnetic parameters, magnetic moment and magneto crystalline anisotropy constant of the cobalt-substituted nanoparticles estimated using equations (5.7) and (5.8) respectively are listed in Table 5.5.

$$\mu_B = \frac{M_W M_S}{5585} \tag{5.7}$$

Where $M_W$ is the molecular weight and $M_s$ is the saturation magnetisation (30)

The coercivity, $H_c = \frac{0.64K}{M_S}$ [40] (5.8)

Anisotropy energy is the energy required to rotate the spin system of a domain away from the easy direction or to overcome the spin-orbit coupling. In a cubic crystal energy E can be expressed as

$$E = K_0 + K_1\ (\propto_1^2\propto_2^2+\propto_2^2\propto_3^2+\propto_3^2\propto_1^2) + K_2\ (\propto_1^2\propto_2^2\propto_3^2) + \ \ldots \tag{5.9}$$

where $K_0, K_1, K_2$ are constants for a particular material at a particular temperature are expressed in erg/cm$^3$ [28]. When $K_2$ is zero, the direction of easy magnetisation is determined by the sign of $K_1$ and it is positive for the cubic ferrites containing cobalt.

**Table 5.5.** Magnetic moment, Anisotropy constant of $Cu_{1-x}Co_xFe_2O_4$ samples at 5K and 300K

| x | $n_B$ ($\mu_B$) | | K x$10^6$ (erg/cm$^3$) | |
|---|---|---|---|---|
| | 5 K | 300 K | 5 K | 300 K |
| **0** | 1.01 | 0.918 | 0.33 | 0.254 |
| **0.1** | 1.57 | 1.387 | 1.24 | 0.257 |
| **0.2** | 1.95 | 1.737 | 2.44 | 0.368 |
| **0.3** | 2.26 | 2.03 | 3.12 | 0.46 |
| **0.4** | 2.63 | 2.376 | 3.74 | 0.564 |
| **0.5** | 2.75 | 2.47 | 4.09 | 0.49 |
| **0.7** | 3.31 | 3.00 | 4.69 | 0.57 |
| **0.8** | 3.48 | 3.211 | 4.29 | 0.52 |
| **0.9** | 3.26 | 2.93 | 6.61 | 0.66 |
| **1** | 3.13 | 2.835 | 6.41 | 0.666 |

It is clear from Table 5.5 that the magnetic moment of $Cu_{1-x}Co_xFe_2O_4$ increases with the substitution of cobalt. It is because of the higher value of the magnetic moment of cobalt ($3\mu_B$) as compared to copper ($1\ \mu_B$).

The variation of the anisotropy constant K with x is shown in Fig. 5.15. The anisotropy constant K increases with the substitution of cobalt in $Cu_{1-x}Co_xFe_2O_4$ samples. The anisotropic constant K increases enormously at a lower temperature of 5K. The value of K varies from 0.666 x$10^6$ (erg/cm$^3$) to 6.41 x$10^6$ (erg/cm$^3$) for the $CoFe_2O_4$ sample when the temperature changes from 300K to 5 K. A remarkable increase in the anisotropy constant is observed at 5K rather than 300 K.

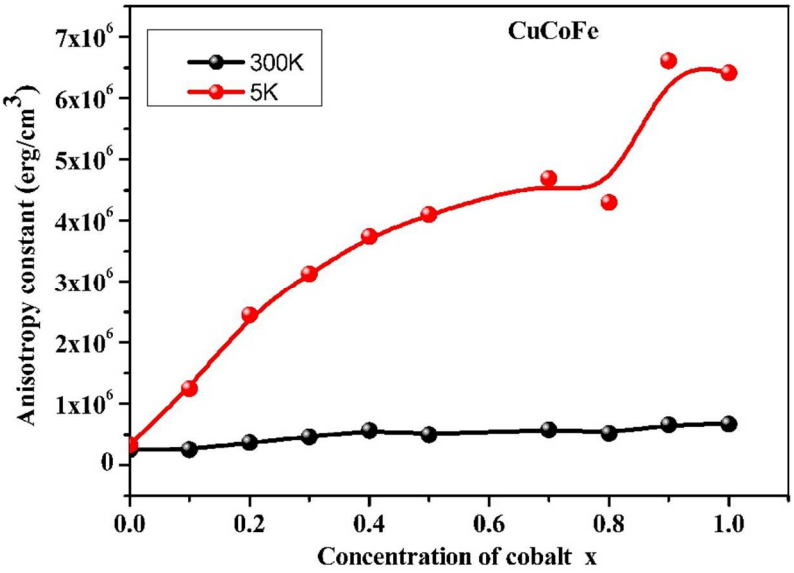


**Figure 5.15.** Variation of anisotropy constant $Cu_{1-x}Co_xFe_2O_4$ samples at 5K and 300K.

Nakagomi *et al*. [41] reported that the $Co^{2+}$ ions occupy both A and B sites, thus, the strong anisotropy of pure cobalt ferrite is primarily due to the presence of $Co^{2+}$ ions on the octahedral sites of the spinel structure. In $Cu_{1-x}Co_xFe_2O_4$ nanoparticles, the value of K increases with the substitution of cobalt which verifies the presence of $Co^{2+}$ ions in the octahedral site. $CoFe_2O_4$ samples exhibit the maximum positive anisotropy value as well as a large M–H loop area at 5K, which is attributed to the strong spin-orbit coupling at $Co^{2+}$ lattice sites. This is in agreement with the estimated value of $H_c$ and K, as shown in Tables 5.3 and 5.5, respectively. The crystal field is not capable of removing the orbital degeneracy of $Co^{2+}$ at the octahedral sites, so the orbital magnetic moment is not quenched. Therefore, there is a strong spin-orbit coupling that produces a large magneto crystalline anisotropy energy [37]. The observed value of the anisotropy constant of $CoFe_2O_4$ in the present work is greater than the reported value[26]. The so-prepared $Cu_{1-x}Co_xFe_2O_4$ samples can be used for technological applications at or below room temperature.

## 5.4. Conclusion

Nanocrystalline cobalt substituted copper ferrite samples $Cu_{1-x}Co_xFe_2O_4$ (x= 0, 0.1, 0.2, 0.3, 0.4, 0.5, 0.7, 0.8, 0.9 and 1) are prepared by the modified sol-gel auto combustion method. It is confirmed from XRD analysis that the samples prepared by this route exhibit a cubic structure with crystallite sizes in the range 12nm – 32nm. The saturation magnetization of the samples shows an increasing pattern with the concentration of Cobalt. The values of magnetic parameters, coercive field, remanent magnetisation, and magnetocrystalline anisotropy constant increase with cobalt substitution. The enhanced values of coercive field and magnetocrystalline anisotropy of $Cu_{1-x}Co_xFe_2O_4$ samples at 5K reveal that it can be a prominent candidate in technological and biomedical applications like magnetic resonance imaging, etc.

## REFERENCES

[1] N. Somaiah, T. V. Jayaraman, P.A. Joy, D. Das, J Magn Magn Mater 324 (2012) 2286–2291.

[2] D.C. Jiles, C.C.H. Lo, Sens Actuators A Phys 106 (2003) 3–7.

[3] B.Y. Geng, J.Z. Ma, X.W. Liu, Q.B. Du, M.G. Kong, L.D. Zhang, Appl Phys Lett 90 (2007) 2005–2008.

[4] R.C. Kambale, K.M. Song, Y.S. Koo, N. Hur, J Appl Phys 110 (2011).

[5] R.S. Yadav, I. Kuřitka, J. Vilcakova, J. Havlica, J. Masilko, L. Kalina, J. Tkacz, M. Hajdúchová, V. Enev, Journal of Materials Science: Materials in Electronics 28 (2017) 6245–6261.

[6] A. Hussain, T. Abbas, S.B. Niazi, Ceram Int 39 (2013) 1221–1225.

[7] R. Jabbar, S.H. Sabeeh, A.M. Hameed, J Magn Magn Mater 494 (2020) 165726.

[8] A. V. Raut, R.S. Barkule, D.R. Shengule, K.M. Jadhav, J Magn Magn Mater 358–359 (2014) 87–92.

[9] M.H. Abdellatif, C. Innocenti, I. Liakos, A. Scarpellini, S. Marras, M. Salerno, J Magn Magn Mater 424 (2017) 402–409.

[10] A.M. Balagurov, I.A. Bobrikov, M.S. Maschenko, D. Sangaa, V.G. Simkin, Crystallography Reports 58 (2013) 710–717.

[11] C. Murugesan, N. Kambhala, S. Angappane, G. Chandrasekaran, J Magn Magn Mater 443 (2017) 334–342.

[12] E.R. Kumar, R. Jayaprakash, G.S. Devi, P.S.P. Reddy, J Magn Magn Mater 355 (2014) 87–92.

[13] M. Saini, S.K. Singh, R. Shukla, A. Kumar, J Inorg Organomet Polym Mater 28 (2018) 2306–2315.

[14] B.G. Manju, P. Raji, Ceram Int 44 (2018) 7329–7333.

[15] M. Margabandhu, S. Sendhilnathan, S. Senthilkumar, D. Gajalakshmi, Brazilian Archives of Biology and Technology 59 (2016) 1–10.

[16] M.A. Dar, D. Varshney, J Magn Magn Mater 436 (2017) 101–112.

[17] C. Singh, S. Bansal, V. Kumar, K.B. Tikoo, S. Singhal, RSC Adv 5 (2015) 39052–39061.

[18] A. Samavati, A. F. Ismail, Particuology 30 (2017) 158–163.

[19] M.I.A. Abdel Maksoud, G.S. El-Sayyad, A.H. Ashour, A.I. El-Batal, M.S. Abd-Elmonem, H.A.M. Hendawy, E.K. Abdel-Khalek, S. Labib, E. Abdeltwab, M.M. El-Okr, Materials Science and Engineering C 92 (2018) 644–656.

[20] A. Azam, J Alloys Compd 540 (2012) 145–153.

[21] M. Hashim, Alimuddin, S. Kumar, B.H. Koo, S.E. Shirsath, E.M. Mohammed, J. Shah, R.K. Kotnala, H.K. Choi, H. Chung, R. Kumar, J Alloys Compd 518 (2012) 11–18.

[22] P. Tailhades, C. Villette, A. Rousset, G.U. Kulkarni, K.R. Kannan, C.N.R. Rao, M. Lenglet, J Solid State Chem 141 (1998) 56–63.

[23] S. Burianova, J. Poltierova-Vejpravova, P. Holec, J. Plocek, J Phys Conf Ser 200 (2010).

[24] V. Gopalan, Al-Omari I, Kumar D, Yoshida Y, Joy P, Anantharaman M, Appl Phys A 99 (2010): 497–503.

[25] M. Albino, E. Fantechi, C. Innocenti, A. López-Ortega, V. Bonanni, G. Campo, F. Pineider, M. Gurioli, P. Arosio, T. Orlando, G. Bertoni, C. De Julián Fernández, A. Lascialfari, C. Sangregorio, Journal of Physical Chemistry C 123 (2019) 6148–6157.

[26] E.E. Ateia, A.A. El-Bassuony, G. Abdelatif, F.S. Soliman, Journal of Materials Science: Materials in Electronics 28 (2017) 241–249.

[27] R.S. Yadav, I. Kuřitka, J. Vilcakova, J. Havlica, J. Masilko, L. Kalina, J. Tkacz, M. Hajdúchová, V. Enev, Journal of Materials Science: Materials in Electronics 28 (2017) 6245–6261.

[28] B.D. Cullity, S.R. Stock, Elements of X ray Diffraction, Prentice-Hall, New York (2001).

[29] X. Zuo, A. Yang, C. Vittoria, V.G. Harris, J Appl Phys 99 (2006) 4–7.

[30] N. Somaiah, T. V. Jayaraman, P.A. Joy, D. Das, J Magn Magn Mater 324 (2012) 2286–2291.

[31] G.A. Sawatzky, F. Van Der Woude, A.H. Morrish, J Appl Phys 39 (1968) 1204–1205.

[32] C. Singh, S. Bansal, V. Kumar, K.B. Tikoo, S. Singhal, RSC Adv 5 (2015) 39052–39061.

[33] S. Jandl, J. Deslandes, Phys Rev B 24 (1981) 1040–1044.

[34] A. Tony Dhiwahar, M. Sundararajan, P. Sakthivel, C.S. Dash, S. Yuvaraj, Journal of Physics and Chemistry of Solids 138 (2020) 109257.

[35] C. Murugesan, N. Kambhala, S. Angappane, G. Chandrasekaran, J Magn Magn Mater 443 (2017) 334–342.

[36] A.B. Patil, R.N. Panda, New Journal of Chemistry (2024) 109–123.

[37] Chikazumi S., Graham C. D., Physics of Ferromagnetism, Clarendon Press, Oxford, 1997

[38] S.H. Noh, W. Na, J.T. Jang, J.H. Lee, E.J. Lee, S.H. Moon, Y. Lim, J.S. Shin, J. Cheon, Nano Lett 12 (2012) 3716–3721.

[39] B. Debnath, H.G. Salunke, S. Bhattacharyya, Journal of Physical Chemistry C 124 (2020) 25992–26000.

[40] B. Geng, Z. Ding, Y. Ma, Nano Research 9 (2016) 2772–2781.

[41] F. Nakagomi, S.W. Da Silva, V.K. Garg, A.C. Oliveira, P.C. Morais, A. Franco Júnior, E.C.D. Lima, J Appl Phys 101 (2007) 2005–2008.

…..ര*ര…..

# Chapter 6

# Synthesis, Structural and Magnetic Properties of Zinc Substituted Copper Ferrite Nanoparticles $Cu_{1-x}Zn_xFe_2O_4$

## Objectives

The synthesis, structural, and magnetic properties of zinc substituted copper ferrite nanoparticles $Cu_{1-x}Zn_xFe_2O_4$ (x=0, 0,1, 0,2, 0.3, 0.4, 0.5, and 0.6) are detailed. The samples are synthesized by a modified sol-gel auto-combustion method. The effect of substitution of a magnetic and nonmagnetic cation on the structural and magnetic properties of copper ferrite is also compared.

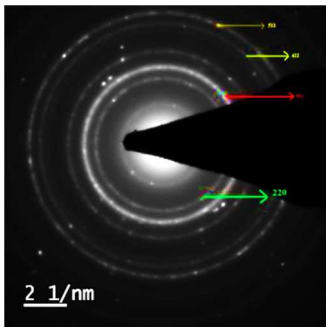


*S. Bhaskaran, I.A. Al-Omari, V.E. Gopalan, Effect of magnetic and nonmagnetic cation substitution on structural and magnetic properties of copper ferrite nanoparticles, AIP Conf Proc 2783 (2023) 0–4. https://doi.org/10.1063/5.0158619.*

## 6.1 Introduction

The structural, electrical, and magnetic properties of nano ferrites strongly depend on cation distribution among tetrahedral and octahedral sites, synthesis conditions, and grain size[1]. The physical properties of a magnetic cation(cobalt) substituted copper ferrite nanoparticles were detailed in Chapter 5. Copper ferrite is considered to have an inverse spinel structure with most $Cu^{2+}$ ions occupying octahedral sites, and zinc ferrite has a normal spinel structure with $Zn^{2+}$ ions preferably occupying tetrahedral sites. Studying the effect of a nonmagnetic cation substitution for copper in copper ferrite nanoparticles will be interesting. According to the literature, the substitution of different metal cations can modify the properties of the copper ferrite system to tune it for different applications[2–6]. Among the cations, the substitution of nonmagnetic $Zn^{2+}$ can appreciably modify the magnetic properties of ferrite nanoparticles[7–9]. Zinc substituted copper ferrites are attractive among the group of ferrites as zinc substitution can change the magnetic and electrical properties across a wide range. Many research works have been reported on the magnetic properties of zinc substituted copper ferrite [10–17].

While numerous studies have documented the structural and magnetic characteristics of zinc-substituted copper ferrites, only a few groups of researchers have reported the magnetocaloric properties of these ferrites[10–14]. The present chapter is focused on the structural and magnetic studies of zinc substituted copper ferrite at room temperature (300K) and a lower temperature (5K). The magnetic parameters like coercivity, squareness ratio, anisotropic constant, etc., are studied, and this may be one of the few reports on magnetic studies at a lower temperature of 5 K. The substitutional effects of cobalt and zinc cations in $CuFe_2O_4$ ($Cu_{1-x}Co_xFe_2O_4$ and $Cu_{1-x}Zn_xFe_2O_4$ series) are also compared in this chapter.

## 6.2 Synthesis and characterisation

The zinc substituted copper ferrite samples with molecular formula $Cu_{1-x}Zn_xFe_2O_4$(x=0, 0.1, 0.2, 0.3, 0.4, 0.5 and 0.6) were synthesized by a modified sol-gel

autocombustion method. Precursors used in this synthesis method are copper nitrate trihydrate $Cu(NO_3)_2.3H_2O$, zinc nitrate hexahydrate ($Zn(NO_3)_2.6H_2O$), iron (III) nitrate nonahydrate purified $Fe(NO_3)_3.9H_2O$ and citric acid($C_6H_8O_7$) as the chelating agent. Metal nitrates are dissolved separately in distilled water in the stoichiometric ratio, and the solution is stirred well with a magnetic stirrer. The stoichiometric amount of citric acid is added to the metal nitrate solution in the molar ratio 1:1 and stirred using a magnetic stirrer for half an hour. The solution is shifted to a hot plate and heated. It turned into a brown coloured gel and ultimately underwent auto combustion. The powder samples of $Cu_{1-x}Zn_xFe_2O_4$ nanoparticles are obtained, and they are labelled as CuZnFe. The synthesized samples are labeled as CuZn1, CuZn2, CuZn3, CuZn4, CuZn5, and CuZn6, respectively, for the compositions x=0.1, 0.2, 0.3, 0.4, 0.5, and 0.6.

## 6.3 Results and Discussion

### Structural Characterisation

#### *6.3.1 XRD Analysis*

The XRD patterns of the parent $CuFe_2O_4$ and $Cu_{1-x}Zn_xFe_2O_4$ nanoparticles are shown in Fig.6.1 (a)and Fig.6.1(b), respectively. The crystal structure, lattice parameters, and crystallite size are estimated from the XRD pattern.

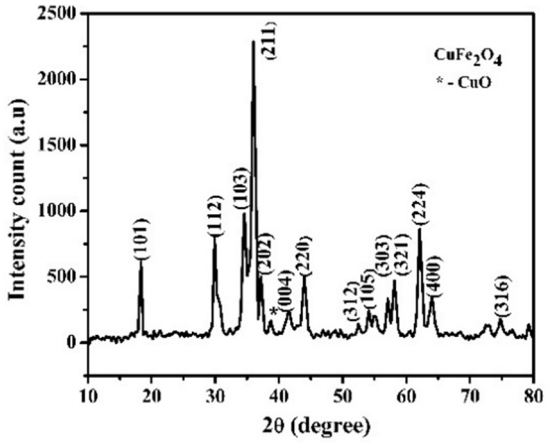


(a)

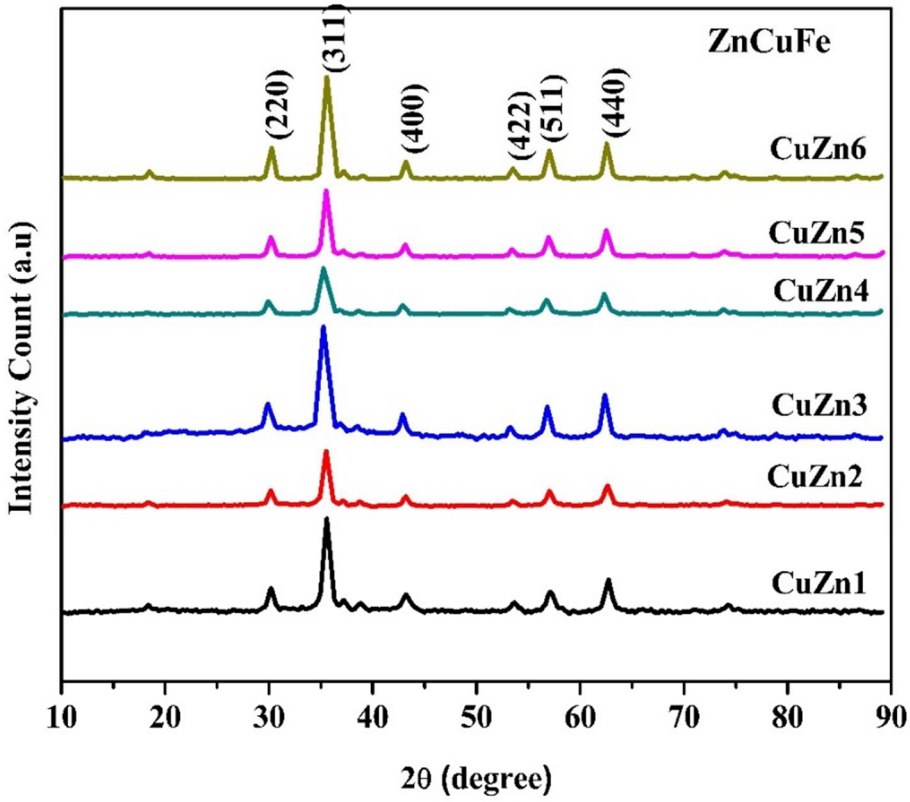


(b)

**Figure.6.1.** XRD pattern of (a) $CuFe_2O_4$ and (b) $Cu_{1-x}Zn_xFe_2O_4$

The XRD pattern of the copper ferrite sample displayed in Fig. 6.1 depicts that the indexed lattice planes are consistent with the body centered tetragonal crystal structure of $CuFe_2O_4$ with I41/amd space group (JCPDS No: 34- 0425)[15]. The XRD pattern of $Cu_{1-x}Zn_xFe_2O_4$ shown in Fig. 6.1 (b) reveals that all peaks are indexed to pure cubic phase with *fd3m* space group. The diffraction peaks corresponding to (220), (311), (400), (422), (511), and (440) crystal planes exhibited the face-centered cubic crystal and are indexed to JCPDS No:89–4926 [16]. Obviously, a change in the structure from tetragonal to cubic symmetry has been observed with the substitution of zinc in the copper ferrite system. Similar observations have been reported in zinc substituted copper ferrite [17]. The XRD pattern shows that there is a shift in 2θ towards the lower angle side with the

substitution of zinc, which indicates an increase in the lattice parameter. This confirms the incorporation of $Zn^{2+}$ in the tetrahedral site of the $CuFe_2O_4$ lattice. The estimated value of crystallite size and lattice parameter is listed in Table 6.1.

The average crystallite size *D* of the samples was estimated from the most intense peak (311) by employing the Scherrer formula[18]. The calculated value of crystallite size shown in Table 6.1 indicates that the particles are in the nano range. It is noteworthy that no significant variation can be observed in crystallite size with zinc substitution in $CuFe_2O_4$.The lattice parameter of tetragonal structured $CuFe_2O_4$ and cubic structured $Cu_{1-x}Zn_xFe_2O_4$ nanoparticles was calculated using equations (5.1) and (5.2) respectively described in Chapter 5.

**Table 6.1.** Structural parameters of $Cu_{1-x}Zn_xFe_2O_4$ nanoparticles

| x | Lattice Parameter (Å) | Crystallite size (nm) | X-ray density ($g/cm^3$) | Structure |
|---|---|---|---|---|
| **0.0** | a = 5.8156, c = 8.6934 | 18 | 4.836 | Tetragonal |
| **0.1** | 8.361 | 12 | 5.441 | Cubic |
| **0.2** | 8.374 | 14 | 5.420 | Cubic |
| **0.3** | 8.43 | 12 | 5.316 | Cubic |
| **0.4** | 8.44 | 10 | 5.302 | Cubic |
| **0.5** | 8.375 | 14 | 5.430 | Cubic |
| **0.6** | 8.358 | 13 | 5.467 | Cubic |

The estimated value of lattice parameter of tetragonally structured $CuFe_2O_4$ are *a=5.8156*Å and *c=8.6934*Å. The *c/a* ratio of copper ferrite, 1.49, indicates that the prepared $CuFe_2O_4$ is an inverse spinel with a strong Jahn-Teller distortion. The cation distribution in the inverse spinel copper ferrite is described in Chapter 5. When zinc is substituted in $CuFe_2O_4$, $Zn^{2+}$ ions in $Cu_{1-x}Zn_xFe_2O_4$ have an affinity to occupy the tetrahedral A lattice. So, the $Zn^{2+}$ ions are expected to replace the $Fe^{3+}$

ions from the tetrahedral A site to the octahedral B site. The lattice parameter values displayed in Table 6.1. reveals that it increases with the substitution of zinc in copper ferrite from x=0.1 to x=0.4 and thereafter it decreases. The variation of lattice parameter with zinc concentration is shown in Fig. 6.2. The increase in lattice constant is due to the substitution of larger $Zn^{2+}$ (0.74 Å) for smaller $Cu^{2+}$ (0.72Å). Further decrease in lattice constant for x > 0.5 may be due to the cation redistribution in the lattice. With the substitution of Zn in $CuFe_2O_4$, for x > 0.4, $Fe^{3+}$ ions with a lower ionic radius in the tetrahedral site shift to the octahedral site and replace the larger $Cu^{2+}$ ions resulting in a lattice contraction.

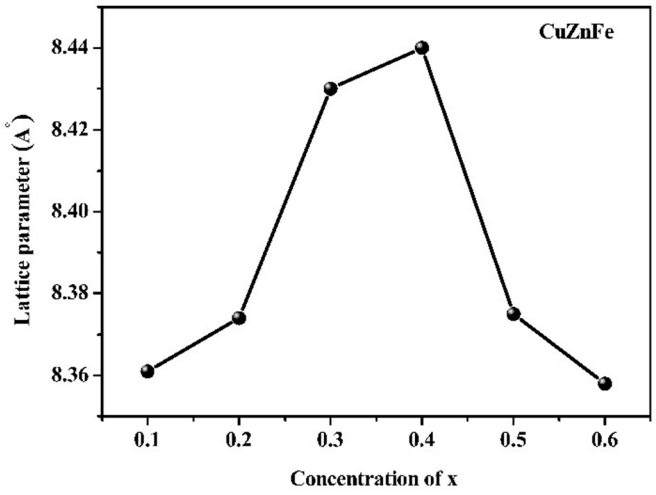


**Figure 6.2.** Variation of lattice parameter of $Cu_{1-x}Zn_xFe_2O_4$ with x

### *Rietveld Analysis*

Rietveld refined pattern of a typical sample CuZn3 is shown in Fig. 6.3. The refined XRD pattern agrees well with the original XRD pattern of the $Cu_{0.7}Zn_{0.3}Fe_2O_4$. The crystal planes were consistent with the cubic structure. The refined lattice parameter *a=8.402 Å* is consistent with the values obtained from the XRD pattern *a=8.43 Å*. The value of the Goodness factor $\chi^2$, 1.34, indicates that the XRD data of the CuZn3 sample is refined best with the least difference. The refined parameters are listed in Table 6.2

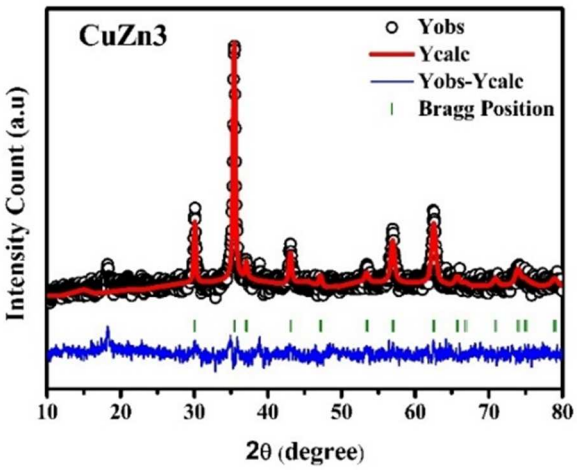


**Figure 6.3.** Rietveld refinement of $Cu_{1-x}Zn_xFe_2O_4$ (x=0.3, 0.5, 0.6)

**Table 6.2.** The refined structural parameters of $Cu_{1-x}Zn_xFe_2O_4$ (x=0.3, 0.5, 0.6)

| **Sample** | **CuZn3** |
|---|---|
| **Lattice parameter a (Å)** | 8.402 |
| **V (Å$^3$)** | 593.08 |
| **$R_{wp}$** | 29.6 |
| **$R_e$** | 25.53 |
| **$R_{Bragg}$** | 1.05 |
| **($\chi^2$)** | 1.34 |

### *6.3.2 FTIR Spectroscopy*

The various absorption and vibration bands present in the CuZnFe samples have been identified from the FTIR spectra shown in Fig.6.4. The vibrational bands observed around 560 cm$^{-1}$ ($\nu_1$) and 400 cm$^{-1}$ ($\nu_2$) in the FTIR spectrum of CuZnFe samples are associated with the tetrahedral and octahedral groups [16]. The bands observed around 547 -561 cm$^{-1}$ correspond to the effect of stretching vibrations of Fe-O at the tetrahedral sites and the band present around 457 cm$^{-1}$ is associated with the stretching vibrations of Cu ions in the octahedral site [16,19]. The intensity of the band at 457 cm$^{-1}$ decreases with an increase in zinc concentration, indicating the

incorporation of zinc for copper in copper ferrite.

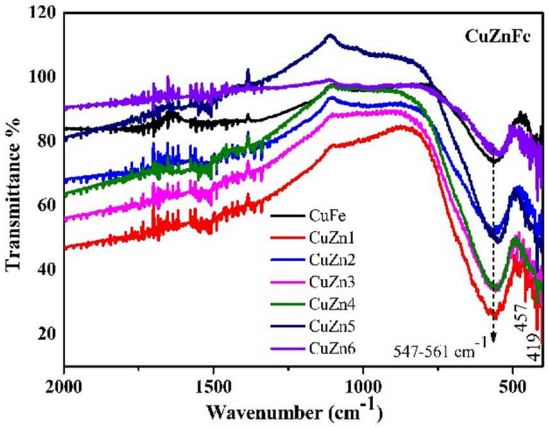


**Figure 6.4.** FTIR spectrum of $Cu_{0.7}Zn_{0.3}Fe_2O_4$ samples.

The FTIR spectrum depicts that the band that appeared at 561 $cm^{-1}$ in copper ferrite is shifted to the lower wavenumber region for samples with x > 0.2. The $Zn^{2+}$ substitution in copper ferrite causes the redistribution of $Fe^{3+}$ ions in A and B sites, resulting in a change in bond length and, hence, a lowering of the force constant and wavenumber[20].The shift towards the lower wavenumber region in the present work is consistent with the reported value [20,21]. The bands located around 419 $cm^{-1}$ are associated with Zn-O bonds[22].

### *6.3.3 Transmission Electron Microscopy (TEM)*

Structural analysis was also carried out using HRTEM measurement of the $Zn_{0.3}Cu_{0.7}Fe_2O_4$ sample shown in Fig.6.5. The TEM images show that $Zn_{0.3}Cu_{0.7}Fe_2O_4$ particles are spherically shaped and less agglomerated. From the histogram, it is clear that most of the particles are in 10-20 nm range, and the crystallite size obtained from it (12.4 nm) is in good agreement with that obtained from the XRD pattern (11.9 nm). The diffraction pattern confirmed the crystallinity of the samples.

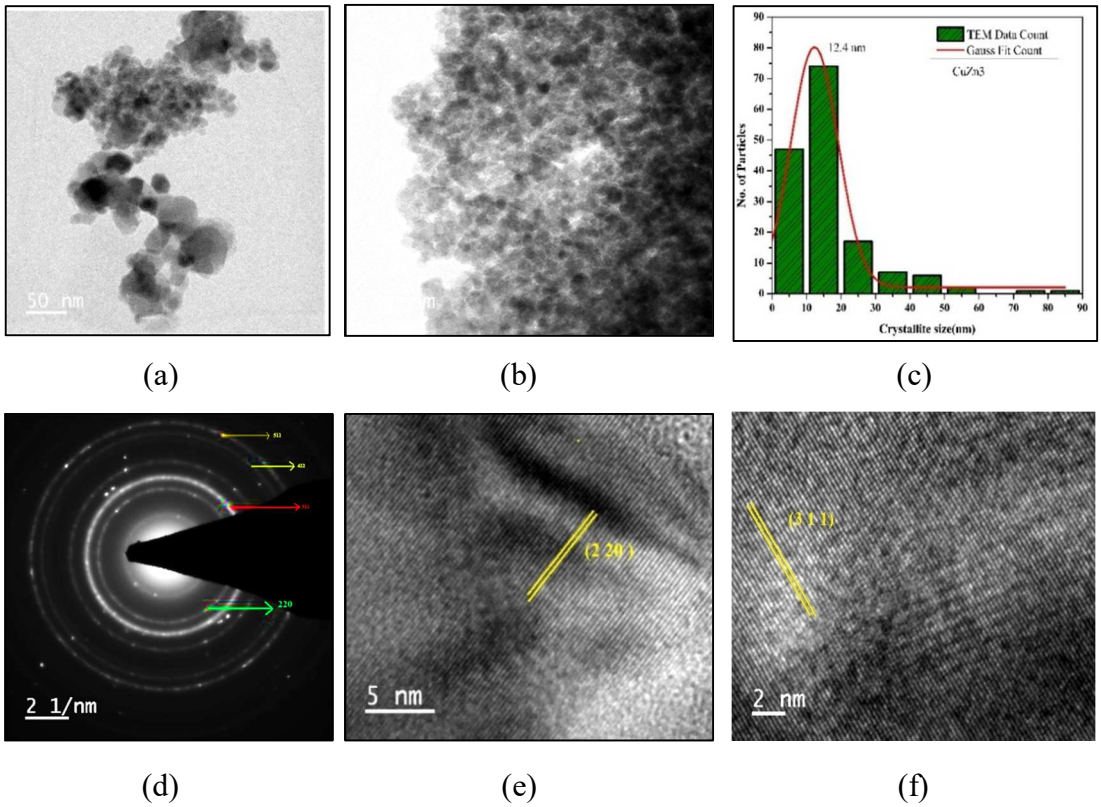


**Figure 6.5.** (a) TEM image b) Histogram c) SAED pattern (d) HRTEM of $Zn_{0.3}Cu_{0.7}Fe_2O_4$

The interplanar distance *d* is estimated from the HRTEM pattern, and the planes (220) and (311) are identified and indexed. The estimated *d* value of the planes from TEM measurements is in good agreement with the value estimated from the XRD pattern. The lattice parameter calculated from the TEM measurement for the most intense peak (311*), a=8.291 Å*, is comparable to the value calculated from XRD, which is 8.43 Å. The SAED pattern confirms the nanocrystalline behaviour of the synthesized CuZn3 sample, and the reflection planes corresponding to the cubic structure are identified.

### *6.3.4 Scanning Electron Microscopy (SEM) and EDAX Spectrum*

The surface morphology and the distribution of the synthesized particles are examined by Scanning Electron Microscopy. The SEM micrographs of $Cu_{1-x}Zn_xFe_2O_4$ are shown in Fig.6.6. Flake like behaviour has been observed for CuZnFe

nanoparticles for a magnification in the micrometer range which is characteristic of sol-gel autocombustion synthesis technique and spherical shape can be observed in the higher magnification. The agglomeration can arise from the magnetic dipole-dipole and exchange interaction between the particles, which is usually observed in superparamagnetic iron oxides[7,23].

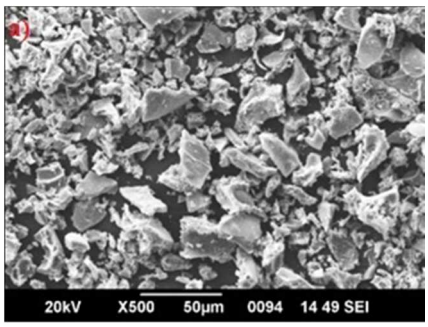


(a) CuZn1

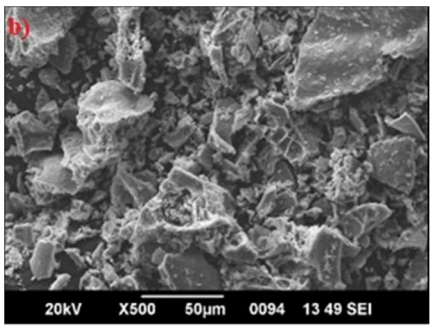


(b) CuZn3

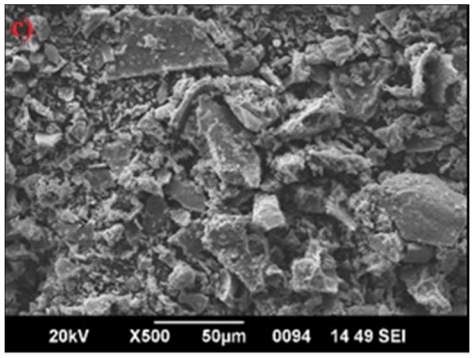


(c ) CuZn6

**Figure 6.6.** SEM Micrograph of $Cu_{1-x}Zn_xFe_2O_4$.

Elemental and compositional studies of a typical sample $Cu_{0.7}Zn_{0.3}Fe_2O_4$ among the series had been carried out by EDAX measurement, and the spectrum is shown in Fig. 6.7. The stoichiometric ratio is estimated from the spectrum and is compared with the theoretical value. The estimated values of stoichiometry are in good agreement with the calculated value. It is listed in Table 6.3.

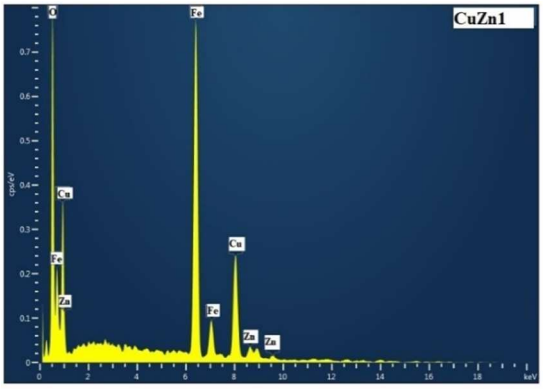


(a)

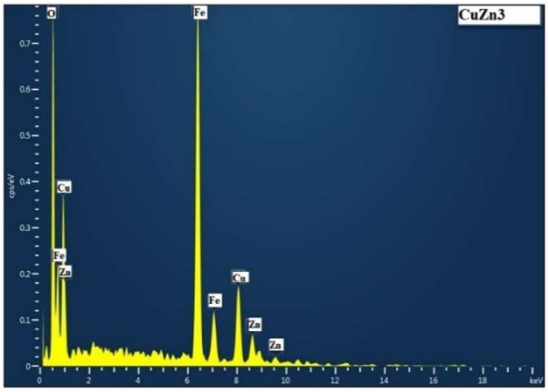


(b)

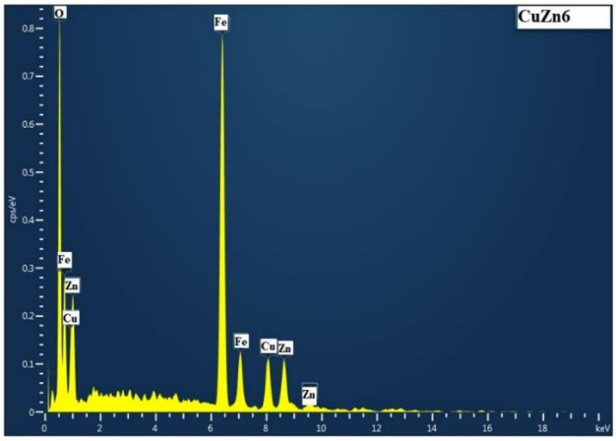


(c)

**Figure 6.7.** .EDAX spectrum of (a) CuZn1 (b) CuZn3 (c ) CuZn6

**Table 6.3.** Estimated stoichiometry from EDAX.

| Sample | Stoichiometric ratio Cu:Zn | | Stoichiometric ratio Cu:Fe | | Stoichiometric Composition |
|---|---|---|---|---|---|
| | Expt | Theor | Expt | Theor | |
| $Cu_{0.9}Zn_{0.1}Fe_2O_4$ | 6.35 | 9 | 0.54 | 0.45 | $Cu_{0.86}Zn_{0.14}Fe_{1.67}O_4$ |
| $Cu_{0.7}Zn_{0.3}Fe_2O_4$ | 2.16 | 2.33 | 0.38 | 0.35 | $Cu_{0.68}Zn_{0.32}Fe_{1.84}O_4$ |
| $Cu_{0.4}Zn_{0.6}Fe_2O_4$ | 0.83 | 0.67 | 0.23 | 0.2 | $Cu_{0.52}Zn_{0.48}Fe_{1.74}O_4$ |

## *Magnetic Characterisation*

### *6.3.5 M-H Curves*

The field dependent magnetisation (M-H) curves of $Cu_{1-x}Zn_xFe_2O_4$ samples at 300K and 5K were recorded and are shown in Fig.6.8 and Fig. 6.9 respectively.

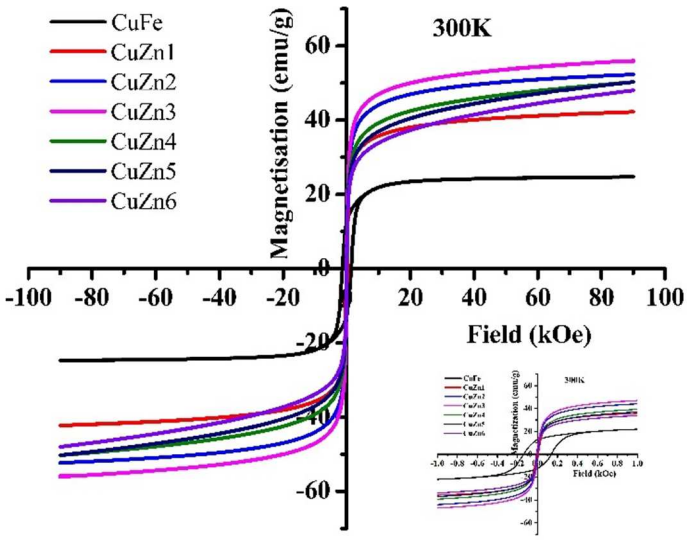


**Figure 6.8.** M-H curves of $Cu_{1-x}Zn_xFe_2O_4$ at 300K

It is evident from Fig. 6.8 that the copper ferrite exhibits ferromagnetic behaviour at room temperature, 300 K, with finite coercivity and retentivity. The substitution of $Zn^{2+}$ for $Cu^{2+}$ in the copper ferrite system reduces the ferromagnetic behaviour, and the M-H loop changes to a reversible *'s'* shape, indicating a superparamagnetic nature. An assembly of superparamagnetic nanoparticles experiences net magnetisation when an external magnetic field H is applied because the magnetic moments of the particles prefer to align along the applied field. The superparamagnetic behaviour of the samples can also be evident from the estimated crystallite size from the XRD pattern because superparamagnetism appears in small ferrimagnetic or ferromagnetic nanoparticles. For x=0 and x=0.1 in $Cu_{1-x}Zn_xFe_2O_4$, a saturation magnetisation can be observed, whereas the samples with x>0.1, exhibit a

non-saturating behaviour. Similar behaviour can also be observed in the magnetisation curves of $Cu_{1-x}Zn_xFe_2O_4$ samples at a lower temperature of 5 K.

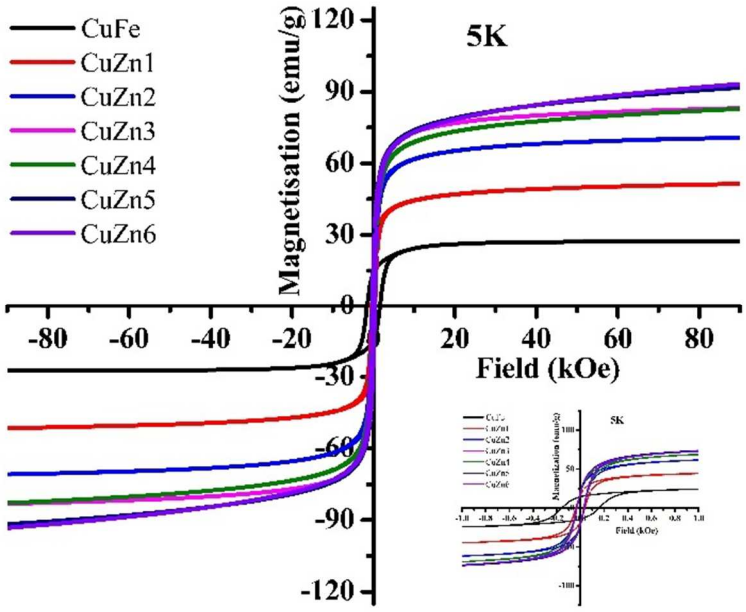


**Figure 6.9.** M-H curves of $Cu_{1-x}Zn_xFe_2O_4$ at 5K

The M-H curves of $Cu_{1-x}Zn_xFe_2O_4$ samples at 300 K and 5 K revealed that the samples exhibit a ferromagnetic behaviour at these temperatures. The reported value of $M_s$ for bulk $CuFe_2O_4$ is about 33.3 emu/g, and that of nanocrystalline $CuFe_2O_4$ at 300 K is 21.45 emu/g[24]. It was observed that the magnetisation was not saturated for samples x>0.2 even in the highest applied magnetic field of 80 kOe. The non saturating behaviour of the samples with x>0.2 is more pronounced due to the superparamagnetic effect and spin canting of the samples. The spins of the superparamagnetic particles flip between the easy axis of magnetisation resulting near zero coercivity and nonsaturation in magnetisation. The magnetic parameters, maximum magnetization $M_s$, coercive field $H_c$, remanent magnetisation $M_r$, remanence ratio $M_r/M_s$, and magneto-crystalline anisotropic constant K estimated from M-H curves of $Cu_{1-x}Zn_xFe_2O_4$ at 300 K and 5 K are displayed in Table 6.4.

**Table 6.4.** Magnetic parameters of $Cu_{1-x}Zn_xFe_2O_4$ at 300 K and 5 K.

| x | $M_s$ (emu/g) | | $H_c$ (Oe) | | $M_r$ (emu/g) | | $M_r/M_s$ | | $n_B$ | |
|---|---|---|---|---|---|---|---|---|---|---|
| | **300K** | **5K** | **300K** | **5K** | **300K** | **5 K** | **300K** | **5K** | **300K** | **5K** |
| **0** | 24.73 | 27.35 | 1361 | 1632 | 10.21 | 12.215 | 0.41 | 0.45 | 0.9 | 1.0 |
| **0.1** | 42.24 | 51.36 | 103 | 391 | 7.165 | 18.023 | 0.17 | 0.35 | 1.8 | 2.2 |
| **0.2** | 44.22 | 67.78 | 65 | 310 | 6.821 | 21.726 | 0.15 | 0.32 | 1. 9 | 2.9 |
| **0.3** | 56.11 | 83.10 | 40 | 264 | 6.379 | 19.279 | 0.11 | 0.23 | 2.4 | 3.6 |
| **0.4** | 50.26 | 82.83 | 33 | 314 | 2.450 | 19.716 | 0.05 | 0.24 | 2.2 | 3.6 |
| **0.5** | 50.28 | 91.71 | 17.5 | 282.1 | 1.570 | 22.310 | 0.03 | 0.24 | 2.2 | 3.9 |
| **0.6** | 48.02 | 93.24 | 12.75 | 282.54 | 0.980 | 21.640 | 0.02 | 0.23 | 2.1 | 4.0 |

The maximum magnetisation initially increases with nonmagnetic Zn substitution and then decreases. Many researchers have reported similar findings in Zn-substituted ferrite samples [16,17,19,25]. This can be explained based on Neel's two sublattice models. As $Zn^{2+}$ ions have an affinity for A sites, they occupy A sites, and some $Fe^{3+}$ ions in the A site shift to the B site. The magnetic moment of the A site decreases and that of the B site increases due to the large number of $Fe^{3+}$ ions. So net magnetic moments increase and this raises the value of $M_s$ with the concentration of Zn up to x=0.3. A maximum value of magnetization of 56.11 emu/g has been observed for the sample x=0.3. It is greater than the reported value of magnetisation of zinc substituted copper ferrite nanoparticles for x=0.2 at 300K [16]. Thereafter, with the increase in concentration of zinc, $Zn^{2+}$ ions occupy tetrahedral A sites, and more $Fe^{3+}$ ions migrate into the octahedral B site. The magnetic moments of the tetrahedral A site are weakened because the $Fe^{3+}$ - $Fe^{3+}$ interaction increases and the $Zn^{2+}$ - $Fe^{3+}$ interaction between tetrahedral A and octahedral B site decreases and hence resulting in a decrease in the magnetic moment of the samples. Due to the increased number of $Fe^{3+}$ ions in the octahedral B site, the moments are no longer

collinear, and a canted spin structure can be formed. The decrease in the magnetic moment for the samples x > 0.3 indicates a possibility of noncollinear spin structure in the system, which can be explained on the basis of the three sublattice model suggested by Yafet–Kittel YK[26].

The variation of maximum magnetisation with x at 300 K and 5K is shown in Fig. 6.10. The $Cu_{1-x}Zn_xFe_2O_4$ samples exhibit an interesting magnetic behavior at a low temperature 5K. The saturation magnetisation increases gradually with the substitution of $Zn^{2+}$ ions in copper ferrite. It exhibits an enhanced magnetisation value at 5K ($M_s$ =93.24 emu/g) for x=0.6 when $Cu^{2+}$ is replaced by non- magnetic $Zn^{2+}$ ions. This is higher than the reported value of magnetisation of cobalt substituted copper ferrite at 5K even though $Co^{2+}$ is a magnetic ion[27].

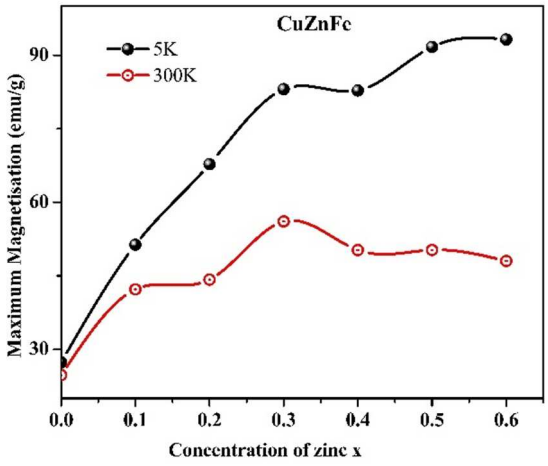


**Figure 6.10.** Variation of Magnetisation with x of $Cu_{1-x}Zn_xFe_2O_4$ at 300 K and 5 K

The values of coercivity and remanent magnetisation at room temperature and 5K show that the $Cu_{1-x}Zn_xFe_2O_4$ samples are soft magnets. Table 6.4. reveals that the remanent magnetiastion, $M_r$, decreases with the substitution of $Zn^{2+}$ at room temperature. $M_r$ values vary from 10.21 emu/g to 0.98 emu/g for x=0 to x=0.6, indicating that the $Cu_{1-x}Zn_xFe_2O_4$ samples possess the properties of soft magnets. It should be noted that the remanent magnetisation decreases at room temperature

whereas increases at a lower temperature with zinc concentration. The increase in the value of $M_r$ is due to the ferrimagnetic property of zinc substituted samples. At lower temperatures remanent magnetisation varies in the same manner as that of the maximum magnetisation. This significant result indicates that the lower temperature measurements reveal the intrinsic property of the magnetic particles. The $Zn^{2+}$ substitution enhances the $Fe^{3+}$ interactions in the B site, and at lower temperatures the thermal agitation reduces, which suppresses the spin canting and makes the system more ferrimagnetic. But at room temperature, $M_r$ decreases whereas M increases, favouring superparamagnetism. The variation of remanent magnetisation and squareness ratio $M_r/M_s$ with the concentration of zinc at 5 K and 300 K is shown in Fig.6.11 (a) and (b), respectively.

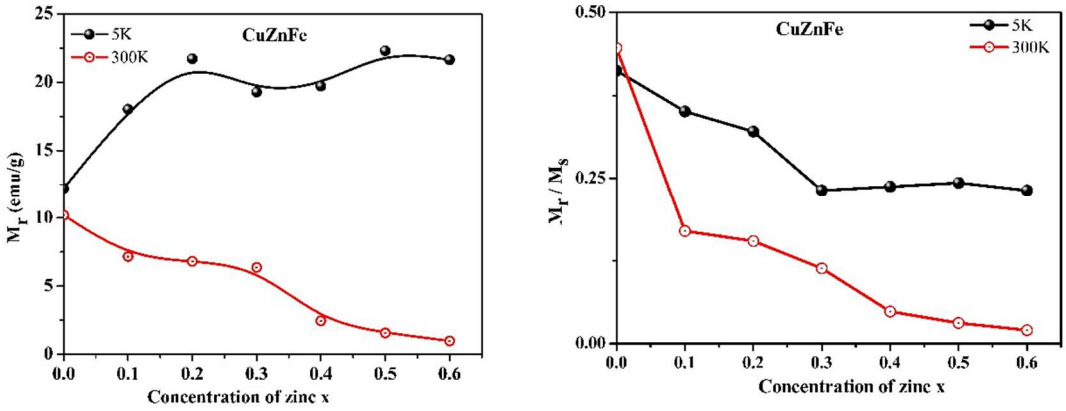


(a) (b)

**Figure 6.11.** (a) Variation of $M_r$ (b) $M_r/M_s$ with x in $Cu_{1-x}Zn_xFe_2O_4$ at 300K and 5K.

$M_r/M_s$ ratio decreases with the substitution of zinc, and it attains a very low value of 0.02 for x=0.6 at room temperature. The existence or absence of the different types of inter-grain group exchanges is determined by the value of $M_r/M_s$ which varies from 0 to 1[28]. It has been reported that Mr/Ms = 0.5 is for the particle interaction by magnetostatic interaction. The squareness ratio $M_r/M_s$ is found to be less than 0.5, indicating that the particles are non-interacting.

The coercivity of the samples is observed to be small, and it decreases with zinc substitution. The rapid decrease of coercivity with zinc substitution can be explained on the basis of Brown's relation[29]. According to this relation, the coercivity decreases inversely with saturation magnetisation. The smaller values of particle size, coercivity, and $M_r$ with the non-saturating behavior of the hysteresis loop exhibit a superparamagnetic behavior for the higher concentrations of zinc. A magnetic transition from ferromagnetic to superparamagnetic can be observed when $CuFe_2O_4$ is substituted with $Zn^{2+}$, which is evident from the M-T curves discussed in Chapter 7. This is due to the reduction of crystallite size with the substitution of zinc in copper ferrite.

The variation of coercivity with zinc concentration at 300 K and 5 K is shown in Fig. 6.12. It can be observed that the coercivity decreases with Zn substitution in Copper Ferrite at room temperature. The decreases in coercivity and squareness ratio ($M_r/M_s$ ) can be mainly due to the paramagnetic relaxation effect and magnetisation dilution [30]. The property is typical of superparamagnetic nanomagnetic materials.

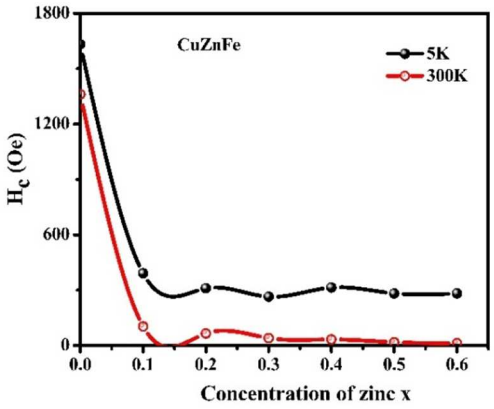


**Figure 6.12.** (a) Variation of $H_c$ with x in $Cu_{1-x}Zn_xFe_2O_4$ at 300 K and 5 K

A significant decrease in coercivity from 1361Oe to 12.75 Oe has been observed when $Cu^{2+}$ is substituted by $Zn^{2+}$ in Copper Ferrite. The highest value of coercivity is due to the larger magnetocrystalline anisotropy of copper ferrite. The small values of coercivity and the smaller crystallite size of the $Cu_{1-x}Zn_xFe_2O_4$

samples for x>0.1 indicate a single domain behavior resulting in the superparamagnetic nature of the samples. A similar variation can also be observed in $M_r$ values from 10.21 emu/g to 0.98 emu/g, indicating that the $Cu_{1-x}Zn_xFe_2O_4$ samples possess the properties of soft magnets. At lower temperatures, 5K, coercivity also varied in the same manner as that has been observed at room temperature in $Cu_{1-x}Zn_xFe_2O_4$. There was no noticeable change between the coercivity at 300K and 5K contrary to what was observed in $Cu_{1-x}Co_xFe_2O_4$ in Chapter 5. All the magnetic parameters except the squareness ratio are enhanced at 5K when compared to 300K because at lower temperatures, magnetic properties are dominant rather than the thermal properties. The magnetisation curves at 300K were fitted with the Langevin function to examine the superparamagnetic behaviour of the samples and are shown in 6.13.

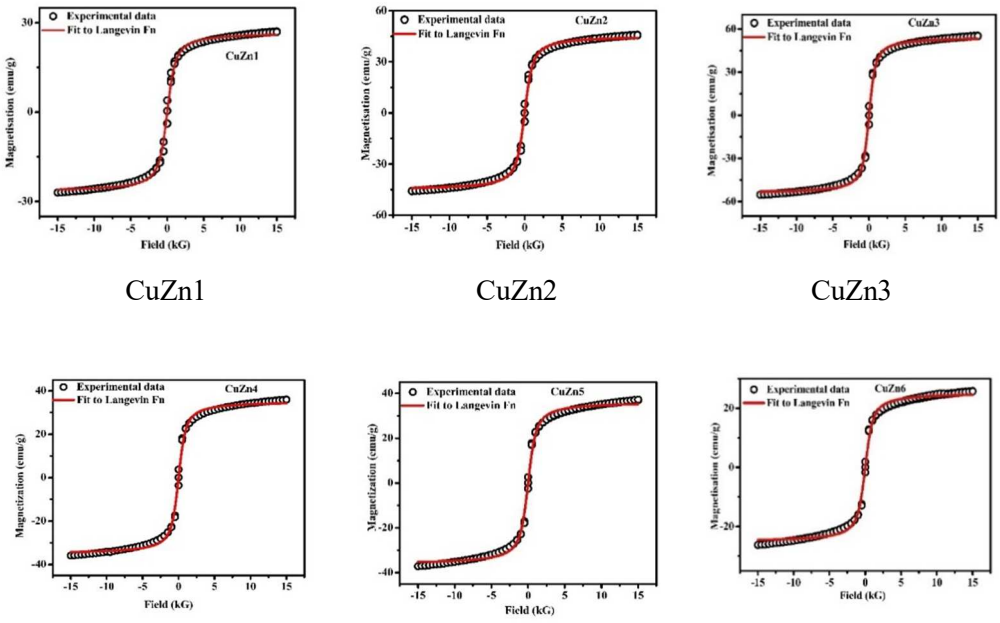


CuZn1 CuZn2 CuZn3

CuZn4 CuZn5 CuZn6

**Figure 6.13.** M-H curves fitted with Langevin function.

It is clear from the figure that the Langevin function is best fitted with the least difference for all the samples all zinc substituted copper ferrites, indicating the superparamagnetic nature.

The variation of magneto magneto-crystalline anisotropic constant with zinc concentration is shown in Fig. 6.14. The collective behavior of the magnetic nanoparticles is controlled by the magneto crystalline anisotropy energy. The magneto crystalline anisotropic constant is also decreased with the substitution of $Cu^{2+}$ by $Zn^{2+}$ in copper ferrite. The spin–orbital interactions in Cu–ferrite with a tetragonal crystal lattice distortion due to the cooperative Jahn–Teller effect is responsible for the significant magnetocrystalline anisotropy [31]. $Cu^{2+}$ ($3d^9$) in $CuFe_2O_4$ has one unpaired electron and has an orbital angular momentum, L=2, and spin angular momentum, $S = \frac{1}{2}$, which is mainly responsible for the strong L-S coupling, resulting in significant anisotropy. But $Zn^{2+}$ ($3d^{10}$) has no unpaired electrons and leads to zero net electron spin, which causes a decrease in anisotropy with an increase in zinc concentration in $Cu_{1-x}Zn_xFe_2O_4$.

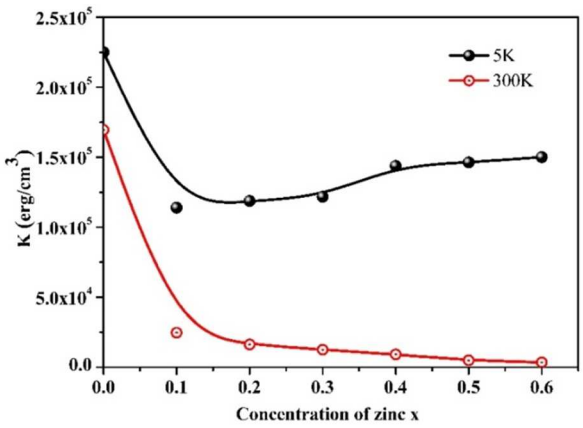


**Figure 6.14.** Variation of *K* with x at 300 K and 5 K.

A sharp decrease in the anisotropic constant *K* can be observed in Fig. 6.14. for the initial composition of $Cu_{1-x}Zn_xFe_2O_4$ samples. As the anisotropy constant K strongly depends on $H_c$, it decreases with x at room temperature in the same way $H_c$ varies at room temperature. The anisotropy constant is enhanced at the lower temperature of 5K. Although $H_c$ value falls too low, it is worth mentioning that the typical sample CuZn6 shows an enhanced value of *K* at 5K, which is 43 times greater than the value at 300 K due to its high $M_s$ value at 5K..

## 6.4. Effect of a magnetic and non-magnetic cation on the structural and magnetic properties of copper ferrite.

A magnetic cation, cobalt, and a non magnetic cation, zinc are substituted in copper ferrite to prepare two series of samples $Cu_{1-x}Zn_xFe_2O_4$ and $Cu_{1-x}Co_xFe_2O_4$ by a modified solgel auto combustion method. The structural and magnetic properties of the samples in these two series up to x=0.6 were compared. It can be found that structural and magnetic properties can be modified by the substitution of cobalt and zinc in copper ferrite. It is evident from the XRD pattern shown in Fig. 5.2 (Chapter 5) and Fig. 6.2 described in the structural analysis that the crystal structure changes from a body-centered tetragonal to a face centered cubic symmetry with the substitution of $Co^{2+}$ and $Zn^{2+}$ in $CuFe_2O_4$. The initial composition x=0.1 can change the crystal structure to a cubic structure. The tetragonal copper ferrite of inverse spinel changes to a normal spinel with $Zn^{2+}$ substitution, whereas $Co^{2+}$ can change it into an inverse spinel cubic symmetry. The variation of crystallite size and lattice parameter of $Cu_{1-x}Co_xFe_2O_4$ and $Cu_{1-x}Zn_xFe_2O_4$ are shown in Fig.6.15(a) and (b), respectively.

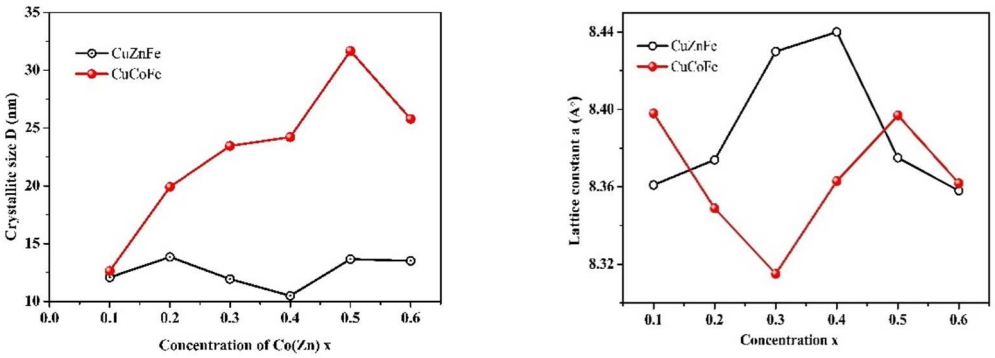


(a) (b)

**Figure 6.15.** Variation of (a) crystallite size (b) lattice parameter in $Cu_{1-x}A_xFe_2O_4$ (A=Co, Zn)

Fig.6.15(a) reveals that the crystallite size increases with $Co^{2+}$ substitution whereas substitution of $Zn^{2+}$ shows a decrease in crystallite size. It has been observed from the Fig. 6.15 (b) that the lattice constant is higher in $Cu_{1-x}Zn_xFe_2O_4$ than $Cu_{1-}$

$_xCo_xFe_2O_4$. So, lattice expansion can be observed for $Cu_{1-x}Zn_xFe_2O_4$ even though the ionic radius of $Co^{2+}$ and $Zn^{2+}$ are almost comparable (0.74 Å). It is due to the redistribution of cations in the tetrahedral and octahedral sites. $Co^{2+}$ ions have an affinity to octahedral site whereas $Zn^{2+}$ has a tetrahedral affinity. The crystallite size also plays an important role in the lattice expansion of CuCoFe samples because the crystallite size of CuCoFe particles is greater than that of CuZnFe.

The morphological studies detailed in section 5.3.4. (Chapter 5) and 6.3.5 show that the particles exhibit similar morphology. The SEM images of typical samples in the two series are shown in Fig.6.16. It can be observed from the TEM that both the particles are nanocrystalline. The $Cu_{1-x}Co_xFe_2O_4$ samples are found to be more agglomerated than $Cu_{1-x}Zn_xFe_2O_4$, which is attributed to the enhanced magnetic properties of cobalt substituted copper ferrite particles at room temperature. The EDAX spectrum indicates that the estimated stoichiometry is consistent with the theoretical value and incorporation of $Co^{2+}$ and $Zn^{2+}$ in $CuFe_2O_4$ can be confirmed.

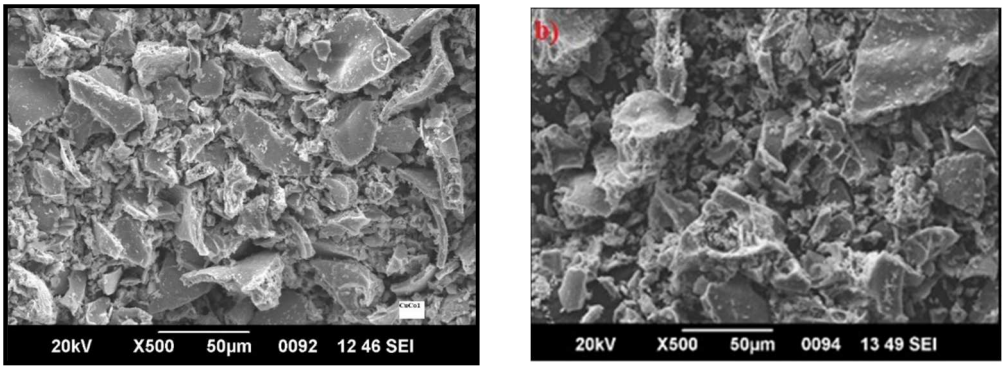


(a) (b)

**Figure 6.16.** SEM micrograph of (a) CuCo1 (b) CuZn3

The magnetic properties of $Cu_{1-x}A_xFe_2O_4$ (A=Co, Zn) have been investigated and compared. The variation of maximum magnetization, coercivity, remanent magnetisation, and anisotropy constant for $Co^{2+}$ and $Zn^{2+}$ substituted $CuFe_2O_4$ at 5K and 300 K is shown in Fig.6.17.

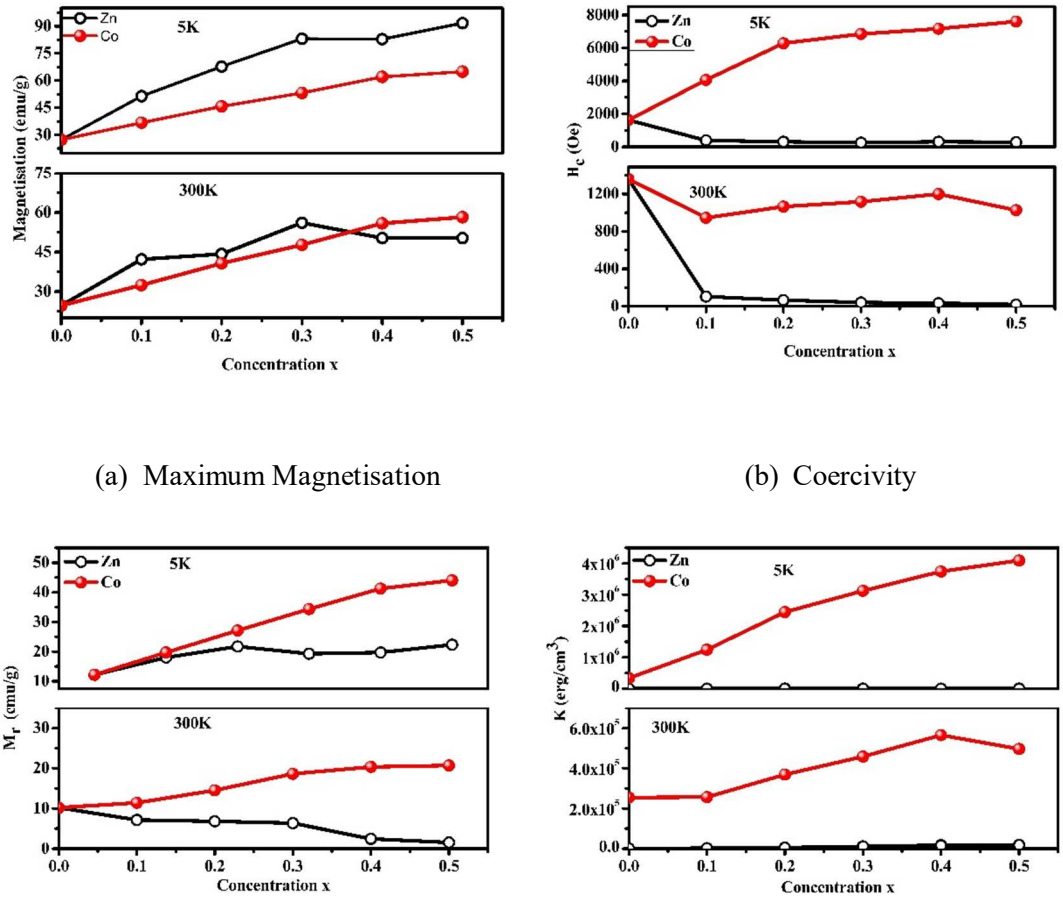


(a) Maximum Magnetisation

(b) Coercivity

(c ) Remanent Magnetisation $M_r$

(d) Anisotropy Constant

**Figure 6.17.** Variation of (a) maximum magnetisation, (b) coercivity, (c) remanent magnetisation and anisotropic constant with concentration of $Co^{2+}$/ $Zn^{2+}$ at 300 K and 5 K.

**Table 6.5.** Comparison of magnetic properties of CuCoFe and CuZnFe at 300K

| Concentration of Co/Zn (x) | Max. Magnetisation (emu/g) | | $H_C$(kOe) | | $M_r$ (emu/g) | | K x$10^6$ (erg/cm$^3$) | |
|---|---|---|---|---|---|---|---|---|
| | ***Co*** | ***Zn*** | ***Co*** | ***Zn*** | ***Co*** | ***Zn*** | ***Co*** | ***Zn*** |
| **0.1** | 32.44 | 42.24 | 945 | 103.1 | 11.4 | 7.165 | 0.257 | 0.024673 |
| **0.2** | 40.71 | 44.22 | 1065 | 65.30 | 14.5 | 6.821 | 0.368 | 0.016302 |
| **0.3** | 47.7 | 56.11 | 1118 | 40.16 | 18.6 | 6.379 | 0.46 | 0.012479 |
| **0.4** | 55.89 | 50.26 | 1200 | 33 | 20.3 | 2.450 | 0.564 | 0.009160 |
| **0.5** | 58.2 | 50.28 | 1027 | 17.5 | 20.7 | 1.570 | 0.49 | 0.004977 |

It is observed from Table 6.4 that the magnetisation increases with both the Co and Zn cation substitution in copper ferrite. It can also be noticed that CuCo5 exhibits a higher value of magnetisation 58.2 emu/g than CuZn3 (50.28 emu/g) at room temperature. However, it is noteworthy that CuZn5 exhibits higher magnetization (91.71 emu/g) than CuCo5 with a magnetisation value of 64.9 emu/g at 5K. The enhanced magnetization of CuZnFe samples can be explained based on Neel's two sublattice model in ferromagnetism. A noticeable increase in $M_s$ of CuZnFe can be observed at lower temperatures when compared with CuCoFe. This is due to the ferrimagnetic property of CuZnFe, which dominates over the thermal agitation at lower temperatures. The coercivity and magnetocrystalline anisotropy constant are maximum for $Cu_{1-x}Co_xFe_2O_4$ compared to $Cu_{1-x}Zn_xFe_2O_4$ due to the intrinsic anisotropic property of cobalt. The remanent magnetisation $M_r$ also exhibits the same behaviour as that of $H_c$.

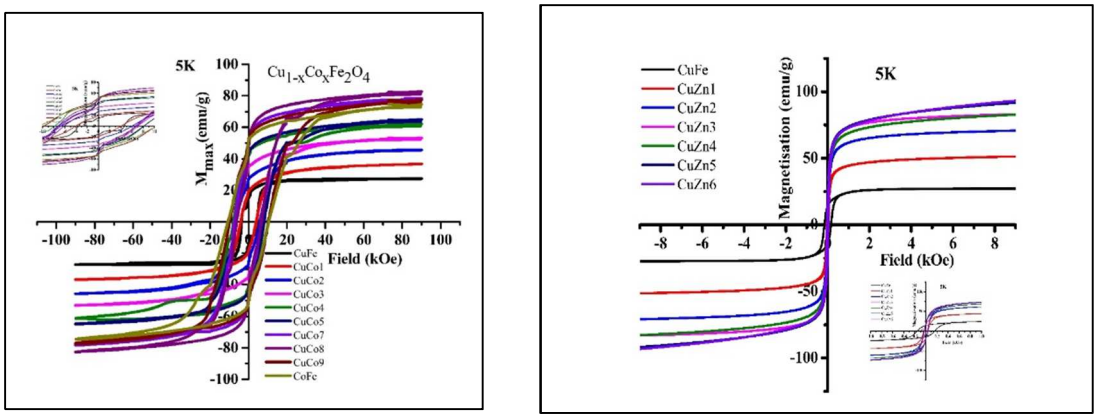


**(a)** **(b)**

**Figure 6.18.** M-H curves of (a) CuCoFe (b) CuZnFe at 5 K.

The hysteresis loops of CuCoFe and CuZnFe are displayed in Fig. 6.18. The hysteresis loop of CuZnFe and CuCoFe reveals that zinc substituted samples are superparamagnetic, whereas cobalt substituted samples are ferromagnetic at room temperature. However, CuZnFe exhibits a ferrimagnetic behaviour at a lower temperature. Zinc substituted copper ferrite can have applications of soft magnets and cobalt substituted samples can act as hard magnets.

## 6.5 Conclusion

$Cu_xZn_{1-x}Fe_2O_4$ (0-0.6) samples have been synthesized by a modified sol-gel auto combustion method. Structural studies of the samples showed that nanocrystalline particles crystallised in the face centered cubic structure. The nano crystalline behaviour of the samples has been confirmed by the TEM images and SAED pattern. Homogeneous, uniform spherical particles of $Cu_xZn_{1-x}Fe_2O_4$ samples were identified from the TEM analysis. The experimental value of the stoichiometry of a typical sample is found to be consistent with the theoretical value using the EDAX spectrum. The magnetic properties showed that the samples exhibit a ferromagnetic behaviour at 300 K and 5 K. Enhanced magnetic properties can be observed with zinc substitution in copper ferrite up to x=0.3 and attain a maximum

value of 56.11 emu/g for x=0.3 at 300 K; thereafter, it decreases. But at 5 K, the magnetization increases with substitution, and a maximum value of 96 emu/g has been observed for x= 0.6. So, the zinc-substituted copper ferrite nanoparticles are promising candidates for technological applications at lower temperatures. On comparing the CuCoFe and CuZnFe samples, it was observed that even though the two series of samples have some similarities in the structure, they differ in their structural and magnetic properties. Both series of samples exhibit a structural change from tetragonal to cubic with cation Co or Zn substitution in copper ferrite. Cobalt substitution in copper ferrite resulted in a lattice contraction while zinc substitution expanded the lattice. This is due to the electron affinity of $Co^{2+}$ and $Zn^{2+}$ to octahedral and tetrahedral sites and cation distribution. The CuCoFe samples are hard ferromagnetic, while CuZnFe are soft and superparamagnetic materials. At room temperature, CuCoFe samples exhibit enhanced magnetic properties whereas CuZnFe samples exhibit high magnetization compared to CuCoFe at lower temperatures. The enhanced values of coercivity and anisotropy constant find application in magnetic storage devices and hyperthermia applications. CuZnFe samples can be used as cryogenic soft ferrites as their magnetic properties are enhanced at lower temperatures.

**REFERENCES**

[1] M.A. Dar, D. Varshney, J Magn Magn Mater 436 (2017) 101–112.

[2] E.R. Kumar, R. Jayaprakash, G.S. Devi, P.S.P. Reddy, J Magn Magn Mater 355 (2014) 87–92.

[3] M. Rahimi-Nasrabadi, M. Behpour, A. Sobhani-Nasab, M.R. Jeddy, Journal of Materials Science: Materials in Electronics 27 (2016) 11691–11697.

[4] M. Saini, S.K. Singh, R. Shukla, A. Kumar, J Inorg Organomet Polym Mater 28 (2018) 2306–2315.

[5] A Mallah, jnsm.qu., 11 (2018) 15–28.

[6] M.A. Ahmed, H.H. Afify, I.K. El Zawawia, A.A. Azab, J Magn Magn Mater 324 (2012) 2199–2204.

[7] S.S. Jadhav, S.E. Shirsath, S.M. Patange, K.M. Jadhav, J Appl Phys 108 (2010).

[8] V. Mameli, A. Musinu, A. Ardu, G. Ennas, D. Peddis, D. Niznansky, C. Sangregorio, C. Innocenti, N.T.K. Thanh, C. Cannas, Nanoscale 8 (2016) 10124.

[9] E. Veena Gopalan, I.A. Al-Omari, K.A. Malini, P.A. Joy, D. Sakthi Kumar, Y. Yoshida, M.R. Anantharaman, J Magn Magn Mater 321 (2009) 1092–1099.

[10] T. Hu, X. Chi, Q. Lu, L. Yu, R. Li, Y. Liu, A. Du, Z. Li, F. Shi, Y. Hu, J Alloys Compd 801 (2019) 465–472.

[11] A. Tawfik, O.M. Hemeda, D.M. Hemeda, M. Mostafa, Eur Phys J Plus 129 (2014).

[12] S. Bahhar, A. Boutahar, L.H. Omari, H. Lemziouka, E.K. Hlil, H. Bioud, E. Dhahri, J Magn Magn Mater 539 (2021).

[13] T.L. Phan, N. Tran, D.H. Kim, N.T. Dang, D.H. Manh, T.N. Bach, C.L. Liu, B.W. Lee, J Electron Mater 46 (2017) 4214–4226.

[14] J. Zhao, X. Liu, X. Kan, C. Liu, W. Wang, J. Hu, Q. Lv, J. Huang, M. Shazeda, Ceram Int 47 (2021) 7906–7917.

[15] M. Kanagaraj, P. Sathishkumar, G.K. Selvan, I.P. Kokila, S. Arumugam, Indian Journal of Pure and Applied Physics 52 (2014) 124–130.

[16] C. Murugesan, N. Kambhala, S. Angappane, G. Chandrasekaran, J Magn Magn Mater 443 (2017) 334–342.

[17] K. Verma, A. Kumar, D. Varshney, Current Applied Physics 13 (2013) 467–473.

[18] B.D. Cullity, S.R. Stock, Elements of X ray Diffraction, Prentice-Hall, New York (2001).

[19] A. Tony Dhiwahar, M. Sundararajan, P. Sakthivel, C.S. Dash, S. Yuvaraj, Journal of Physics and Chemistry of Solids 138 (2020) 109257.

[20] A.H. Al-Hammadi, S.H. Khoreem, W.F. Al-Ryani, Letters in Applied NanoBioScience 12 (2023).

[21] S. Muthukumaran, R. Gopalakrishnan, Opt Mater (Amst) 34 (2012) 1946–1953.

[22] Z.N. Kayani, M. Iqbal, S. Riaz, R. Zia, S. Naseem, Materials Science- Poland 33 (2015) 515–520.

[23] M.N. Akhtar, M.A. Khan, M. Ahmad, M.S. Nazir, M. Imran, A. Ali, A. Sattar, G. Murtaza, J Magn Magn Mater 421 (2017) 260–268.

[24] F.A. Wahaab, L.L. Adebayo, A.A. Adekoya, I.G. Hakeem, B. Alqasem, A.M. Obalalu, J Alloys Compd 836 (2020) 155272.

[25] C. Choodamani, B. Rudraswamy, G.T. Chandrappa, Ceram Int 42 (2016) 10565–10571.

[26] C. Kittel, J. Chem. Phys 7 (1947) 174.

[27] S. Bhaskaran, I.A. Al-Omari, E.V. Gopalan, J Alloys Compd 884 (2021) 161095.

[28] E.E. Ateia, A.A. El-Bassuony, G. Abdelatif, F.S. Soliman, Journal of Materials Science: Materials in Electronics 28 (2017) 241–249.

[29] K.H. Maria, S. Choudhury, M.A. Hakim, Int Nano Lett 3 (2013) 1–10.

[30] W. Pan, F. Gu, K. Qi, Q. Liu, J. Wang, Mater Chem Phys 134 (2012) 1097–1101.

[31] I. Nedkov, R.E. Vandenberghe, T. Marinova, P. Thailhades, T. Merodiiska, I. Avramova, Appl Surf Sci 253 (2006) 2589–2596.

…..ಞ*ಞ…..

# Chapter 7

# Tuning the Magnetocaloric Properties of $Cu_{1-x}Co_xFe_2O_4$ and $Cu_{1-x}Zn_xFe_2O_4$ Nanoparticles

## Objectives

The magnetocaloric properties of magnetic ($Co^{2+}$) and non-magnetic cation ($Zn^{2+}$) substituted copper ferrite nanoparticles ($Cu_{1-x}Co_xFe_2O_4$ and $Cu_{1-x}Zn_xFe_2O_4$) are studied. The temperature dependent magnetisation (ZFC-FC) curves and magnetisation isotherms are used to estimate the isothermal magnetic entropy change ($\Delta S_m$), the MCE characteristic value of the ferrite nanoparticles.

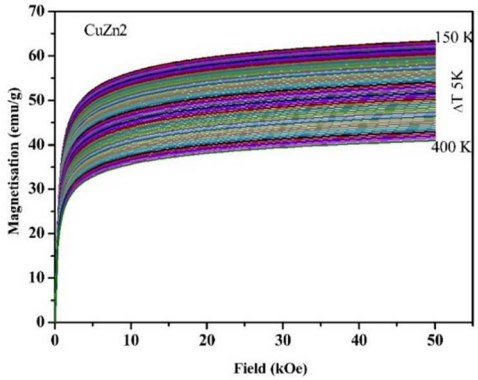

## 7.1 Introduction

According to the literature review, spinel ferrites also exhibit magnetocaloric characteristics in addition to the perovskite material. However, the magnetocaloric properties and their applications in ferrites have not been widely investigated. Recently, all over the world, scientists have been interested in the MCE properties of iron oxide compounds because of their significant relative cooling power and magnetic entropy change. Spinel ferrites are considered to be a good candidate as an MCE material owing to their tunable magnetic transition temperature, by controlling the particle size its shape, and stoichiometry. The magnetocaloric properties have been reported mostly in Mg, Co, Ni and Zn ferrites[1–8]. The literature review suggests that due to the higher transition temperature of ferrite materials, the majority of the reported studies on the MCE in ferrites were carried out at higher temperatures. M.S. Anwar *et.al*. reported an isothermal magnetic entropy change, $\Delta S_m$, of 1.39 J/kg/K for $Ni_{0.7}Zn_{0.3}Fe_2O_4$ under an applied field of 2.5 T. However, this is an appreciable value among ferrite groups, it is exhibited at a higher temperature of 664 K [9].

Shahida Aktar *et. al.* reported a maximum value of $\Delta S_m$, 1.77 J/kg/K in $Cu_{0.4}Zn_{0.6}Fe_2O_4$ under a field of 5T [10]. Chau *et. al.* reported a maximum entropy change of 0.98 J/kg/K under 1.3T in $Ni_{0.3}Zn_{0.7}Fe_2O_4$ [11]. Materials with magnetocaloric properties close to room temperature will be preferred for residential and commercial use as magnetic refrigerants. Refrigerant techniques have been extensively investigated for residential cooling, medical applications, consumer goods, space and defence applications, etc. Even though there are numerous research works on the magnetic properties of copper ferrite, one of the important ferrites among the transition metal ferrites, its magnetocaloric properties are not available in the literature. The present chapter describes the magnetocaloric properties of copper ferrite and $Zn^{2+}$ and $Co^{2+}$ substituted copper ferrites near room temperature.

The magnetocaloric properties of Co substituted copper ferrite samples $Cu_{1-x}A_xFe_2O_4$ (A=Co, Zn) synthesised by a modified sol-gel auto combustion method are described in this chapter. For the MCE measurements, the normal procedures adopted in Chapter 4 are followed. The ZFC-FC measurements of the $Cu_{1-x}Co_xFe_2O_4$ and $Cu_{1-x}Zn_xFe_2O_4$ samples were carried out initially to determine the transition temperature in a temperature range of 10 K to 400 K under an applied field of 50 Oe. Followed by the temperature-dependent measurements, the magnetisation isotherms will be recorded around the observed transition temperature. The characteristic property of MCE, isothermal magnetic entropy change, is estimated from the magnetisation isotherms at different temperatures using the equation (1.33).

## Results and Discussion

## 7.2 MCE Characterisation of $Cu_{1-x}Co_xFe_2O_4$

### *7.2.1 ZFC-FC measurements*

All the samples in the series were found to be ferromagnetic at 300 K and 5 K (Chapter 5, section 5.3.5). The ZFC-FC curves of $Cu_{1-x}Co_xFe_2O_4$ samples with x=0 to 1 are shown in Fig. 7.1 to Fig. 7.8. The ZFC-FC curves of all the samples in the $Cu_{1-x}Co_xFe_2O_4$ series show a similar pattern, except for CuCo1. The ZFC-FC curves reveal that no ferromagnetic to paramagnetic transition can be identified in the measured temperature region of 5 K to 400 K for all the samples. Thus the Curie transition temperature of the samples is above 400 K. However, the ZFC-FC curve of CuCo1 displayed in Fig.7.2., shows a cusp followed by a sharp peak in the ZFC magnetisation curve around 360 K. Usually, the ZFC magnetisation curve of a nanocrystalline material is characterised by a cusp at the blocking temperature ($T_B$). The blocking temperature of the CuCo1 sample is estimated to be 340 K from the derivative plot $\left(\frac{-d(ZFC-FC)}{dT}\right)$. However, the ZFC-FC curves have a noticeable similarity for the CuCo4 and CuCo8 samples, indicating a crossover of ZFC and FC curves at temperatures 209 K and 153 K respectively. It is reported that in magnetic systems with strong anisotropy or slow relaxation dynamics FC magnetisation may drop due to spins being frozen in unfavorable directions during cooling in a field[7].

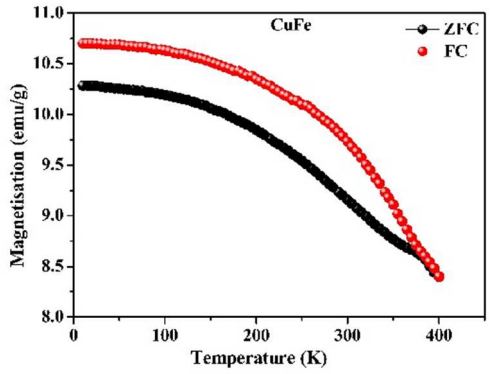


**Figure 7.1.** ZFC-FC -$CuFe_2O_4$

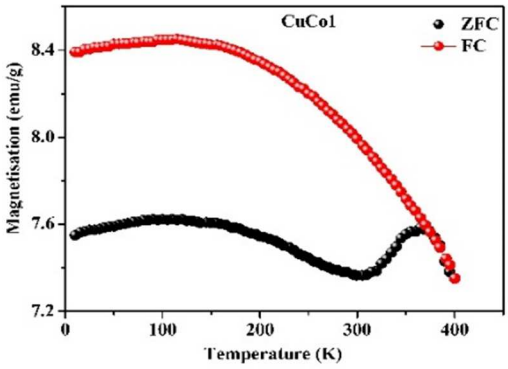


**Figure 7.2.** ZFC-FC -$Cu_{0.9}Co_{0.1}Fe_2O_4$

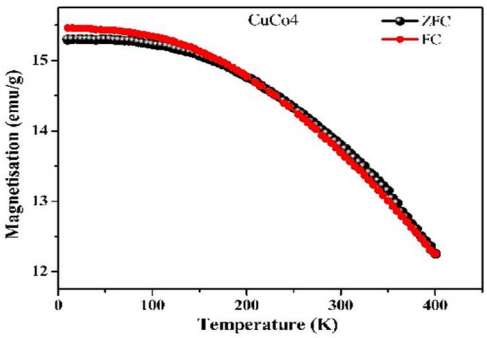


**Figure 7.3.** ZFC-FC -$Cu_{0.6}Co_{0.4}Fe_2O_4$

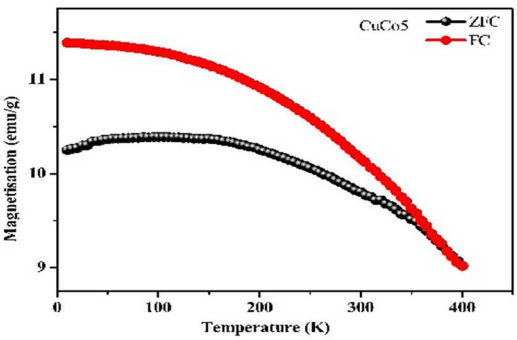


**Figure 7.4.** ZFC-FC -$Cu_{0.5}Co_{0.5}Fe_2O_4$

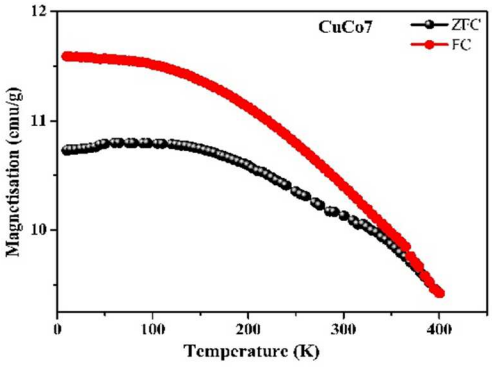


**Figure 7.5.** ZFC-FC -$Cu_{0.3}Co_{0.7}Fe_2O_4$

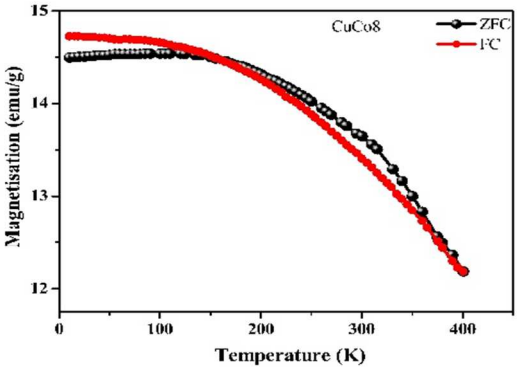


**Figure 7.6.** ZFC-FC -$Cu_{0.2}Co_{0.8}Fe_2O_4$

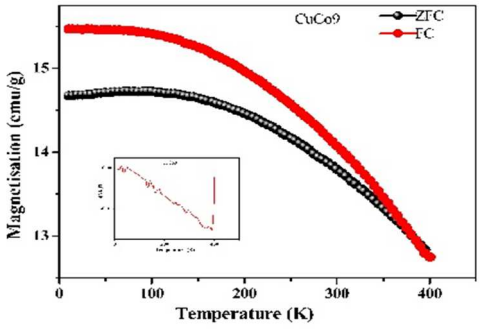


**Figure 7.7.** ZFC-FC -$Cu_{0.1}Co_{0.9}Fe_2O_4$

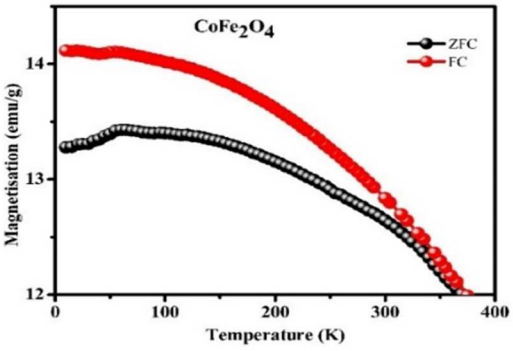


**Figure 7.8.** ZFC-FC -$CoFe_2O_4$

### *7.2.2 Isothermal Magnetisation Curves*

Magnetocaloric properties are typically investigated by analysing the magnetisation isotherms at a lower temperature range of the $Cu_{1-x}Co_xFe_2O_4$ samples. The magnetisation isotherms were recorded in a temperature range from 210 K – 360 K with a step size of 5K for the samples with x=0 to 1 for an applied field of 50 kOe, which are shown in Fig.7.9 to 7.16 respectively.

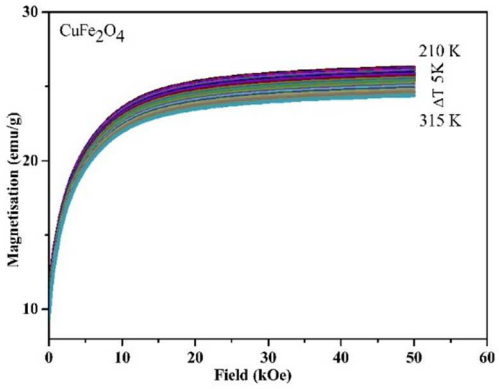


**Figure 7.9.** Magnetisation isotherms of $CuFe_2O_4$

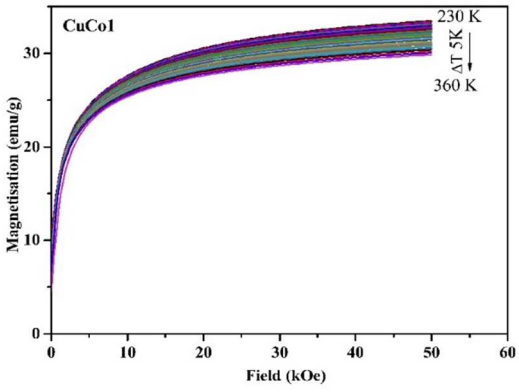


**Figure 7.10.** Magnetisation isotherms of $Cu_{0.9}Co_{0.1}Fe_2O_4$ (CuCo1)

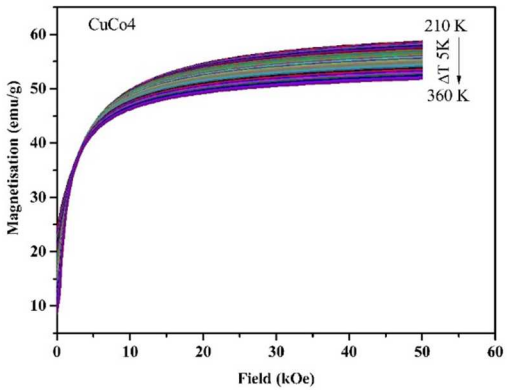


**Figure7.11.** Magnetisation isotherms of $Cu_{0.6}Co_{0.4}Fe_2O_4$ (CuCo4)

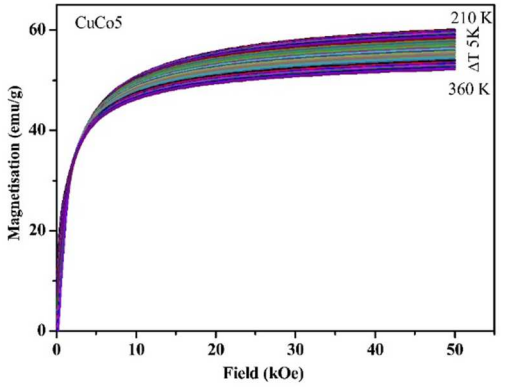


**Figure 7.12.** Magnetisation isotherms of $Cu_{0.5}Co_{0.5}Fe_2O_4$ (CuCo5)

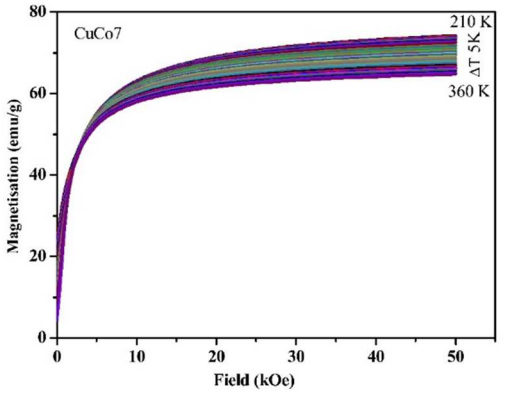


**Figure 7.13.** Magnetisation isotherms of $Cu_{0.3}Co_{0.7}Fe_2O_4$ (CuCo7)

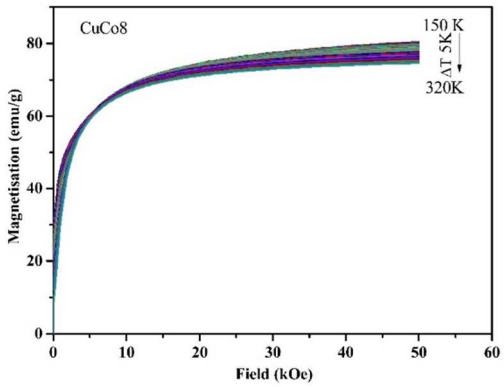


**Figure 7.14.** Magnetisation isotherms of $Cu_{0.2}Co_{0.8}Fe_2O_4$ (CuCo8)

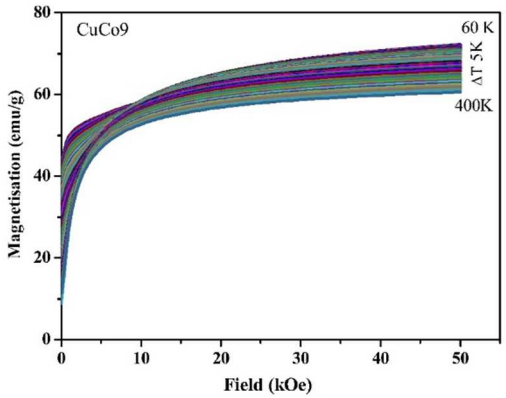


**Figure 7.15.** Magnetisation isotherms of $Cu_{0.1}Co_{0.9}Fe_2O_4$ (CuCo9)

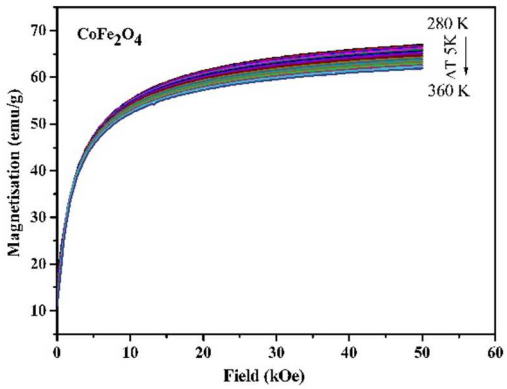


**Figure 7.16.** Magnetisation isotherms of $CoFe_2O_4$

The increase in magnetisation with the applied field and the saturation behaviour of the magnetisation isotherms confirmed the ferromagnetic property of the CuCoFe (x=0.1, 0.5, 0.7, 0.8, 0.9 and 1) samples. The magnetisation isotherms of the CuCoFe exhibit ferromagnetic behaviour in the room temperature range, and a blocking temperature is expected to be observed at high temperatures. A ferromagnetic to superparamagnetic transition is expected to be above room temperature for $Cu_{1-x}Co_xFe_2O_4$. As the ZFC and FC curves are reversible for CuCo4 and CuCo8 samples, a strong ferromagnetic to superparamagnetic transition is anticipated in comparison to other samples.

### *7.2.3 Isothermal Magnetic Entropy Change*

The magnetic entropy change is estimated from the magnetisation isotherms by multiplying the area between adjacent isotherms by the reciprocal of the temperature change by employing equation (1.20). Magnetic entropy change $-\Delta S_m$ was estimated for $Cu_{1-x}Co_xFe_2O_4$ samples, under different applied fields, ranging from 0-50 kOe. The temperature dependence of magnetic entropy change for various applied magnetic fields for $Cu_{1-x}Co_xFe_2O_4$ (x=0.1, 0.5, 0.7, 0.8, 0.9 and 1) samples is displayed in Figs. 7.17 to 7.24, respectively. All the samples except CuCo9 exhibit a normal magnetic entropy change, indicating that heat is released when the magnetic field is adiabatically applied, which is due to the ferromagnetic characteristic of the samples. The magnetic entropy curves revealed that $-\Delta S_m$ increases with temperature and applied magnetic field for all the samples.

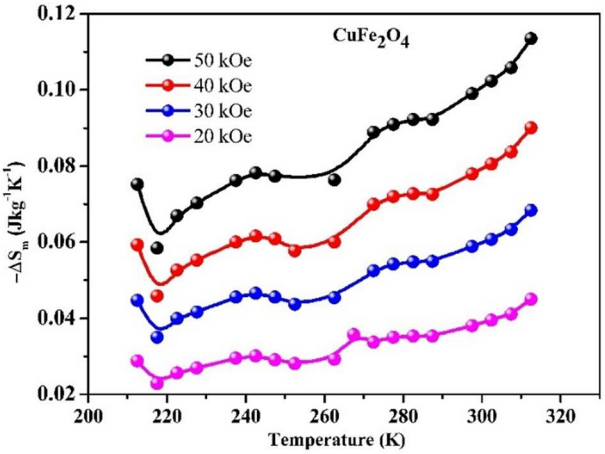


**Figure 7.17.** Variation of $-\Delta S_m$ with temperature of $CuFe_2O_4$ sample

The magnetic entropy curve of $CuFe_2O_4$ shown in Fig.7.17 reveals that the $-\Delta S_m$ varies from 0.035 J/kg/K to 0.113 J/kg/K when the applied field changes from 0-50 kOe in a temperature range of 210 K -310 K. As there is no specific magnetic transition observed in this region, no peak in the entropy curve was observed. A maximum value of $-\Delta S_m$ 0.113 J/kg/K has been observed for a 50 kOe magnetic field at 312.5 K for copper ferrite. As the MCE properties of copper ferrite nanoparticles are not available in the literature, it is expected to be reported for the first time.

Fig.7.18 reveals that the $-\Delta S_m$ varies from 0.0340 to 0.143 J/kg/K under an applied field of 50 kOe for the CuCo1 sample at a temperature of 347.5 K. The sample CuCo4 exhibits a maximum value of $-\Delta S_m$, 0.25 J/kg/K, at 352.5 K for an applied field of 50 kOe, which is displayed in Fig. 7.19. The entropy curve of sample CuCo5 displayed in Fig. 7.20 shows a maximum $-\Delta S_m$ of 0.313 J/kg/K under an applied field of 50 kOe at 347.5 K. A maximum entropy change of 0.324 J/kg/K at 297.5 K for 50 kOe is observed for the sample CuCo7 from Fig.7.21. The sample CuCo8 exhibits a maximum value of magnetic entropy change, $-\Delta S_m$, of 0.23 J/kg/K at 297.5 K for an applied field of 50 kOe. It can be observed from Fig. 7.24 that the maximum $-\Delta S_m$ is found to vary from 0.162 to 0.295 J/kg/K for an applied field of 50 kOe at 352.5 K for the cobalt ferrite sample, which is greater than the reported value

[12]. It is really interesting that CuCo9 exhibits inverse MCE values together with normal MCE. It can be observed from Fig.7.23 that CuCo9 exhibits a maximum $-\Delta S_m$ of 0.322 J/kg/K at 382.5K. The inverse MCE of CuCo9 at lower temperatures can be due to the high anisotropic constant of cobalt[8]. The observed $-\Delta S_m$ for $Cu_{0.2}Co_{0.8}Fe_2O_4$ nanoparticles is greater than the reported values for the same applied magnetic fields [4,10,13,14]

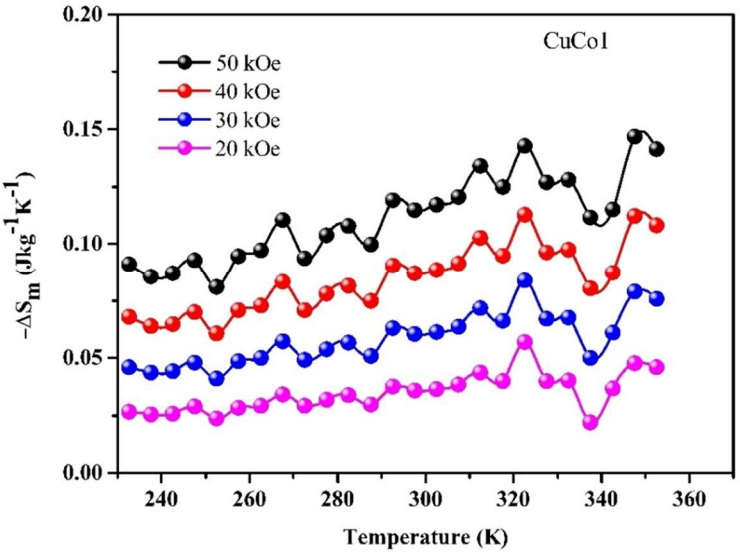


**Figure 7.18.** Variation of $-\Delta S_m$ with temperature of $Cu_{0.9}Co_{0.1}Fe_2O_4$

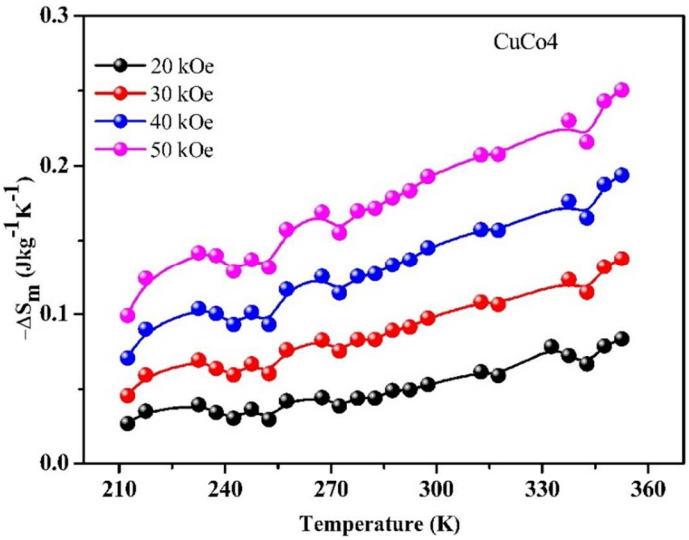


**Figure 7.19.** Variation of $-\Delta S_m$ with temperature of $Cu_{0.6}Co_{0.4}Fe_2O_4$

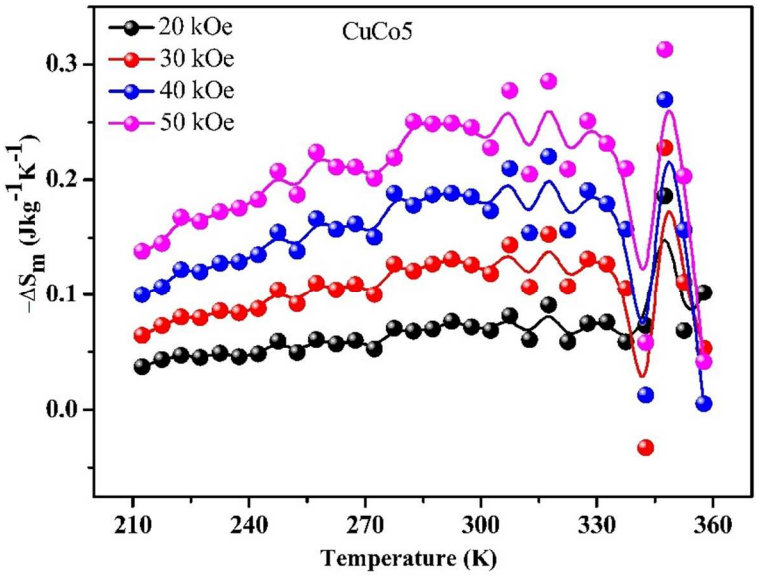


**Figure 7.20.** Variation of $-\Delta S_m$ with temperature of $Cu_{0.5}Co_{0.5}Fe_2O_4$

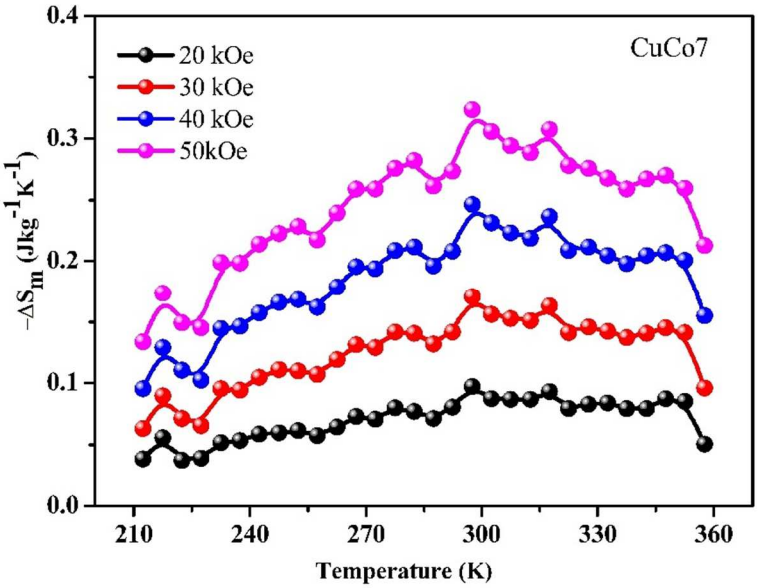


**Figure 7.21.** Variation of $-\Delta S_m$ with temperature of $Cu_{0.3}Co_{0.7}Fe_2O_4$

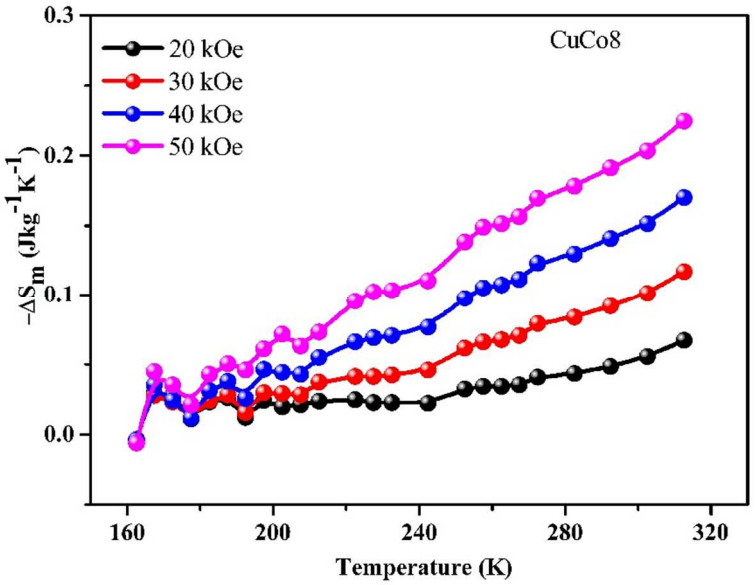


**Figure 7.22.** Variation of $-\Delta S_m$ with temperature of $Cu_{0.2}Co_{0.8}Fe_2O_4$

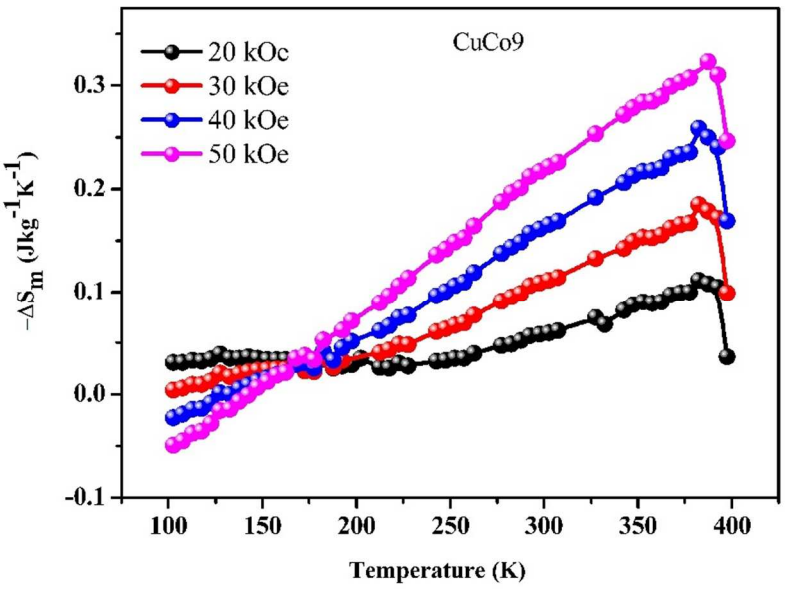


**Figure 7.23.** Variation of $-\Delta S_m$ with temperature of $Cu_{0.1}Co_{0.9}Fe_2O_4$

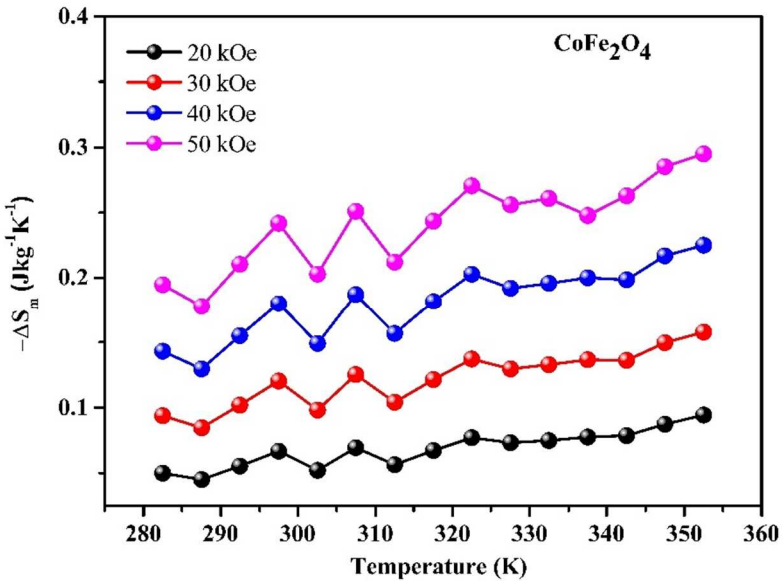


**Figure 7.24.** Variation of $-\Delta S_m$ with temperature of $CoFe_2O_4$

When the magnetocaloric properties of the $Cu_{1-x}Co_xFe_2O_4$ were studied, it was evident that the cobalt substitution in copper ferrite nanoparticles increases the magnetic entropy change, and the peak temperature is observed to be shifted to a higher temperature region. Cobalt substitution increases the magnetic entropy change from 0.11J/kg/K to 0.0.324 J/kg/K for an applied magnetic field of 50 kOe. The temperature corresponding to maximum magnetic entropy change in the measured range (5K- 400K) shifts from 312.5 K to 357.5K when x increases from 0 to 1 in $Cu_{1-x}Co_xFe_2O_4$. This shift in temperature to the higher region is due to the increase in magnetisation of the B sublattice with the incorporation of $Co^{2+}$ ions. The maximum entropy change and the peak temperature for the samples are displayed in Table 7.1.

**Table 7.1.** The maximum entropy change *(-$\Delta S_m$)* and the temperature corresponding to the maximum -$\Delta S_m$ of $Cu_{1-x}Co_xFe_2O_4$

| Sample Code | -$\Delta S_m$ (J/kg/K) | Peak Temperature (K) |
|---|---|---|
| **CuFe (x=0)** | 0.113 | 312.5 |
| **CuCo1 (x=0.1)** | 0.143 | 347.5 |
| **CuCo4 (x=0.4)** | 0.25 | 352.5 |
| **CuCo5 (x=0.5)** | 0.313 | 347.5 |
| **CuCo7 (x=0.7)** | 0.324 | 297.5 |
| **CuCo8 (x=0.8)** | 0.23 | 297.5 |
| **CuCo9 (x=0.9)** | 0.322 | 382.5 |
| **$CoFe_2O_4$ (x=1)** | 0.295 | 352.5 |

When we examined the MCE properties of the samples at room temperature, it is clear that the nanocrystalline copper ferrite sample exhibited an appreciable magnetic entropy change near room temperature. The cobalt substitution increases the magnetic entropy change of the copper ferrite system. $Cu_{0.3}Co_{0.7}Fe_2O_4$ nanoparticle exhibits the maximum-$\Delta S_m$ of 0.0.324 J/kg/K at 297.5 K for 50 kOe magnetic field among the synthesised ferrites.

## 7.3 Magnetocaloric Characterisation of $Cu_{1-x}Zn_xFe_2O_4$

### *7.3.1 ZFC-FC measurements of $Cu_{1-x}Zn_xFe_2O_4$*

Temperature dependent magnetisation measurements of $Cu_{1-x}Zn_xFe_2O_4$ (x=0 to 0.6) samples were recorded in an applied field of 50 kOe at a temperature range of 10 K- 400 K. The ZFC-FC magnetisation curves of $Cu_{1-x}Zn_xFe_2O_4$ samples are shown in Fig. 7.25 to Fig. 7.30.

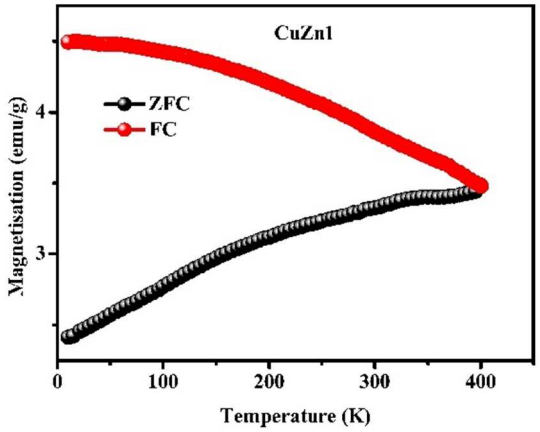


**Figure 7.25.** ZFC-FC curves of $Cu_{0.9}Zn_{0.1}Fe_2O_4$

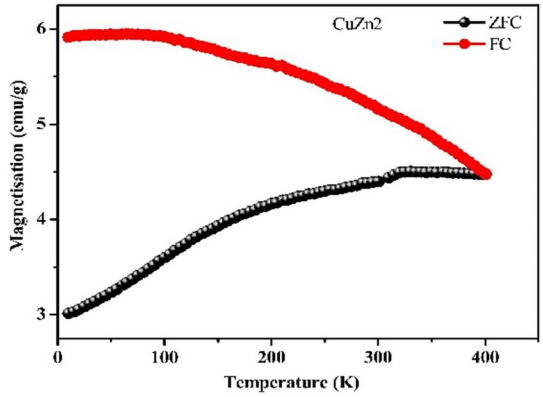


**Figure 7.26.** ZFC-FC curves of $Cu_{0.8}Zn_{0.2}Fe_2O_4$

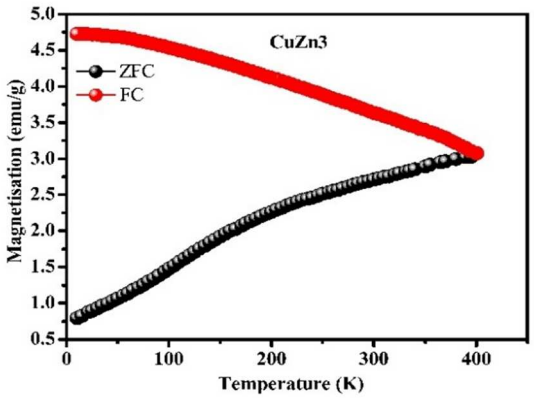


**Figure 7.27.** ZFC-FC curves of $Cu_{0.7}Zn_{0.3}Fe_2O_4$

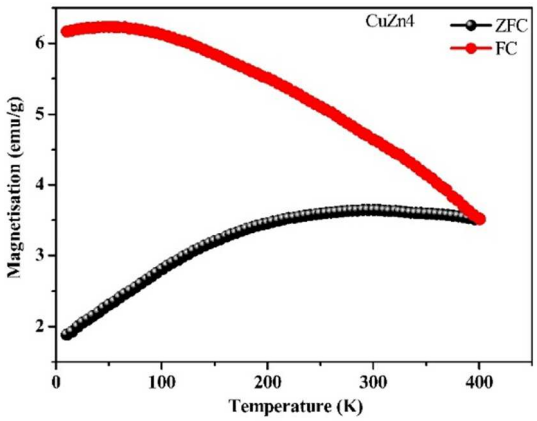


**Figure 7.28.** ZFC-FC curves of $Cu_{0.6}Zn_{0.4}Fe_2O_4$

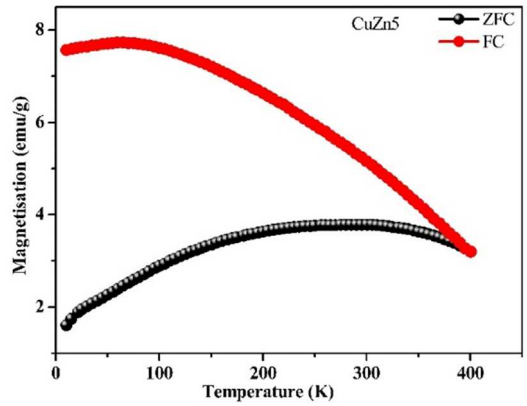


**Figure 7.29.** ZFC-FC curves of $Cu_{0.5}Zn_{0.5}Fe_2O_4$

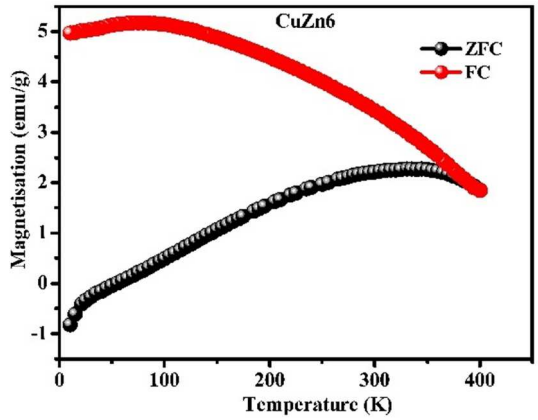


**Figure 7.30.** ZFC-FC curves of $Cu_{0.4}Zn_{0.6}Fe_2O_4$

The ZFC-FC curves of zinc-substituted copper ferrite samples $Cu_{1-x}Zn_xFe_2O_4$ exhibit a decrease in magnetisation with an increase in temperature for x=0.1 to x=0.6. No transition has been observed from the ZFC-FC magnetisation curves for the samples x=0, 0.1, and 0.3 in the recorded temperature region. But for the samples with x > 0.3 the ZFC curve shows a broad peak corresponding to maximum magnetisation near room temperature, which can be explained by the blocking transition. A transition from ferromagnetic to superparamagnetic can be observed at this temperature, which agrees well with the superparamagnetic behaviour of the M-H curve of the sample at room temperature (Fig.6.8). The estimated crystallite size, in the range of 10 nm -14 nm of the sample, is also in agreement with the superparamagnetic behaviour.

### *7.3.2 Isothermal Magnetisation Curves*

The magnetisation isotherms of $Cu_{1-x}Zn_xFe_2O_4$ have been recorded in a temperature range of 100 K to 400 K in an interval of $\Delta T$ = 5K for various applied fields in the range of 0- 50 kOe. The magnetisation isotherms of the sample $Cu_{0.1-x}Zn_xFe_2O_4$, for x=0.1 to 0.6 are shown in Fig. 7.31 to 7.36 respectively.

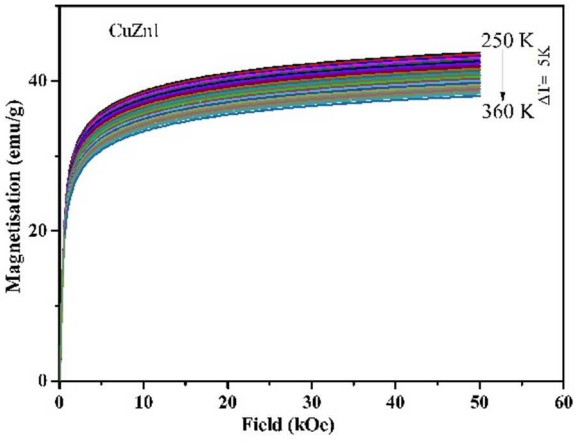


**Figure 7.31.** Magnetisation isotherms of $Cu_{0.9}Zn_{0.1}Fe_2O_4$.

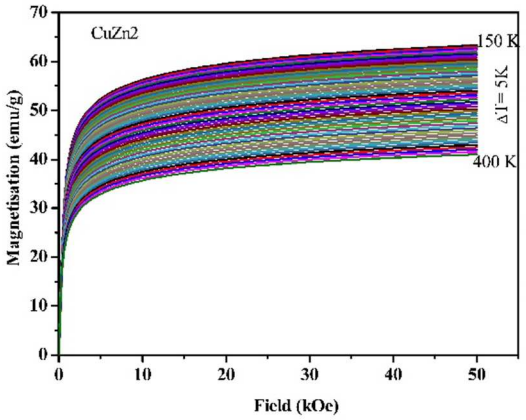


**Figure 7.32.** Magnetisation isotherms of $Cu_{0.8}Zn_{0.2}Fe_2O_4$.

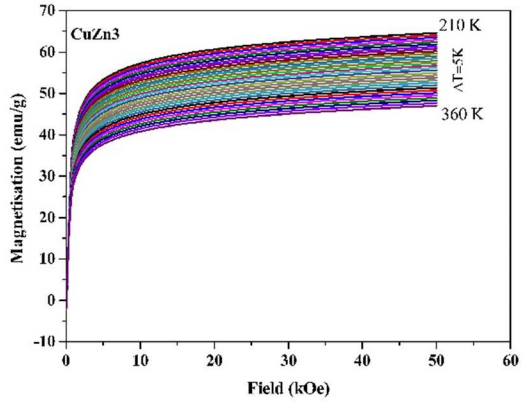


**Figure 7.33**. Magnetisation isotherms of $Cu_{0.7}Zn_{0.3}Fe_2O_4$.

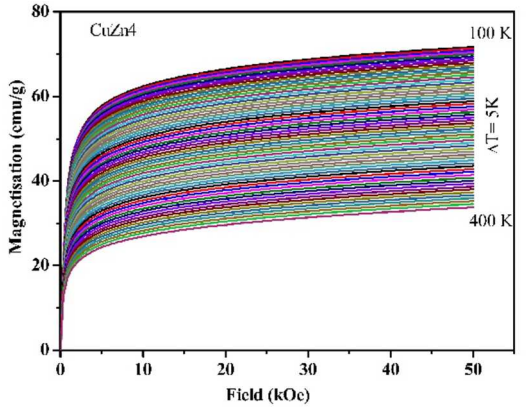


**Figure 7.34.** Magnetisation isotherms of $Cu_{0.6}Zn_{0.4}Fe_2O_4$.

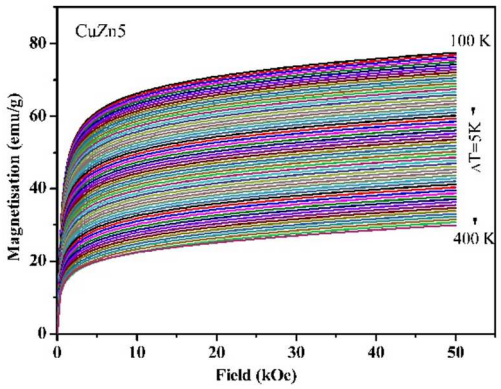


**Figure** 7.35. Magnetisation isotherms of $Cu_{0.5}Zn_{0.5}Fe_2O_4$.

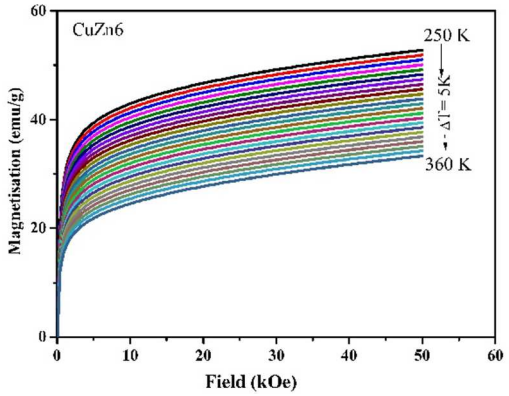


**Figure 7.36**. Magnetisation isotherms of $Cu_{0.4}Zn_{0.6}Fe_2O_4$.

The ferromagnetic behaviour of the CuZn1, CuZn2, CuZn3, and CuZn4 samples below room temperature can be observed from the M-H isotherms. Whereas Fig. 7.35 and 7.36 reveal that the magnetic moment is not saturated even at 50 kOe for the samples CuZn5 and CuZn6, indicating a superparamagnetic behaviour. The increase in magnetisation with applied field and the decreasing saturation behaviour with temperature indicate that MCE property can be estimated for these samples in the recorded temperature region [13].

As the saturation behaviour of the M-H loop decreases with the increase in zinc concentration, the ferromagnetic property is found to be reduced with the concentration of $Zn^{2+}$ in copper ferrite. It should be noted that for the initial sample in the $Cu_{1-x}Zn_xFe_2O_4$ series, x=0.1, the difference in maximum magnetisation at the two extreme temperatures is found to be small. The CuZn5 and CuZn6 samples, on the other hand, exhibit a significant change in the magnetisation value, which can be caused by a magnetic transition from ferromagnetic to a superparamagnetic nature.

### *7.3.3. Isothermal Magnetic Entropy Change*

The variation of entropy change $-\Delta S_m$, as a function of temperature of $Cu_{1-x}Zn_xFe_2O_4$ (x=0.1 - 0.6) samples are displayed in Figs. 7.37 to 7.42, respectively.

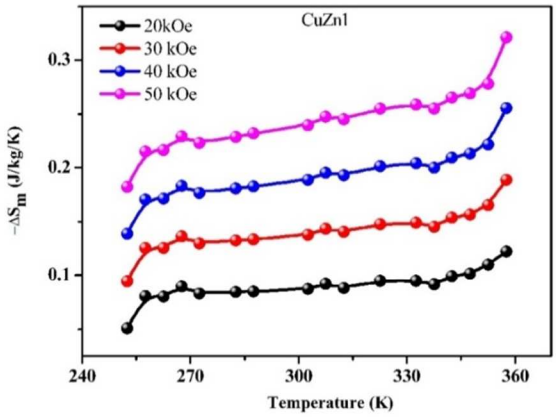


**Figure 7.37.** Variation of $-\Delta S_m$ with temperature of $Cu_{0.9}Zn_{0.1}Fe_2O_4$

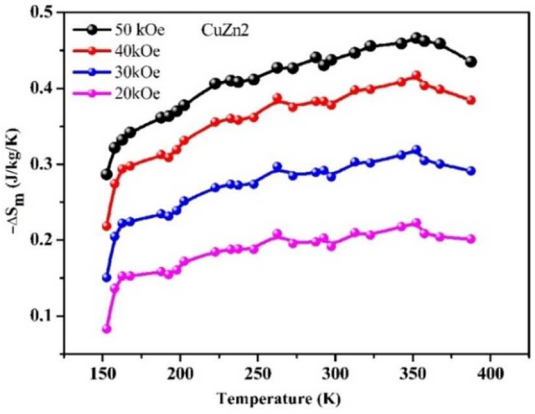


**Figure 7.38.** Variation of $-\Delta S_m$ with temperature of $Cu_{0.8}Zn_{0.2}Fe_2O_4$

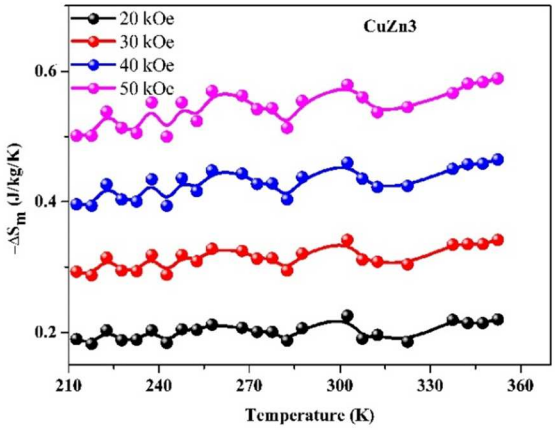


**Figure 7.39.** Variation of $-\Delta S_m$ with temperature of $Cu_{0.7}Zn_{0.3}Fe_2O_4$

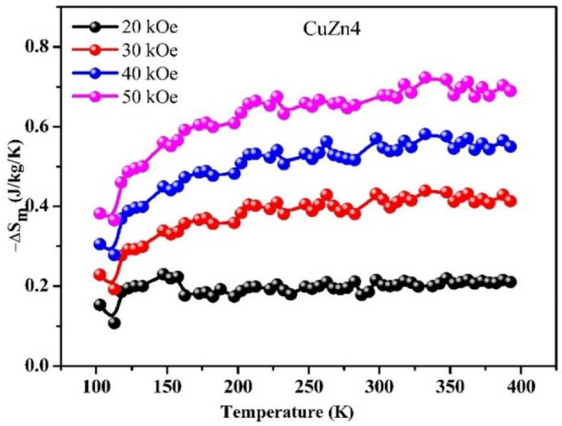


**Figure 7.40.** Variation of $-\Delta S_m$ with temperature of $Cu_{0.6}Zn_{0.4}Fe_2O_4$

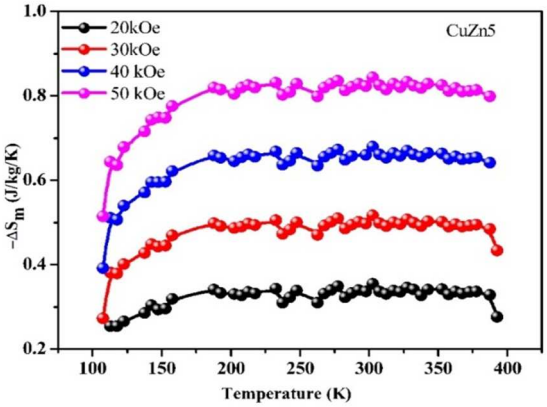


**Figure 7.41.** Variation of $-\Delta S_m$ with temperature of $Cu_{0.5}Zn_{0.5}Fe_2O_4$

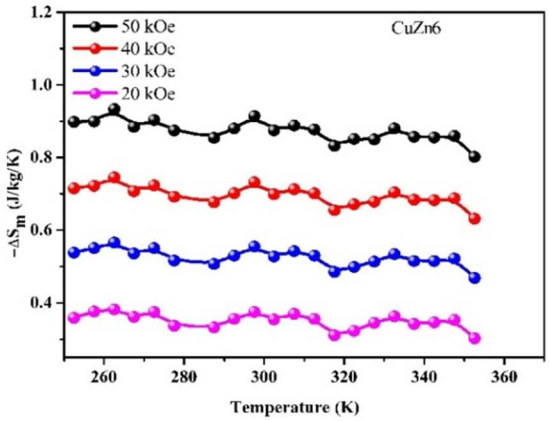


**Figure. 7.42.** Variation of $-\Delta S_m$ with temperature of $Cu_{0.4}Zn_{0.6}Fe_2O_4$.

It can be observed from the figures that $-\Delta S_m$ estimated from the magnetic isotherms varies with the temperature and the applied magnetic fields. Fig. 7.37 depicts that for $Cu_{0.9}Zn_{0.1}Fe_2O_4$., the entropy change increases from 0.0899 J/kg/K to 0.321 J/kg/K when the applied magnetic field increases from 20 kOe to 50 kOe. The maximum magnetic entropy change of 0.321 J/kg/K has been observed for $Cu_{0.9}Zn_{0.1}Fe_2O_4$ at 357.5 K. A maximum $-\Delta S_m$ of 0.466 J/kg/K is observed at 352.5 K from Fig.7.38 for CuZn2 sample for an applied field of 50 kOe. Fig.7.39 reveals a maximum $-\Delta S_m$ of 0.58 J/kg/K at 300 K for the sample CuZn3. A maximum $-\Delta S_m$ of 0.742 J/kg/K is observed at 332.5 K from Fig.7.40 for CuZn4 sample. It is clear from Fig. 7.41 that CuZn5 exhibits a maximum $-\Delta S_m$ of 0.84 J/kg/K at 302.5 K at an applied magnetic field of 50 kOe. The temperature-dependent entropy curve shown in Fig. 7.42 reveals that $Cu_{0.4}Zn_{0.6}Fe_2O_4$ exhibits an increase in $-\Delta S_m$ from 0.397 to 0.917 J/kg/K when the applied magnetic field changes from 20 kOe to 50 kOe. A maximum entropy change of 0.917 J/kg/K has been observed for this sample at 297.5 K.

It should be noted that in the $Cu_{1-x}Zn_xFe_2O_4$ series of samples, as zinc concentration increases, the magnetic entropy change increases in the recorded temperature region, 260 K- 360 K, for an applied field of 50 kOe. It is also interesting that the peak temperature corresponds to maximum magnetic entropy

change decreases with the zinc substitution in copper ferrite, and the blocking temperature of the zinc rich sample, $Cu_{0.4}Zn_{0.6}Fe_2O_4$, falls in the room temperature region. The maximum entropy change of 0.917 J/kg/K has been observed for the sample with x=0.6 concentration at 297.5 K under an applied field of 50 kOe. It can be explained by the fact that in $Cu_{0.4}Zn_{0.6}Fe_2O_4$, the recorded temperature region includes the blocking transition region of this sample, and $-\Delta S_m$ is found to be maximum around the transition temperature. The maximum entropy change and the peak temperature, the temperature at which the entropy change is maximum for $Cu_{1-x}Zn_xFe_2O_4$ are listed in Table 7.2.

**Table 7.2.** The entropy change ($-\Delta S_m$) and the temperature corresponding to maximum $-\Delta S_m$ of $Cu_{1-x}Zn_xFe_2O_4$

| Sample Code | $-\Delta S_m$ (J/kg/K) | Peak Temperature (K) |
|---|---|---|
| **$CuFe_2O_4$** | 0.113 | 312.5 |
| **$Cu_{0.9}Zn_{0.1}Fe_2O_4$** | 0.321 | 357.5 |
| **$Cu_{0.8}Zn_{0.2}Fe_2O_4$** | 0.466 | 352.5 |
| **$Cu_{0.7}Zn_{0.3}Fe_2O_4$** | 0.581 | 300 |
| **$Cu_{0.6}Zn_{0.4}Fe_2O_4$** | 0.742 | 332.5 |
| **$Cu_{0.5}Zn_{0.5}Fe_2O_4$** | 0.844 | 302.5 |
| **$Cu_{0.4}Zn_{0.6}Fe_2O_4$** | 0.917 | 297.5. |

We have investigated the effect of a magnetic and a non magnetic cation substitution on the magnetocaloric properties of copper ferrite nanoparticles. It can be observed that the magnetic entropy change, one of the characteristic properties of MCE, has been enhanced in $Cu_{1-x}Zn_xFe_2O_4$ than in $Cu_{1-x}Co_xFe_2O_4$. Among the $Cu_{1-x}Zn_xFe_2O_4$ series of samples, $Cu_{0.4}Zn_{0.6}Fe_2O_4$ exhibited a maximum value of $-\Delta S_m$, and among $Cu_{1-x}Co_xFe_2O_4$ series, $Cu_{0.3}Co_{0.7}Fe_2O_4$ exhibited the maximum value of $-\Delta S_m$ and $Cu_{0.1}Co_{0.9}Fe_2O_4$ exhibited a combination of inverse and normal MCE. The variation of $-\Delta S_m$ for the $Cu_{0.4}Zn_{0.6}Fe_2O_4$ and $Cu_{0.3}Co_{0.7}Fe_2O_4$ and for an applied field of 50 kOe is shown in Fig. 7.43

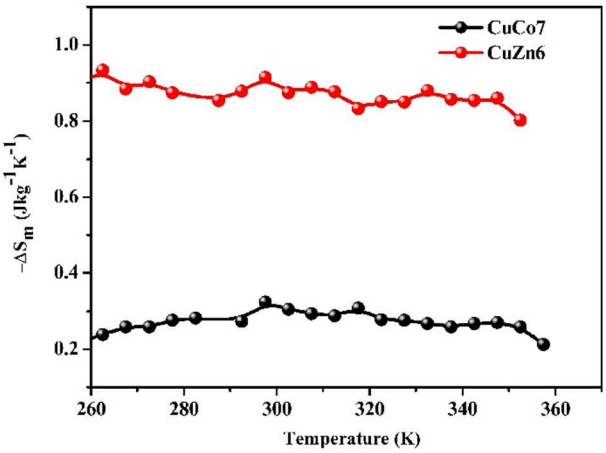


**Figure.7.43.** MCE in ferrites

Shahida Akhter *et. al.* reported a maximum entropy change of 0.36 J/kg/K for zinc doped copper ferrite nanoparticles at 272 K [10]. Felhi *et. al*. reported $\Delta S_m$ of 0.68 J/kg/K for $Zn_{0.7}Ni_{0.3-x}Cu_xFe_2O_4$ ($0 \leq x \leq 0.2$) at a temperature of 282 K [15]. M.S. Anwar *et. al*. reported the potential application of $Ni_{1-x}Zn_xFe_2O_4$ at higher Curie temperatures [9]. A comparative study of the reported values of MCE and the present study is listed in Table 7.3.

**Table 7.3. Comparative study of MCE of ferrites**

| Sample | $\Delta S_m$ (J/kg/K) | Applied Field | Temp | Reference |
|---|---|---|---|---|
| **CuZnFe** | 0.36 | - | 272 K | [10] |
| **$Cu_{0.3}Zn_{0.7}Fe_2O_4$** | 0.91 | 3T | 272 | [10] |
| **$Zn_{0.7}Ni_{0.3-x}Cu_xFe_2O$** | 0.68 | - | 282 K | [15] |
| **$Ni_{0.3}Zn_{0.7}Fe_2O_4$** | 0.86 | 2.5 T | 302 | [9] |
| **$ZnFe_2O_4$** | 0.04 | 2 T | 150 | [16] |
| **$NiFe_2O_4$** | 0.75 | 2T | - | [9] |
| **$Cu_{0.5}Zn_{0.5}Fe_2O_4$** | 0.844 | 5T (50 kOe) | 302.5 | Present Work |
| **$Cu_{0.4}Zn_{0.6}Fe_2O_4$** | 0.917 | 5T (50 kOe) | 297.5 | Present Work |
| **$Cu_{0.3}Co_{0.7}Fe_2O_4$** | 0.324 | 5T (50 kOe) | 297.5 | Present work |

The synthesized $Cu_{0.4}Zn_{0.6}Fe_2O_4$ sample among the $Cu_{1-x}Zn_xFe_2O_4$ series exhibits an appreciable magnetic entropy change compared to other reported values near room temperature. $Cu_{0.4}Zn_{0.6}Fe_2O_4$ can be used for magnetic refrigerant application at room temperature.

## 7.4 Conclusion

We have synthesised a series of $Cu_{1-x}Co_xFe_2O_4$ and $Cu_{1-x}Zn_xFe_2O_4$ samples by a modified sol-gel auto combustion technique. The temperature dependent magnetic properties of the samples have been studied, using FC-ZFC curves. Even though the transition temperature of ferrite materials is expected to be in the higher temperature region, we have tried to investigate the MCE properties of the synthesised samples around room temperature. Copper ferrite exhibits a maximum $-\Delta S_m$ of 0.11 J/kg/K near room temperature, which is one of the rare reports of magnetocaloric properties of copper ferrite. The $-\Delta S_m$ increases with cobalt substitution and reaches a maximum value, of 0.324 J/kg/K for CuCo7 at 297.5 K and 0.322 J/kg/K for CuCo9 at 387 K for an applied field of 50 kOe. The observed magnetic entropy change for $Cu_{1-x}Co_xFe_2O_4$ indicates that copper ferrite and $Cu_{1-x}Co_xFe_2O_4$ (x=0.7) are promising materials for magnetic refrigerant applications near and above room temperature respectively. Among the $Cu_{1-x}Zn_xFe_2O_4$ series of samples, $Cu_{0.4}Zn_{0.6}Fe_2O_4$ exhibited a maximum entropy change of 0.917 J/kg/K at 297.5 K for a 50 kOe magnetic field. So, it can be concluded from our work, that the $Cu_{1-x}Zn_xFe_2O_4$ samples are potential ferrite nanomaterials for magnetic refrigerant applications near room temperature compared to $Cu_{1-x}Co_xFe_2O_4$ samples.

**REFERENCES**

[1] C. Vâzquez-Vázquez, M. Lovelle, C. Mateo, M.A. López-Quintela, M.C. Buján-Nũñez, D. Serantes, D. Baldomir, J. Rivas, Physica Status Solidi (A) Applications and Materials Science 205 (2008) 1358–1362.

[2] T. Prabhakaran, R. V. Mangalaraja, J.C. Denardin, J Magn Magn Mater 444 (2017) 297–306.

[3] H. Mamiya, N. Terada, T. Furubayashi, H.S. Suzuki, H. Kitazawa, J Magn Magn Mater 322 (2010) 1561–1564.

[4] E. Oumezzine, S. Hcini, M. Baazaoui, E.K. Hlil, M. Oumezzine, Powder Technol 278 (2015) 189–195.

[5] A Mallah, F AI Thuwayb, M Khitouni, A.Alsawi, J. Sunol, J.M.Greneche, M.Almoneef, Crystals,13 (6) (2023) 894.

[6] S. Burianova, J. Poltierova-Vejpravova, P. Holec, J. Plocek, J Phys Conf Ser 200 (2010).

[7] M.A. Islam, A.K.M.A. Hossain, Heliyon 9 (2023) e15106.

[8] M. Bohra, S. Prasad, N. Kumar, D.S. Misra, S.C. Sahoo, N. Venkataramani, R. Krishnan, Appl Phys Lett 88 (2006) 1–4.

[9] M.S. Anwar, F. Ahmed, B.H. Koo, Acta Mater 71 (2014) 100–107.

[10] S. Akhter, D.P. Paul, S.M. Hoque, M.A. Hakim, M. Hudl, R. Mathieu, P. Nordblad, J Magn Magn Mater 367 (2014) 75–80.

[11] D. Le Minh, N.H. Luong, N. Chau, N.K. Thuan, D.L. Minh, N.H. Luong, VNU Journal of Science, Mathematics-Physics 24 (2008) 155–162.

[12] P. Poddar, J. Gass, D.J. Rebar, S. Srinath, H. Srikanth, S.A. Morrison, E.E. Carpenter, J Magn Magn Mater 307 (2006) 227–231.

[13] E. Veena Gopalan, I.A. Al-Omari, K.A. Malini, P.A. Joy, D. Sakthi Kumar, Y. Yoshida, M.R. Anantharaman, J Magn Magn Mater 321 (2009) 1092–1099.

[14] A.A. Khan, U. Hira, Z. Iqbal, M. Usman, F. Sher, Ceram Int 43 (2017) 7088–7093.

[15] R. Felhi, H. Omrani, M. Koubaa, W.C. Koubaa, A. Cheikhrouhou, J Alloys Compd 758 (2018) 237–246.

[16] M. Bohra, N. Singh, A. Annadi, S.V. Battula, V. Singh, Mater Res Bull 169 (2024) 112547.

…..ര*ര…..

# Chapter 8

# Magnetocaloric Properties of Cobalt-Polystyrene Nanocomposites

## Objectives

The synthesis, structural and magnetic properties of cobalt nanoparticles embedded in a polystyrene matrix are described. The initial investigation of the magnetocaloric properties of these magnetic nanocomposites is elucidated.

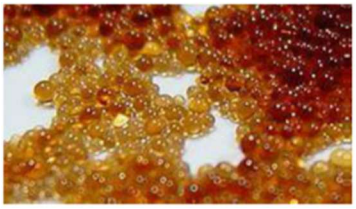

## 8.1 Introduction

Metal nanoparticles have been immensely attractive in the area of research due to their unique optical, electronic, magnetic, and chemical properties compared to bulk metal. They find potential applications in recording media, magnetic sensors, magnetic memories, magnetic fluids, various optoelectronic devices, as catalysts in chemical reactions, and also as biosensors[1,2]. Due to the antibacterial and anti-inflammatory activities of metal nanoparticles, they are used in the field of biomedicine[3]. Metal nanoparticles are also used as biosensors and heat mediators for cancer hyperthermia [4]. Metal nanoparticles are highly unstable and hence are very difficult to synthesize Co/Ni/Fe metal particles in nano dimensions. Conventional methods for the synthesis of metal nanoparticles are not feasible, as the large surface area of unprotected nanoparticles is prone to oxidation. Various stabilization techniques, including the use of capping agents, surfactants, and host matrices, are used to prevent aggregation and oxidation of metal nanoparticles[5]. It is reported that carbon graphitic structures like graphite, diamond, graphene, and CNT's can be fabricated using metal nanoparticles[6,7]. Metal nanocomposites have extensive applications in conductive devices, sensors and biomedical products[8]. M. Yaseem *et al.* reported the applications of thermally stable metal polystyrene nanocomposites for antioxidant and antibacterial food packing[9].

A nanocomposite is nanoparticle added to a matrix to improve a particular property of the material. The nanocomposite, like other composites, consists of a base media, or matrix, made of ceramic, metal, or plastic, mixed with suspended nanoparticles. In recent years, magnetic nanocomposites, which are made up of magnetic particles in the nano regime embedded in a nonmagnetic matrix, have attracted much attention because they combine the mechanical and physical characteristics of the nonmagnetic matrix with the magnetic properties of the inorganic component. Magnetic nanocomposites can be fabricated by embedding the magnetic nanoparticles in a polymer matrix like polystyrene resin. Magnetic nanocomposites, Fe, Ni and Co nanocomposites have applications in drug delivery, catalysis, waste water treatment, sensors, biomedical applications, etc[4,8,10–12].

There are reports on the investigation of the magnetic properties and applications of cobalt metal nanoparticles[5,13–15].

Cobalt nanocomposites are chosen for our work due to their unique and wide applications in society. Since self-protected metal nanoparticles in a host matrix are needed, polystyrene resin is preferred as the matrix for the synthesis of cobalt nanocomposites in the present work. The structure and the mechanism of ion exchange in the polystyrene resins are detailed in the experimental part of the thesis (Chapter 2, section 2.2.3.)

## 8.2 Synthesis and Characterisation

Cobalt nanocomposites are synthesised by an ion exchange reduction method[16]. The precursors used for the synthesis of cobalt nanocomposites are cobalt sulphate ($CoSo_4.7H_2O$), sodium borohydride ($NaBH_4$) and SRC-120 (Amberlite IRC120). SRC -120 is a strongly Acidic Cation Exchange Resin. The structure is as shown in Fig. 8.1.

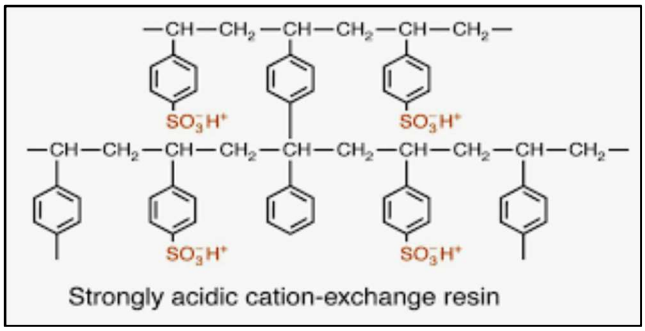


**Figure 8.1.** Structure of SRC 120 (Amberlite IRC120)

For the preparation of cobalt polystyrene nanocomposites, SRC-120 (Amberlite IRC120), was initially soaked in distilled water so that they were swollen and the pores were open. The swollen resin is soaked for 48 hours in a saturated solution of 1.25M $CoSO_4$. The ion exchange process is initiated at this stage. The $Co^{2+}$ ions are exchanged with the $H^+$ ions in the resin. A dilute solution of $NaBH_4$ is added drop-wise to the resin. Further reduction of $Co^{2+}$ ions to Cobalt inside the

polymer matrix occurs with the addition of $NaBH_4$. Cobalt ions are reduced to metallic cobalt particles by the following reduction reaction.

$$2Co^{2+} + 4BH_4^- + 9H_2O \rightarrow Co_2B + 3B(OH)_3 + 13H_2 \uparrow \quad (8.1)$$

$$4Co_2B + 3O_2 \rightarrow 8Co + 2B_2O_3 \quad (8.2)$$

The resins with cobalt are then washed several times with distilled water to remove the by-products of the reaction. Thus, Co particles are expected to be trapped within the interstitial channels of polymer beads. The schematic diagram of the ion exchange mechanism is shown in Fig 8.2. The physical appearance of the pure ion exchange resins and IRC cobalt composites are displayed in Fig. 8.3.

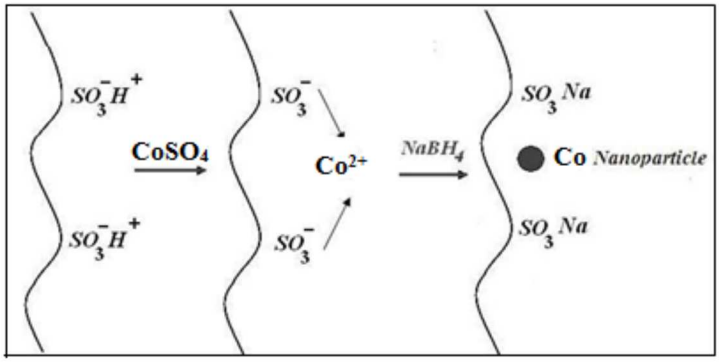


**Figure 8.2.** Schematic diagram of synthesis of Co polystyrene nanocomposites

a) SRC beads b) Cobalt incorporated beads

**Figure 8.3.** Polystyrene beads and Cobalt -Polystyrene beads

These cobalt-containing beads were again soaked in a cobalt sulphate solution, and the procedure was repeated four times to increase the cobalt content in the metal-polystyrene nanocomposites. Hence, the metal polystyrene composites of cobalt after four cycles were labelled as the Co-Re samples. The composite samples were observed to become darker with the increased number of cycles. All the samples were found to be magnetic. The physical appearance of the SRC polystyrene beads during the four cycles is shown in Fig. 8.4.

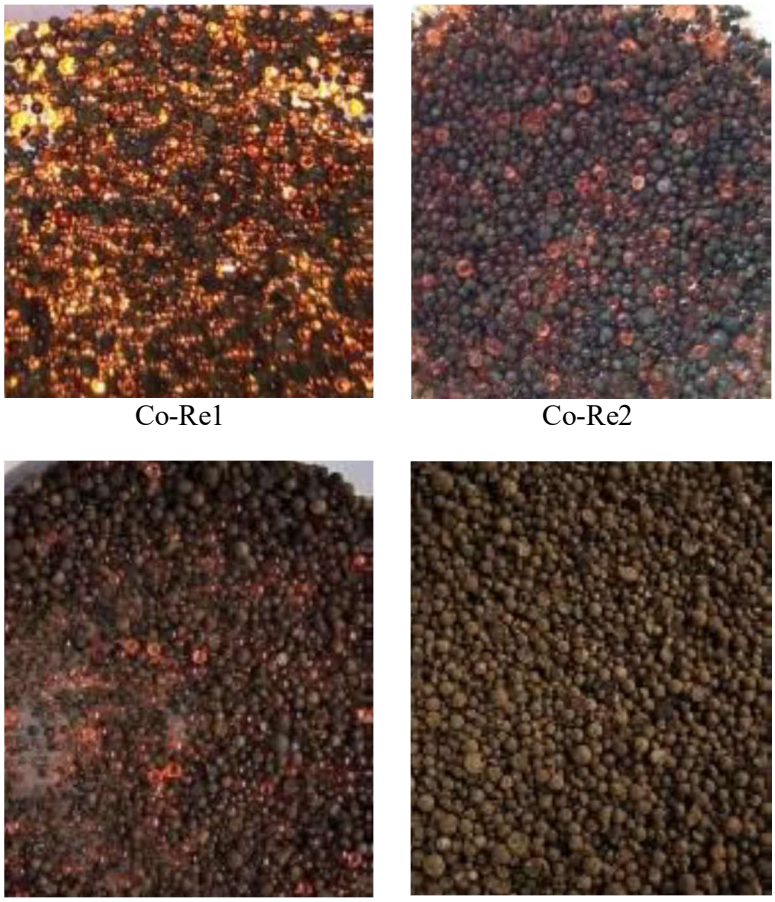


**Figure 8.4.** Physical appearance of the polystyrene beads under the 4 cycles

The samples after the first, second, third and fourth cycles are labelled as Co-Re1, CoRe2, Co-Re3, and Co-Re4, respectively. Co-Re4 is taken as the Co-Re sample for characterisation.

# Results and Discussion

## 8.3 Structural characterisation

### *8.3.1 XRD Analysis*

The magnetic nature of the synthesised samples points towards the formation of cobalt in the sample. The cobalt nanoparticles are expected to be formed inside the channel-like pores of the gel-type resin by the ion exchange reduction method. Although the presence of an amorphous polystyrene matrix hides the crystalline nature of cobalt, attempts are made to analyse the structure of the cobalt nanocomposite using XRD pattern. The structure, lattice parameter and crystallite size of the Co nanonacomposites are estimated from the XRD pattern of the final sample Co -Re. The XRD pattern of Co-Re is shown in Fig. 8.5.

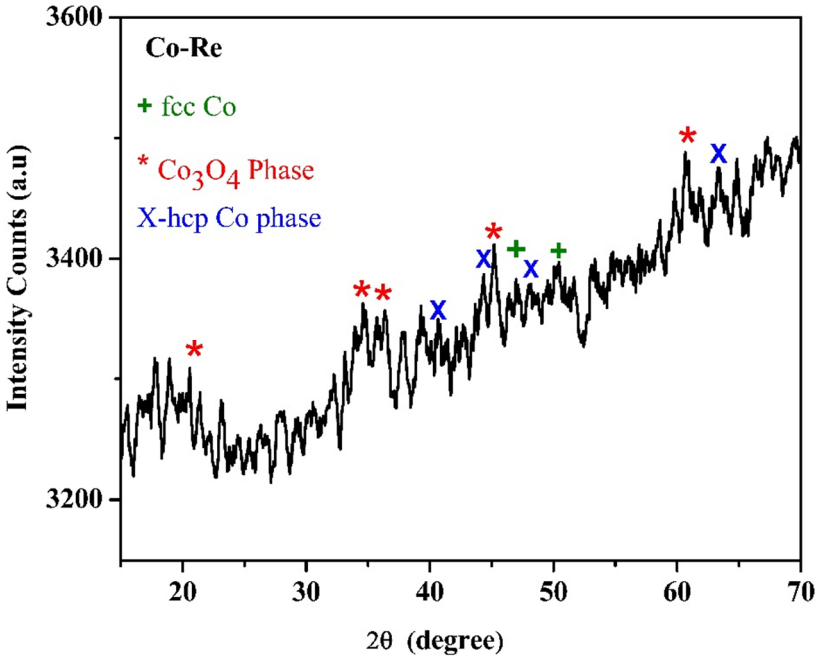


**Figure 8.5.** XRD pattern of Co nanocomposites

The XRD spectra show the crystalline structure of the various peaks of cobalt and cobalt oxide particles. The XRD pattern of Co nanocomposites reveals that cobalt is incorporated into the polystyrene resins, whereas some peaks of cobalt

oxide, $Co_3O_4$, are observed. The peak positions 2θ = 20.7º, 34.15º, 36.57º, 45.18º, 59.83º and 66.03º and relative intensities obtained for the $Co_3O_4$ match with the JCPDS card No: 073-1701 file, identifying it as $Co_3O_4$ with a cubic structure with *fd-3m* (227) space group. The main cobalt phase was identified to be that of a hexagonal close-packed structure, hcp-Co. The diffraction peaks observed at 2θ values of 41.05º, 44.45º, 47.77º, and 62.24º can be assigned to the (100), (002), (101) and (102) planes of hcp-Co (JCPDS 05-0727), respectively. Additionally, the double peaking at around 46.74º and the peak observed at 50.86º were found and could be assigned to the (111) and (200) planes of fcc-Co (JCPDS file:15-0806). The phase corresponding to fcc cobalt was also present here as the main phase, along with the hcp phase. The presence of cobalt oxide peaks in the XRD pattern indicated the oxide formation.

### *8.3.2 FTIR Spectroscopy*

The FTIR spectrum of Co nanocomposite is displayed in Fig. 8.6. The FTIR spectrum of nanoparticles showed significant absorption peaks at 416 $cm^{-1}$, 445 $cm^{-1}$, 581 $cm^{-1}$, 669 $cm^{-1}$, 780 $cm^{-1}$, 836 $cm^{-1}$, 1010 $cm^{-1}$, 1039 $cm^{-1}$, 1128 $cm^{-1}$ and 1341 $cm^{-1}$.

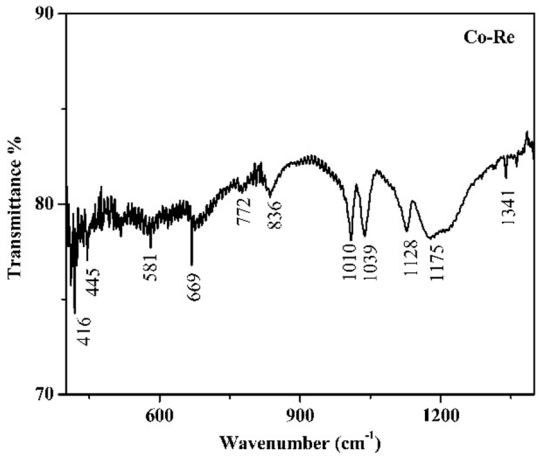


**Figure. 8.6.** FTIR spectrum of Co nanocomposite

The stretching vibrations in the frequency region (417 -478 $cm^{-1}$) shown in Fig. 8.6 reveal the Co ions in the octahedral sites[17]. The absorption bands at 581$cm^{-1}$ was assigned to Co-O stretching vibration mode and 669 $cm^{-1}$ was assigned to the bridging vibration of O-Co-O bonds in the $Co_3O_4$ phase of the sample. The bands around 772 $cm^{-1}$ are associated with the out of plane bending vibrations of C-H groups in the benzene ring. The bands located around 836 $cm^{-1}$ are characteristic of out-of-plane bending vibrations of C-H [18]. The appearance of a peak at 1341 $cm^{-1}$ may be due to the presence of tertiary C–OH groups, which may be formed due to the adsorption of $CO_2$ or $O_2$ on $Co_3O_4$ oxide layers of Cobalt. The bands located around 1175 $cm^{-1}$ and around 1010 - 1040 $cm^{-1}$ are assigned to the asymmetric and symmetric stretching vibrations of the S═O bond[19] . The band appeared at 1128 $cm^{-1,}$ which is attributed to the in-plane skeletal vibrations of the distributed benzene ring[20]. So, the FTIR spectrum confirmed the incorporation of the Co in the polystyrene resin.

## 8.4. Magnetic Characterisation

### *8.4.1. M-H curves*

The magnetic properties of Co nanocomposite are probed with the M-H hysteresis, temperature-dependent magnetisation under the ZFC and FC conditions, and magnetisation isotherms in the room temperature range. Field dependent magnetisation measurements were recorded at 10K and 300 K to study the magnetic behaviour of Co resin. The M-H curves of Co-Re at 300 K and 10 K are shown in Fig.8.7 and Fig.8.8, respectively.

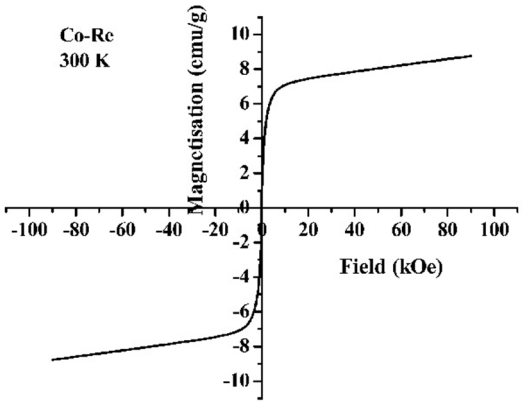


**Figure. 8.7.** M-H curve of Co Re at 300 K.

. It is observed from the magnetisation curve that the magnetisation increases rapidly at a low applied field. The magnetisation does not saturate at a field of 90 kOe. It attains a maximum magnetisation of 8.77 emu/g and negligible coercivity (82.7 Oe) at room temperature and remanence of 1emu/g. This refers to the superparamagnetic behaviour of the Co-Re sample at room temperature. In general, the superparamagnetic behaviour appears above the blocking temperature $T_{B,}$ which can be due to the presence of the hcp phase of cobalt metal nanoparticles in the matrix. It is reported that the hcp cobalt of crystallite size near 12 nm exhibits a superparamagnetic behaviour at room temperature[21].

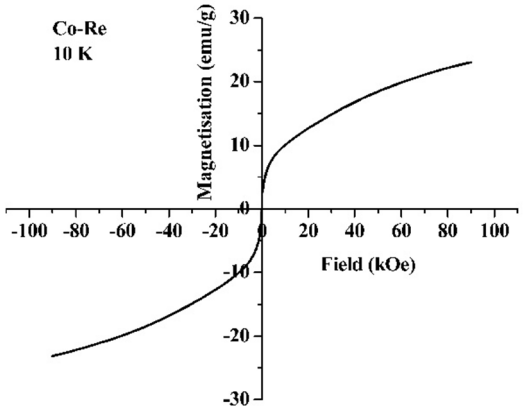


**Figure. 8.8.** M-H curve of Co Re at 10 K.

The M-H curves at a lower temperature, 10K show an 'S' shaped curve in which the magnetisation increases slowly and is not saturated at higher fields. The maximum magnetisation estimated from the M-H curves is 23.08 emu/g at 10 K. It is also noted from the M-H curve that the Co-Re can have a spin glass behaviour at a lower temperature. The spin glass behaviour is seen at temperatures greater than the freezing temperature $T_f$, where the spins are locked in a disordered state. The cobalt oxide $Co_3O_4$ has an antiferromagnetic behaviour at a lower temperature [22]. The freezing temperature of antiferromagnetic $Co_3O_4$ is normally between 30 K and 40 K, which is size-dependent. Here, the exchange interaction between the ferromagnetic Co and antiferromagnetic $Co_3O_4$ can lead to a spin glass-like behaviour. As the spin glasses require low thermal energy to freeze the spins, the freezing temperature is lower than the blocking temperature ($T_B$) of a superparamagnetic system. However, the maximum magnetisation of the sample at lower temperatures is greater than at room temperature.

## 8.5 Magnetocaloric Characterisation

### *8.5.1 ZFC-FC Measurements*

The room temperature MCE properties of the Co-Re sample are studied in the present work, which has not been reported so far. As described in Chapters 4 and 7, to investigate the MCE properties of the Co Re sample, the initial step to identify a transition, if any, ZFC FC measurements were recorded in the lower temperature region. The ZFC-FC measurements of the Co-Re sample are shown in Figure 8.9.

The temperature-dependent magnetisation curves reveal that the magnetisation initially decreases to a minimum value near 48 K and then increases. This can be due to the freezing temperature of the cobalt oxide phase present in the sample. Although the magnetisation increases in both ZFC and FC conditions with an increase in temperature, is getting closer to a maximum value, a peak corresponding to the maximum value of magnetisation in the ZFC and FC measurements cannot be

observed in the measured temperature region. A bifurcation between the ZFC and FC curves is observed for the Co Re sample at a higher temperature, expecting a transition at a higher temperature for this sample. This can also be evident from the superparamagnetic behaviour of the sample observed from the room temperature M-H curve at 300 K. It is reported that the blocking temperature of hcp cobalt nanoparticles is at 290K, and the bulk Curie temperature is observed at 1388 K[23]. The blocking temperature can change according to the size and synthesis conditions of cobalt nanoparticles.

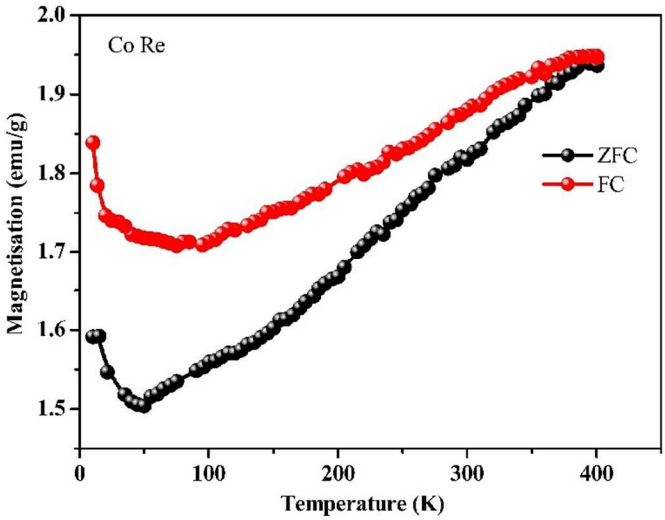


**Figure. 8.9.** ZFC-FC measurements of Co-Re sample

The minimum value of magnetisation in ZFC measurements at 48K can be the freezing temperature at which the sample exhibits a spin glass behaviour. It is also consistent with the spin-glass behaviour of the sample observed from the MH curves at 10 K.

### *8.5.2 Magnetisation isotherms*

Magnetisation isotherms are probed to study the MCE properties of the Co nanocomposites. M-H isotherms were measured in a temperature range of 250 K-400 K with a temperature interval of 5K for an applied magnetic field of 50 kOe. The magnetisation isotherms of the Co nanocomposite are shown in Fig. 8.10. The figure

depicts that the magnetisation does not saturate even at higher fields of 50kOe. The enhancement of magnetisation at low temperatures can be due to the progressive alignment of magnetic spins in the direction of the field, which is associated with the superparamagnetic behaviour of the sample. The M-H curve at room temperature also revealed the superparamagnetic behaviour of the sample at room temperature.

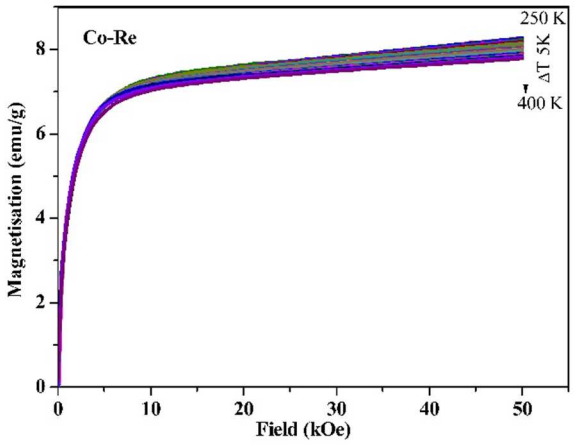


**Figure. 8.10.** Magnetisation isotherms of Co-Re sample.

The magnetic entropy change of the sample is estimated from the magnetic isotherms at different temperatures and is shown in Fig. 8.11.

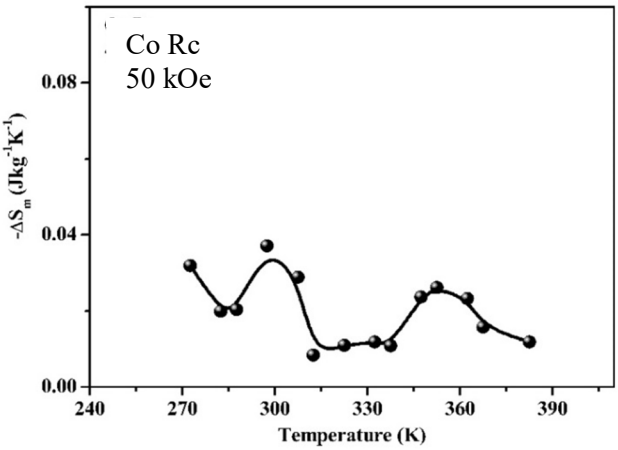


**Figure 8.11.** Variation of $-\Delta S_m$ with temperature of Co-Re sample.

It is observed from the figure that the magnetic entropy change varies in a random order. The maximum value of estimated entropy 0.037 J/kg/K is observed at 297 K. Even though there are numerous reports on the structural and magnetic properties of polystyrene nanocomposites, there is no extensive research on the magnetocaloric properties of metal nanoparticles embedded in the polystyrene resins. The cobalt nanocomposite exhibits a maximum entropy change of 0.037 J/kg/K at 297 K, near the blocking temperature of the sample. Recently, Naglaa Hussain Saleh Nasralla *et al*. reported the optical, dielectric and magnetic properties of cobalt nanoparticles embedded in a polystyrene matrix [24]. However, the magnetocaloric properties of cobalt metal nanoparticles embedded in polystyrene nanocomposites have not been reported so far in the literature.

## 8.6 Conclusion

Cobalt metal nanoparticles were embedded in polystyrene resins by the ion exchange reduction method, and cobalt nanocomposites were fabricated. The cobalt nanocomposites crystallise in the hcp and fcc phases. Additional peaks of $Co_3O_4$ are also present in the XRD pattern. The bands of cobalt and cobalt oxide peaks were identified from the FTIR spectrum. The Co-Re exhibits a superparamagnetic behaviour of the sample at room temperature and a spin glass behaviour at a lower temperature 10K. The ZFC -FC curves of the Co-Re sample indicate a magnetic transition at a higher temperature. Room temperature magnetocaloric properties were examined from the magnetisation isotherms recorded in the lower temperature range. A maximum entropy change of 0.037 J/kg/K is observed at 297 K for cobalt nanocomposites. Even though the observed magnetic entropy change is not very high, this is the first time the near-room temperature magnetocaloric property of cobalt nanoparticles embedded in a polystyrene matrix is being reported.

## REFERENCES


[1] L. Wang, M. Hasanzadeh Kafshgari, M. Meunier, Adv Funct Mater 30 (2020) 1–28.

[2] G.Z. Gayda, O.M. Demkiv, N.Y. Stasyuk, R.Y. Serkiz, M.D. Lootsik, A. Errachid, M. V. Gonchar, M. Nisnevitch, Applied Sciences (Switzerland) 9 (2019).

[3] G. Angajala, R. Subashini, Inflamm Cell Signal (2014).

[4] M. Vaseem, N. Tripathy, G. Khang, Y.B. Hahn, RSC Adv 3 (2013) 9698–9704.

[5] K.S. Rao, T. Balaji, Y. Lingappaa, M.R.P. Reddy, T.L. Prakash, J Exp Nanosci 8 (2013) 162–170.

[6] Y. Çelik, A. Kurt, Appl Surf Sci 568 (2021) 150946.

[7] K. Bala, J. Suriyaprakash, P. Singh, K. Chauhan, A. Villa, N. Gupta, New Journal of Chemistry 42 (2018) 6604–6608.

[8] Y. Zare, I. Shabani, Materials Science and Engineering: C 60 (2016) 195–203.

[9] M.W. Yaseen, M.A. Asghar, E.M. Bakhsh, K. Akhtar, S.B. Khan, M. Iqbal, Ind Crops Prod 209 (2024) 117959.

[10] Q.A. Pankhurst, N.K.T. Thanh, S.K. Jones, J. Dobson, J Phys D Appl Phys 42 (2009).

[11] H. Takacs, B. Viala, J.H. Tortai, V. Hermán, F. Duclairoir, J Appl Phys 119 (2016).

[12] V. Gopalan, Al-Omari I, Kumar D, Yoshida Y, Joy P, Anantharaman M, Appl Phys A 99 (2010): 497–503.

[13] N.H.S. Nasralla, S.M. Mousa, G.T. El-Bassyouni, G.M.E. Komy, Surfaces and Interfaces 48 (2024) 104291.

[14] V. Hermán, H. Takacs, F. Duclairoir, O. Renault, J.H. Tortai, B. Viala, RSC Adv 5 (2015) 51371–51381.

[15] M. Zeisberger, S. Dutz, R. Müller, R. Hergt, N. Matoussevitch, H. Bönnemann, J Magn Magn Mater 311 (2007) 224–227.

[16] E.V. Gopalan, K.A. Malini, G. Santhoshkumar, T.N. Narayanan, P.A. Joy, I.A. Al-Omari, S.S. Kumar, Y. Yoshida, M.R. Anantharaman, Nanoscale Res Lett 5 (2010) 889–897.

[17] R. Jabbar, S.H. Sabeeh, A.M. Hameed, J Magn Magn Mater 494 (2020) 165726.

[18] N. Joseph, K. Kizhakkinakath, M. Illam, R. Vedavyasa, N. Edathil, A. Kaipamangalath, M. Raama, S. Thomas, Journal of Physics and Chemistry of Solids 145 (2020) 109527.

[19] S.B. Brijmohan, S. Swier, R.A. Weiss, M.T. Shaw, (2005) 8039–8045.

[20] Q. Wang, Q. Yao, J. Chang, L. Chen, J Mater Chem 22 (2012) 17612–17618.

[21] V.F. Puntes, K.M. Krishnan, A.P. Alivisatos, Science 291 (5511) (2001) 2115-7.

[22] H.T. Zhu, J. Luo, J.K. Liang, G.H. Rao, J.B. Li, J.Y. Zhang, Z.M. Du, Physica B: Condensed Matter, 403 (2008) 3141–3145.

[23] V. Siva, S.S. Sahu, D.P. Datta, P.C. Pradhan, M. Nayak, V. Solanki, D. Topwal, K. Senapati, P.K. Sahoo, J Alloys Compd 680 (2016) 722–728.

[24] N. Nasralla, W Abdelrhman, G El Komy, G Turky, E.J.Chem. 68(3) (2025) 511-524

…..ಞ*ಞ…..

# Chapter 9

# Conclusion & Recommendations

## 9.1 Conclusion

Magnetic cooling technology based on solid state materials as magnetic refrigerants is developing as an environmentally friendly, cheap technology which enhance energy efficiency and eliminates all toxic refrigerant gases that drive global warming. Our research focuses on tuning the magnetocaloric properties of nanomagnetic materials for magnetic refrigerant application. The synthesis, structural, magnetic, and magnetocaloric properties of the materials are thoroughly detailed in the previous chapters. Numerous research has been reported on the MCE properties of perovskites, while only a few reports are available for ferrites and metal nanocomposites. We have selected three systems of materials, perovskites, ferrites, and nanocomposites, to investigate the MCE properties and to develop a magnetic refrigerant material. As a part of the investigation, primarily the structural and magnetic properties of the samples were characterised and analysed. Following the magnetic characterisation, the temperature-dependent magnetisation was performed to identify the possible magnetic phase transitions in the measured temperature range from the ZFC-FC curves. Then magnetisation isotherms were recorded in the vicinity of the transition temperature. The magnetic entropy change ($-\Delta S_m$) is subsequently calculated from the magnetisation isotherms and finally identified a potential magnetic refrigerant material. The adiabatic temperature change ($\Delta T_{ad}$) is estimated indirectly from $\Delta S_m$ and specific heat capacity values ($\Delta C_H$). This methodology was adopted in our research work.

***Perovskite Manganites***

The perovskite manganites are of great interest among the near room temperature MCE materials. According to the literature, the lanthanum sodium manganite exhibits an appreciable magnetic entropy change near room temperature. So, we have chosen the lanthanum sodium manganite $La_{0.5}Na_{0.5}MnO_3$ as the parent element to investigate the MCE properties. It is evident from the literature that cobalt substitution for Mn in lanthanum manganite can modify the structural and

magnetic properties of lanthanum manganites. So, cobalt is substituted for Mn in $La_{0.5}Na_{0.5}MnO_3$ and these samples were synthesised by a sol-gel autocombustion method. These $La_{0.5}Na_{0.5}Co_xMn_{1-x}O_3$ (x=0,0.1, 0.3,0.5, 0.7, 0.9 and 1) samples were synthesised by a novel method in which the synthesised samples were sintered for a short duration, instead of sintering for very long hours (48-72 hrs) as reported in the perovskite manganite system. The structural and magnetic properties of as prepared $La_{0.5}Na_{0.5}Co_xMn_{1-x}O_3$ samples were investigated. The structural analysis shows that the as-prepared samples crystallised in the orthorhombic symmetry, whereas, the Rietveld refinement confirmed the rhombohedral symmetry of the sintered $La_{0.5}Na_{0.5}Co_xMn_{1-x}O_3$ samples with JCPDS No (50-0298). The incomplete phase formation observed for the higher concentrations (x>0.3) of as prepared cobalt substituted samples was rectified with sintering. The HRTEM measurement is consistent with the nano behavior of the synthesised particles and confirms the structure formation. In the as prepared samples, the estimated stoichiometric ratio of La/Na is consistent with the theoretical value, while sodium volatilisation was observed in the sintered samples. The analysis of the magnetic characterisation of as prepared samples indicates a paramagnetic to ferromagnetic behaviour with the substitution of cobalt in lanthanum sodium manganite due to the cobalt phases in the cobalt rich samples. It can be observed that the magnetic properties were increased on sintering. In the sintered samples, the parent sample $La_{0.5}Na_{0.5}MnO_3$ (LNMO) is superparamagnetic with large magnetisation at room temperature. With the cobalt substitution in LNMO, the antiferromagnetic super exchange interactions exceed the double exchange interaction and show a paramagnetic behaviour at room temperature.

The ZFC-FC measurements were carried out for the $La_{0.5}Na_{0.5}Co_xMn_{1-x}O_3$ samples to look into the possible magnetic transitions. The Arrott plots constructed from the magnetisation isotherms recorded near the transition temperature confirmed the second-order magnetic phase transition. The estimated value of magnetic entropy

change from the magnetic isotherms reveals that the parent element LNMO exhibited a maximum magnetic entropy change near room temperature, 2.344 J/kg/K at 317.5 K for an applied magnetic field of 50 kOe, which is greater than the reported value. Field dependence of $|\Delta S_m|$ is observed for the LNMO samples and the estimated value of local exponent agrees with a second order magnetic phase transition of the sample. The estimated change in specific heat, $\Delta C_H$, from the magnetic isotherms is found to be negative for temperatures $T < T_c$ and positive for $T > T_c$ and it crosses over from negative to positive values near the transition temperature. The adiabatic temperature change $\Delta T_{ad}$ of 0.7K is estimated for the LNMO sample indirectly from $\Delta S_m$ and $\Delta C_H$ values. A maximum entropy change $|\Delta S_m|$ of 1.591 J/kg/K, 1.583 J/kg/K and 0.298 J/kg/K is obtained for $La_{0.5}Na_{0.5}Mn_{1-x}Co_xO_3$ for x=0.1, 0.3 and 0.7 (LNCMO1, LNCMO3 and LNCMO7) samples respectively at an applied field of 50kOe. Eventhough the $|\Delta S_m|$ values decreased with increase in cobalt concentration, the relative cooling power RCP attains a maximum of 150 J/kg for the LNCMO1 sample, and then it decreases with cobalt substitution. The cobalt substitution in LNMO decreases the temperature corresponding to the maximum $\Delta S_m$ from 312.5 K to 130 K when x changes from 0 to 0.7. The critical behaviour analysis of magnetisation isotherms is done in accordance with the Mean field theory. The critical exponents $\beta=0.43$, $\gamma=1.00$ and $\delta=2.8$ evaluated for the LNMO sample are consistent with the Mean field theory, confirmed the long range interaction associated with a second order phase transition. For the other samples LNCMO1, LNCMO3, LNCMO7 the critical behavioural analysis does not match with the Mean Field Theory. The cytotoxicity measurement of the sample LNMO on normal cells (8% cell death) confirmed the biocompatibility of the samples while 29% of cell death was obtained for tumour cells. The combination of these properties with the material's magnetocaloric characteristics near room temperature highlights its potential for biomedical applications like hyperthermia treatment of cancer/tumour cells. Our research on the investigation of $La_{0.5}Na_{0.5}Co_xMn_{1-x}O_3$ is being reported for the first time since the structural,

magnetic, and MCE characteristics of $La_{0.5}Na_{0.5}Co_xMn_{1-x}O_3$ nanoparticles are not available in literature.

***Ferrites***

Copper ferrite and cobalt ferrite are the two attractive members of the spinel ferrite group because of their intriguing structural and magnetic properties. Literature suggests that the zinc substitution can change the magnetic properties of copper ferrite. This thesis mainly focuses on the effect of magnetic and nonmagnetic cation substitution in copper ferrite nanoparticles. The structural and magnetic properties of $Cu_{1-x}Zn_xFe_2O_4$ and $Cu_{1-x}Co_xFe_2O_4$ nanoparticles synthesised by a modified sol-gel autocombustion method were investigated.

The structural analysis of $Cu_{1-x}Co_xFe_2O_4$ samples reveals a structural change from tetragonal to cubic with the substitution of cobalt in copper ferrite. The HRTEM measurement confirmed the nanocrystalline behaviour of the synthesised samples. The EDAX spectrum confirmed the stoichiometry of the $Cu_{1-x}Co_xFe_2O_4$.The magnetic analysis reveals that the samples exhibited a ferromagnetic behaviour at room temperature and magnetisation, the coercivity and anisotropic constant were increased at a lower temperature by 10 times that of room temperature. The MCE properties of $Cu_{1-x}Co_xFe_2O_4$ samples were investigated and the cobalt substitution is found to increase the magnetic entropy change $|\Delta S_m|$ from 0.11 J/kg/K to 0.324 J/kg/K for an applied magnetic field of 50 kOe. Among the $Cu_{1-x}Co_xFe_2O_4$ series, CuCo7(x=0.7) exhibits a maximum $|\Delta S_m|$ of 0.324 J/kg/K near room temperature, at 297.5 K.

The structural analysis of $Cu_{1-x}Zn_xFe_2O_4$ samples reveals a structural change from tetragonal to cubic with the substitution of zinc in copper ferrite. The HRTEM measurement confirmed the nanocrystalline behaviour of the synthesised samples. The EDAX spectrum confirmed the stoichiometry of the $Cu_{1-x}Zn_xFe_2O_4$. The magnetic characterisation reveals the ferromagnetic behaviour of copper ferrite and

the superparamagnetic behaviour of the samples with the substitution of zinc in copper ferrite at room temperature and at a lower temperature. The maximum magnetisation also increases with the zinc substitution up to x=0.3 in $Cu_{1-x}Zn_xFe_2O_4$ and it enhances at a lower temperature of 5 K. The ZFC -FC measurements recorded in the lower temperature region indicate that the transition temperature decreases to room temperature with increase in zinc substitution. It should be noted that in the $Cu_{1-x}Zn_xFe_2O_4$ series of samples, as zinc concentration increases, the magnetic entropy change increases in the recorded temperature region, 260 K-360 K, for an applied field of 50 kOe. The peaking temperature corresponding to maximum magnetic entropy change decreases with the zinc substitution in copper ferrite, and the blocking temperature of the zinc rich sample, $Cu_{0.4}Zn_{0.6}Fe_2O_4$, falls in the room temperature region. The maximum entropy change of 0.917 J/kg/K has been observed for the sample with x=0.6 concentration at 297.5 K under an applied field of 50 kOe

So, it can be concluded from the investigations of magnetocaloric properties of ferrite samples that the copper ferrite exhibits a maximum $-\Delta S_m$ of 0.11 J/kg/K near room temperature, which is one of the rare reports of magnetocaloric properties of copper ferrite. Among the $Cu_{1-x}Co_xFe_2O_4$ series of samples $Cu_{0.3}Co_{0.7}Fe_2O_4$ and $Cu_{0.1}Co_{0.9}Fe_2O_4$ can be used for magnetic refrigerant applications near and above room temperature. Among the $Cu_{1-x}Zn_xFe_2O_4$ samples $Cu_{0.4}Zn_{0.6}Fe_2O_4$ exhibits maximum entropy and hence it can have magnetic refrigerant application near room temperature. It is evident from our work that the $Cu_{1-x}Zn_xFe_2O_4$ samples are potential candidates for magnetic refrigerant applications near room temperature than $Cu_{1-x}Co_xFe_2O_4$ samples.

***Cobalt Nanocomposites***

Magnetic nanocomposite synthesised in a polystyrene matrix exhibits unique magnetic properties as they exhibit the properties of both magnetic nanoparticles and nonmagnetic polystyrene matrix. The physical properties of

nanocomposite can be tuned by embedding metal nanoparticles into a polystyrene matrix. In the present work cobalt nanocomposites were synthesised by ion exchange method. The synthesis, structural magnetic and magnetocaloric properties of cobalt nanocomposites were investigated in the present work.

Cobalt nanocomposites were fabricated by embedding cobalt metal nanoparticles in polystyrene resins by the ion exchange reduction method. The structural analysis reveals that the cobalt nanocomposites crystallise in the hcp and fcc phases. Additional peaks of $Co_3O_4$ were observed in the XRD pattern. The FTIR spectrum confirmed the incorporation of cobalt metal nanoparticles in the polystyrene matrix. The Co Re exhibits a superparamagnetic behaviour of the sample at room temperature and a spin glass behaviour at a lower temperature 10K. The ZFC -FC curves of the CoRe sample indicate a magnetic transition at a higher temperature. The magnetocaloric properties were examined from the magnetisation isotherms recorded in the lower temperature range. A maximum entropy change of 0.037 J/kg/K is observed at 297 K for cobalt nanocomposites. However, the magnetic properties of cobalt nanoparticles were reported in the literature, the magnetocaloric properties of cobalt resin are reporting for the first time in the present work.

In the present investigation, we have synthesised three nanomagnetic systems which are tuned for their MCE characteristics. The MCE properties of the synthesised perovskites ($La_{0.5}Na_{0.5}Co_xMn_{1-x}O_3$), ferrites $Cu_{1-x}B_xFe_2O_4$(B=Co/Zn) and nanocomposite samples (cobalt polystyrene) are listed in Table 1.

**Table 1.** Summary of MCE of synthesised Perovskites.

| Sample | Magnetic Entropy Change ($Jkg^{-1}K^{-1}$) | | | | | Transition Temperature (K) | | | | | RCP ($Jkg^{-1}$) |
|---|---|---|---|---|---|---|---|---|---|---|---|
| | 10kOe | 20kOe | 30kOe | 40kOe | 50kOe | 10kOe | 20kOe | 30kOe | 40kOe | 50kOe | |
| LNMO AP | 0.104 | 0.101 | 0.098 | 0.095 | 0.487 | 155 | 155 | 155 | 155 | 155 | - |
| **LNMO** | 0.612 | 1.122 | 1.566 | 1.973 | **2.344** | 312.5 | 312.5 | 317.5 | 317.5 | 317.5 | 103 |
| LNCMO1 | 0.368 | 0.727 | 0.956 | 1.316 | 1.591 | 212.5 | 212.5 | 212.5 | 217.5 | 222.5 | 150 |
| LNCMO3 | 0.366 | 0.743 | 1.052 | 1.328 | 1.583 | 185 | 185 | 185 | 185 | 185 | 188 |
| LNCMO7 | 0.036 | 0.22 | 0.147 | 0.082 | 0.03 | 135 | 145 | 145 | 145 | 145 | - |

**Table 2.** Summary of MCE of synthesised Ferrite and composites.

| Sample | Magnetic Entropy Change($Jkg^{-1}K^{-1}$) | | | | Transition Temperature (K) | | | |
|---|---|---|---|---|---|---|---|---|
| | 20 kOe | 30 kOe | 40 kOe | 50 kOe | 20 kOe | 3 kOe | 40 kOe | 50 kOe |
| CuFe | 0.045 | 0.068 | 0.09 | 0.113 | 312.5 | 312.5 | 312.5 | 312.5 |
| CuCo1 | 0.048 | 0.079 | 0.112 | 0.143 | 347.5 | 347.5 | 347.5 | 347.5 |
| CuCo4 | 0.084 | 0.138 | 0.194 | 0.25 | 352.5 | 352.5 | 352.5 | 352.5 |
| CuCo5 | 0.186 | 0.228 | 0.27 | 0.313 | 347.5 | 347.5 | 347.5 | 347.5 |
| CuCo7 | 0.097 | 0.17 | 0.246 | 0.324 | 297.5 | 297.5 | 297.5 | 297.5 |
| CuCo8 | 0.067 | 0.117 | 0.17 | 0.23 | 297.5 | 297.5 | 297.5 | 297.5 |
| CuCo9 | 0.111 | 0.184 | 0.259 | 0.322 | | 382.5 | | |
| CoFe | 0.094 | 0.157 | 0.225 | 0.295 | 352.5 | 352.5 | 352.5 | 352.5 |
| CuZn1 | 0.122 | 0.189 | 0.256 | 0.321 | 357.5 | 357.5 | 357.5 | 357.5 |
| CuZn2 | 0.22 | 0.319 | 0.417 | 0.466 | | 352.5 | | |
| CuZn3 | 0.235 | 0.355 | 0.478 | 0.581 | 292.5 | 292.5 | 292.5 | 300 |
| CuZn4 | 0.25 | 0.439 | 0.581 | 0.742 | | 332.5 | | |
| CuZn5 | 0.355 | 0.517 | 0.68 | 0.844 | | 302.5 | | |
| **CuZn6** | 0.375 | 0.554 | 0.732 | **0.917** | | **297.5** | | |
| **CoRe** | | | | 0.037 | | | | 297 |

When comparing the MCE properties of the perovskite and ferrite samples, it is observed that the LNMO sample exhibits the maximum $-\Delta S_m$ near room temperature. It also exhibits an adiabatic temperature change of 0.7 K. In the ferrite system, CuZn6 exhibits a maximum entropy change of 0.917 J/kg/K at 297.5 K which is an appreciable value among the ferrite groups. In this research work, LNMO, synthesised by an easy and simple method involving short sintering period , is identified as a promising candidate for magnetic refrigerant application near room temperature.

The MCE applications of the samples synthesised in this research are listed below.

- All samples including the as-prepared samples exhibited MCE characteristics.
- $La_{0.5}Na_{0.5}MnO_3$ ($LNMO_)$ can be used for magnetic refrigerant applications near room temperature. The biocompatibility of LNMO and its cytotoxic behaviour against tumour cells points towards the possible biomedical applications of the sample.
- LNCMO samples can be tuned for magnetic refrigerant applications over a wide temperature range of 324 K to 135 K.
- $CuFe_2O_4$, CuZn3, CuZn5 and CuZn6 synthesised by an easy and cost-effective method can be used for magnetic refrigerant application near room temperature.
- $Cu_{1-x}Co_xFe_2O_4$ samples can be used in magnetic storage devices, magnetic heat pump and hyperthermia applications
- CoRe sample exhibits a low value of magnetic entropy change near room temperature. However, it can be used as soft magnets.

## 9.2 Recommendations

Our research work advances the knowledge of temperature-dependent magnetisation and magnetocaloric properties of lanthanum sodium manganite perovskites, cobalt and zinc substituted copper ferrite and cobalt nanocomposites, providing information on the potential of a material as a magnetic refrigerant. The future recommendations of our research are listed below.

- ***Optimisation of materials:***

  Further studies can focus on the doping of cobalt instead of substitution to tune the magnetocaloric properties accurately to room temperature. Other transition elements like calcium, presmodium, and barium can be substituted to tune the MCE property to an enhanced value.

- ***Computational Simulations:***

  Advanced computational simulations can be used to model and anticipate magnetocaloric properties with much more accuracy.

- ***Device level applications***

  Integration of the prepared nanomagnetic materials: lanthanum sodium manganite perovskite/ferrite/nanocomposites as magnetic refrigerant materials in prototype magnetic refrigerator.

…..ര*ര…..